

**NONLINEAR STABILITY ANALYSIS OF FRAME-TYPE STRUCTURES  
WITH RANDOM GEOMETRIC IMPERFECTIONS USING A  
TOTAL-LAGRANGIAN FINITE ELEMENT FORMULATION**

by

J.E. WARREN, Jr.

Dissertation submitted to the Faculty of the  
Virginia Polytechnic Institute and State University  
in partial fulfillment of the requirements for the degree of  
Doctor of Philosophy  
in  
Engineering Mechanics

APPROVED:

S. Thangjitham, Chairman

S. M. Holzer

D. T. Mook

D. H. Morris

R. H. Plaut

January, 1997  
Blacksburg, Virginia

Keywords: Finite Element, Nonlinear, Stability, Imperfection, Reliability

Copyright 1997, J.E. Warren

**NONLINEAR STABILITY ANALYSIS OF FRAME-TYPE STRUCTURES  
WITH RANDOM GEOMETRIC IMPERFECTIONS USING A  
TOTAL-LAGRANGIAN FINITE ELEMENT FORMULATION**

by

J.E. Warren, Jr.

Committee Chairman: S. Thangjitham  
Engineering Science and Mechanics

**Abstract**

With the increasing use of lightweight frame-type structures that span long distances, there is a need for a method to determine the probability that a structure having random initial geometric imperfections will become unstable at a load less than a specified fraction of the perfect critical load. The overall objective of this dissertation is to present such a method for frame-type structures that become unstable at limit points. The overall objective may be broken into three parts. The first part concerns the development of a three-dimensional total Lagrangian beam finite element that is used to determine the critical load for the structure. The second part deals with a least squares method for modeling the random initial imperfections using the mode shapes from a linear buckling analysis, and a specified maximum allowable magnitude for the imperfection at any imperfect node in the structure. The third part deals with the calculation of the probability of failure using a combined response surface/first-order second-moment method. Numerical results are presented for two example problems, and indicate that the proposed method is reasonably accurate. Several problems with the proposed method were noted during the course of this work and are discussed in the final chapter.

## **Acknowledgements**

I would like to thank my advisor Dr. Surot Thangjitham for his support during the course of this work. Special thanks are due to Professor S.M. Holzer who has provided excellent guidance throughout my undergraduate and graduate career. Also, special thanks are due to Professor N.E. Dowling, Professor R.W. Landgraf, and Professor R.A. Heller for the advice and guidance they have given me during the time I have spent in the Department of Engineering Science and Mechanics. I would also like to extend my thanks to Professor D.T. Mook, Professor D.H. Morris, and Professor R.H. Plaut for taking the time to review my work and serve on my committee.

I would also like to thank the many good friends that I have had during my stay at VPI&SU. Without their friendship this work would not have been possible. Thanks are also due to Ford Motor Company for the Silicon Graphics workstations and the College of Engineering for the use of the Silicon Graphics Power Challenge. This work would not have been possible without these systems. I would also like to thank the Department of Engineering Science and Mechanics for allowing me to teach class during my stay at VPI&SU. The experience was very rewarding and contributed a great deal to my education.

Finally, I would like to dedicate this dissertation to my parents and thank them for standing by me throughout my entire life. Without their guidance I would never have come this far. I can never express how much their support has meant to me.

## Table of Contents

<b>List of Figures</b> .....	vii
<b>List of Tables</b> .....	x
<b>INTRODUCTION</b> .....	1
1.1 Objectives .....	2
<b>LITERATURE REVIEW</b> .....	5
2.1 Three-Dimensional Beam Finite Elements .....	5
2.2 Solution of Nonlinear Systems of Equations .....	7
2.3 Reliability and Response Surface Methods .....	9
2.4 Buckling with Random Initial Imperfections .....	10
2.4.1 Imperfection Modeling .....	12
2.4.2 Use of Imperfections .....	14
<b>EQUILIBRIUM EQUATIONS</b> .....	17
3.1 Preliminaries .....	18
3.2 Displacement Functions .....	24
3.3 Rotation Matrices .....	28
3.4 Strain-Displacement Relationships .....	33
3.5 Equilibrium Equations .....	40
<b>INCREMENTAL EQUILIBRIUM EQUATIONS</b> .....	52
4.1 Incremental Displacement Functions .....	52
4.2 Incremental Strain-Displacement Relationships .....	54
4.3 Incremental Equilibrium Equations .....	57
4.4 Local to Global Transformation .....	68
4.5 Numerical Solution Techniques .....	74
4.5.1 Newton-Raphson Method .....	75

4.5.2 Riks-Wempner Method on a Normal Plane .....	77
4.5.3 Riks-Wempner Method on a Sphere .....	84
4.5.4 Convergence Criteria .....	88
4.6 Example Problems .....	90
4.6.1 Single Element Eigenvalue Test .....	90
4.6.2 Cantilever Beam with a Concentrated End Moment .....	90
4.6.3 Cantilever Beam with a Concentrated End Load .....	93
4.6.4 45-Degree Circular Bend .....	93
4.6.5 Williams' Toggle Frame .....	96
4.6.6 12-Member Hexagonal Frame .....	96
4.6.7 24-Member Hexagonal Star-Shaped Shallow Cap .....	100
<b>RELIABILITY ANALYSIS AND RESPONSE SURFACE METHODS .....</b>	<b>104</b>
5.1 Concepts of Reliability .....	105
5.2 First-Order Second-Moment Method .....	109
5.3 Least Squares Analysis .....	114
5.3.1 Linear Approximation .....	114
5.3.2 Quadratic Approximation .....	117
5.4 Experimental Designs .....	118
5.4.1 Two-Level Factorial Designs .....	118
5.4.2 Central Composite Design .....	120
5.4.3 Two-Level Fractional Factorial Designs .....	123
5.5 Significance of Individual Regression Coefficients .....	125
5.6 Modeling of the Performance Function .....	127
5.6.1 Linear Model .....	127
5.6.2 Quadratic Model .....	129
<b>STABILITY ANALYSIS WITH RANDOM IMPERFECTIONS .....</b>	<b>133</b>
6.1 Imperfection Modeling .....	133
6.2 Reliability Analysis .....	137
6.2.1 Definition of the Limit State .....	137
6.2.2 Response Surface/First-Order Second-Moment Method .....	138
6.3 Example Problems .....	139
6.3.1 Example 1: Williams' Toggle Frame .....	139

6.3.1.1 Case 1: 10 mode imperfection .....	140
6.3.1.2 Case 2: 6 mode imperfection .....	150
6.3.2 Example 2: Star-Shaped Cap .....	158
<b>CONCLUSIONS AND FURTHER RESEARCH .....</b>	<b>170</b>
7.1 Conclusions .....	170
7.2 Further Research .....	174
<b>REFERENCES .....</b>	<b>176</b>
<b>APPENDIX A: FIRST VARIATION OF ROTATION AND DERIVATIVE OF ROTATION MATRICES .....</b>	<b>183</b>
A.1 First Variation of the Rotation Matrix .....	183
A.2 First Variation of the Derivative of the Rotation Matrix .....	186
<b>APPENDIX B: EXPANSION AND LINEARIZATION OF THE LARGE ROTATION MATRIX .....</b>	<b>194</b>
<b>APPENDIX C: EXPANSION AND LINEARIZATION OF THE DERIVATIVE OF THE LARGE ROTATION MATRIX .....</b>	<b>202</b>
<b>VITA .....</b>	<b>212</b>

## List of Figures

Figure 3.1 Large deformation of a body from the initial configuration, 0, to the final configuration, 2. ....	19
Figure 3.2 Coordinate systems for a three-dimensional beam. ....	25
Figure 3.3 Typical cross-sectional plane for a three-dimensional beam. ....	26
Figure 3.4 Two-node three-dimensional beam finite element and the corresponding parent element. ....	48
Figure 3.5 Matrices $\mathbf{N}_{u'_o}$ , $\mathbf{N}_\phi$ , and $\mathbf{N}_{\phi'}$ from the partitioned matrix <b>SHPMAT</b> . ....	50
Figure 4.1 Large deformation of a body from the initial configuration, 0, to an intermediate configuration, 1, and a small deformation from configuration, 1, to the final configuration, 2. ....	53
Figure 4.2 Matrices <b>EPSMA</b> , <b>EPSMB</b> , and <b>EPSMC</b> from the partitioned matrix <b>EPSM</b> . ....	58
Figure 4.3 Matrices <b>RSAA01</b> , <b>RSAB01</b> , and <b>RSAC01</b> from the partitioned matrix <b>RSA01</b> . ....	63
Figure 4.4 Matrix <b>RSBA01</b> from the partitioned matrix <b>RSB01</b> . ....	64
Figure 4.5 Matrices <b>RSBB01</b> and <b>RSBC01</b> from the partitioned matrix <b>RSB01</b> . ....	65
Figure 4.6 Global orientation of a three-dimensional finite element. ....	69
Figure 4.7 Newton-Raphson method for a single degree-of-freedom system. ....	76
Figure 4.8 Riks-Wempner method on a normal plane for a single degree-of-freedom system. ....	78
Figure 4.9 First iteration for the Riks-Wempner method. ....	81
Figure 4.10 Riks-Wempner method on a sphere for a single degree-of-freedom system. ....	85

Figure 4.11 Geometry for the single element eigenvalue test. ....	91
Figure 4.12 Load-deflection curves for the cantilever with a concentrated end moment. ....	92
Figure 4.13 Load-deflection curve for the cantilever beam with a concentrated end load. ....	94
Figure 4.14 Load-deflection curves for the 45-degree circular bend. ....	95
Figure 4.15 Load-deflection curves for Williams' toggle frame. ....	97
Figure 4.16 Geometry for the 12-member hexagonal frame. ....	98
Figure 4.17 Load-deflection curves for the 12-member hexagonal frame; demonstrating convergence of the proposed formulation. ....	99
Figure 4.18 Load-deflection curves for the 12-member hexagonal frame using the proposed formulation and ABAQUS. ....	101
Figure 4.19 Geometry for the 24-member shallow reticulated cap. ....	102
Figure 4.20 Load-deflection curves for the 24-member shallow cap. ....	103
Figure 5.1 Probability distributions of supply and demand (Ang and Tang 1984). ....	106
Figure 5.2 Probability density function for the safety margin $G$ (Ang and Tang 1984). ....	108
Figure 5.3 The Central Composite Design for Three Variables (Myers 1995). ....	122
Figure 6.1 Linear buckling modes 1-5 for Williams' toggle frame. ....	141
Figure 6.2 Linear buckling modes 6-10 for Williams' toggle frame. ....	142
Figure 6.3 Frequency density diagram for the full 10 mode simulation for Williams' toggle frame. ....	146
Figure 6.4 Cumulative distribution functions, for the 10 mode case, for Williams' toggle frame. ....	148
Figure 6.5 Frequency density diagram for the 10/3 mode simulation data for Williams' toggle frame. ....	151



Figure 6.6 Frequency density diagram for the 6 mode simulation for Williams' toggle frame. ....	156
Figure 6.7 Cumulative distribution functions for the 6 mode case for Williams' toggle frame. ....	157
Figure 6.8 Frequency density diagram for the 6/2 mode simulation for Williams' toggle frame. ....	159
Figure 6.9 Frequency density diagram for the 20 mode simulation for the shallow reticulated cap. ....	166
Figure 6.10 Cumulative distribution functions for the shallow reticulated cap. ....	167
Figure 6.11 Frequency density diagram for the 10 mode simulation for the shallow reticulated cap. ....	168
Figure A.1 Expanded form of the first derivative of the rotation matrix. ....	187
Figure A.2 Matrices <b>OMGM1</b> and <b>RM1</b> from the matrix expression for the first variation of the derivative of the rotation components. ....	188
Figure A.3 Matrix <b>PHPM1</b> required for the calculation of ${}^2\omega$ . ....	190
Figure A.4 Final expression for the variation of the first derivative of the rotation matrix. ....	193
Figure B.1 Matrices ${}^1\mathbf{R}_{III}$ and $\mathbf{R}_{III}$ from the expansion of the matrix ${}^2\mathbf{R}_{III}$ . ....	196
Figure B.2 Matrix <b>RDM01</b> from the expression for the vector $\mathbf{\tilde{R}}_D$ . ....	201
Figure C.1 Matrix <b>OMGM01</b> from the expression for ${}_0\mathbf{\tilde{R}}'_A$ . ....	204
Figure C.2 Matrix <b>DDM01</b> from the expression for $\mathbf{\tilde{D}}_D$ . ....	210

## List of Tables

Table 6.1	Modal variances for the 10 mode case for Williams' toggle frame. ....	143
Table 6.2	Calculated failure probabilities, for the 10 mode case for Williams' toggle frame, using simulation data and the RS/FOSM method. ....	144
Table 6.3	RS/FOSM results for the 10 mode case for Williams' toggle frame, with $\lambda_{frac}$ equal to 0.968. ....	145
Table 6.4	Values of $t_0$ for the 10 modal imperfection amplitudes for Williams' toggle frame. ....	149
Table 6.5	Modal variances for the 6 mode case for Williams' toggle frame. ....	152
Table 6.6	Calculated failure probabilities, for the 6 mode case for Williams' toggle frame, using simulation data and the RS/FOSM method. ....	153
Table 6.7	RS/FOSM results for the 6 mode case for Williams' toggle frame, with $\lambda_{frac}$ equal to 0.95. ....	155
Table 6.8	Modal variances for the 20 mode analysis for the shallow reticulated cap. ....	161
Table 6.9	Modal ranking and direction cosines for the 20 modal imperfection amplitudes for the shallow reticulated cap. ....	163
Table 6.10	Calculated failure probabilities, for the 20 mode analysis for the shallow reticulated cap with a 4 mm imperfection, using simulation data and the RS/FOSM method. ....	164
Table 6.11	RS/FOSM results for the 10 mode analysis for the shallow reticulated cap, with $\lambda_{frac}$ equal to 0.94. ....	165

# **CHAPTER 1**

## **INTRODUCTION**

Over the years, a lot of research has centered around determining the effects of initial imperfections on the stability of a structure. Interest in this area began to grow when investigators found large discrepancies between theoretical buckling loads and actual experimental results. Koiter (1945) hypothesized that all structures have some form of small initial imperfections, in spite of how carefully they were manufactured, and that it is these small unavoidable imperfections that cause the large differences between theoretical and experimental results. Koiter (1945) went on to identify two specific types of instability that cause structures to be sensitive to geometric imperfections. The first is bifurcation at an unstable symmetric bifurcation point, and the second is bifurcation at an unstable asymmetric bifurcation point. The most common form of instability occurs at a limit point and is not as sensitive to geometric imperfections (El Naschie 1991), but a significant variation in the critical load can still occur for realistic imperfections.

Since the work of Koiter (1945), the imperfection sensitivity of various types of structures has been analyzed. Analysis of the imperfection sensitivity of cylindrical shells and stiffened cylindrical shells has been the focus of most of this work. An extensive review of work pertaining to perfect and imperfect analysis of cylindrical shells can be found in the review paper by Simitses (1986). Various types of analyses have been proposed for examining the distribution of the critical load for cylindrical shells with random geometric imperfections. Most of these analyses determine the mean values and

variances of the imperfections using imperfection data from previously manufactured shells of a similar type. Very few results have been presented for structures where the shape and magnitude of the initial imperfections is not known. These types of structures include one-of-a-kind structures where there is no prior experience with the different types of possible geometric imperfections.

Some of the more interesting types of structures are lattice domes or shallow reticulated caps that span long distances. These structures function as space frames, and are often used in place of continuous shell-type structures. The most common mode of failure for these structures is instability, which occurs at a limit point. The complex geometry used in the design of reticulated structures usually prevents a closed form solution for the critical load. Large deformations before the limit point require a geometrically nonlinear finite element analysis to determine the critical load.

Most reticulated structures are one-of-a-kind type structures where little if any knowledge is known about the initial geometric imperfections. Since most of these structures become unstable at a limit point, the imperfect critical load will not be extremely sensitive to geometric imperfections. However, from a probabilistic standpoint, the variation in the critical load is important when calculating the reliability of the structure. If a maximum tolerance for the initial imperfection at any point on the structure is specified, the resulting distribution of the critical load may be approximated using probabilistic methods.

## **1.1 OBJECTIVES**

The objective of this work is to investigate the distribution of the critical load, due to random initial imperfections, for frame-type structures that become unstable at limit points. The distribution of the critical load is found by determining the probability that the

critical load will be less than specified fractions of the perfect critical load. The above objective may be broken into three parts. The first part concerns the development of a three-dimensional total Lagrangian beam finite element that will be used to determine the critical load for the structure. The second part deals with a least squares method for applying initial imperfections to a structure using the mode shapes from a linear buckling analysis, and a specified tolerance for the maximum allowable imperfection at any single point on the structure. The third part addresses the problem of approximating the probability that the structure will become unstable at a load less than a specified fraction of the perfect critical load.

Chapter 2 contains a short review of the references that were most helpful in carrying out the above objective. The first section deals with existing nonlinear three-dimensional beam finite element formulations, and the second deals with the solution of nonlinear systems of equations. The third section contains the references that were most useful for reliability and response surface methods. The fourth section contains a brief review of some of the more interesting work dealing with stability of structures having initial geometric imperfections.

The third chapter describes in detail the development of the equilibrium equations for a total Lagrangian formulation of a three-dimensional nonlinear beam finite element that allows large cross-sectional rotations. The resulting finite element is required for the calculation of the critical load for the structure. Chapter 3 also includes all of the matrices required for programming of the proposed element.

The fourth chapter deals with solution of the nonlinear system of equations that result from the finite element formulation presented in Chapter 3. The first part of the chapter contains the incremental form of the equilibrium equations and the second presents three numerical solution techniques to solve nonlinear systems of equations. The third

part of Chapter 4 contains some example problems to test the proposed finite element formulation and the solution technique for the nonlinear system of equations.

Chapter 5 covers reliability methods and response surface methods. The first portion of Chapter 5 covers the first-order second-moment method which is used to approximate the probability of failure for a system. The second part of the chapter deals with response surface methods. These methods are used to approximate the performance or output of a system using simple polynomial relationships. The last part of Chapter 5 covers the combined use of the first-order second-moment method and the response surface method. The response surface method is used to generate an approximate expression for the performance of a system which is then used by the first-order second-moment method to calculate the probability of failure.

Chapter 6 describes the proposed technique for modeling initial geometric imperfections and then demonstrates how the technique is used to calculate the probability of failure for two different structures. The first part of the chapter presents an imperfection modeling scheme which is based on a least squares distribution of the geometric imperfections using linear buckling modes as imperfection shapes. The resulting imperfections are then used to modify the nodal coordinates of the perfect structure. The second part of the chapter covers the specific use of the response surface/first-order second-moment method for calculating the probability of failure. The final part of Chapter 6 demonstrates the proposed technique on two example problems: Williams' toggle frame and a 24-member star-shaped shallow reticulated cap.

The seventh chapter discusses some of the results and trends from the examples presented in Chapter 6. Also, Chapter 7 discusses some of the problems with the proposed method and some recommendations for future work in the area of probabilistic stability analysis of structures with random initial geometric imperfections.

## **CHAPTER 2**

### **LITERATURE REVIEW**

Investigation of the stability of an imperfect geometrically nonlinear frame-type structure requires knowledge of nonlinear finite element analysis, solution of large systems of nonlinear equations, reliability methods, and techniques for modeling initial imperfections. Using each of these tools, it is possible to examine the distribution of the critical load for a structure having random initial geometric imperfections.

#### **2.1 THREE-DIMENSIONAL BEAM FINITE ELEMENTS**

Over the years, various researchers have proposed different finite element formulations for the analysis of space-frame structures. Oran (1973, 1976) pointed out that a large rotation in three-dimensional space cannot be treated as a vector. Oran (1973) also noted some of the problems with formulations from earlier works and mentioned that these formulations would only be good for small displacements because of the way that rotations were treated during the analysis. Oran (1973) presented a corotational formulation in which the rotations and translations of the joints were large, but the basic force-displacement relationships for each member were based on conventional beam-column theory. This type of method assumes that deformations within a given load increment are small.

Significant progress in the analysis of space-frame structures came when Bathe and Bolourchi (1979) and Bathe (1982) introduced an updated Lagrangian and a total

Lagrangian formulation for a large deformation, large rotation beam finite element. Once again, Bathe and Bolourchi (1979) note the difficulty of the problem due to large rotations. In both the updated and the total Lagrangian formulations, Bathe and Bolourchi (1979) use Euler angles to define the rotations of the beam and conclude that the updated formulation is computationally more efficient because less effort is required to calculate the strain-displacement transformation matrix.

More recent research in the formulation of finite elements for the analysis of space-frames has focused on the use of total Lagrangian formulations with alternative parametrizations for the large rotations. The equilibrium equations for large deformation and large rotation analysis of a three-dimensional beam were presented by Novozhilov (1953). In this work, Novozhilov notes that the cross-sectional rotations are equivalent to the large rotations of a rigid body and suggests that Euler angles may be used to solve the problem. As mentioned above, Bathe and Bolourchi (1979) found that the total Lagrangian formulation was very inefficient when combined with the use of Euler angles. As an alternative, Fellipa and Crivelli (1991) and Crivelli (1991) introduced a formulation that allowed the use of alternative rotational parameters such as the rotational vector or Euler parameters. The results presented by Crivelli (1991) are based on a formulation that uses Euler parameters, but specific mention is made of a formulation that would include the rotational vector. Crivelli (1991) concludes that his constant curvature formulation using Euler parameters is superior to the formulation using the rotational vector but provides no numerical results to support his conclusion. The work presented by Crivelli (1991) was later duplicated by Ibrahimbegovic et al. (1995) which presented their version of a total Lagrangian formulation using the rotational vector. One interesting addition is a rescaling factor for the magnitude of the total rotation. The proposed rescaling factor cures the problem of non-uniqueness near the total rotation magnitude  $\pi$ .



## **2.2 SOLUTION OF NONLINEAR SYSTEMS OF EQUATIONS**

Large deformation analysis of space-frame structures requires solution of a nonlinear system of equations. Nonlinear systems of equations are most commonly solved using iterative incremental techniques where small incremental changes in displacement are found by imposing small incremental changes in load on the structure. The resulting solutions are used to plot a curve in space, which is referred to as the equilibrium path for the structure. An excellent review of solution techniques for nonlinear finite element analysis is given by Crisfield and Shi (1991). Explanation and details of implementation, for the most popular solution techniques, are given by Crisfield (1991). The most common technique for solving nonlinear finite element equations is the Newton-Raphson method. The Newton-Raphson method is famous for its rapid convergence but is known to fail at points (limit points) on the equilibrium path where the Jacobian (tangent stiffness) is singular or nearly singular. Bathe and Cimento (1980) talk about some of the problems with the Newton-Raphson method and present various forms of the method that involve accelerations or line searches to maintain convergence during the solution process.

More recently, arc length methods have been used to overcome the problem of tracing the equilibrium path in the neighborhood of limit points. The arc length methods are very similar to the Newton-Raphson method except that the applied load increment becomes an additional unknown. A comparative study of arc length methods was presented by Clarke and Hancock (1990). The original idea behind the arc length method was introduced by Riks (1972, 1979) and Wempner (1971). The original method proposed by Riks and Wempner destroyed the symmetry of the finite element equations and made the numerical solution inefficient. The Riks-Wempner method was later modified by Crisfield (1981) and Ramm (1981) to retain the symmetry of the finite element equations. Both researchers proposed two methods for modifying the original

procedure of Riks and Wempner. The first constrained the iterative process to lie on a plane normal to a tangent to the equilibrium path. The second, constrained iteration to the surface of a sphere whose radius is a tangent to the equilibrium path. In both cases the length of the tangent is specified by the user. Both methods are used extensively in current finite element work. Iteration on a normal plane is the easiest solution to implement, but iteration on a sphere has proven to converge in more cases. A study of the convergence of iteration on a sphere was presented by Watson and Holzer (1983). The method was found to have quadratic convergence for a single degree-of-freedom system, and a slightly lower average rate of convergence for a 21-dimensional numerical example. The major problem with iteration on a sphere is that the technique gives two approximations to the unknown load increment and in some cases does not give a real solution at all. Crisfield (1981, 1991a) proposes a method for choosing the correct solution from the two given approximations. Meek and Tan (1984) and Meek and Loganathan (1989a,b) examined the problem of imaginary solutions and found that this problem only occurred for certain types of structures and made recommendations on how to correct the problem. Meek and Tan (1984) and Meek and Loganathan (1989a,b) also looked into the problem of determining the correct sign of the load increment in the neighborhood of limit points. The authors made some recommendations on how to choose the proper sign based on numerical results presented in the above papers. Crisfield (1991a) has also proposed a version of the spherical arc length method which is known as the cylindrical arc length method. Many of the same problems encountered with the spherical arc length method also occur when using the cylindrical arc length method.

## **2.3 RELIABILITY AND RESPONSE SURFACE METHODS**

In recent years, the popularity of probabilistic methods in engineering has grown. As a result, books have been written that contain information that was previously only available in individual journal publications or conference proceedings. The books by Thoft-Christensen and Baker (1981) and Ang and Tang (1975, 1984) contain detailed introductions to reliability theory and demonstrate the use of reliability theory for solving common engineering problems. The book by Madsen et al. (1986) presents a more advanced discussion of reliability theory as well as some new extensions that only became available after publication of the books mentioned above. All three of the text books listed above contain a historical account of current probabilistic methods and the individual references that were most significant in developing these methods.

As with probabilistic methods, engineering use of response surface methods has increased significantly in recent years. However, the theory behind response surface methods is only available in textbooks on statistics and very few examples that relate to common engineering problems are available. Some of the more popular references that deal exclusively with response methods are the books by Myers (1971), Khuri and Cornell (1987), and Myers and Montgomery (1995). Response surface methods depend heavily on designed experiments. There are many references that deal specifically with designed experiments, but two of the more recent references that link designed experiments to response surface methods are Montgomery (1991) and Myers and Montgomery (1995).

Until recently, response surface methods were used almost exclusively by statisticians and system engineers for process optimization. Over the past decade, researchers in different branches of engineering have explored the use of response surface methods in conjunction with probabilistic methods. Current probabilistic methods require the gradient of the performance of a system to assess reliability. Therefore, if an explicit

expression for the performance is not known the gradient must be approximated numerically. Numerical approximation of the gradient is a difficult task that relies on evaluating system performance at various points using physical experiments or numerical simulation. If values of system performance are difficult to obtain, then the cost of calculating the required derivatives will be high. In some cases the cost of approximating the derivatives may be so high that solution of the problem may be impractical. To overcome this problem, researchers have used response surface methods to approximate the performance of a system in a specific region of interest. Since the response surface method relies heavily on designed experiments, the error in the approximate performance is minimized and the resulting approximation can be used to calculate the reliability of the system.

The book by Casciati and Faravelli (1991) gives a complete historical account of how response surface methods have been combined with probabilistic methods to assess the reliability of structural systems. Detailed examples for the combined use of response surface methods and probabilistic methods are given by Faravelli (1989) and Faravelli (1992). Separate work by Janajreh (1992) and Janajreh et al. (1994) demonstrated the use of response surface methods to predict the storage life of rocket motors under various conditions. The work by Bucher and Borgund (1990) and Brenner and Bucher (1995) has also played a significant part in introducing the use of response surface methods for calculating system reliability.

## **2.4 BUCKLING WITH RANDOM INITIAL IMPERFECTIONS**

Very early on investigators noticed large discrepancies between theoretical and experimental buckling loads. These discrepancies were largely unexplained until the work of Koiter (1945). Koiter showed that unavoidable small imperfections in actual structures

were to blame for the large differences in theoretical and experimental results. In his theory Koiter recognized three different forms of branching: stable symmetric, unstable symmetric, and asymmetric. By introducing an imperfection parameter, Koiter (1945) found that the perfect and imperfect systems were related by a two-thirds power law for the unstable symmetric case and by a parabolic relationship for the asymmetric case. Koiter (1945) also realized that for the stable symmetric case there was no imperfection sensitivity. For the case of a limit point, which was not examined by Koiter, the imperfection reduces the critical load linearly (El-Naschie 1991). The unstable symmetric and asymmetric cases are often referred to as imperfection sensitive since small imperfections can cause a drastic decrease in the predicted critical load. Researchers have also discovered that the critical points for the unstable symmetric and asymmetric cases degenerate to limit points when imperfections are introduced.

Upon recognizing the significance of initial imperfections, research turned toward developing models of characteristic imperfections for specific structures and then using these imperfections to gain a better estimate of the critical load. Researchers quickly realized that very detailed models of the initial imperfections were necessary in order to duplicate experimental results. There have been many analytical and numerical studies (e.g., Bolotin 1958; Roorda 1972; Amazigo 1976; Elishakoff 1979; Brendel and Ramm 1980) which assume simplified forms of actual imperfections. These studies usually use a single mode representation of the imperfections in which the amplitude is allowed to vary or in some cases is treated as a random variable. Results from this type of work are useful in obtaining the imperfection sensitivity of a structure but usually do not give an accurate prediction of the actual buckling load. Also, over the years many experimental studies have been conducted. In most of the recent studies the initial geometric imperfections are measured very carefully and are then stored, along with experimental results for the

buckling load, in a data base for future use (Arbocz and Hol 1991). This data base is structured so that information for shells of similar type and manufacturing process are grouped together. Since experimental methods are costly and time consuming, in recent years a lot of emphasis has been placed on predicting buckling loads using numerical methods. The finite element method in conjunction with characteristic imperfections determined from actual measurements has proven to yield results comparable to those from experimental investigations. Also, attempts have been made to produce random imperfections that yield lower bounds on the buckling load or to just solve for the worst-case imperfection directly. Numerical studies have proven to be the most effective and least costly technique for predicting buckling loads if an accurate representation of the initial imperfections is included in the analysis.

#### **2.4.1 Imperfection Modeling**

In the design of structures, most specifications indicate a maximum amplitude of initial geometric imperfection but not the corresponding imperfection pattern. Two methods of modeling imperfections are widely used. The first is deterministic modeling of imperfections and the second treats the imperfections as random fields. Using different variations of these methods, researchers have been able to numerically predict buckling loads that are in good agreement with experimental values.

Deterministic modeling of imperfections is widely used in conjunction with commercial structural analysis codes to predict buckling loads. The most common form of deterministic modeling uses imperfection data taken from actual test specimens of a type similar to the structure being analyzed. As mentioned earlier, measured imperfections of structures are now stored in an imperfection data bank and are grouped according to structure type and manufacturing process. The measured imperfections are usually made

ready for analysis or design using a modal or Fourier series representation (Elishakoff and Arbocz 1982; Elishakoff et al. 1987; Ben-Haim and Elishakoff 1990; Arbocz and Hol 1991; Chryssanthopoulos et al. 1991a,b; Ikeda et al. 1996). The modal amplitudes or coefficients of the Fourier series are then chosen so as to match the measured data of a similar structure. In general this technique yields good results as long as the shape and manufacturing process of the structure being analyzed are similar to those used to obtain the imperfection data (Arbocz and Hol 1991).

Deterministic imperfections are also applied to a structure in the form of a typical shape which is based on previous experience. For example, imperfections of spherical shells are often modeled as a dimple or flat spot of varying magnitude at the crown. Good agreement with experimental results has been obtained (Blachut and Galletly 1990; Galletly and Blachut 1991), but for general structures where a good understanding of the initial imperfections does not exist, this technique may or may not produce good results.

Another form of deterministic modeling yields imperfections in the form of the buckling modes of a structure (Morris 1991). Often the first buckling mode is chosen as the imperfection pattern and results are obtained for various amplitudes. This method is useful in determining the imperfection sensitivity of a structure but may or may not produce results that agree with experimental data. Work has been done in the area of directly predicting the most critical imperfection mode for a structure (Nushino and Hartono 1989; Ikeda and Murota 1990a,b; Hartono and Nishino 1991; Murota and Ikeda 1991). This technique searches for the mode shape of a given structure which reduces the critical load most rapidly. Results from analyses that use a critical imperfection mode yield a lower bound on the buckling loads obtained from other types of analyses.

Bolotin (1958) was the first to recognize that the geometric imperfections for a structure could be represented as random fields by using random amplitudes multiplied by

deterministic spatial functions. With the values of the imperfections given as random variables, a probability density function or cumulative distribution function for the buckling load can be obtained and used to assess the reliability of the structure. In recent studies, measured imperfections from past experiments are once again represented by a Fourier series whose coefficients are now random variables (Elishakoff and Arbocz 1982; Elishakoff et al. 1987; Arbocz and Hol 1991; Chryssanthopoulos et al. 1991a,b; Ikeda and Murota 1991; Ikeda and Murota 1993; Ikeda et al. 1996). Some studies have also produced excellent results by generating the necessary statistical moments of the Fourier coefficients using a nearly white noise approximation for the imperfections (Lindberg 1988). The strong point of this technique is that knowledge of the exact imperfection shape is not necessary.

In most of the literature to date, researchers conclude that in order to achieve reasonable estimates for the actual buckling loads of structures the analyst must use accurate representations of initial geometric imperfections (Arbocz and Hol 1991; Elishakoff et al. 1987; Chryssanthopoulos et al. 1991a). Most studies indicate that use of experimentally measured imperfections from past tests on similar structures must be used in order to obtain accurate imperfection models. Attempts to bypass the use of measured imperfections have produced reasonable results. Techniques that use white noise, or attempt to solve for a critical imperfection pattern directly deserve a lot of attention since it is often impractical or impossible to find or generate measured imperfection data for most structures.

#### **2.4.2 Use of Imperfections**

Once an appropriate imperfection model has been determined, the critical buckling load for a given structure is usually calculated by some form of numerical method. Some



of the more popular methods are the finite element method, the boundary element method, or the finite difference method. From a survey of recent literature (e.g., Elishakoff et al. 1987; Ikeda and Murota 1990a; Arbocz and Hol 1991; Galletly and Blachut 1991; Liaw and Yang 1991a,b) the finite element method appears to be the most popular of the three previously mentioned methods. The finite element codes used in most studies range from specialty codes with only one element type to more general commercial codes with many element types. A short review of two common methods of introducing geometric imperfections into a numerical analysis is given below.

One suggested method of including geometric imperfections is through the use of imperfect strain displacement relationships (Liaw and Yang 1991a,b). The imperfect strain displacement relationships are used to derive stiffness matrices that directly include the initial geometric imperfections. In developing the stiffness matrices, the imperfections are interpolated in the same way as displacements so that initial imperfections over an element may be expressed in terms of nodal values. This is very convenient since most of the available imperfection data is obtained by taking measurements at discrete points. This method also allows efficient use of the mean centered second-moment perturbation technique (Liaw and Yang 1991a,b). Using this technique a random variable can be expressed as the sum of its mean value and a random variable with zero mean and a standard deviation equal to that of the original random variable. The expansion for each random variable is then substituted into the finite element formulation and the various order terms are collected and the resulting equations are solved.

Another proposed technique suggests moving the nodal coordinates of the perfect structure by an amount equal to the specified imperfection and then analyzing the structure (Morris 1991). Analysis using this method is very simple when doing deterministic work, but without the explicit appearance of the imperfections in the governing equations

probabilistic analyses can be more difficult. However, when using commercial finite element programs this technique may be unavoidable since access to the actual computer code is often limited. When using commercial finite element programs, successive values of imperfections may have to be generated by an external subroutine which in turn modifies the coordinates and resumes the analysis. The same external subroutine may also create a link between the finite element code and a reliability analysis code which would constantly update the initial imperfections by either a Monte Carlo technique or the first-order second-moment method.

Much of the current research has been devoted to coupling finite element analysis with either Monte Carlo simulation methods or first-order second-moment reliability methods. The geometric imperfections as well as the material properties and cross-section properties are treated as random variables. The result of these type of analyses is usually a probability density function or cumulative distribution function of the buckling load. The techniques mentioned above are both useful in representing imperfections in a probabilistic analysis. The use of imperfect strain displacement relationships and moving of nodal coordinates are directly applicable to finite element based reliability methods.

## **CHAPTER 3**

### **EQUILIBRIUM EQUATIONS**

Nonlinear analysis of solids and structures is usually carried out by using either a total Lagrangian approach or an updated Lagrangian approach. In a total Lagrangian formulation, all quantities such as displacements, stresses, strains, cross-sectional properties, and material properties are referred to the initial configuration of the structure. In an updated Lagrangian formulation, all of the above quantities are referred to a deformed intermediate configuration of the structure. A third approach, which is rarely used in structural analysis, is an Eulerian formulation. In an Eulerian formulation, all quantities are referred to the current deformed configuration of the structure.

Large displacement analysis of space-frame structures requires the cross-sectional rotation of each member to be modeled as a large rotation which is not a vector quantity. Early formulations (Oran 1973; Oran and Kassimali 1976; Bathe and Bolourchi 1979) used either corotational or updated Lagrangian formulations. In both formulations, a coordinate system is attached to each element and allowed to move with the element during deformation. The orientation of the displaced coordinate system for each element is given by Euler angles, and all of the quantities in the analysis are referred to the displaced coordinate system. More recent formulations (Crivelli 1991; Fellipa and Crivelli 1991; Ibrahimbegovic et al. 1995) make use of the total Lagrangian approach in which all quantities in the analysis are referred to the initial configuration of the structure. In these formulations, various forms of the large rotation matrix are used to model the cross-

sectional rotation for each element. Two of the more commonly used forms for the analysis of large rotations are Euler parameters and the Euler axis/angle parametrization.

### 3.1 PRELIMINARIES

In Fig. 3.1, a general body is shown in an initial reference configuration 0 and in a final deformed configuration 2. The initial position of a point,  $P$ , is given by the coordinates  ${}^0X_i$  and the final position of the same point is given by the coordinates

$${}^2X_i = {}^0X_i + {}^2u_i \quad (3.1)$$

The left superscripts on the above coordinates indicate the configuration where point  $P$  is located. The terms  ${}^2u_i$  represent the displacement of point  $P$  from the initial configuration to the final configuration. For the remainder of this work, the left superscripts on any displacement quantities represent a displacement from the initial configuration to the configuration given by the left superscript.

If the displacements  ${}^2u_i$  in Eq. 3.1 are written in terms of the original coordinates  ${}^0X_i$  then the strain-displacement relationships for a body undergoing large displacements are

$${}^2_0\varepsilon_{ij} = \frac{1}{2} \left[ \frac{\partial({}^2u_i)}{\partial {}^0X_j} + \frac{\partial({}^2u_j)}{\partial {}^0X_i} + \frac{\partial({}^2u_k)}{\partial {}^0X_i} \frac{\partial({}^2u_k)}{\partial {}^0X_j} \right] \quad (3.2)$$

The quantities  ${}^2_0\varepsilon_{ij}$  are known as the Green-Lagrange strain-displacement relationships. In short-hand notation the above expression reduces to

$${}^2_0\varepsilon_{ij} = \frac{1}{2} \left[ {}^2_0u_{i,j} + {}^2_0u_{j,i} + {}^2_0u_{k,i} {}^2_0u_{k,j} \right] \quad (3.3)$$

The left subscript on the displacement gradients indicate that the derivatives are taken with respect to the original coordinates of point  $P$ . The left superscript on  ${}^2_0\varepsilon_{ij}$  indicates the

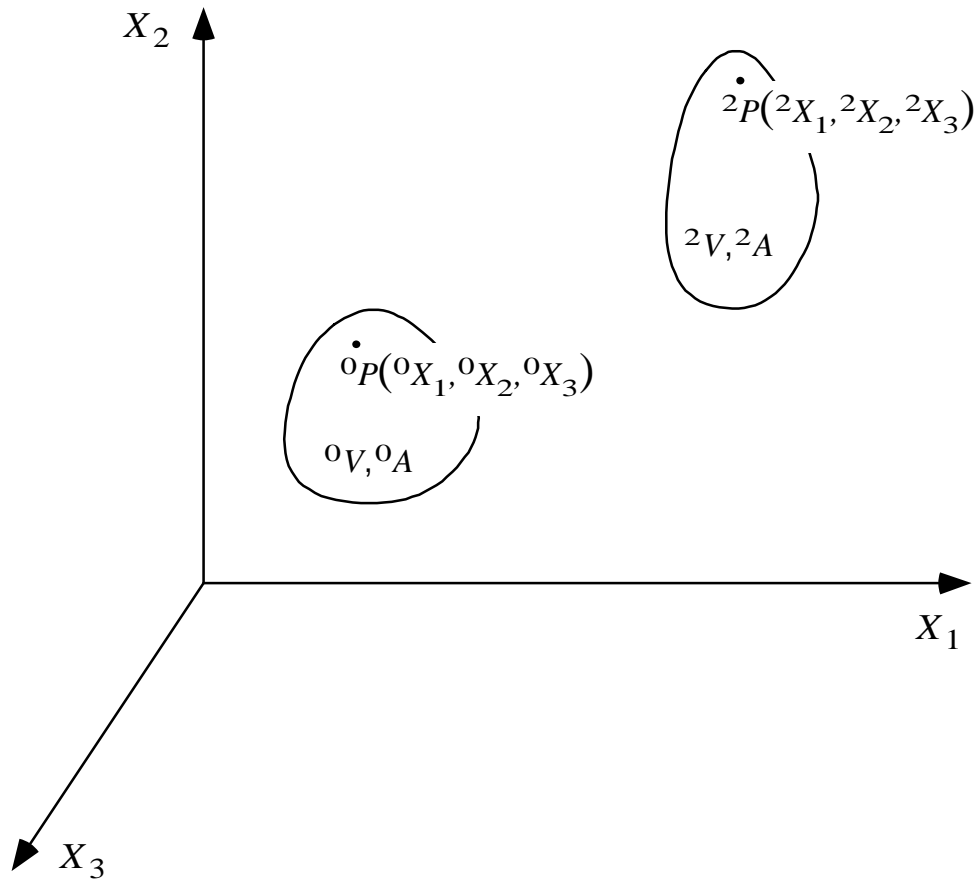


Figure 3.1 Large deformation of a body from the initial configuration, 0, to the final configuration, 2.

configuration of the strained body and the left subscript indicates the configuration where the strains are measured. Therefore, the Green-Lagrange strains are the strains in the body at configuration 2 but measured in the original configuration 0. A very important feature of the Green-Lagrange strain-displacement relationships is that the components remain zero under rigid body motion (Bathe 1982).

If the displacements  ${}^2u_i$  in Eq. 3.1 are written in terms of the deformed coordinates  ${}^2X_i$  then the resulting strain-displacement relationships for a body undergoing large displacements are

$${}^2E_{ij} = \frac{1}{2} \left[ {}^2u_{i,j} + {}^2u_{j,i} + {}^2u_{k,i} {}^2u_{k,j} \right] \quad (3.4)$$

The quantities  ${}^2E_{ij}$  are known as Eulerian or Almansi strains (Fung 1965). The Almansi strains are the strains in the body at configuration 2 that are measured with respect to the deformed coordinates  ${}^2X_i$ . In cases where the left superscripts and subscripts match, the left subscript is usually dropped and  ${}^2E_{ij}$  is abbreviated as  $E_{ij}$ . The Almansi strain tensor is rarely used in the analysis of solids and structures because the components are given in terms of the instantaneous or deformed position of the body.

If the displacement gradients are assumed to be small, both the Green-Lagrange and Almansi strains reduce to the same familiar form which is known as Cauchy's infinitesimal strain tensor. An arbitrary function  $f({}^2X_i)$  is required (Dym and Shames 1973) to show that

$$\frac{\partial({}^2u_i)}{\partial {}^0X_j} = \frac{\partial({}^2u_i)}{\partial {}^2X_j} \quad (3.5)$$

Using the chain rule results in

$$\frac{\partial f}{\partial {}^0X_i} = \frac{\partial f}{\partial {}^2X_j} \frac{\partial {}^2X_j}{\partial {}^0X_i} = \frac{\partial f}{\partial {}^2X_j} \frac{\partial}{\partial {}^0X_i} [{}^0X_j + {}^2u_j] \quad (3.6)$$

The above expression reduces to

$$\frac{\partial f}{\partial {}^0X_i} = \left[ \delta_{ij} + \frac{\partial({}^2u_j)}{\partial {}^0X_i} \right] \frac{\partial f}{\partial {}^2X_j} \quad (3.7)$$

where  $\delta_{ij}$  is the Kronecker delta whose value equals one if  $i$  equals  $j$  and zero if  $i$  is not equal to  $j$ . Since the displacement gradients are small compared to one, the term  $\partial({}^2u_j)/\partial {}^0X_i$  may be neglected leaving

$$\frac{\partial f}{\partial {}^0X_i} = \frac{\partial f}{\partial {}^2X_i}, \quad (3.8)$$

or

$$\frac{\partial}{\partial {}^0X_i} = \frac{\partial}{\partial {}^2X_i} \quad (3.9)$$

This result indicates that there is no longer any distinguishable difference between the undeformed and deformed coordinates for small displacement gradients. The resulting expression for the components of Cauchy's infinitesimal strain tensor is

$${}^2e_{ij} = \frac{1}{2} \left[ {}^2u_{i,j} + {}^2u_{j,i} \right] \quad (3.10)$$

Note that the left subscripts have been dropped because there is no difference in the  ${}^0X_i$  and  ${}^2X_i$  coordinate systems.

The stresses in the deformed body, measured in the deformed configuration, are known as Cauchy or Eulerian stresses,  ${}^2\tau_{ij}$  (Fung 1965). Using the notation from above,  ${}^2\tau_{ij}$  is abbreviated as  ${}^2\tau_{ij}$ . As the body deforms, its volume, surface area, density, stresses, and strains change continuously (Reddy 1988). The 2nd Piola-Kirchhoff stresses are often used in nonlinear analysis of solids and structures and are denoted by  ${}^2_0S_{ij}$ . As indicated by the left superscript and subscript, the 2nd Piola-Kirchhoff stresses are stresses in the deformed body measured in the undeformed reference configuration. The Cauchy stresses

are related to the 2nd Piola-Kirchhoff stresses by the expression (Bathe 1982)

$${}^2\tau_{ij} = \frac{{}^2\rho}{{}_0\rho} {}^2X_{i,m} {}^2S_{mn} {}^2X_{j,n} \quad (3.11)$$

Since the mass of the body is conserved,

$$\int_{{}^2V} {}^2\rho d^2X_1 d^2X_2 d^2X_3 = \int_{{}_0V} {}_0\rho d^0X_1 d^0X_2 d^0X_3 \quad (3.12)$$

where  $\rho$  is the mass per unit volume of the body in the configuration given by the left superscript. The relationship between the differential change in coordinates is

$$d^2X_1 d^2X_2 d^2X_3 = \det({}_0^2J) d^0X_1 d^0X_2 d^0X_3 \quad (3.13)$$

where

$$\det({}_0^2J) = \begin{vmatrix} {}^2X_{1,1} & {}^2X_{1,2} & {}^2X_{1,3} \\ {}^2X_{2,1} & {}^2X_{2,2} & {}^2X_{2,3} \\ {}^2X_{3,1} & {}^2X_{3,2} & {}^2X_{3,3} \end{vmatrix} \quad (3.14)$$

Therefore, the change in mass density can be calculated by

$${}_0\rho = {}^2\rho \det({}_0^2J), \quad (3.15)$$

and the relationship for the Cauchy stresses in terms of the 2nd Piola-Kirchhoff stresses becomes

$${}^2\tau_{ij} = \frac{1}{\det({}_0^2J)} {}^2X_{i,m} {}^2S_{mn} {}^2X_{j,n} \quad (3.16)$$

The linear portions of the Almansi strains,  ${}^2\bar{E}_{ij}$ , are energetically conjugate to the Cauchy stresses,  ${}^2\tau_{ij}$ , and the Green-Lagrange strains,  ${}^2\varepsilon_{ij}$ , are energetically conjugate to the 2nd Piola-Kirchhoff stresses,  ${}^2S_{ij}$  (Bathe 1982). Therefore, the strain energy for the deformed body in Fig. 3.1 in terms of the Cauchy stresses and Almansi strains is



$${}^2U = \frac{1}{2} \int_{{}^2V} {}^2\tau_{ij} {}^2\bar{E}_{ij} d^2V \quad (3.17)$$

The strain energy for the deformed body in terms of 2nd Piola-Kirchhoff stresses and Green-Lagrange strains is

$${}^2_0U = \frac{1}{2} \int_{{}^0V} {}^2_0S_{ij} {}^2_0\varepsilon_{ij} d^0V \quad (3.18)$$

The equations of equilibrium for the deformed body in Fig. 3.1 can be developed using the principle of virtual work. Virtual work is defined as the work done by actual forces in displacing the body through virtual displacements that are consistent with the geometric constraints imposed on the body (Reddy 1988). The principle of virtual work states that a body is in equilibrium if and only if the virtual work of all forces is zero for any virtual displacement (Holzer 1985). For the deformed body in Fig. 3.1 the principle of virtual work is

$$\delta U + \delta W_E = 0 \quad (3.19)$$

where  $\delta U$  is the virtual work due to internal forces, which is the first variation of the strain energy, and  $\delta W_E$  is the virtual work due to the external forces. Using Eq. 3.17 the equilibrium equation in terms of the Cauchy stresses and Almansi strains is

$$\begin{aligned} \int_{{}^2V} {}^2\tau_{ij} \delta({}^2\bar{E}_{ij}) d^2V - \int_{{}^2V} {}^2f_i \delta({}^2u_i) d^2V \\ - \int_{{}^2S} {}^2t_i \delta({}^2u_i) d^2S = 0 \end{aligned} \quad (3.20)$$

where  ${}^2f_i$  are body forces and  ${}^2t_i$  are forces acting on the surface of the body. The equilibrium equation in terms of the 2nd Piola-Kirchhoff stresses and Green-Lagrange strains is

$$\int_{^0V} {}^2S_{ij} \delta({}^2\varepsilon_{ij}) d^0V - \int_{^2V} {}^2f_i \delta({}^2u_i) d^2V - \int_{^2S} {}^2t_i \delta({}^2u_i) d^2S = 0 \quad (3.21)$$

Solutions to both forms of the equilibrium equations is, in general, very difficult. To solve the first form of the equilibrium equation, the final deformed configuration must be known in order to perform the required integration. The second form of the equilibrium equation is a nonlinear function of the displacement gradients and requires special solution techniques.

### 3.2 DISPLACEMENT FUNCTIONS

A three-dimensional beam is shown in Fig. 3.2. The coordinate system for the member shown is the  ${}^0X_i$  system which is assumed to be aligned with the principal axes of the member. The orientation of the  ${}^0X_i$  system is given by the unit vectors  ${}^0\mathbf{n}_i$  that are parallel with the  ${}^0X_i$  axes. Assuming that a typical cross-sectional plane remains planar during bending assures that any point  $P$  in the plane remains the same distance from the centroid of the plane, point  $O$ , during bending. This means that each cross-sectional plane along the length of the beam moves as a rigid body during bending. No assumption as to whether or not each plane remains normal to the centroidal axis during bending automatically allows shear deformation to be included in the analysis.

Figure 3.3 shows a typical cross-sectional plane located at some point  $O$  along the centroidal axis of the member. A set of right-handed Cartesian axes  ${}^0x_i$  is attached to this plane and is allowed to move with the plane during deformation. Also shown in Fig. 3.3 is the point  $P$  whose location within the plane is given by the vector

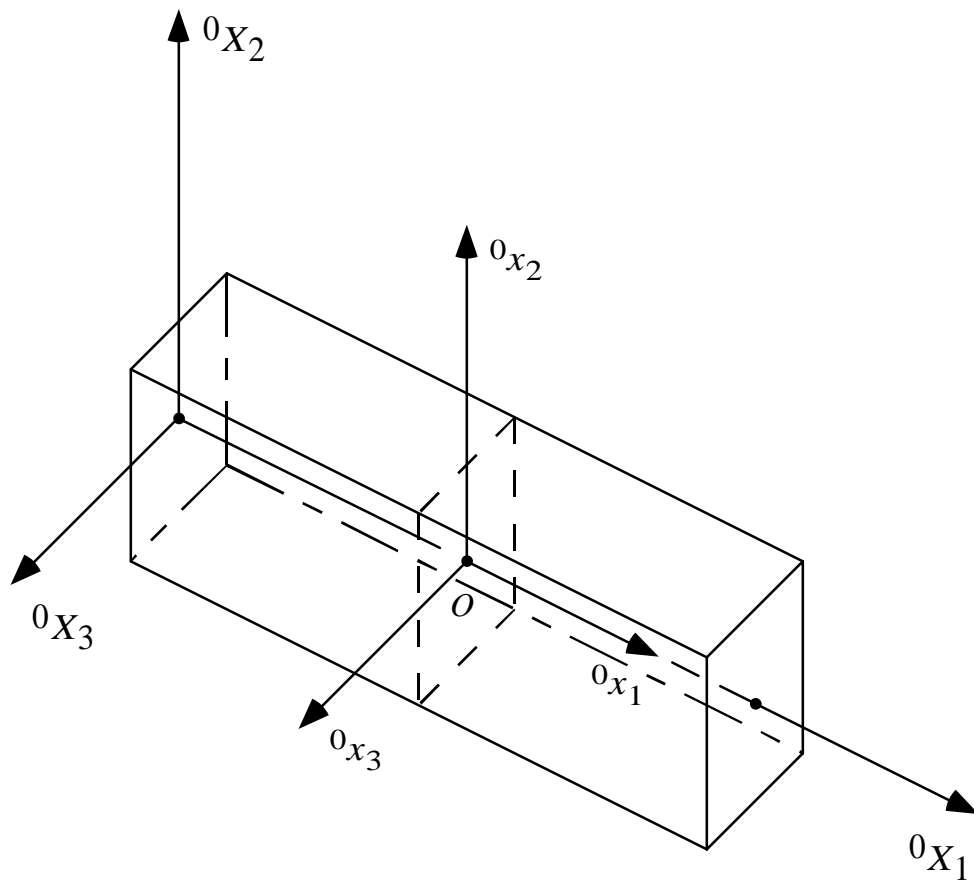


Figure 3.2 Coordinate systems for a three-dimensional beam.

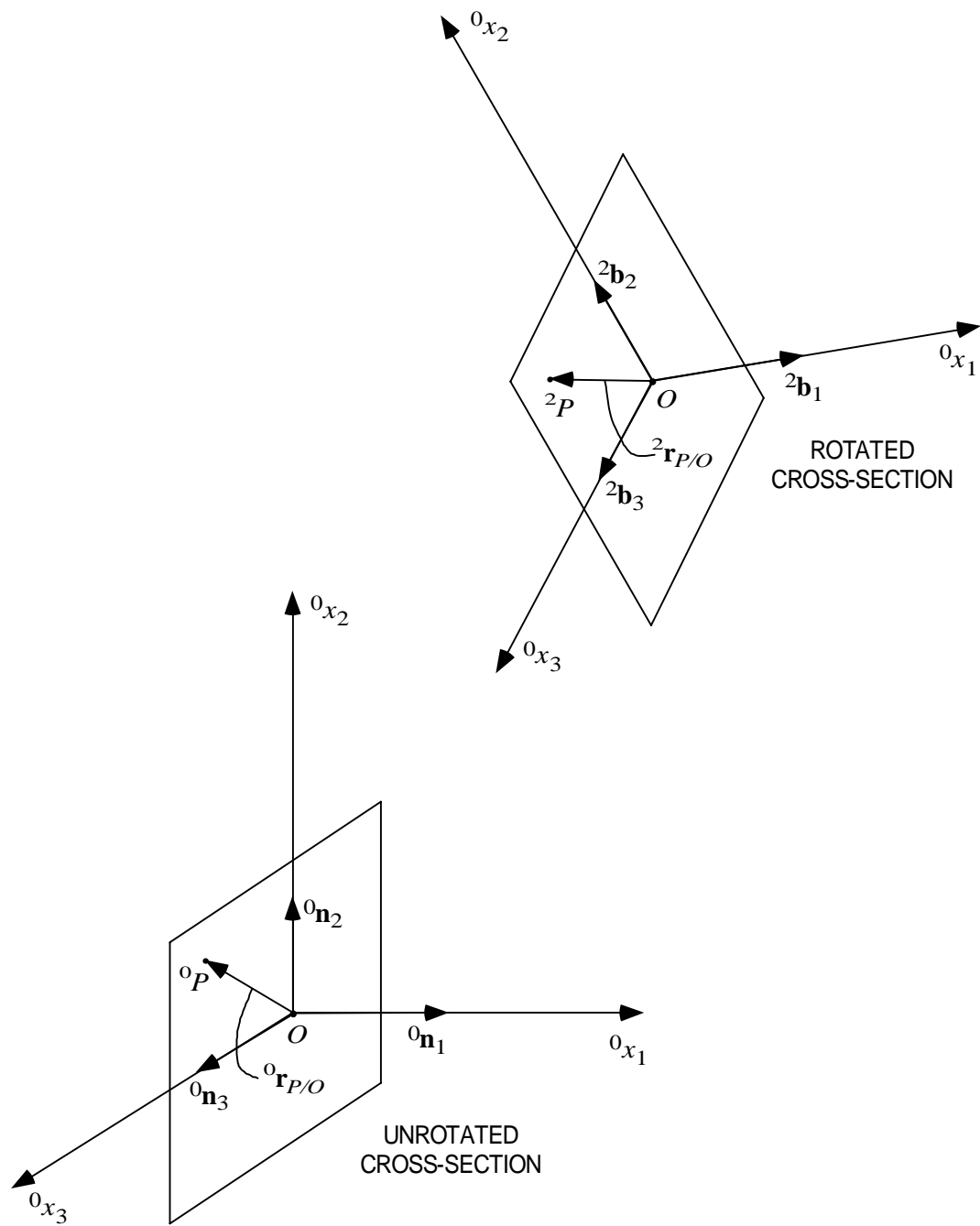


Figure 3.3 Typical cross-sectional plane for a three-dimensional beam.

$${}^0\mathbf{r}_{P/O} = \begin{bmatrix} 0 & {}^0x_2 & {}^0x_3 \end{bmatrix} \begin{bmatrix} {}^0\mathbf{n}_1 \\ {}^0\mathbf{n}_2 \\ {}^0\mathbf{n}_3 \end{bmatrix} = {}^0\mathbf{x}_{P/O}^T {}^0\mathbf{n} \quad (3.22)$$

Before deformation the position of point  $P$  is given by

$${}^0\mathbf{r}_P = {}^0\mathbf{r}_O + {}^0\mathbf{r}_{P/O} \quad (3.23)$$

The vector  ${}^0\mathbf{r}_O$  is equal to

$${}^0\mathbf{r}_O = \begin{bmatrix} {}^0X_1 \\ 0 \\ 0 \end{bmatrix} \quad (3.24)$$

where  ${}^0X_1$  is the location of point  $O$  along the centroidal axis of the member. After deformation the plane translates and rotates as a rigid body to a new position. The vector  ${}^0\mathbf{x}_{P/O}$  rotates along with the plane to its new location given by the vector

$${}^2\mathbf{r}_{P/O} = \begin{bmatrix} 0 & {}^0x_2 & {}^0x_3 \end{bmatrix} \begin{bmatrix} {}^2\mathbf{b}_1 \\ {}^2\mathbf{b}_2 \\ {}^2\mathbf{b}_3 \end{bmatrix} = {}^0\mathbf{x}_{P/O}^T {}^2\mathbf{b} \quad (3.25)$$

where  ${}^2\mathbf{b}_i$  are the unit vectors that define the orientation of the rotated cross-section. Note that the components of the vector  ${}^2\mathbf{r}_{P/O}$ , in the system attached to the plane, remain the same before and after deformation due to the fact that the plane rotates as a rigid body. The new position of point  $P$  is equal to the translated position of point  $O$  plus the projection of the vector  ${}^2\mathbf{r}_{P/O}$  along the original  ${}^0X_i$  axes. The projection of the vector  ${}^2\mathbf{r}_{P/O}$  is found by taking into account the difference in the orientation of the unit vectors  ${}^2\mathbf{b}_i$  and the unit vectors  ${}^0\mathbf{n}_i$ . The relationship between  ${}^2\mathbf{b}_i$  and  ${}^0\mathbf{n}_i$  is

$${}^2\mathbf{b} = {}^2\mathbf{R} {}^0\mathbf{n} \quad (3.26)$$

The  $3 \times 3$  matrix  ${}^2\mathbf{R}$  contains the direction cosines between the original axes and the rotated axes. The matrix  ${}^2\mathbf{R}$  is often referred to as the rotation matrix or the direction cosine matrix. Using this relationship, the vector  ${}^2\mathbf{r}_{P/O}$  can be written as

$${}^2\mathbf{r}_{P/O} = {}^0\mathbf{x}_{P/O}^T {}^2\mathbf{R} {}^0\mathbf{n} \quad (3.27)$$

The projection of  ${}^2\mathbf{r}_{P/O}$  along the  ${}^0X_i$  axes is given by the components of the above vector as

$$\mathbf{p}_{P/O}^T = {}^0\mathbf{x}_{P/O}^T {}^2\mathbf{R}, \quad (3.28)$$

or

$$\mathbf{p}_{P/O} = {}^2\mathbf{R}^T {}^0\mathbf{x}_{P/O} \quad (3.29)$$

The final position of point  $P$  is

$${}^2\mathbf{r}_P = {}^0\mathbf{r}_O + {}^2\mathbf{u}_O + {}^2\mathbf{R}^T {}^0\mathbf{x}_{P/O} \quad (3.30)$$

The vector  ${}^0\mathbf{r}_O$  was given by Eq. 3.24 and the vector  ${}^2\mathbf{u}_O$  contains the components of the translation of point  $O$  which are only a function of the  ${}^0X_1$  coordinate. The displacement of point  $P$  is found by subtracting the initial position of  $P$  from the final position of  $P$  which results in

$${}^2\mathbf{u} = {}^2\mathbf{u}_O + ({}^2\mathbf{R}^T - \mathbf{I}) {}^0\mathbf{x}_{P/O} \quad (3.31)$$

In expanded form, the displacement functions are:

$${}^2u_1 = {}^2u_{O1}({}^0X_1) + {}^0x_2 {}^2R_{21}({}^0X_1) + {}^0x_3 {}^2R_{31}({}^0X_1) \quad (3.32)$$

$${}^2u_2 = {}^2u_{O2}({}^0X_1) + {}^0x_2 ({}^2R_{22}({}^0X_1) - 1) + {}^0x_3 {}^2R_{32}({}^0X_1) \quad (3.33)$$

$${}^2u_3 = {}^2u_{O3}({}^0X_1) + {}^0x_2 {}^2R_{23}({}^0X_1) + {}^0x_3 ({}^2R_{33}({}^0X_1) - 1) \quad (3.34)$$

### 3.3 ROTATION MATRICES

In the previous section, it was shown that for a three-dimensional beam the displacement of a point  $P$  can be described by the translation and rigid body rotation of

the cross-sectional plane containing the point  $P$ . As mentioned above, the rigid body rotation of the cross-sectional plane is defined by the rotation matrix.

The rotation matrix, or direction cosine matrix, has several important properties (Junkins and Turner 1986):

- 1.) The *inverse equals transpose* property

$${}^2\mathbf{R}^{-1} = {}^2\mathbf{R}^T$$

which is characteristic of orthogonal matrices. An orthogonal matrix has the important property that the dot product between a column/row and itself is equal to 1, while the dot product between a column/row and another column/row is equal to zero.

- 2.) The  $\text{Det}[^2\mathbf{R}] = \pm 1$ , and more specifically  $\text{Det}[^2\mathbf{R}] = +1$  if right-handed coordinate systems are used.
- 3.) The rotation matrix  ${}^2\mathbf{R}$  has only one real eigenvalue  $\pm 1$ , and the one eigenvalue is equal to  $+1$  if right-handed coordinate systems are used.
- 4.) Successive rotations

$${}^2\mathbf{b} = \mathbf{R}_2 \mathbf{c}$$

$$\mathbf{c} = \mathbf{R}_1 \mathbf{d}$$

$$\mathbf{d} = \mathbf{R}_0 {}^0\mathbf{n}$$

from the initial to the final configuration can be written as one composite rotation

$${}^2\mathbf{b} = {}^2\mathbf{R} {}^0\mathbf{n}$$

where the matrix  ${}^2\mathbf{R}$  is

$${}^2\mathbf{R} = \mathbf{R}_2\mathbf{R}_1\mathbf{R}_0$$

and the matrices  ${}^2\mathbf{b}$ ,  $\mathbf{c}$ ,  $\mathbf{d}$ , and  ${}^0\mathbf{n}$  contain the unit vectors  ${}^2\mathbf{b}_i$ ,  $\mathbf{c}_i$ ,  $\mathbf{d}_i$ , and  ${}^0\mathbf{n}_i$  that orient the body at the various configurations. Since  $\mathbf{R}_0$ ,  $\mathbf{R}_1$ , and  $\mathbf{R}_2$  are orthogonal, the matrix  ${}^2\mathbf{R}$  is also orthogonal, and if  $\mathbf{R}_0$ ,  $\mathbf{R}_1$ , and  $\mathbf{R}_2$  follow (1.) and (2.) then  ${}^2\mathbf{R}$  will also follow (1.) and (2.).

One of the most popular methods for characterizing the rotation of a rigid body involves the use of three sequential rotations. The resulting angles of rotation are called Euler angles and the corresponding rotation matrix takes on different forms depending upon how the angles are defined and in which sequence the rotations are performed. The major disadvantage in using Euler angles in a total Lagrangian formulation of a three-dimensional beam finite element is that two of the angles are not referenced to the original axes of the body or structure being analyzed. The last two angles represent rotations about axes that are already rotated from the original axes. Therefore, it is very difficult to compute the virtual work of moments about the original axes of the body acting through these angles. Or, in other words, the moments have no physical meaning because they are referred to intermediate axes that are not aligned with the original principal axes of the cross-section of the member.

The general rotation of a rigid body can be described using Euler's Principal Rotation Theorem. This theorem states that the rotation of a body about a point can be accomplished by a single rotation through a principal angle  ${}^2\phi$  about a principal axis located by the unit vector  ${}^2\mathbf{a}$  (Junkins and Turner 1986). The resulting rotation matrix is

$${}^2\mathbf{R} = \cos({}^2\phi) \mathbf{I} + (1 - \cos({}^2\phi)) {}^2\mathbf{a} {}^2\mathbf{a}^T - \sin({}^2\phi) {}^2\tilde{\mathbf{a}} \quad (3.35)$$

The matrix  ${}^2\tilde{\mathbf{a}}$  is often referred to as the spin of the vector  ${}^2\mathbf{a}$  which in expanded form is



given by

$${}^2\tilde{\mathbf{a}} = \begin{bmatrix} 0 & -{}^2a_3 & {}^2a_2 \\ {}^2a_3 & 0 & -{}^2a_1 \\ -{}^2a_2 & {}^2a_1 & 0 \end{bmatrix} \quad (3.36)$$

The matrix  ${}^2\tilde{\mathbf{a}}$  has the property that

$${}^2\tilde{\mathbf{a}}^T = -{}^2\tilde{\mathbf{a}} \quad (3.37)$$

Another interesting parametrization of  ${}^2\mathbf{R}$  involves the introduction of a rotation vector which is equal to

$${}^2\boldsymbol{\phi} = {}^2\phi {}^2\mathbf{a} = \begin{bmatrix} {}^2\phi_1 \\ {}^2\phi_2 \\ {}^2\phi_3 \end{bmatrix} \quad (3.38)$$

One important point that must be emphasized is that the rotation vector is not a true vector in the sense that the components of the rotation vector from two or more successive rotations cannot be added to form one composite rotation (Hughes 1986). However, the rotation vector does follow one important property; if a rotation  ${}^2\phi$  is multiplied by scalar to give  $\kappa {}^2\phi$ , then the vector  ${}^2\boldsymbol{\phi}$  becomes  $\kappa {}^2\boldsymbol{\phi}$  (Hughes 1986). The resulting rotation matrix for the three variable form of the Euler axis/angle parametrization is

$${}^2\mathbf{R} = \mathbf{I} + {}^2b_2 {}^2\tilde{\boldsymbol{\phi}} + {}^2b_3 {}^2\tilde{\boldsymbol{\phi}} {}^2\tilde{\boldsymbol{\phi}} \quad (3.39)$$

where

$${}^2b_2 = -|{}^2\boldsymbol{\phi}|^{-1} \sin|{}^2\boldsymbol{\phi}|, \quad (3.40)$$

$${}^2b_3 = 2|{}^2\boldsymbol{\phi}|^{-2} \sin^2 \frac{|{}^2\boldsymbol{\phi}|}{2}, \quad (3.41)$$

and the matrix  ${}^2\tilde{\boldsymbol{\phi}}$  is the spin of the rotation vector  ${}^2\boldsymbol{\phi}$ . This parametrization only requires

three quantities to describe the rotation while the previous definition required four. The major disadvantages of the three parameter characterization are that sign ambiguities arise once the body has rotated past 360 degrees and that numerical difficulties may arise when trying to evaluate  $|\phi|^{-1}$  for small values of  $\phi$ . Problems with sign ambiguities or singularities are common to all three parameter forms of the rotation matrix. In practice the problem with sign ambiguities is not a problem when  ${}^2\mathbf{R}$  is used in the analysis of a three-dimensional beam. For the finite element formulation sign ambiguities would arise only when an individual element rotates more than 360 degrees. Numerical difficulties for small values of  $\phi$  are also not a problem since  $|\phi|$  can be compared to the smallest number the computer will recognize to prevent overflow errors when computing terms involving  $|\phi|^{-1}$ .

There are other useful forms of the rotation matrix. The rotation matrices for some of the more important parametrizations, such as Euler parameters, Euler-Rodriquez parameters, and the direction cosines themselves, are given by Hughes (1986). A couple of the more exotic forms of the rotation matrix, such as Cayley-Klein parameters and quaternions, are outlined by Junkins and Turner (1986). In spite of the problems with sign ambiguity, the three parameter Euler axis/angle parametrization will be used in the development of the three-dimensional beam finite element.

When used in rotational dynamics, the time behavior of the rotation matrix  ${}^2\mathbf{R}$  is usually required. For use in the development of a three-dimensional beam finite element, the behavior of  ${}^2\mathbf{R}$  along the length of each element is needed. Therefore, the rotation matrix used in the finite element formulation will be a function of the coordinate along the length of the member,  ${}^0X_1$ , rather than time.

As in dynamics, the first derivative of the rotation matrix is required. For the three-dimensional beam, the derivative will be taken with respect to  ${}^0X_1$  rather than time.

In dynamics the derivative is computed by introducing an angular velocity vector,  ${}^2\boldsymbol{\omega}$ , whose components are angular velocities about the three coordinate axes. For the three-dimensional beam, the vector  ${}^2\boldsymbol{\omega}$  contains the curvatures about the three coordinate axes (Crivelli 1991). The expression for the first derivative of the rotation matrix is

$${}^2_0\mathbf{R}' = - {}^2\tilde{\boldsymbol{\omega}} {}^2\mathbf{R} \quad (3.42)$$

where  ${}^2\tilde{\boldsymbol{\omega}}$  is the spin of the vector  ${}^2\boldsymbol{\omega}$ . The prime in the above equation represents the first derivative with respect to the coordinate  ${}^0X_1$ .

For the three parameter form of the Euler axis/angle representation of the rotation matrix the angular velocity vector is related to the first derivative of the rotation angles,  ${}^2\phi_i$ , about the three coordinate axes by the expression

$${}^2\boldsymbol{\omega} = (\mathbf{I} + {}^2c_2 {}^2\tilde{\boldsymbol{\phi}} + {}^2c_3 {}^2\tilde{\boldsymbol{\phi}} {}^2\tilde{\boldsymbol{\phi}}) {}^2_0\boldsymbol{\phi}' = {}^2\mathbf{D}_0 {}^2\boldsymbol{\phi}' \quad (3.43)$$

where

$${}^2c_2 = -2|{}^2\boldsymbol{\phi}|^{-2} \sin^2 \frac{|{}^2\boldsymbol{\phi}|}{2} \quad (3.44)$$

$${}^2c_3 = |{}^2\boldsymbol{\phi}|^{-3} (|{}^2\boldsymbol{\phi}| - \sin |{}^2\boldsymbol{\phi}|) \quad (3.45)$$

Once  ${}^2\boldsymbol{\omega}$  is known, the values can be substituted into the expression for  ${}^2_0\mathbf{R}'$  and the resulting matrix will then be a function of only  ${}^2\phi_i$  and  ${}^2_0\phi'_i$ .

### 3.4 STRAIN-DISPLACEMENT RELATIONSHIPS

From Section 3.1, the general expressions for the Green-Lagrange strain-displacement relationships are

$${}^2\varepsilon_{ij} = \frac{1}{2} \left[ {}^2_0u_{i,j} + {}^2_0u_{j,i} + {}^2_0u_{k,i} {}^2_0u_{k,j} \right] \quad (3.46)$$

For a three-dimensional beam, the  ${}^2u_i$  represent the displacement of point  $P$ . Substituting the assumed displacement functions, Eqs. 3.32-3.34, into the expression for the Green-Lagrange strains gives the following strain-displacement relationships for a three-dimensional beam:

$$\begin{aligned}
{}^2\varepsilon_{11} = & {}^2u'_{o_1} + \frac{1}{2} \left( {}^2u'_{o_1}{}^2 + {}^2u'_{o_2}{}^2 + {}^2u'_{o_3}{}^2 \right) \\
& + {}^0x_2 \left[ \left( 1 + {}^2u'_{o_1} \right) {}^2R'_{21} + {}^2u'_{o_2} {}^2R'_{22} + {}^2u'_{o_3} {}^2R'_{23} \right] \\
& + {}^0x_3 \left[ \left( 1 + {}^2u'_{o_1} \right) {}^2R'_{31} + {}^2u'_{o_2} {}^2R'_{32} + {}^2u'_{o_3} {}^2R'_{33} \right] \\
& + {}^0x_2 {}^0x_3 \left[ {}^2R'_{21} {}^2R'_{31} + {}^2R'_{22} {}^2R'_{32} + {}^2R'_{23} {}^2R'_{33} \right] \\
& + \frac{{}^0x_2^2}{2} \left[ {}^2R_{21}{}^2 + {}^2R_{22}{}^2 + {}^2R_{23}{}^2 \right] + \frac{{}^0x_3^2}{2} \left[ {}^2R_{31}{}^2 + {}^2R_{32}{}^2 + {}^2R_{33}{}^2 \right] \quad (3.47)
\end{aligned}$$

$${}^2\varepsilon_{22} = \left( {}^2R_{22} - 1 \right) + \frac{1}{2} \left[ {}^2R_{21}{}^2 + \left( {}^2R_{22} - 1 \right)^2 + {}^2R_{23}{}^2 \right] \quad (3.48)$$

$${}^2\varepsilon_{33} = \left( {}^2R_{33} - 1 \right) + \frac{1}{2} \left[ {}^2R_{31}{}^2 + {}^2R_{32}{}^2 + \left( {}^2R_{33} - 1 \right)^2 \right] \quad (3.49)$$

$$\begin{aligned}
{}^2\gamma_{12} = 2 {}^2\varepsilon_{12} = & \left( 1 + {}^2u'_{o_1} \right) {}^2R_{21} + {}^2u'_{o_2} {}^2R_{22} + {}^2u'_{o_3} {}^2R_{23} \\
& + {}^0x_2 \left[ {}^2R_{21} {}^2R'_{21} + {}^2R_{22} {}^2R'_{22} + {}^2R_{23} {}^2R'_{23} \right] \\
& + {}^0x_3 \left[ {}^2R_{21} {}^2R'_{31} + {}^2R_{22} {}^2R'_{32} + {}^2R_{23} {}^2R'_{33} \right] \quad (3.50)
\end{aligned}$$

$$\begin{aligned}
{}^2_0\gamma_{13} = 2 {}^2_0\varepsilon_{13} &= \left(1 + {}^2_0u'_{o_1}\right) {}^2R_{31} + {}^2_0u'_{o_2} {}^2R_{32} + {}^2_0u'_{o_3} {}^2R_{33} \\
&+ {}^0x_2 \left[ {}^2R_{31} {}^2R'_{21} + {}^2R_{32} {}^2R'_{22} + {}^2R_{33} {}^2R'_{23} \right] \\
&+ {}^0x_3 \left[ {}^2R_{31} {}^2R'_{31} + {}^2R_{32} {}^2R'_{32} + {}^2R_{33} {}^2R'_{33} \right] \quad (3.51)
\end{aligned}$$

$${}^2_0\gamma_{23} = 2 {}^2_0\varepsilon_{23} = {}^2R_{21} {}^2R_{31} + {}^2R_{22} {}^2R_{32} + {}^2R_{23} {}^2R_{33} \quad (3.52)$$

Assuming that each cross-sectional plane moves as a rigid body implies that  ${}^2_0\varepsilon_{22}$ ,  ${}^2_0\varepsilon_{33}$ , and  ${}^2_0\gamma_{23}$  should be equal to zero. The strain components  ${}^2_0\varepsilon_{22}$  and  ${}^2_0\varepsilon_{33}$  deal with the change in height and the change in width of the cross-section, while  ${}^2_0\gamma_{23}$  deals with the in-plane distortion of the cross-sectional plane. When taking into account the orthogonality of the rotation matrix  ${}^2\mathbf{R}$ , the expressions for  ${}^2_0\varepsilon_{22}$ ,  ${}^2_0\varepsilon_{33}$ , and  ${}^2_0\gamma_{23}$  reduce to zero as shown below.

Examining the expression for  ${}^2_0\varepsilon_{22}$  and recalling that, due to the orthogonality of  ${}^2\mathbf{R}$ ,

$${}^2R_{21}^2 + {}^2R_{22}^2 + {}^2R_{23}^2 = 1, \quad (3.53)$$

the expression for  ${}^2_0\varepsilon_{22}$  reduces to

$${}^2_0\varepsilon_{22} = \left( {}^2R_{22} - 1 \right) + \frac{1}{2} \left[ 2 - 2 {}^2R_{22} \right], \quad (3.54)$$

or

$${}^2_0\varepsilon_{22} = 0 \quad (3.55)$$

The expression for  ${}^2_0\varepsilon_{33}$  can also be shown to equal zero by using the same procedure along with the dot product of the third row of  ${}^2\mathbf{R}$  with itself.

The expression for the shear strain  ${}^2_0\gamma_{23}$  is found to equal zero by taking the dot product between the second and third rows of  ${}^2\mathbf{R}$ . The resulting dot product is equal to  ${}^2_0\gamma_{23}$  and is also equal to zero, because of the orthogonality of  ${}^2\mathbf{R}$ .

The remaining strains may be written in a more compact form as:

$$\begin{aligned} {}^2_0\bar{\varepsilon}_{11} = & {}^2_0\bar{\varepsilon}_{11} + {}^0x_2 {}^2_0\kappa_{22} + {}^0x_3 {}^2_0\kappa_{33} + {}^0x_2^2 {}^2_0\nu_{22} + {}^0x_3^2 {}^2_0\nu_{33} \\ & + {}^0x_2 {}^0x_3 {}^2_0\nu_{23} \end{aligned} \quad (3.56)$$

$${}^2_0\gamma_{12} = {}^2_0\bar{\gamma}_{12} + {}^0x_2 {}^2_0\rho_{12} + {}^0x_3 {}^2_0\rho_{13} \quad (3.57)$$

$${}^2_0\gamma_{13} = {}^2_0\bar{\gamma}_{13} + {}^0x_2 {}^2_0\omega_{12} + {}^0x_3 {}^2_0\omega_{13} \quad (3.58)$$

where:

$${}^2_0\bar{\varepsilon}_{11} = {}^2_0u'_{o_1} + \frac{1}{2} \left( {}^2_0u'^2_{o_1} + {}^2_0u'^2_{o_2} + {}^2_0u'^2_{o_3} \right) \quad (3.59)$$

$${}^2_0\kappa_{22} = \left( 1 + {}^2_0u'_{o_1} \right) {}^2_0R'_{21} + {}^2_0u'_{o_2} {}^2_0R'_{22} + {}^2_0u'_{o_3} {}^2_0R'_{23} \quad (3.60)$$

$${}^2_0\kappa_{33} = \left( 1 + {}^2_0u'_{o_1} \right) {}^2_0R'_{31} + {}^2_0u'_{o_2} {}^2_0R'_{32} + {}^2_0u'_{o_3} {}^2_0R'_{33} \quad (3.61)$$

$${}^2_0\nu_{22} = \frac{1}{2} \left[ {}^2_0R'^2_{21} + {}^2_0R'^2_{22} + {}^2_0R'^2_{23} \right] \quad (3.62)$$

$${}^2_0\nu_{33} = \frac{1}{2} \left[ {}^2_0R'^2_{31} + {}^2_0R'^2_{32} + {}^2_0R'^2_{33} \right] \quad (3.63)$$

$${}^2_0\nu_{23} = {}^2_0R'_{21} {}^2_0R'_{31} + {}^2_0R'_{22} {}^2_0R'_{32} + {}^2_0R'_{23} {}^2_0R'_{33} \quad (3.64)$$

$${}^2_0\bar{\gamma}_{12} = \left( 1 + {}^2_0u'_{o_1} \right) {}^2_0R_{21} + {}^2_0u'_{o_2} {}^2_0R_{22} + {}^2_0u'_{o_3} {}^2_0R_{23} \quad (3.65)$$

$${}^2_0\bar{\gamma}_{13} = \left( 1 + {}^2_0u'_{o_1} \right) {}^2_0R_{31} + {}^2_0u'_{o_2} {}^2_0R_{32} + {}^2_0u'_{o_3} {}^2_0R_{33} \quad (3.66)$$

$${}^2_0\rho_{12} = {}^2_0R_{21} {}^2_0R'_{21} + {}^2_0R_{22} {}^2_0R'_{22} + {}^2_0R_{23} {}^2_0R'_{23} \quad (3.67)$$

$${}^2_0\rho_{13} = {}^2R_{21_0}{}^2R'_{31} + {}^2R_{22_0}{}^2R'_{32} + {}^2R_{23_0}{}^2R'_{33} \quad (3.68)$$

$${}^2_0\omega_{12} = {}^2R_{31_0}{}^2R'_{21} + {}^2R_{32_0}{}^2R'_{22} + {}^2R_{33_0}{}^2R'_{23} \quad (3.69)$$

$${}^2_0\omega_{13} = {}^2R_{31_0}{}^2R'_{31} + {}^2R_{32_0}{}^2R'_{32} + {}^2R_{33_0}{}^2R'_{33} \quad (3.70)$$

Once again, the primes in the above equations represent the first derivative with respect to the coordinate  ${}^0X_1$ .

The shear strains  ${}^2_0\gamma_{12}$  and  ${}^2_0\gamma_{13}$  may be further reduced by once again considering the orthogonality of  ${}^2\mathbf{R}$ . The expression for  ${}^2_0\rho_{12}$  can be rewritten as

$${}^2_0\rho_{12} = \frac{d}{d^0X_1} \left[ \frac{1}{2} \left( {}^2R_{21}^2 + {}^2R_{22}^2 + {}^2R_{23}^2 \right) \right] = \frac{d}{d^0X_1} \left[ \frac{1}{2} \right] \quad (3.71)$$

which, due to the orthogonality of  ${}^2\mathbf{R}$ , is equal to zero. By a similar process, the expression for  ${}^2_0\omega_{13}$  is also found to be zero. Therefore, the equations for the shear strains reduce to

$${}^2_0\gamma_{12} = {}^2_0\bar{\gamma}_{12} + {}^0x_3 {}^2_0\rho_{13} \quad (3.72)$$

$${}^2_0\gamma_{13} = {}^2_0\bar{\gamma}_{13} + {}^0x_2 {}^2_0\omega_{12} \quad (3.73)$$

The expression for  ${}^2_0\rho_{13}$  is found to be equal to the opposite of the expression for  ${}^2_0\omega_{12}$  by examining the derivative of the dot product between the second and third columns of  ${}^2\mathbf{R}$ :

$$\frac{d}{d^0X_1} \left[ {}^2R_{21} {}^2R_{31} + {}^2R_{22} {}^2R_{32} + {}^2R_{23} {}^2R_{33} \right] = 0 \quad (3.74)$$

Expanding the above equation results in

$$\begin{aligned} & \left( {}^2R_{21_0}{}^2R'_{31} + {}^2R_{22_0}{}^2R'_{32} + {}^2R_{23_0}{}^2R'_{33} \right) = \\ & - \left( {}^2R_{31_0}{}^2R'_{21} + {}^2R_{32_0}{}^2R'_{22} + {}^2R_{33_0}{}^2R'_{23} \right), \end{aligned} \quad (3.75)$$

or

$${}^2_0\rho_{13} = - {}^2_0\omega_{12} \quad (3.76)$$

The resulting expressions for the shear strains are:

$${}^2_0\gamma_{12} = {}^2_0\overline{\gamma}_{12} + {}^0x_3 {}^2_0\rho_{13} \quad (3.77)$$

$${}^2_0\gamma_{13} = {}^2_0\overline{\gamma}_{13} - {}^0x_2 {}^2_0\rho_{13} \quad (3.78)$$

The expression for  ${}^2_0\varepsilon_{11}$  may be simplified by introducing the nondimensional displacements:

$${}^2u_{o1}^* = \frac{{}^2u_{o1}}{{}^0L} \quad (3.79)$$

$${}^2u_{o2}^* = \frac{{}^2u_{o2}}{{}^0L} \quad (3.80)$$

$${}^2u_{o3}^* = \frac{{}^2u_{o3}}{{}^0L} \quad (3.81)$$

and the nondimensional coordinates:

$${}^0\xi = \frac{{}^0X_1}}{{}^0L} \quad (3.82)$$

$${}^0\eta = \frac{{}^0x_2}}{{}^0h} \quad (3.83)$$

$${}^0\psi = \frac{{}^0x_3}}{{}^0b} \quad (3.84)$$

In the above expressions,  ${}^0L$  is the length of the member,  ${}^0b$  is the width of the cross-section, and  ${}^0h$  is the height of the cross-section. Substituting the nondimensional quantities into the expression for  $\varepsilon_{11}$  gives



$$\begin{aligned}
{}^2_0\varepsilon_{11}^* &= {}^2_0u_{o1}^{*'} + \frac{1}{2} \left( {}^2_0u_{o1}^{*'}^2 + {}^2_0u_{o2}^{*'}^2 + {}^2_0u_{o3}^{*'}^2 \right) \\
&+ \frac{{}^0\eta^0 h}{{}^0L} \left[ \left( 1 + {}^2_0u_{o1}^{*'} \right) {}^2_0R'_{21} + {}^2_0u_{o2}^{*'} {}^2_0R'_{22} + {}^2_0u_{o3}^{*'} {}^2_0R'_{23} \right] \\
&+ \frac{{}^0\psi^0 b}{{}^0L} \left[ \left( 1 + {}^2_0u_{o1}^{*'} \right) {}^2_0R'_{31} + {}^2_0u_{o2}^{*'} {}^2_0R'_{32} + {}^2_0u_{o3}^{*'} {}^2_0R'_{33} \right] \\
&+ \frac{{}^0\eta^0 \psi^0 h^0 b}{{}^0L^2} \left[ {}^2_0R'_{21} {}^2_0R'_{31} + {}^2_0R'_{22} {}^2_0R'_{32} + {}^2_0R'_{23} {}^2_0R'_{33} \right] \\
&+ \frac{{}^0\eta^{20} h^2}{2 {}^0L^2} \left[ {}^2_0R_{21}'^2 + {}^2_0R_{22}'^2 + {}^2_0R_{23}'^2 \right] \\
&+ \frac{{}^0\psi^{20} b^2}{2 {}^0L^2} \left[ {}^2_0R_{31}'^2 + {}^2_0R_{32}'^2 + {}^2_0R_{33}'^2 \right]
\end{aligned} \tag{3.85}$$

where the primes now denote derivatives with respect to the nondimensional coordinate  ${}^0\xi$ . For a typical shear deformable member, the quantities  ${}^0h/{}^0L$  and  ${}^0b/{}^0L$  will be much less than one. This will make the terms containing  $({}^0h/{}^0L)^2$ ,  $({}^0b/{}^0L)^2$ , and  $({}^0h/{}^0L)({}^0b/{}^0L)$  negligible when compared to the rest of the terms in the above equation. As a result, the terms involving  ${}^0x_2^2$ ,  ${}^0x_3^2$ , and  ${}^0x_2 {}^0x_3$  are neglected in the final expression for  ${}^2_0\varepsilon_{11}$ .

To summarize, the final strain-displacement relationships for the three-dimensional beam are:

$${}^2_0\varepsilon_{11} = {}^2_0\bar{\varepsilon}_{11} + {}^0x_2^2 \kappa_{22} + {}^0x_3^2 \kappa_{33} \tag{3.86}$$

$${}^2_0\gamma_{12} = {}^2_0\bar{\gamma}_{12} + {}^0x_3^2 \rho_{13} \tag{3.87}$$

$${}^2_0\gamma_{13} = {}^2_0\bar{\gamma}_{13} - {}^0x_2^2 \rho_{13} \tag{3.88}$$

where:

$${}^2_{\bar{\varepsilon}}_{11} = {}^2u'_{o_1} + \frac{1}{2} \left( {}^2u'^2_{o_1} + {}^2u'^2_{o_2} + {}^2u'^2_{o_3} \right) \quad (3.89)$$

$${}^2\kappa_{22} = \left( 1 + {}^2u'_{o_1} \right) {}^2R'_{21} + {}^2u'_{o_2} {}^2R'_{22} + {}^2u'_{o_3} {}^2R'_{23} \quad (3.90)$$

$${}^2\kappa_{33} = \left( 1 + {}^2u'_{o_1} \right) {}^2R'_{31} + {}^2u'_{o_2} {}^2R'_{32} + {}^2u'_{o_3} {}^2R'_{33} \quad (3.91)$$

$${}^2\bar{\gamma}_{12} = \left( 1 + {}^2u'_{o_1} \right) {}^2R_{21} + {}^2u'_{o_2} {}^2R_{22} + {}^2u'_{o_3} {}^2R_{23} \quad (3.92)$$

$${}^2\bar{\gamma}_{13} = \left( 1 + {}^2u'_{o_1} \right) {}^2R_{31} + {}^2u'_{o_2} {}^2R_{32} + {}^2u'_{o_3} {}^2R_{33} \quad (3.93)$$

$${}^2\rho_{13} = {}^2R_{21} {}^2R'_{31} + {}^2R_{22} {}^2R'_{32} + {}^2R_{23} {}^2R'_{33} \quad (3.94)$$

### 3.5 EQUILIBRIUM EQUATIONS

The expression for the internal virtual work for an individual three-dimensional beam element is

$$\begin{aligned} \delta({}^2_0U) = \int_{^0V} & \left[ {}^2S_{11} \delta({}^2_0\varepsilon_{11}) + 2 {}^2S_{12} \delta({}^2_0\varepsilon_{12}) \right. \\ & \left. + 2 {}^2S_{13} \delta({}^2_0\varepsilon_{13}) \right] d^0V, \end{aligned} \quad (3.95)$$

or

$$\begin{aligned} \delta({}^2_0U) = \int_{^0V} & \left[ {}^2S_{11} \delta({}^2_0\varepsilon_{11}) + {}^2S_{12} \delta({}^2_0\gamma_{12}) \right. \\ & \left. + {}^2S_{13} \delta({}^2_0\gamma_{13}) \right] d^0V \end{aligned} \quad (3.96)$$

Assuming the material remains linear elastic, Hooke's law for a three-dimensional beam reduces to:

$${}^2_0S_{11} = E {}^2_0\varepsilon_{11} \quad (3.97)$$

$${}^2_0S_{12} = G {}^2_0\gamma_{12} \quad (3.98)$$

$${}^2_0S_{13} = G {}^2_0\gamma_{13} \quad (3.99)$$

Substituting the stress-strain relationships into Eq. 3.96 gives

$$\begin{aligned} \delta({}^2_0U) = \int_{^0V} & \left[ E {}^2_0\varepsilon_{11} \delta({}^2_0\varepsilon_{11}) + G {}^2_0\gamma_{12} \delta({}^2_0\gamma_{12}) \right. \\ & \left. + G {}^2_0\gamma_{13} \delta({}^2_0\gamma_{13}) \right] d^0V \end{aligned} \quad (3.100)$$

Using the strain-displacement relationships, Eqs. 3.86-3.88, and integrating over the volume of the beam element, the first variation of the strain energy becomes

$$\begin{aligned} \delta({}^2_0U) = \int_0^{^0L} \int_{^0A} & \left\{ E \left[ {}^2_0\bar{\varepsilon}_{11} + {}^0x_2 {}^2_0\kappa_{22} + {}^0x_3 {}^2_0\kappa_{33} \right] \right. \\ & \times \left[ \delta({}^2_0\bar{\varepsilon}_{11}) + {}^0x_2 \delta({}^2_0\kappa_{22}) + {}^0x_3 \delta({}^2_0\kappa_{33}) \right] \\ & + G \left[ {}^2_0\bar{\gamma}_{12} + {}^0x_3 {}^2_0\rho_{13} \right] \\ & \times \left[ \delta({}^2_0\bar{\gamma}_{12}) + {}^0x_3 \delta({}^2_0\rho_{13}) \right] \\ & + G \left[ {}^2_0\bar{\gamma}_{13} - {}^0x_2 {}^2_0\rho_{13} \right] \\ & \left. \times \left[ \delta({}^2_0\bar{\gamma}_{13}) - {}^0x_2 \delta({}^2_0\rho_{13}) \right] \right\} d^0A d^0X_1 \end{aligned} \quad (3.101)$$

Recognizing that

$$\int_{^0A} {}^0x_2^2 d^0A = {}^0I_z \quad (3.102)$$

$$\int_{^0A} {}^0x_3^2 d^0A = {}^0I_y \quad (3.103)$$

and

$${}^0J = {}^0I_y + {}^0I_z \quad (3.104)$$

the above expression reduces to

$$\begin{aligned} \delta({}^2_0U) = \int_0^L \bigg\{ & E {}^0A {}^2_0\bar{\varepsilon}_{11} \delta({}^2_0\bar{\varepsilon}_{11}) + E {}^0I_y {}^2_0\kappa_{22} \delta({}^2_0\kappa_{22}) \\ & + E {}^0I_z {}^2_0\kappa_{33} \delta({}^2_0\kappa_{33}) + G {}^0A_S {}^2_0\bar{\gamma}_{12} \delta({}^2_0\bar{\gamma}_{12}) \\ & + G {}^0A_S {}^2_0\bar{\gamma}_{13} \delta({}^2_0\bar{\gamma}_{13}) + G {}^0J {}^2_0\rho_{13} \delta({}^2_0\rho_{13}) \bigg\} d^0X_1 \end{aligned} \quad (3.105)$$

The first variation of the strain components is:

$$\delta({}^2_0\bar{\varepsilon}_{11}) = (1 + {}^2_0u'_{o_1}) \delta({}^2_0u'_{o_1}) + {}^2_0u'_{o_2} \delta({}^2_0u'_{o_2}) + {}^2_0u'_{o_3} \delta({}^2_0u'_{o_3}) \quad (3.106)$$

$$\begin{aligned} \delta({}^2_0\kappa_{22}) = & {}^2_0R'_{21} \delta({}^2_0u'_{o_1}) + {}^2_0R'_{22} \delta({}^2_0u'_{o_2}) + {}^2_0R'_{23} \delta({}^2_0u'_{o_3}) \\ & + (1 + {}^2_0u'_{o_1}) \delta({}^2_0R'_{21}) + {}^2_0u'_{o_2} \delta({}^2_0R'_{22}) \\ & + {}^2_0u'_{o_3} \delta({}^2_0R'_{23}) \end{aligned} \quad (3.107)$$

$$\begin{aligned} \delta({}^2_0\kappa_{33}) = & {}^2_0R'_{31} \delta({}^2_0u'_{o_1}) + {}^2_0R'_{32} \delta({}^2_0u'_{o_2}) + {}^2_0R'_{33} \delta({}^2_0u'_{o_3}) \\ & + (1 + {}^2_0u'_{o_1}) \delta({}^2_0R'_{31}) + {}^2_0u'_{o_2} \delta({}^2_0R'_{32}) \\ & + {}^2_0u'_{o_3} \delta({}^2_0R'_{33}) \end{aligned} \quad (3.108)$$

$$\begin{aligned}
\delta({}^2\bar{\gamma}_{12}) &= {}^2R_{21}\delta({}^2u'_{o_1}) + {}^2R_{22}\delta({}^2u'_{o_2}) + {}^2R_{23}\delta({}^2u'_{o_3}) \\
&+ (1 + {}^2u'_{o_1})\delta({}^2R_{21}) + {}^2u'_{o_2}\delta({}^2R_{22}) \\
&+ {}^2u'_{o_3}\delta({}^2R_{23})
\end{aligned} \tag{3.109}$$

$$\begin{aligned}
\delta({}^2\bar{\gamma}_{13}) &= {}^2R_{31}\delta({}^2u'_{o_1}) + {}^2R_{32}\delta({}^2u'_{o_2}) + {}^2R_{33}\delta({}^2u'_{o_3}) \\
&+ (1 + {}^2u'_{o_1})\delta({}^2R_{31}) + {}^2u'_{o_2}\delta({}^2R_{32}) \\
&+ {}^2u'_{o_3}\delta({}^2R_{33})
\end{aligned} \tag{3.110}$$

$$\begin{aligned}
\delta({}^2\rho_{13}) &= {}^2R'_{31}\delta({}^2R_{21}) + {}^2R'_{32}\delta({}^2R_{22}) + {}^2R'_{33}\delta({}^2R_{23}) \\
&+ {}^2R_{21}\delta({}^2R'_{31}) + {}^2R_{22}\delta({}^2R'_{32}) + {}^2R_{23}\delta({}^2R'_{33})
\end{aligned} \tag{3.111}$$

Substituting the above quantities into the expression for the internal virtual work results in

$$\begin{aligned}
\delta({}^2U) &= \int_0^L \left\{ \left[ E^0 A_0 {}^2\bar{\varepsilon}_{11} (1 + {}^2u'_{o_1}) + E^0 I_y {}^2\kappa_{22} {}^2R'_{21} \right. \right. \\
&\quad + E^0 I_z {}^2\kappa_{33} {}^2R'_{31} + G^0 A_S {}^2\bar{\gamma}_{12} {}^2R_{21} \\
&\quad \left. \left. + G^0 A_S {}^2\bar{\gamma}_{13} {}^2R_{31} \right] \delta({}^2u'_{o_1}) \right. \\
&\quad + \left[ E^0 A_0 {}^2\bar{\varepsilon}_{11} {}^2u'_{o_2} + E^0 I_y {}^2\kappa_{22} {}^2R'_{21} + E^0 I_z {}^2\kappa_{33} {}^2R'_{31} \right. \\
&\quad \left. \left. + G^0 A_S {}^2\bar{\gamma}_{12} {}^2R_{21} + G^0 A_S {}^2\bar{\gamma}_{13} {}^2R_{31} \right] \delta({}^2u'_{o_2}) \right. \\
&\quad + \left[ E^0 A_0 {}^2\bar{\varepsilon}_{11} {}^2u'_{o_3} + E^0 I_y {}^2\kappa_{22} {}^2R'_{21} + E^0 I_z {}^2\kappa_{33} {}^2R'_{31} \right. \\
&\quad \left. \left. + G^0 A_S {}^2\bar{\gamma}_{12} {}^2R_{21} + G^0 A_S {}^2\bar{\gamma}_{13} {}^2R_{31} \right] \delta({}^2u'_{o_3}) \right\}
\end{aligned}$$

$$\begin{aligned}
& + \left[ G^0 A_S {}^2\bar{\gamma}_{12} (1 + {}^2u'_{o_1}) + G^0 J {}^2\rho_{13} {}^2R'_{31} \right] \delta({}^2R_{21}) \\
& + \left[ G^0 A_S {}^2\bar{\gamma}_{12} {}^2u'_{o_2} + G^0 J {}^2\rho_{13} {}^2R'_{32} \right] \delta({}^2R_{22}) \\
& + \left[ G^0 A_S {}^2\bar{\gamma}_{12} {}^2u'_{o_3} + G^0 J {}^2\rho_{13} {}^2R'_{33} \right] \delta({}^2R_{23}) \\
& + \left[ G^0 A_S {}^2\bar{\gamma}_{13} (1 + {}^2u'_{o_1}) \right] \delta({}^2R_{31}) \\
& + \left[ G^0 A_S {}^2\bar{\gamma}_{13} {}^2u'_{o_2} \right] \delta({}^2R_{32}) \\
& + \left[ G^0 A_S {}^2\bar{\gamma}_{13} {}^2u'_{o_3} \right] \delta({}^2R_{33}) \\
& + \left[ E^0 I_y {}^2\kappa_{22} (1 + {}^2u'_{o_1}) \right] \delta({}^2R'_{21}) \\
& + \left[ E^0 I_y {}^2\kappa_{22} {}^2u'_{o_2} \right] \delta({}^2R'_{22}) \\
& + \left[ E^0 I_y {}^2\kappa_{22} {}^2u'_{o_3} \right] \delta({}^2R'_{23}) \\
& + \left[ E^0 I_z {}^2\kappa_{33} (1 + {}^2u'_{o_1}) + G^0 J {}^2\rho_{13} {}^2R_{21} \right] \delta({}^2R'_{31}) \\
& + \left[ E^0 I_z {}^2\kappa_{33} {}^2u'_{o_2} + G^0 J {}^2\rho_{13} {}^2R_{22} \right] \delta({}^2R'_{32}) \\
& + \left[ E^0 I_z {}^2\kappa_{33} {}^2u'_{o_3} + G^0 J {}^2\rho_{13} {}^2R_{23} \right] \delta({}^2R'_{33}) \Big\} d^0 X_1 \tag{3.112}
\end{aligned}$$

The above expression may be rewritten in a more compact form as

$$\delta({}^2U) = \int_0^{^0L} \delta({}^2\mathcal{U}) d^0 X_1 \tag{3.113}$$

where

$$\delta \left( {}^2_0\mathcal{U} \right) = \delta \left( \begin{matrix} {}^2\mathbf{3}^T \\ 0 \\ 1 \times 21 \end{matrix} \right) {}^2_0\mathcal{R} \quad (3.114)$$

The vector  ${}^2_0\mathcal{R}$  contains the coefficients of the first variations of the unknown displacement gradients, rotation parameters, and first derivative of the rotation parameters found in the internal virtual work. The vector  $\delta \left( {}^2_0\mathbf{3} \right)$  is a partitioned vector that is given by

$$\delta \left( {}^2_0\mathbf{3}^T \right) = \left[ \delta \left( \begin{matrix} {}^2\mathbf{u}'^T_o \\ 0 \\ 1 \times 3 \end{matrix} \right) \quad \delta \left( \begin{matrix} {}^2\mathbf{R}^T \\ 1 \times 9 \end{matrix} \right) \quad \delta \left( \begin{matrix} {}^2\mathbf{R}'^T \\ 0 \\ 1 \times 9 \end{matrix} \right) \right] \quad (3.115)$$

Each of the components of the rotation matrix is a function of all three angles of rotation  ${}^2\phi_i$ . Therefore, the first variation of each component will in general have three terms. For a typical component of the rotation matrix the first variation is given by

$$\delta \left( {}^2\mathbf{R}_{ij} \right) = \sum_{k=1}^3 \frac{\partial \left( {}^2\mathbf{R}_{ij} \right)}{\partial \left( {}^2\phi_k \right)} \delta \left( {}^2\phi_k \right) \quad (3.116)$$

The vector form of the first variation of the rotation matrix may be expressed in terms of the angles of rotation as

$$\delta \left( \begin{matrix} {}^2\mathbf{R} \\ 9 \times 1 \end{matrix} \right) = \mathbf{DR02} \delta \left( \begin{matrix} {}^2\boldsymbol{\phi} \\ 3 \times 1 \end{matrix} \right) \quad (3.117)$$

Details concerning the calculation of the matrix  $\mathbf{DR02}$  are dealt with in Appendix A. The first variation of the derivatives of the rotations is a function of the rotation angles and the first derivative of the rotation angles. From Appendix A the resulting expression is

$$\delta \left( \begin{matrix} {}^2\mathbf{R}' \\ 9 \times 1 \end{matrix} \right) = \left[ \begin{matrix} \mathbf{DRP1} & \mathbf{DRP2} \\ 9 \times 3 & 9 \times 3 \end{matrix} \right] \left[ \begin{matrix} \delta \left( \begin{matrix} {}^2\boldsymbol{\phi} \\ 3 \times 1 \end{matrix} \right) \\ \delta \left( \begin{matrix} {}^2\boldsymbol{\phi}' \\ 0 \\ 3 \times 1 \end{matrix} \right) \end{matrix} \right] \quad (3.118)$$

With  $\delta \left( {}^2\mathbf{R} \right)$  and  $\delta \left( {}^2_0\mathbf{R}' \right)$  defined, the partitioned vector of variational quantities may be expressed as

$$\begin{bmatrix} \delta \begin{pmatrix} {}^2\mathbf{u}'_o \\ 0 \\ 3 \times 1 \end{pmatrix} \\ \delta \begin{pmatrix} {}^2\mathbf{R} \\ 9 \times 1 \end{pmatrix} \\ \delta \begin{pmatrix} {}^2\mathbf{R}' \\ 0 \\ 9 \times 1 \end{pmatrix} \end{bmatrix} = \begin{bmatrix} \mathbf{I}_{3 \times 3} & 0 & 0 \\ 0 & \mathbf{DR02}_{9 \times 3} & 0 \\ 0 & \mathbf{DRP1}_{9 \times 3} & \mathbf{DRP2}_{9 \times 3} \end{bmatrix} \begin{bmatrix} \delta \begin{pmatrix} {}^2\mathbf{u}'_o \\ 0 \\ 3 \times 1 \end{pmatrix} \\ \delta \begin{pmatrix} {}^2\boldsymbol{\phi} \\ 3 \times 1 \end{pmatrix} \\ \delta \begin{pmatrix} {}^2\boldsymbol{\phi}' \\ 0 \\ 3 \times 1 \end{pmatrix} \end{bmatrix} \quad (3.119)$$

In a more compact form the above relationship becomes

$$\delta \begin{pmatrix} {}^2\mathbf{3} \\ 0 \\ 21 \times 1 \end{pmatrix} = \mathbf{DELTR1}_{21 \times 9} \delta \begin{pmatrix} {}^2\mathbf{u} \\ 0 \\ 9 \times 1 \end{pmatrix} \quad (3.120)$$

The integrand of the internal energy, Eq. 3.114, becomes

$$\delta({}^2\mathcal{U}) = \delta \begin{pmatrix} {}^2\mathbf{u}^T \\ 0 \\ 1 \times 9 \end{pmatrix} \mathbf{DELTR1}_{9 \times 21}^T \begin{pmatrix} {}^2\mathcal{R} \\ 0 \\ 21 \times 1 \end{pmatrix} \quad (3.121)$$

Multiplying the transpose of  $\mathbf{DELTR1}$  and  ${}^2\mathcal{R}$  yields a  $9 \times 1$  vector of internal forces that correspond to the nine degrees of freedom for the three-dimensional beam.

The formulation of the three-dimensional beam finite element requires that the continuous quantities  ${}^2\mathbf{u}'_o$ ,  ${}^2\boldsymbol{\phi}$ , and  ${}^2\boldsymbol{\phi}'$  be expressed in terms of displacements at discrete points along the length of the member. For the problem at hand, a two-noded isoparametric formulation has been chosen. The resulting formulation requires the coordinates of the member as well as the displacements to be written in terms of the coordinates and displacements at the ends of the member by using the linear interpolation functions

$$N_1 = \frac{1}{2}(1 - {}^0\xi) \quad (3.122)$$

and

$$N_2 = \frac{1}{2}(1 + {}^0\xi) \quad (3.123)$$

The variable  ${}^0\xi$  is the natural (nondimensional) coordinate along the length of the beam, as



shown in Fig. 3.4. The coordinate of any point along the length of the member is given as

$${}^0X_1({}^0\xi) = N_1({}^0\xi){}^0X_{1_1} + N_2({}^0\xi){}^0X_{1_2} \quad (3.124)$$

where  ${}^0X_{1_1}$  and  ${}^0X_{1_2}$  are the locations of the ends of a typical element. The change in  ${}^0X_1$  with respect to  ${}^0\xi$  is

$$\frac{d({}^0X_1)}{d({}^0\xi)} = \frac{1}{2}({}^0X_{1_2} - {}^0X_{1_1}), \quad (3.125)$$

but

$${}^0L = {}^0X_{1_2} - {}^0X_{1_1} \quad (3.126)$$

Therefore, the change in  ${}^0X_1$  with respect to  ${}^0\xi$  is

$$\frac{d({}^0X_1)}{d({}^0\xi)} = \frac{{}^0L}{2} \quad (3.127)$$

which is only a function of the original length of the member.

The displacement functions are interpolated using the same method as the coordinates:

$${}^2u_{o_i} = N_1{}^2u_{o_{i_1}} + N_2{}^2u_{o_{i_2}} \quad (3.128)$$

$${}^2\phi_i = N_1{}^2\phi_{i_1} + N_2{}^2\phi_{i_2} \quad (3.129)$$

The first derivative of the transverse displacements is equal to

$$\frac{d({}^2u_{o_i})}{d({}^0X_1)} = \frac{d({}^2u_{o_i})}{d({}^0\xi)} \frac{d({}^0\xi)}{d({}^0X_1)} = \frac{2}{{}^0L} N_{1,{}^0\xi} {}^2u_{o_{i_1}} + \frac{2}{{}^0L} N_{2,{}^0\xi} {}^2u_{o_{i_2}} \quad (3.130)$$

In a similar manner, the first derivative of the rotations is

$$\frac{d({}^2\phi_i)}{d({}^0X_1)} = \frac{2}{{}^0L} N_{1,{}^0\xi} {}^2\phi_{i_1} + \frac{2}{{}^0L} N_{2,{}^0\xi} {}^2\phi_{i_2} \quad (3.131)$$

Storing the nodal displacements in a vector  ${}^2\mathbf{d}$ , the vector

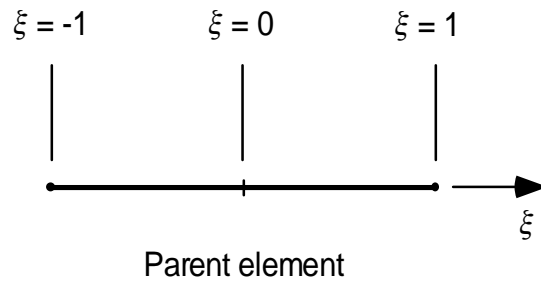
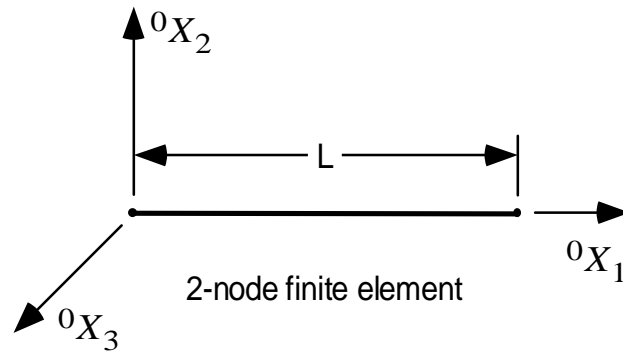


Figure 3.4 Two-node three-dimensional beam finite element and the corresponding parent element.

$$\delta \begin{pmatrix} {}^2\mathbf{u} \\ {}^0 \\ {}^9 \times 1 \end{pmatrix} = \underset{9 \times 12}{\mathbf{SHPMAT}} \delta \begin{pmatrix} {}^2\mathbf{d} \\ {}^0 \\ {}^{12 \times 1} \end{pmatrix} \quad (3.132)$$

The matrix **SHPMAT** is often referred to as the interpolation matrix and is given by the partitioned matrix

$$\underset{9 \times 12}{\mathbf{SHPMAT}} = \begin{bmatrix} \underset{3 \times 12}{\mathbf{N}_{u'_o}} \\ \underset{3 \times 12}{\mathbf{N}_\phi} \\ \underset{3 \times 12}{\mathbf{N}_{\phi'}} \end{bmatrix} \quad (3.133)$$

where the matrices  $\mathbf{N}_{u'_o}$ ,  $\mathbf{N}_\phi$ , and  $\mathbf{N}_{\phi'}$  are shown in Fig. 3.5.

Introducing the discretized displacements into the internal virtual work results in the expression

$$\delta({}^2U) = \delta \begin{pmatrix} {}^2\mathbf{d}^T \\ {}^0 \\ {}^1 \times 12 \end{pmatrix} \int_0^{0L} \left( \underset{12 \times 9}{\mathbf{SHPMAT}^T} \underset{9 \times 21}{\mathbf{DELTR1}^T} \underset{21 \times 1}{{}^2\mathcal{R}} \right) d^0X_1 \quad (3.134)$$

The integral over the coordinate  ${}^0X_1$  must be changed to an integral over the natural coordinate  ${}^0\xi$ . From Eq. 3.127

$$d^0X_1 = \frac{{}^0L}{2} d^0\xi \quad (3.135)$$

Therefore,

$$\delta({}^2U) = \delta \begin{pmatrix} {}^2\mathbf{d}^T \\ {}^0 \\ {}^1 \times 12 \end{pmatrix} \frac{{}^0L}{2} \int_{-1}^{+1} \left( \underset{12 \times 9}{\mathbf{SHPMAT}^T} \underset{9 \times 21}{\mathbf{DELTR1}^T} \underset{21 \times 1}{{}^2\mathcal{R}} \right) d^0\xi \quad (3.136)$$

The resulting integral is evaluated using single point Gauss quadrature. Integration leads to a  $12 \times 1$  vector of internal forces,  ${}^2\mathbf{f}_I$ , that correspond to the nodal degrees of freedom for the element. The internal virtual work is further simplified to

$$\delta({}^2U) = \delta \begin{pmatrix} {}^2\mathbf{d}^T \\ {}^0 \\ {}^1 \times 12 \end{pmatrix} \underset{12 \times 1}{{}^2\mathbf{f}_I} \quad (3.137)$$

$$\mathbf{N}_{u'_o} = \begin{bmatrix} N_{1,0\xi} & 0 & 0 & 0 & 0 & 0 & N_{2,0\xi} & 0 & 0 & 0 & 0 & 0 \\ 0 & N_{1,0\xi} & 0 & 0 & 0 & 0 & 0 & N_{2,0\xi} & 0 & 0 & 0 & 0 \\ 0 & 0 & N_{1,0\xi} & 0 & 0 & 0 & 0 & 0 & N_{2,0\xi} & 0 & 0 & 0 \end{bmatrix}$$

$$\mathbf{N}_\phi = \begin{bmatrix} 0 & 0 & 0 & N_1 & 0 & 0 & 0 & 0 & 0 & N_2 & 0 & 0 \\ 0 & 0 & 0 & 0 & N_1 & 0 & 0 & 0 & 0 & 0 & N_2 & 0 \\ 0 & 0 & 0 & 0 & 0 & N_1 & 0 & 0 & 0 & 0 & 0 & N_2 \end{bmatrix}$$

$$\mathbf{N}_{\phi'} = \begin{bmatrix} 0 & 0 & 0 & N_{1,0\xi} & 0 & 0 & 0 & 0 & 0 & N_{2,0\xi} & 0 & 0 \\ 0 & 0 & 0 & 0 & N_{1,0\xi} & 0 & 0 & 0 & 0 & 0 & N_{2,0\xi} & 0 \\ 0 & 0 & 0 & 0 & 0 & N_{1,0\xi} & 0 & 0 & 0 & 0 & 0 & N_{2,0\xi} \end{bmatrix}$$

Figure 3.5 Matrices  $\mathbf{N}_{u'_o}$ ,  $\mathbf{N}_\phi$ , and  $\mathbf{N}_{\phi'}$  from the partitioned matrix **SHPMAT**.

The external virtual work due to applied forces was given in Eq. 3.21. If the external forces are only applied at the nodes, and if the direction of the loads does not change during deformation, then the external virtual work reduces to

$$\delta({}_0^2W_E) = \delta\left({}_0^2\mathbf{d}^T\right) {}_{1 \times 12}^{12 \times 1} {}_{12 \times 1}^2\mathbf{f}_E \quad (3.138)$$

where the vector  ${}^2\mathbf{f}_E$  contains the external forces corresponding to the nodal degrees of freedom of the element.

Equilibrium for the three-dimensional beam finite element is given by

$$\delta({}_0^2U) - \delta({}_0^2W_E) = 0 \quad (3.139)$$

In general,

$$\delta\left({}_0^2\mathbf{d}^T\right) \neq 0 \quad (3.140)$$

so that the equilibrium condition reduces to

$${}_{12 \times 1}^2\mathbf{f}_I = {}_{12 \times 1}^2\mathbf{f}_E \quad (3.141)$$

The resulting equilibrium equation is a nonlinear function of the nodal displacements,  ${}_0^2\mathbf{d}$ , and special methods must be used to solve the problem.

## **CHAPTER 4**

### **INCREMENTAL EQUILIBRIUM EQUATIONS**

The result of the total Lagrangian formulation presented in Chapter 3 was a system of equations that are nonlinear in the unknown nodal displacements. Solution of the nonlinear equations is usually accomplished with numerical techniques that are incremental and iterative in nature. All of these types of numerical methods require that the nonlinear system of equations be written in terms of small incremental changes of the unknown displacements. For the three-dimensional beam, the equilibrium equations presented in Chapter 3 must be written in an incremental form and then linearized in the resulting unknown incremental displacements. Once the incremental equilibrium equations are found, any one of a number of available numerical solutions may be used to solve the resulting nonlinear system of equations.

#### **4.1 INCREMENTAL DISPLACEMENT FUNCTIONS**

Generation of the incremental form of the equilibrium equations begins with replacing the displacements from configuration 0 to configuration 2 by incremental displacements which consist of displacements from configuration 0 to a new intermediate configuration 1, and small incremental displacements from configuration 1 to the final configuration 2. The deformable body shown in Fig. 3.1 is reillustrated in Fig. 4.1 with the additional intermediate configuration 1. Configuration 1 in the incremental formulation replaces configuration 2 in the previous chapter in the sense that the

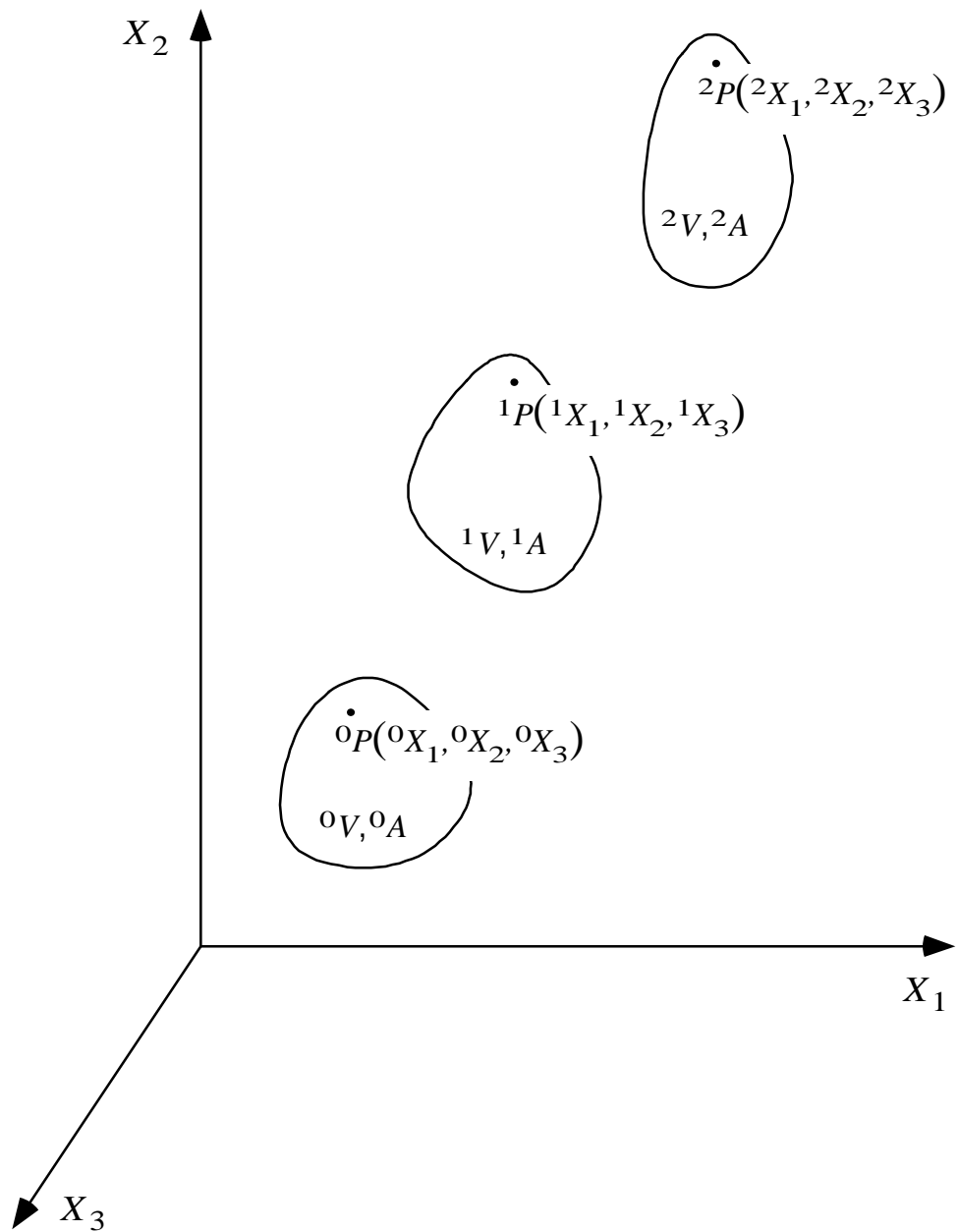


Figure 4.1 Large deformation of a body from the initial configuration, 0, to an intermediate configuration, 1, and a small deformation from configuration, 1, to the final configuration, 2.

displacements from configuration 0 to configuration 1 are also arbitrarily large. The incremental form of the displacement functions is

$${}^2\mathbf{u} = {}^1\mathbf{u} + \mathbf{u} \quad (4.1)$$

where

$${}^1\mathbf{u} = {}^1\mathbf{u}_O + ({}^1\mathbf{R}^T - \mathbf{I}) {}^0\mathbf{x}_{P/O} \quad (4.2)$$

and

$$\mathbf{u} = \mathbf{u}_O + \mathbf{R}^T {}^0\mathbf{x}_{P/O} \quad (4.3)$$

The vector  ${}^1\mathbf{u}$  contains the arbitrarily large displacements from configuration 0 to configuration 1 and the vector  $\mathbf{u}$  contains the incremental displacements from configuration 1 to configuration 2. As in the previous chapter, the displacements and rotations take place between the initial configuration 0 and the configuration indicated by the left superscript. The small incremental displacements and rotations are indicated by the absence of a left superscript.

## 4.2 INCREMENTAL STRAIN-DISPLACEMENT RELATIONSHIPS

The strain due to the displacement from configuration 0 to configuration 2 was given by the Green-Lagrange strain-displacement relationship

$${}^2_0\varepsilon_{ij} = \frac{1}{2} \left[ {}^2_0u_{i,j} + {}^2_0u_{j,i} + {}^2_0u_{k,i} {}^2_0u_{k,j} \right] \quad (4.4)$$

As in Chapter 3, the left subscript indicates that the derivatives are taken with respect to the initial coordinate axes of the member. The incremental form of  ${}^2_0\varepsilon_{ij}$  is found by substituting the incremental displacements, Eq. 4.1, into the Green-Lagrange relationships above. The resulting incremental strains are written in the form

$${}^2_0\varepsilon_{ij} = {}^1_0\varepsilon_{ij} + {}_0\varepsilon_{ij} \quad (4.5)$$



where

$${}_0^1\varepsilon_{ij} = \frac{1}{2} \left[ {}_0^1u_{i,j} + {}_0^1u_{j,i} + {}_0^1u_{k,i} {}_0^1u_{k,j} \right] \quad (4.6)$$

and

$${}_0\varepsilon_{ij} = \frac{1}{2} \left[ {}_0u_{i,j} + {}_0u_{j,i} + {}_0^1u_{k,j} {}_0u_{k,i} + {}_0^1u_{k,i} {}_0u_{k,j} + {}_0u_{k,i} {}_0u_{k,j} \right] \quad (4.7)$$

Because the incremental displacements are small, the term  ${}_0^1u_{k,i} {}_0u_{k,j}$  is neglected and  ${}_0\varepsilon_{ij}$  reduces to

$${}_0\varepsilon_{ij} = \frac{1}{2} \left[ {}_0u_{i,j} + {}_0u_{j,i} + {}_0^1u_{k,j} {}_0u_{k,i} + {}_0^1u_{k,i} {}_0u_{k,j} \right] \quad (4.8)$$

One noteworthy point is the appearance of the terms containing the displacements from configuration 0 to configuration 1 in  ${}_0\varepsilon_{ij}$ . These terms represent an initial displacement effect due to the displacement from 0 to 1.

For the three-dimensional beam, the Green-Lagrange strains  ${}_0\varepsilon_{11}$ ,  ${}_0\varepsilon_{12}$ , and  ${}_0\varepsilon_{13}$  were given in the previous chapter. These strain components were then simplified and written in a more compact form with components that were also given in Chapter 3. The incremental form of the strain components is given by:

$${}_0^2\bar{\varepsilon}_{11} = {}_0^1\bar{\varepsilon}_{11} + {}_0\bar{\varepsilon}_{11} \quad (4.9)$$

$${}_0^2\kappa_{22} = {}_0^1\kappa_{22} + {}_0\kappa_{22} \quad (4.10)$$

$${}_0^2\kappa_{33} = {}_0^1\kappa_{33} + {}_0\kappa_{33} \quad (4.11)$$

$${}_0^2\bar{\gamma}_{12} = {}_0^1\bar{\gamma}_{12} + {}_0\bar{\gamma}_{12} \quad (4.12)$$

$${}_0^2\bar{\gamma}_{13} = {}_0^1\bar{\gamma}_{13} + {}_0\bar{\gamma}_{13} \quad (4.13)$$

$${}_0^2\rho_{13} = {}_0^1\rho_{13} + {}_0\rho_{13} \quad (4.14)$$

The strains from configuration 0 to configuration 1 have the same form as the corresponding strains from configuration 0 to configuration 2, found in Chapter 3. The incremental portions of the strains are given by:

$${}_0\bar{\epsilon}_{11} = (1 + {}^1u'_{o_1}) {}_0u'_{o_1} + {}^1u'_{o_2} {}_0u'_{o_2} + {}^1u'_{o_3} {}_0u'_{o_3} \quad (4.15)$$

$$\begin{aligned} {}_0\kappa_{22} = & {}^1R'_{21} {}_0u'_{o_1} + {}^1R'_{22} {}_0u'_{o_2} + {}^1R'_{23} {}_0u'_{o_3} \\ & + (1 + {}^1u'_{o_1}) {}_0R'_{21} + {}^1u'_{o_2} {}_0R'_{22} + {}^1u'_{o_3} {}_0R'_{23} \end{aligned} \quad (4.16)$$

$$\begin{aligned} {}_0\kappa_{33} = & {}^1R'_{31} {}_0u'_{o_1} + {}^1R'_{32} {}_0u'_{o_2} + {}^1R'_{33} {}_0u'_{o_3} \\ & + (1 + {}^1u'_{o_1}) {}_0R'_{31} + {}^1u'_{o_2} {}_0R'_{32} + {}^1u'_{o_3} {}_0R'_{33} \end{aligned} \quad (4.17)$$

$$\begin{aligned} {}_0\bar{\gamma}_{12} = & {}^1R_{21} {}_0u'_{o_1} + {}^1R_{22} {}_0u'_{o_2} + {}^1R_{23} {}_0u'_{o_3} \\ & + (1 + {}^1u'_{o_1}) {}_0R_{21} + {}^1u'_{o_2} {}_0R_{22} + {}^1u'_{o_3} {}_0R_{23} \end{aligned} \quad (4.18)$$

$$\begin{aligned} {}_0\bar{\gamma}_{13} = & {}^1R_{31} {}_0u'_{o_1} + {}^1R_{32} {}_0u'_{o_2} + {}^1R_{33} {}_0u'_{o_3} \\ & + (1 + {}^1u'_{o_1}) {}_0R_{31} + {}^1u'_{o_2} {}_0R_{32} + {}^1u'_{o_3} {}_0R_{33} \end{aligned} \quad (4.19)$$

$$\begin{aligned} {}_0\rho_{13} = & {}^1R'_{31} {}_0R_{21} + {}^1R'_{32} {}_0R_{22} + {}^1R'_{33} {}_0R_{23} \\ & + {}^1R_{21} {}_0R'_{31} + {}^1R_{22} {}_0R'_{32} + {}^1R_{23} {}_0R'_{33} \end{aligned} \quad (4.20)$$

The above expressions can be written in matrix form as

$${}_0^6\epsilon = \mathbf{EPSM} {}_0^{21}\mathbf{z} \quad (4.21)$$

The vector  ${}_0\epsilon$  is given by

$${}^0_{6 \times 1} \boldsymbol{\epsilon} = \begin{bmatrix} {}^0\bar{\epsilon}_{11} \\ {}^0\kappa_{22} \\ {}^0\kappa_{33} \\ {}^0\bar{\gamma}_{12} \\ {}^0\bar{\gamma}_{13} \\ {}^0\rho_{13} \end{bmatrix}, \quad (4.22)$$

and the vector  ${}^0\mathbf{z}$  is the incremental form of the partitioned vector  ${}^2_0\mathbf{z}$ , which is given by

$${}^0_{21 \times 1} \mathbf{z} = \begin{bmatrix} {}^0_{3 \times 1} \mathbf{u}'_o \\ \mathbf{R} \\ {}^0_{9 \times 1} \tilde{\mathbf{R}}' \end{bmatrix} \quad (4.23)$$

The matrix **EPSM** is a partitioned matrix which can be written as

$$\mathbf{EPSM} = \begin{bmatrix} \mathbf{EPSMA} & \mathbf{EPSMB} & \mathbf{EPSMC} \end{bmatrix} \quad (4.24)$$

$\begin{matrix} 6 \times 21 & 6 \times 3 & 6 \times 9 \end{matrix}$

The matrices **EPSMA**, **EPSMB**, and **EPSMC** are shown in Fig. 4.2.

### 4.3 INCREMENTAL EQUILIBRIUM EQUATIONS

Equilibrium for the three-dimensional beam finite element was given in Chapter 3 as

$$\delta({}^2_0U) - \delta({}^2_0W_E) = 0 \quad (4.25)$$

The linearized incremental form of the equilibrium equation results from expanding the above equilibrium equation about the known intermediate configuration 1 in terms of the small incremental displacements from configuration 1 to configuration 2. The resulting incremental equilibrium equation is

$$\delta({}^1_0U) + \delta({}_0U) - \delta({}^1_0W_E) - \delta({}_0W_E) = 0 \quad (4.26)$$

Since configuration 1 is a known equilibrium configuration the two terms

$$\begin{aligned}
\mathbf{EPSMA}_{6 \times 3} &= \begin{bmatrix} (1 + {}^1_0 u'_{o_1}) & {}^1_0 u'_{o_2} & {}^1_0 u'_{o_3} \\ {}^1_0 R'_{21} & {}^1_0 R'_{22} & {}^1_0 R'_{23} \\ {}^1_0 R'_{31} & {}^1_0 R'_{32} & {}^1_0 R'_{33} \\ {}^1_0 R_{21} & {}^1_0 R_{22} & {}^1_0 R_{23} \\ {}^1_0 R_{31} & {}^1_0 R_{32} & {}^1_0 R_{33} \\ 0 & 0 & 0 \end{bmatrix} \\
\mathbf{EPSMB}_{6 \times 9} &= \begin{bmatrix} 0 & 0 & 0 & 0 & 0 & 0 & 0 & 0 & 0 \\ 0 & 0 & 0 & 0 & 0 & 0 & 0 & 0 & 0 \\ 0 & 0 & 0 & 0 & 0 & 0 & 0 & 0 & 0 \\ 0 & 0 & 0 & (1 + {}^1_0 u'_{o_1}) & {}^1_0 u'_{o_2} & {}^1_0 u'_{o_3} & 0 & 0 & 0 \\ 0 & 0 & 0 & 0 & 0 & 0 & (1 + {}^1_0 u'_{o_1}) & {}^1_0 u'_{o_2} & {}^1_0 u'_{o_3} \\ 0 & 0 & 0 & {}^1_0 R'_{31} & {}^1_0 R'_{32} & {}^1_0 R'_{33} & 0 & 0 & 0 \end{bmatrix} \\
\mathbf{EPSMC}_{6 \times 9} &= \begin{bmatrix} 0 & 0 & 0 & 0 & 0 & 0 & 0 & 0 & 0 \\ 0 & 0 & 0 & (1 + {}^1_0 u'_{o_1}) & {}^1_0 u'_{o_2} & {}^1_0 u'_{o_3} & 0 & 0 & 0 \\ 0 & 0 & 0 & 0 & 0 & 0 & (1 + {}^1_0 u'_{o_1}) & {}^1_0 u'_{o_2} & {}^1_0 u'_{o_3} \\ 0 & 0 & 0 & 0 & 0 & 0 & 0 & 0 & 0 \\ 0 & 0 & 0 & 0 & 0 & 0 & 0 & 0 & 0 \\ 0 & 0 & 0 & 0 & 0 & 0 & {}^1_0 R_{21} & {}^1_0 R_{22} & {}^1_0 R_{23} \end{bmatrix}
\end{aligned}$$

Figure 4.2 Matrices **EPSMA**, **EPSMB**, and **EPSMC** from the partitioned matrix **EPSM**.

$$\delta({}_0^1U) = 0 \quad (4.27)$$

and

$$\delta({}_0^1W_E) = 0 \quad (4.28)$$

The resulting incremental equilibrium equation is

$$\delta({}_0U) - \delta({}_0W_E) = 0 \quad (4.29)$$

Both of the terms  $\delta({}_0U)$  and  $\delta({}_0W_E)$  are linear functions of the unknown incremental displacements.

The expression for the internal virtual work was given in Chapter 3 as

$$\delta({}_0^2U) = \int_0^{0L} \delta({}_0^2\mathcal{U}) d^0X_1 \quad (4.30)$$

where

$$\delta({}_0^2\mathcal{U}) = \delta \left( \begin{matrix} 2 \\ 0 \end{matrix} \mathbf{3}^T \right) \begin{matrix} 2 \\ 0 \end{matrix} \mathcal{R} \quad (4.31)$$

$\begin{matrix} 1 \times 21 & 21 \times 1 \end{matrix}$

The definitions of the vectors  $\begin{matrix} 2 \\ 0 \end{matrix} \mathcal{R}$  and  $\begin{matrix} 2 \\ 0 \end{matrix} \mathbf{3}$  were also given in Chapter 3. The incremental form of the internal virtual work is found by expanding about the known equilibrium configuration 1. The resulting incremental expression for the integrand of the internal virtual work is

$$\delta({}_0^2\mathcal{U}) = \left[ \delta \left( \begin{matrix} 1 \\ 0 \end{matrix} \mathbf{3}^T \right) + \delta \left( \begin{matrix} 2 \\ 0 \end{matrix} \mathbf{3}^T \right) \right] \left( \begin{matrix} 1 \\ 0 \end{matrix} \mathcal{R} + \begin{matrix} 0 \\ 21 \end{matrix} \mathcal{R} \right) \quad (4.32)$$

$\begin{matrix} 1 \times 21 & 21 \times 1 \end{matrix}$

Since the displacements at configuration 1 are known, the term

$$\delta \left( \begin{matrix} 1 \\ 0 \end{matrix} \mathbf{3}^T \right) = 0 \quad (4.33)$$

The expanded incremental form of  $\delta({}_0^2\mathcal{U})$  becomes

$$\delta({}_0^2\mathcal{U}) = \delta\left({}_0^1\mathbf{3}^T\right)\left({}_0^1\mathbf{R} + {}_0^1\mathbf{R}\right), \quad (4.34)$$

which will be computed in two parts given by:

$$\delta({}_0^2\mathcal{U}_A) = \delta\left({}_0^1\mathbf{3}^T\right){}_0^1\mathbf{R} \quad (4.35)$$

and

$$\delta({}_0^2\mathcal{U}_B) = \delta\left({}_0^1\mathbf{3}^T\right){}_0^1\mathbf{R} \quad (4.36)$$

The vector  $\delta({}_0^1\mathbf{3}^T)$  is a partitioned vector that has the same form as Eq. 4.23;

$$\delta({}_0^1\mathbf{3}^T) = \left[ \delta\left({}_0^1\mathbf{u}_o'^T\right) \quad \delta\left({}_0^1\mathbf{R}^T\right) \quad \delta\left({}_0^1\mathbf{R}'^T\right) \right] \quad (4.37)$$

Details of the calculation of the vector form of the incremental rotations is given in Appendix B. The resulting expression for  $\mathbf{R}$  is

$$\mathbf{R} = \mathbf{RTM01} \boldsymbol{\phi} \quad (4.38)$$

where the matrix  $\mathbf{RTM01}$  is a nonlinear function of the rotations to the known intermediate configuration 1 and the vector  $\boldsymbol{\phi}$  contains the incremental rotations from configuration 1 to configuration 2. Using Eq. 4.38,  $\delta(\mathbf{R})$  is given by

$$\delta(\mathbf{R}) = \mathbf{RTM01} \delta(\boldsymbol{\phi}) \quad (4.39)$$

A complete explanation of the expansion and linearization of the derivative of the incremental rotation matrix,  ${}_0^1\mathbf{R}'$ , is given in Appendix C. The resulting expression for the vector form of  ${}_0^1\mathbf{R}'$  is

$${}_0^1\mathbf{R}' = \left[ \mathbf{RPR1} \quad \mathbf{RPR2} \right] \begin{bmatrix} \boldsymbol{\phi} \\ \boldsymbol{\phi}' \end{bmatrix} \quad (4.40)$$

where the matrices **RPR1** and **RPR2** are defined by Eqs. C.38 and C.39. Since the matrices **RPR1** and **RPR2** are only functions of the rotations to the known configuration 1, the first variation of  ${}_0\tilde{\mathbf{R}}'$  becomes

$$\delta \begin{pmatrix} {}_0\tilde{\mathbf{R}}' \\ 9 \times 1 \end{pmatrix} = \begin{bmatrix} \mathbf{RPR1} & \mathbf{RPR2} \end{bmatrix} \begin{bmatrix} \delta \begin{pmatrix} \boldsymbol{\phi} \\ 3 \times 1 \end{pmatrix} \\ \delta \begin{pmatrix} \boldsymbol{\phi}' \\ 3 \times 1 \end{pmatrix} \end{bmatrix} \quad (4.41)$$

Using Eqs. 4.39 and 4.41 the vector

$$\delta \begin{pmatrix} {}_0\mathbf{3} \\ 21 \times 1 \end{pmatrix} = \begin{bmatrix} \mathbf{I} & 0 & 0 \\ 0 & \mathbf{RTM01} & 0 \\ 0 & \mathbf{RPR1} & \mathbf{RPR2} \end{bmatrix} \begin{bmatrix} \delta \begin{pmatrix} {}_0\mathbf{u}'_o \\ 3 \times 1 \end{pmatrix} \\ \delta \begin{pmatrix} \boldsymbol{\phi} \\ 3 \times 1 \end{pmatrix} \\ \delta \begin{pmatrix} \boldsymbol{\phi}' \\ 3 \times 1 \end{pmatrix} \end{bmatrix}, \quad (4.42)$$

or in a more compact form as

$$\delta \begin{pmatrix} {}_0\mathbf{3} \\ 21 \times 1 \end{pmatrix} = \mathbf{DELTR2} \delta \begin{pmatrix} {}_0\mathbf{u} \\ 9 \times 1 \end{pmatrix} \quad (4.43)$$

As in Chapter 3, the continuous incremental displacements are interpolated using linear interpolation functions. Using the interpolation matrix defined by Eq. 3.133, the incremental displacements may be expressed in terms of nodal displacements as

$$\delta \begin{pmatrix} {}_0\mathbf{u} \\ 9 \times 1 \end{pmatrix} = \mathbf{SHPMAT} \delta \begin{pmatrix} {}_0\mathbf{d} \\ 12 \times 1 \end{pmatrix} \quad (4.44)$$

The vector  $\delta({}_0\mathbf{3})$  becomes

$$\delta \begin{pmatrix} {}_0\mathbf{3} \\ 21 \times 1 \end{pmatrix} = \mathbf{DELTR2} \mathbf{SHPMAT} \delta \begin{pmatrix} {}_0\mathbf{d} \\ 12 \times 1 \end{pmatrix} \quad (4.45)$$

The resulting expression for  $\delta({}_0\mathcal{U}_A)$  is straightforward since the vector  ${}_0^1\mathcal{R}$  has the same form as the vector  ${}_0^2\mathcal{R}$  from Chapter 3. Using Eq. 4.45,  $\delta({}_0\mathcal{U}_A)$  is

$$\delta({}_0\mathcal{U}_A) = \delta \begin{pmatrix} \mathbf{d}^T \\ {}_0 \\ 1 \times 12 \end{pmatrix} \underset{12 \times 9}{\mathbf{SHPMAT}}^T \underset{9 \times 21}{\mathbf{DELTR2}}^T \underset{21 \times 1}{{}_0\mathbf{R}} \quad (4.46)$$

The expression for  $\delta({}_0\mathcal{U}_B)$  involves the vector  ${}_0\mathbf{R}$  which is calculated in two parts:  ${}_0\mathbf{R}_A$  and  ${}_0\mathbf{R}_B$ . The first portion of  ${}_0\mathbf{R}$  is calculated using the incremental strains  ${}_0\boldsymbol{\varepsilon}$ :

$${}_0\mathbf{R}_A = \begin{bmatrix} \underset{3 \times 6}{\mathbf{RSAA01}} \\ \underset{3 \times 6}{\mathbf{RSAB01}} \\ \underset{3 \times 6}{\mathbf{RSAC01}} \end{bmatrix} \underset{6 \times 1}{{}_0\boldsymbol{\varepsilon}} \quad (4.47)$$

where the matrices **RSAA01**, **RSAB01**, and **RSAC01** are shown in Fig. 4.3. In a more compact form

$$\underset{21 \times 1}{{}_0\mathbf{R}_A} = \underset{21 \times 6}{\mathbf{RSA01}} \underset{6 \times 1}{{}_0\boldsymbol{\varepsilon}} \quad (4.48)$$

Using Eq. 4.21 the above expression becomes

$$\underset{21 \times 1}{{}_0\mathbf{R}_A} = \underset{21 \times 6}{\mathbf{RSA01}} \underset{6 \times 21}{\mathbf{EPSM}} \underset{21 \times 1}{{}_0\mathbf{Z}} \quad (4.49)$$

The expression for  ${}_0\mathbf{R}_B$  can be written directly in terms of the vector  ${}_0\mathbf{Z}$  as

$$\underset{21 \times 1}{{}_0\mathbf{R}_B} = \underset{21 \times 21}{\mathbf{RSB01}} \underset{21 \times 1}{{}_0\mathbf{Z}} \quad (4.50)$$

The matrix **RSB01** is a partitioned matrix given by

$$\underset{21 \times 21}{\mathbf{RSB01}} = \begin{bmatrix} \underset{3 \times 21}{\mathbf{RSBA01}} \\ \underset{9 \times 21}{\mathbf{RSBB01}} \\ \underset{9 \times 21}{\mathbf{RSBC01}} \end{bmatrix} \quad (4.51)$$

where the sub-matrix **RSBA01** is shown in Fig. 4.4, and the sub-matrices **RSBB01** and **RSBC01** are shown in Fig. 4.5. The expression for  $\delta({}_0\mathcal{U}_B)$  becomes

$$\delta({}_0\mathcal{U}_B) = \delta \begin{pmatrix} \mathbf{Z}^T \\ {}_0 \\ 1 \times 21 \end{pmatrix} (\underset{21 \times 6}{\mathbf{RSA01}} \underset{6 \times 21}{\mathbf{EPSM}} + \underset{21 \times 21}{\mathbf{RSB01}}) \underset{21 \times 1}{{}_0\mathbf{Z}} \quad (4.52)$$



$$\mathbf{RSAA01}_{3 \times 6} = \begin{bmatrix} E^0 A (1 + {}^1_0 u'_{o_1}) & E^0 I_y {}^1_0 R'_{21} & E^0 I_z {}^1_0 R'_{31} & G^0 A_S {}^1_0 R_{21} & G^0 A_S {}^1_0 R_{31} & 0 \\ E^0 A {}^1_0 u'_{o_2} & E^0 I_y {}^1_0 R'_{22} & E^0 I_z {}^1_0 R'_{32} & G^0 A_S {}^1_0 R_{22} & G^0 A_S {}^1_0 R_{32} & 0 \\ E^0 A {}^1_0 u'_{o_3} & E^0 I_y {}^1_0 R'_{23} & E^0 I_z {}^1_0 R'_{33} & G^0 A_S {}^1_0 R_{23} & G^0 A_S {}^1_0 R_{33} & 0 \end{bmatrix}$$

$$\mathbf{RSAB01}_{9 \times 6} = \begin{bmatrix} 0 & 0 & 0 & 0 & 0 & 0 \\ 0 & 0 & 0 & 0 & 0 & 0 \\ 0 & 0 & 0 & 0 & 0 & 0 \\ 0 & 0 & 0 & G^0 A_S (1 + {}^1_0 u'_{o_1}) & 0 & G^0 J {}^1_0 R'_{31} \\ 0 & 0 & 0 & G^0 A_S {}^1_0 u'_{o_2} & 0 & G^0 J {}^1_0 R'_{32} \\ 0 & 0 & 0 & G^0 A_S {}^1_0 u'_{o_3} & 0 & G^0 J {}^1_0 R'_{33} \\ 0 & 0 & 0 & 0 & G^0 A_S (1 + {}^1_0 u'_{o_1}) & 0 \\ 0 & 0 & 0 & 0 & G^0 A_S {}^1_0 u'_{o_2} & 0 \\ 0 & 0 & 0 & 0 & G^0 A_S {}^1_0 u'_{o_3} & 0 \end{bmatrix}$$

$$\mathbf{RSAC01}_{9 \times 6} = \begin{bmatrix} 0 & 0 & 0 & 0 & 0 & 0 \\ 0 & 0 & 0 & 0 & 0 & 0 \\ 0 & 0 & 0 & 0 & 0 & 0 \\ 0 & E^0 I_y (1 + {}^1_0 u'_{o_1}) & 0 & 0 & 0 & 0 \\ 0 & E^0 I_y {}^1_0 u'_{o_2} & 0 & 0 & 0 & 0 \\ 0 & E^0 I_y {}^1_0 u'_{o_3} & 0 & 0 & 0 & 0 \\ 0 & 0 & E^0 I_z (1 + {}^1_0 u'_{o_1}) & 0 & 0 & G^0 J {}^1_0 R_{21} \\ 0 & 0 & E^0 I_z {}^1_0 u'_{o_2} & 0 & 0 & G^0 J {}^1_0 R_{22} \\ 0 & 0 & E^0 I_z {}^1_0 u'_{o_3} & 0 & 0 & G^0 J {}^1_0 R_{23} \end{bmatrix}$$

Figure 4.3 Matrices **RSAA01**, **RSAB01**, and **RSAC01** from the partitioned matrix **RSA01**.

$$\mathbf{RSBA01}_{21 \times 3}^T = \begin{bmatrix} E^0 A_{0^1 \bar{\varepsilon}_{11}} & 0 & 0 \\ 0 & E^0 A_{0^1 \bar{\varepsilon}_{11}} & 0 \\ 0 & 0 & E^0 A_{0^1 \bar{\varepsilon}_{11}} \\ 0 & 0 & 0 \\ 0 & 0 & 0 \\ 0 & 0 & 0 \\ G^0 A_{S^1 \bar{\gamma}_{12}} & 0 & 0 \\ 0 & G^0 A_{S^1 \bar{\gamma}_{12}} & 0 \\ 0 & 0 & G^0 A_{S^1 \bar{\gamma}_{12}} \\ G^0 A_{S^1 \bar{\gamma}_{13}} & 0 & 0 \\ 0 & G^0 A_{S^1 \bar{\gamma}_{13}} & 0 \\ 0 & 0 & G^0 A_{S^1 \bar{\gamma}_{13}} \\ 0 & 0 & 0 \\ 0 & 0 & 0 \\ 0 & 0 & 0 \\ E^0 I_{y^1 \kappa_{22}} & 0 & 0 \\ 0 & E^0 I_{y^1 \kappa_{22}} & 0 \\ 0 & 0 & E^0 I_{y^1 \kappa_{22}} \\ E^0 I_{z^1 \kappa_{33}} & 0 & 0 \\ 0 & E^0 I_{z^1 \kappa_{33}} & 0 \\ 0 & 0 & E^0 I_{z^1 \kappa_{33}} \end{bmatrix}$$

Figure 4.4 Matrix **RSBA01** from the partitioned matrix **RSB01**.

$$\mathbf{RSBB01}^T =$$

$$\mathbf{RSBC01}_{21 \times 9}^T =$$

Figure 4.5 Matrices **RSBB01** and **RSBC01** from the partitioned matrix **RSB01**.

The vector  ${}_0\mathbf{3}$  has the same form as  $\delta({}_0\mathbf{3})$ , Eq. 4.45, and is given by

$${}_0\mathbf{3} = \underset{21 \times 1}{\mathbf{DELTR2}} \underset{21 \times 9}{\mathbf{SHPMAT}} \underset{9 \times 12}{\mathbf{d}} \underset{12 \times 1}{\mathbf{d}} \quad (4.53)$$

Using Eqs. 4.46, 4.52, and 4.53, the integrand of the incremental internal virtual work  $\delta({}_0\mathcal{U})$  is

$$\begin{aligned} \delta({}_0\mathcal{U}) = & \delta\left({}_0\mathbf{d}^T\right) \underset{12 \times 9}{\mathbf{SHPMAT}}^T \underset{9 \times 21}{\mathbf{DELTR2}}^T \left[ \underset{21 \times 1}{\mathbf{1}} \underset{21 \times 1}{\mathbf{R}} \right. \\ & \left. + \left( \underset{21 \times 6}{\mathbf{RSA01}} \underset{6 \times 21}{\mathbf{EPSM}} + \underset{21 \times 21}{\mathbf{RSB01}} \right) \underset{21 \times 9}{\mathbf{DELTR2}} \underset{9 \times 12}{\mathbf{SHPMAT}} \underset{12 \times 1}{\mathbf{d}} \right] \quad (4.54) \end{aligned}$$

Substituting the above expression into the internal virtual work gives

$$\begin{aligned} \delta({}_0U) = & \delta\left({}_0\mathbf{d}^T\right) \left\{ \frac{{}^0L}{2} \int_{-1}^{+1} \left( \underset{12 \times 9}{\mathbf{SHPMAT}}^T \underset{9 \times 21}{\mathbf{DELTR2}}^T \underset{21 \times 1}{\mathbf{1}} \underset{21 \times 1}{\mathbf{R}} \right) d^0\xi \right. \\ & + \frac{{}^0L}{2} \int_{-1}^{+1} \left[ \underset{12 \times 9}{\mathbf{SHPMAT}}^T \underset{9 \times 21}{\mathbf{DELTR2}}^T \left( \underset{21 \times 6}{\mathbf{RSA01}} \underset{6 \times 21}{\mathbf{EPSM}} \right. \right. \\ & \left. \left. + \underset{21 \times 21}{\mathbf{RSB01}} \right) \underset{21 \times 9}{\mathbf{DELTR2}} \underset{9 \times 12}{\mathbf{SHPMAT}} \underset{12 \times 1}{\mathbf{d}} d^0\xi \right] \quad (4.55) \end{aligned}$$

The resulting integrals are evaluated using single point gauss quadrature, as in Chapter 3. Integration leads to two  $12 \times 1$  vectors of internal forces  ${}_0^1\mathbf{f}_I$  and  ${}_0\mathbf{f}_I$ . The expression for the internal virtual work can be reduced to

$$\delta({}_0U) = \delta\left({}_0\mathbf{d}^T\right) \left( \underset{12 \times 1}{{}_0^1\mathbf{f}_I} + \underset{12 \times 1}{{}_0\mathbf{f}_I} \right) \quad (4.56)$$

The external virtual work can also be expanded in terms of the displacements at configuration 1 and the incremental displacements from configuration 1 to configuration 2. The incremental form of  $\delta({}_0^2W_E)$  is

$$\delta({}_0^2W_E) = \left[ \delta \left( {}_0^1\mathbf{d}^T \right) + \delta \left( {}_0^0\mathbf{d}^T \right) \right] \left( {}_{12 \times 1}^1\mathbf{f}_E + {}_{12 \times 1}^0\mathbf{f}_E \right) \quad (4.57)$$

The term  $\delta({}_0^1\mathbf{d}^T)$  is equal to zero since the intermediate configuration is known. Therefore, the incremental external virtual work is

$$\delta({}_0^2W_E) = \delta \left( {}_0^0\mathbf{d}^T \right) {}_{12 \times 1}^1\mathbf{f}_E + \delta \left( {}_0^0\mathbf{d}^T \right) {}_{12 \times 1}^0\mathbf{f}_E \quad (4.58)$$

where  ${}^1\mathbf{f}_E$  is the external force at the intermediate configuration 1 and  $\mathbf{f}_E$  is a small change in the external force.

The incremental equilibrium condition for the three-dimensional beam finite element was given by Eq. 4.29. Substituting Eqs. 4.56 and 4.58 into 4.29 gives

$$\delta \left( {}_0^0\mathbf{d}^T \right) \left( {}_{12 \times 1}^1\mathbf{f}_I + {}_{12 \times 1}^0\mathbf{f}_I - {}_{12 \times 1}^1\mathbf{f}_E - {}_{12 \times 1}^0\mathbf{f}_E \right) = 0 \quad (4.59)$$

In general  $\delta({}_0^0\mathbf{d}^T)$  is not equal to zero and equilibrium is given by

$${}_{12 \times 1}^1\mathbf{f}_I + {}_{12 \times 1}^0\mathbf{f}_I - {}_{12 \times 1}^1\mathbf{f}_E - {}_{12 \times 1}^0\mathbf{f}_E = 0 \quad (4.60)$$

The term

$${}_{12 \times 1}^1\mathbf{f}_I - {}_{12 \times 1}^1\mathbf{f}_E = 0 \quad (4.61)$$

is the equilibrium condition at configuration 1 which is already known to exist. Therefore, the incremental equilibrium equation reduces to

$${}_{12 \times 1}^0\mathbf{f}_I - {}_{12 \times 1}^0\mathbf{f}_E = 0 \quad (4.62)$$

where the vector  ${}^0\mathbf{f}_I$  is taken from Eq. 4.55 as

$$\begin{aligned}
{}^0\mathbf{f}_I = & \left\{ \frac{{}^0L}{2} \int_{-1}^{+1} \left[ \underset{12 \times 9}{\mathbf{SHPMAT}^T} \underset{9 \times 21}{\mathbf{DELTR2}^T} \left( \underset{21 \times 6}{\mathbf{RSA01}} \underset{6 \times 21}{\mathbf{EPSM}} \right. \right. \right. \\
& \left. \left. \left. + \underset{21 \times 21}{\mathbf{RSB01}} \right) \underset{21 \times 9}{\mathbf{DELTR2}} \underset{9 \times 12}{\mathbf{SHPMAT}} \right] d^0\xi \right\} \underset{12 \times 1}{\mathbf{d}}
\end{aligned} \tag{4.63}$$

The above integral results in a  $12 \times 12$  matrix,  ${}^1\mathbf{k}_T$ , that is often referred to as the tangent stiffness matrix, and is a nonlinear function of the displacements and rotations to the intermediate configuration 1. The incremental equilibrium equation can be further reduced to

$$\underset{12 \times 1}{\mathbf{f}_E} = \underset{12 \times 12}{\underset{12 \times 12}{\underset{12 \times 1}{\mathbf{k}_T}}} \underset{12 \times 1}{\mathbf{d}}, \tag{4.64}$$

which means that for a small change in external forces the incremental displacements  ${}^0\mathbf{d}$  may be found.

#### 4.4 LOCAL TO GLOBAL TRANSFORMATION

Thus far, the local axes,  ${}^0X_i$ , of each finite element have been considered to be aligned with the global axes,  ${}^0X_i^*$ , of the entire structure. In general each element will be arbitrarily oriented with respect to the global axes as shown in Fig. 4.6. The orientation of the unit vectors  ${}^0\mathbf{n}_i$  along the local axes is related to the orientation of the unit vectors,  ${}^0\mathbf{n}_i^*$ , along the global axes by a transformation matrix  $\mathbf{T}$  that has the same properties as the rotation matrix covered in Chapter 3. The rows of the transformation matrix  $\mathbf{T}$  contain the direction cosines of each local axis with respect to the three global axes. The relationship between  ${}^0\mathbf{n}_i$  and  ${}^0\mathbf{n}_i^*$  is

$${}^0\mathbf{n}_i = \mathbf{T} {}^0\mathbf{n}_i^* \tag{4.65}$$

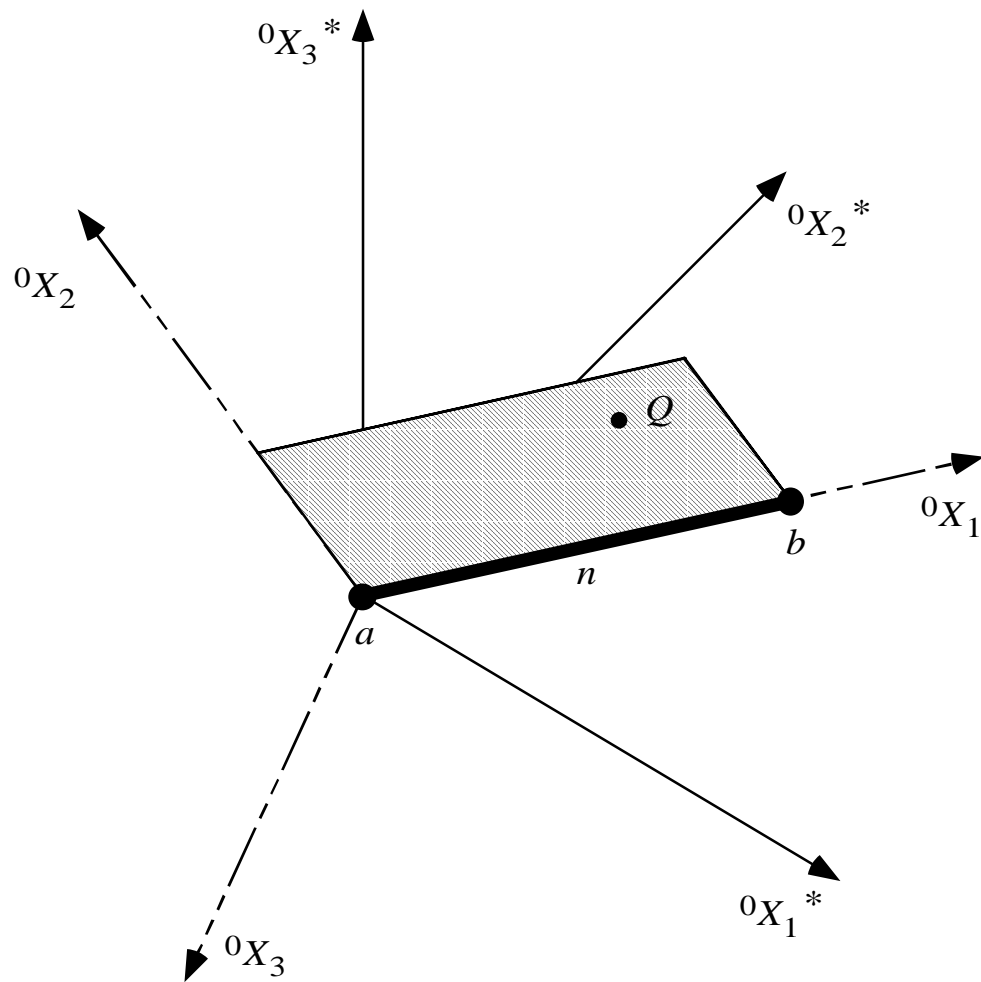


Figure 4.6 Global orientation of a three-dimensional finite element.

The development of  $\mathbf{T}$  for an element  $n$  with nodes  $a$  and  $b$  at either end begins by specifying a unit vector along the centroidal axis of the member. The unit vector  ${}^0\mathbf{n}_1$  along  ${}^0X_1$  is

$$\begin{aligned} {}^0\mathbf{n}_1 = & \underbrace{\frac{({}^0X_{1b}^* - {}^0X_{1a}^*)}{{}^0L}}_{\mathbf{T}_{11}} {}^0\mathbf{n}_1^* + \underbrace{\frac{({}^0X_{2b}^* - {}^0X_{2a}^*)}{{}^0L}}_{\mathbf{T}_{12}} {}^0\mathbf{n}_2^* \\ & + \underbrace{\frac{({}^0X_{3b}^* - {}^0X_{3a}^*)}{{}^0L}}_{\mathbf{T}_{13}} {}^0\mathbf{n}_3^* \end{aligned} \quad (4.66)$$

where  ${}^0L$  is the original length of the member which is given by

$$\begin{aligned} {}^0L = & \left[ ({}^0X_{1b}^* - {}^0X_{1a}^*)^2 + ({}^0X_{2b}^* - {}^0X_{2a}^*)^2 \right. \\ & \left. + ({}^0X_{3b}^* - {}^0X_{3a}^*)^2 \right]^{\frac{1}{2}} \end{aligned} \quad (4.67)$$

To completely describe the orientation of the element, the global coordinates of a point  $Q$  that lies in the local  ${}^0X_1$ - ${}^0X_2$  plane must be specified by the user. A vector along the  ${}^0X_3$  axis is found by taking the cross product between the unit vector  ${}^0\mathbf{n}_1$  and a vector from  $a$  to  $Q$ ,  $\mathbf{r}_{Q/a}$ . The resulting cross product is

$$\begin{aligned} {}^0\mathbf{n}_1 \times \mathbf{r}_{Q/a} = & \left[ \mathbf{T}_{12}({}^0X_{3Q}^* - {}^0X_{3a}^*) - \mathbf{T}_{13}({}^0X_{2Q}^* - {}^0X_{2a}^*) \right] {}^0\mathbf{n}_1^* \\ & + \left[ \mathbf{T}_{13}({}^0X_{1Q}^* - {}^0X_{1a}^*) - \mathbf{T}_{11}({}^0X_{3Q}^* - {}^0X_{3a}^*) \right] {}^0\mathbf{n}_2^* \\ & + \left[ \mathbf{T}_{11}({}^0X_{2Q}^* - {}^0X_{2a}^*) - \mathbf{T}_{12}({}^0X_{1Q}^* - {}^0X_{1a}^*) \right] {}^0\mathbf{n}_3^* \end{aligned} \quad (4.68)$$

To form the unit vector  ${}^0\mathbf{n}_3$  along the  ${}^0X_3$  axis, a constant  $D1$  must be defined as



$$\begin{aligned}
D1 = & \left\{ \left[ T_{12} \left( {}^0X_{3Q}^* - {}^0X_{3a}^* \right) - T_{13} \left( {}^0X_{2Q}^* - {}^0X_{2a}^* \right) \right]^2 \right. \\
& + \left[ T_{13} \left( {}^0X_{1Q}^* - {}^0X_{1a}^* \right) - T_{11} \left( {}^0X_{3Q}^* - {}^0X_{3a}^* \right) \right]^2 \\
& \left. + \left[ T_{11} \left( {}^0X_{2Q}^* - {}^0X_{2a}^* \right) - T_{12} \left( {}^0X_{1Q}^* - {}^0X_{1a}^* \right) \right]^2 \right\}^{\frac{1}{2}} \quad (4.69)
\end{aligned}$$

The unit vector  ${}^0\mathbf{n}_3$  is then equal to

$$\begin{aligned}
{}^0\mathbf{n}_3 = & \underbrace{\frac{\left[ T_{12} \left( {}^0X_{3Q}^* - {}^0X_{3a}^* \right) - T_{13} \left( {}^0X_{2Q}^* - {}^0X_{2a}^* \right) \right]}{D1}}_{T_{31}} {}^0\mathbf{n}_1^* \\
& + \underbrace{\frac{\left[ T_{13} \left( {}^0X_{1Q}^* - {}^0X_{1a}^* \right) - T_{11} \left( {}^0X_{3Q}^* - {}^0X_{3a}^* \right) \right]}{D1}}_{T_{32}} {}^0\mathbf{n}_2^* \\
& + \underbrace{\frac{\left[ T_{11} \left( {}^0X_{2Q}^* - {}^0X_{2a}^* \right) - T_{12} \left( {}^0X_{1Q}^* - {}^0X_{1a}^* \right) \right]}{D1}}_{T_{33}} {}^0\mathbf{n}_3^* \quad (4.70)
\end{aligned}$$

A vector along the  ${}^0X_2$  axis is found by taking the cross product of  ${}^0\mathbf{n}_3$  and  ${}^0\mathbf{n}_1$  which gives

$$\begin{aligned}
{}^0\mathbf{n}_3 \times {}^0\mathbf{n}_1 = & (T_{32}T_{13} - T_{33}T_{12}){}^0\mathbf{n}_1^* + (T_{33}T_{11} - T_{31}T_{13}){}^0\mathbf{n}_2^* \\
& + (T_{31}T_{12} - T_{32}T_{11}){}^0\mathbf{n}_3^* \quad (4.71)
\end{aligned}$$

The unit vector  ${}^0\mathbf{n}_2$  is found by first defining the constant  $D2$  which is equal to

$$\begin{aligned}
D2 = & \left\{ (T_{32}T_{13} - T_{33}T_{12})^2 + (T_{33}T_{11} - T_{31}T_{13})^2 \right. \\
& \left. + (T_{31}T_{12} - T_{32}T_{11})^2 \right\}^{\frac{1}{2}} \quad (4.72)
\end{aligned}$$

The unit vector  ${}^0\mathbf{n}_2$  is given by

$$\begin{aligned} {}^0\mathbf{n}_2 = & \underbrace{\frac{(T_{32}T_{13} - T_{33}T_{12})}{D2}}_{T_{21}} {}^0\mathbf{n}_1^* + \underbrace{\frac{(T_{33}T_{11} - T_{31}T_{13})}{D2}}_{T_{22}} {}^0\mathbf{n}_2^* \\ & + \underbrace{\frac{(T_{31}T_{12} - T_{32}T_{11})}{D2}}_{T_{23}} {}^0\mathbf{n}_3^* \end{aligned} \quad (4.73)$$

The local element displacements are stored in  $12 \times 1$  vectors  $\mathbf{d}$  whose left superscripts and subscripts depend on the configuration under consideration. The vector  $\mathbf{d}$  contains the nodal displacements at both the  $a$  and  $b$  ends of element  $n$ . At each end of the element there are six degrees of freedom that consist of three translations and three rotations. The vector  $\mathbf{d}$  may be partitioned into four  $3 \times 1$  vectors that contain the translations and rotations at each end of the element.

To demonstrate the use of the transformation matrix consider the transformation of the translations at the  $a$  end of element  $n$ . The three translations are stored in a  $3 \times 1$  vector  $\mathbf{d}_{a_t}$ . The local nodal translations can be expanded and written as

$$\mathbf{D}_{a_t} = \mathbf{d}_{a_t}^T {}^0\mathbf{n} \quad (4.74)$$

The same displacement vector along the global axes is

$$\mathbf{D}_{a_t} = \mathbf{q}_{a_t}^T {}^0\mathbf{n}^* \quad (4.75)$$

The matrix  ${}^0\mathbf{n}$  is related to the matrix  ${}^0\mathbf{n}^*$  by the transformation matrix (Eq. 4.65). Substituting Eq. 4.75 into Eq. 4.65 gives

$$\mathbf{D}_{a_t} = \mathbf{d}_{a_t}^T \mathbf{T} {}^0\mathbf{n}^* \quad (4.76)$$

Comparing Eqs. 4.75 and 4.76, the global displacement vector  $\mathbf{q}_{a_t}$  is given by

$$\mathbf{q}_{a_t} = \mathbf{T}^T \mathbf{d}_{a_t} \quad (4.77)$$

Each of the four  $3 \times 1$  vectors of displacements that are contained in the  $12 \times 1$  vector  $\mathbf{d}$  are transformed in the same way. The resulting transformation matrix is a partitioned  $12 \times 12$  matrix given by

$$\mathbf{T}_{12 \times 12}^* = \begin{bmatrix} \mathbf{T}_{3 \times 3} & 0 & 0 & 0 \\ 0 & \mathbf{T}_{3 \times 3} & 0 & 0 \\ 0 & 0 & \mathbf{T}_{3 \times 3} & 0 \\ 0 & 0 & 0 & \mathbf{T}_{3 \times 3} \end{bmatrix} \quad (4.78)$$

Therefore, the total global displacement vector for element  $n$  is

$$\mathbf{q} = \mathbf{T}^{*T} \mathbf{d} \quad (4.79)$$

In a similar manner, the global internal forces may be found using the same transformation,

$$\mathbf{F} = \mathbf{T}^{*T} \mathbf{f} \quad (4.80)$$

The tangent stiffness matrix  ${}^1_0\mathbf{k}_T$  for a specific element may be transformed using the transformation matrix,  $\mathbf{T}^*$ , from above. The relationship between the incremental internal forces and the incremental displacements was given by Eq. 4.63 as

$${}^0_{12 \times 1} \mathbf{f}_I = {}^0_{12 \times 12} \mathbf{k}_T {}^0_{12 \times 1} \mathbf{d} \quad (4.81)$$

Substituting Eqs. 4.79 and 4.80 into Eq. 4.81 gives

$${}^0_{12 \times 1} \mathbf{F}_I = \mathbf{T}_{12 \times 12}^{*T} {}^0_{12 \times 12} \mathbf{k}_T \mathbf{T}_{12 \times 12}^* {}^0_{12 \times 1} \mathbf{q} \quad (4.82)$$

The matrix product

$${}^1_0 \mathbf{K}_T = \mathbf{T}_{12 \times 12}^{*T} {}^0_{12 \times 12} \mathbf{k}_T \mathbf{T}_{12 \times 12}^* \quad (4.83)$$

results in the global tangent stiffness for element  $n$ .

## 4.5 NUMERICAL SOLUTION TECHNIQUES

Most numerical schemes to solve nonlinear systems of equations are incremental iterative processes that use a series of linear solutions to approximate the nonlinear solution. The linear solutions are achieved by expanding the nonlinear equations in terms of small incremental values of the unknowns about some known solution. For problems in structural mechanics the objective of the solution process is to trace the nonlinear equilibrium path for a given structure.

The equilibrium path for a structure is defined by the external load on the structure and the corresponding displacements necessary to maintain equilibrium at a given level of the external load. The nodal displacements of a structure are stored in a  $N \times 1$  vector  $\mathbf{q}$ , while the external nodal forces are stored in a  $N \times 1$  vector  $\mathbf{Q}$ . In both cases  $N$  is the number of nodal degrees of freedom included in the model of the structure. In the solution of most nonlinear structural problems the external load is applied in fractions or increments of the total external load. The external load vector is incremented by multiplying  $\mathbf{Q}$  by a scalar  $\lambda$  which is equal to a number between 0 and 1. For each load increment an iterative process is applied, consisting of a series of linear analyses which are solved for the unknown displacements required to maintain equilibrium of the structure under the specified increment of the external load.

The most basic nonlinear solution methods use load control techniques in which a specified increment of load is applied to the structure and the resulting displacements required to maintain equilibrium are calculated. The most popular load control technique is the Newton-Raphson method. More sophisticated solution techniques treat both the incremental loads and displacements as unknowns in the analysis. These methods are referred to as arc length methods. Arc length methods use a specified length of a vector that is tangent to the equilibrium path at some known point. The most popular of the arc

length methods are derived from the Riks-Wempner method. Each method differs in the way that iterations are constrained within a specified load increment. The first of the two methods used in this work is called the Riks-Wempner method on a normal plane and the second is called the Riks-Wempner method on a sphere. The discussion for both methods follows the fundamental work of Crisfield (1981) and Ramm (1981).

Details for the use of each of the three methods mentioned above are presented in the following sections. For each method, figures are given that demonstrate the procedure for a single degree-of-freedom model. In the development of each method, the displacement quantities will be treated as general  $N \times 1$  vectors which contain the nodal displacements for the entire structure.

#### 4.5.1 Newton-Raphson Method

The Newton-Raphson method begins at a known point  $i$  on the equilibrium path as shown in Fig. 4.7. An increment,  $\Delta\lambda_i$ , of the total external load is applied to the structure making the total load increment equal to

$$\lambda_{i+1} = \lambda_i + \Delta\lambda_i \quad (4.84)$$

The first iteration consists of finding the incremental displacements  $\Delta\mathbf{q}_i$  by solving

$$\underbrace{\mathbf{K}_{T_i}}_{N \times N} \underbrace{\Delta\mathbf{q}_i}_{N \times 1} = \underbrace{(\lambda_{i+1} - \lambda_i)}_{\Delta\lambda_i} \underbrace{\mathbf{Q}}_{N \times 1} = \underbrace{\mathbf{F}_{R_i}}_{N \times 1} \quad (4.85)$$

where  $\mathbf{K}_{T_i}$  is the tangent stiffness matrix at point  $i$ , which is assembled using Eq. 4.83.

Once the displacements  $\Delta\mathbf{q}_i$  are known the total displacements are given by

$$\mathbf{q}_k = \mathbf{q}_i + \Delta\mathbf{q}_i \quad (4.86)$$

The total displacements  $\mathbf{q}_k$  are then used to calculate the internal force vector  $\mathbf{F}_k$  which was defined by Eq. 3.136. The difference between the external loads,  $\lambda_{i+1}\mathbf{Q}$ , and the

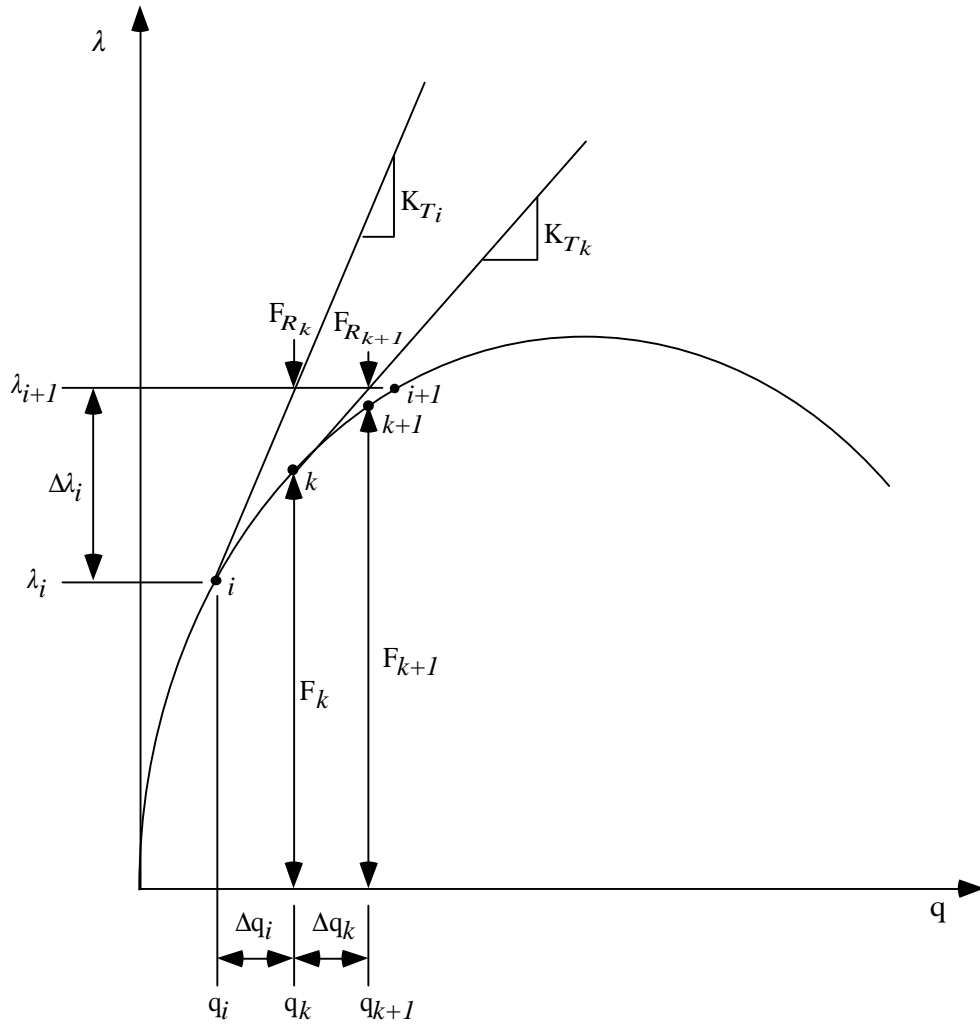


Figure 4.7 Newton-Raphson method for a single degree-of-freedom system.

internal forces,  $\mathbf{F}_k$ , form a vector  $\mathbf{F}_{R_k}$  which is known as the residual force vector. The presence of the residual vector  $\mathbf{F}_{R_k}$  indicates that the structure is not in equilibrium under the current combination of external load  $\lambda_i \mathbf{Q}$  and internal forces  $\mathbf{F}_k$  calculated from the displacements  $\mathbf{q}_k$ .

Subsequent iterations seek the incremental displacements that cause the residual vector  $\mathbf{F}_{R_k}$  to become approximately zero for the given external load  $\lambda_i \mathbf{Q}$ . Actually, the first iteration also seeks to minimize the out of balance forces  $\mathbf{F}_{R_i}$  which is equal to the user specified  $\Delta \lambda_i \mathbf{Q}$ . The incremental displacements,  $\Delta \mathbf{q}_k$ , for subsequent iterations are found from the expression

$$\mathbf{K}_{T_k} \Delta \mathbf{q}_k = \underbrace{\left( \lambda_{i+1} \mathbf{Q} - \mathbf{F}_k \right)}_{\mathbf{F}_{R_k}} \quad (4.87)$$

The total displacements are updated by

$$\mathbf{q}_{k+1} = \mathbf{q}_k + \Delta \mathbf{q}_k \quad (4.88)$$

The residual forces at  $k + 1$  are then computed and if the resulting residual vector is not close to zero then another iteration is performed until the residual force vector is approximately zero.

#### 4.5.2 Riks-Wempner Method on a Normal Plane

Iteration begins at point  $i$  on the load displacement curve and proceeds as shown in Fig. 4.8. A partitioned vector  $\mathbf{t}_i$  which is tangent to the equilibrium path at point  $i$  is defined as

$$\mathbf{t}_i = \begin{bmatrix} \Delta \mathbf{q}_i \\ \Delta \lambda_i \end{bmatrix} \quad (4.89)$$

where the scalar  $\Delta \lambda_i$  is the incremental change in the applied load at  $i$ , and the vector  $\Delta \mathbf{q}_i$

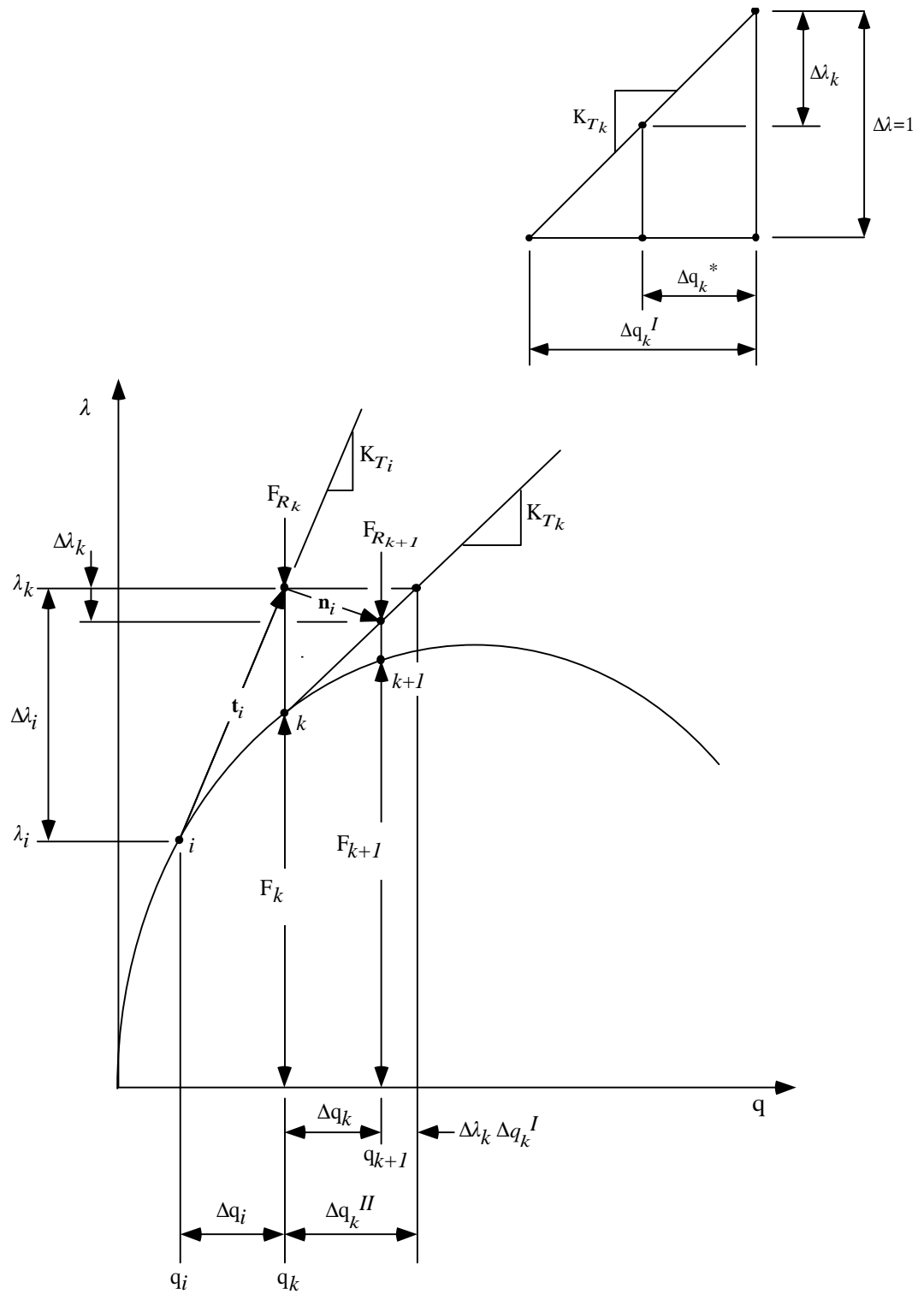


Figure 4.8 Riks-Wempner method on a normal plane for a single degree-of-freedom system.



contains the incremental displacements found from solving

$$\mathbf{K}_{T_i} \Delta \mathbf{q}_i = \Delta \lambda_i \mathbf{Q} \quad (4.90)$$

$N \times N \quad N \times 1 \quad N \times 1$

The matrix  $\mathbf{K}_{T_i}$  is the global tangent stiffness matrix at  $i$  which is assembled using Eq. 4.83. The objective of the method is to iterate along a normal to the tangent vector  $\mathbf{t}_i$  until the next equilibrium point is found. From Fig. 4.8 the normal  $\mathbf{n}_i$  is defined by

$$\mathbf{n}_i = \begin{bmatrix} \Delta \mathbf{q}_k \\ -\Delta \lambda_k \end{bmatrix} \quad (4.91)$$

$N \times 1$

where the vector  $\Delta \mathbf{q}_k$  is a vector of unknown displacements from  $k$  to the point where a tangent at  $k$  intersects with the normal vector  $\mathbf{n}_i$ . The scalar  $\Delta \lambda_k$  is an unknown load increment from  $\lambda_k$  down to the intersection between  $\mathbf{n}_i$  and the tangent from point  $k$ .

Constraining the iterative process to a normal plane requires that the dot product between  $\mathbf{t}_i$  and  $\mathbf{n}_i$  be equal to zero or

$$\mathbf{t}_i \cdot \mathbf{n}_i = 0 \quad (4.92)$$

Substituting Eqs. 4.89 and 4.91 into Eq. 4.92 gives

$$\Delta \mathbf{q}_i^T \Delta \mathbf{q}_k - \Delta \lambda_i \Delta \lambda_k = 0 \quad (4.93)$$

The vector  $\Delta \mathbf{q}_k$  is then split into two parts (Crisfield 1981; Ramm 1981)

$$\Delta \mathbf{q}_k = \Delta \mathbf{q}_k^{II} - \Delta \lambda_k \Delta \mathbf{q}_k^I \quad (4.94)$$

The vector  $\Delta \lambda_k \Delta \mathbf{q}_k^I$  results from the similar triangles which are also shown in Fig. 4.8.

Introducing an intermediate quantity  $\Delta \mathbf{q}_k^*$  the similar triangles relationship is

$$\frac{\Delta \lambda_k}{\Delta \mathbf{q}_k^*} = \frac{1}{\Delta \mathbf{q}_k^I}, \quad (4.95)$$

or

$$\Delta \mathbf{q}_k^* = \Delta \lambda_k \Delta \mathbf{q}_k^I \quad (4.96)$$

The vector  $\Delta \mathbf{q}_k^I$  results from the expression

$$\underset{N \times N}{\mathbf{K}_{T_k}} \underset{N \times 1}{\Delta \mathbf{q}_k^I} = \underset{N \times 1}{\Delta \lambda} \underset{N \times 1}{\mathbf{Q}} \quad (4.97)$$

where

$$\Delta \lambda = 1, \quad (4.98)$$

and  $\mathbf{K}_{T_k}$  is the tangent stiffness at  $k$ . The vector  $\Delta \mathbf{q}_k^{II}$  is computed by the expression

$$\underset{N \times N}{\mathbf{K}_{T_k}} \underset{N \times 1}{\Delta \mathbf{q}_k^{II}} = \underset{N \times 1}{\mathbf{F}_{R_k}} \quad (4.99)$$

where the vector  $\mathbf{F}_{R_k}$  is a residual vector that contains the difference in the externally applied forces and the internal forces at  $k$ . Introducing the expression for  $\Delta \mathbf{q}_k$  into the constraint equation (Eq. 4.93) gives

$$\Delta \mathbf{q}_i^T (\Delta \mathbf{q}_k^{II} - \Delta \lambda_k \Delta \mathbf{q}_k^I) - \Delta \lambda_i \Delta \lambda_k = 0 \quad (4.100)$$

Expanding the above equation and solving for  $\Delta \lambda_k$  yields

$$\Delta \lambda_k = \frac{\Delta \mathbf{q}_i^T \Delta \mathbf{q}_k^{II}}{(\Delta \mathbf{q}_i^T \Delta \mathbf{q}_k^I + \Delta \lambda_i)} \quad (4.101)$$

With  $\Delta \lambda_k$  known, the external load increment may be updated by the expression

$$\lambda_{k+1} = \lambda_k + \Delta \lambda_k \quad (4.102)$$

and the total displacements at  $k + 1$  may be found as

$$\mathbf{q}_{k+1} = \mathbf{q}_k + \Delta \mathbf{q}_k \quad (4.103)$$

or

$$\mathbf{q}_{k+1} = \mathbf{q}_k + (\Delta \mathbf{q}_k^{II} - \Delta \lambda_k \Delta \mathbf{q}_k^I) \quad (4.104)$$

As shown in Fig. 4.9, the Riks-Wempner method usually begins with a user specified load increment  $\Delta \lambda_0$  which is a fraction of the total external load applied to the structure. The load increment  $\Delta \lambda_0$  is used to calculate the displacement vector  $\Delta \mathbf{q}_0$  and

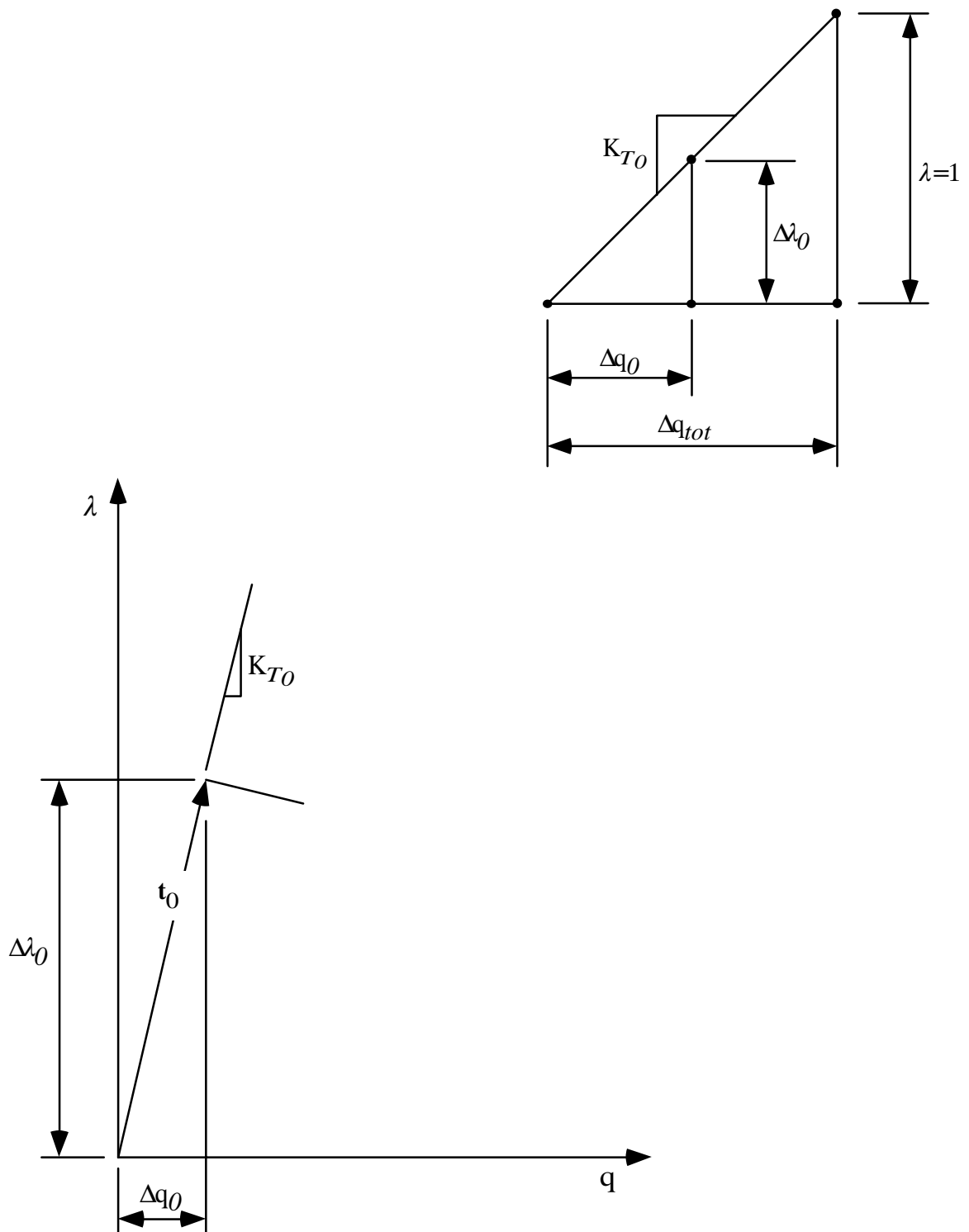


Figure 4.9 First iteration for the Riks-Wempner method.

the length  $\Delta S_0$  of the initial tangent vector  $\mathbf{t}_0$ . The displacements  $\Delta \mathbf{q}_0$  are calculated using the similar triangle relationship also shown in Fig. 4.9. The vector  $\Delta \mathbf{q}_0$  is computed from

$$\frac{\Delta \mathbf{q}_0}{\Delta \lambda_0} = \frac{\Delta \mathbf{q}_{tot}}{1}, \quad (4.105)$$

or

$$\Delta \mathbf{q}_0 = \Delta \lambda_0 \Delta \mathbf{q}_{tot} \quad (4.106)$$

The vector  $\Delta \mathbf{q}_{tot}$  is computed from the expression

$$\underset{N \times N}{\mathbf{K}_{T_0}} \underset{N \times 1}{\Delta \mathbf{q}_{tot}} = \lambda \underset{N \times 1}{\mathbf{Q}} \quad (4.107)$$

where the scalar  $\lambda$  is equal to one. With the vector  $\Delta \mathbf{q}_0$  known, the length of  $\mathbf{t}_0$  can be calculated by

$$|\mathbf{t}_0 \cdot \mathbf{t}_0| = \Delta S_0 = \sqrt{\Delta \lambda_0^2 + \Delta \mathbf{q}_0^T \Delta \mathbf{q}_0}, \quad (4.108)$$

or using Eq. 4.106

$$\Delta S_0 = \Delta \lambda_0 \sqrt{1 + \Delta \mathbf{q}_{tot}^T \Delta \mathbf{q}_{tot}} \quad (4.109)$$

The scalar  $\Delta S_0$  is often referred to as the arc length along the equilibrium path. The arc length for subsequent iterations is usually held constant or is scaled using the relationship

$$\Delta S_i = \Delta S_{i-1} \left( \frac{I_{des}}{I_{i-1}} \right)^{\frac{1}{2}} \quad (4.110)$$

The scalar  $\Delta S_{i-1}$  is the current arc length,  $I_{i-1}$  is the number of iterations required for convergence to the current equilibrium point, and  $I_{des}$  is the desired number of iterations which is usually chosen as a small number approximately equal to 3. A maximum value for  $\Delta S_i$  is usually specified as

$$\Delta S_{max} = 2 \Delta S_0 \quad (4.111)$$

The value of  $\Delta S_i$  is used to compute the value of  $\Delta \lambda_i$  which is required to begin the next iteration (Eq. 4.84). The value of  $\Delta \lambda_i$  is computed from Eq. 4.109 as

$$\Delta \lambda_i = \frac{\pm \Delta S_i}{\sqrt{1 + (\Delta \mathbf{q}_{tot})_i^T (\Delta \mathbf{q}_{tot})_i}} \quad (4.112)$$

The vector  $(\Delta \mathbf{q}_{tot})_i$  is computed from the relationship

$$\underset{N \times N}{\mathbf{K}_{T_i}} (\Delta \mathbf{q}_{tot})_i = \lambda \underset{N \times 1}{\mathbf{Q}} \quad (4.113)$$

where  $\lambda$  is equal to one.

The sign ambiguity in Eq. 4.112 results from the fact that the quantity  $\Delta S_i$  is simply a length (or magnitude) along the path whose direction is uncertain. The correct sign for  $\Delta \lambda_i$  is found by looking at the projection of the hypothetical tangent vector  $\mathbf{t}_i$  on the initial tangent vector for the previous iteration,  $\mathbf{t}_{i-1}$  (ABAQUS 1987). The partitioned tangent vector  $\mathbf{t}_i$  was given by Eq. 4.89. Using the expression

$$\Delta \mathbf{q}_i = \Delta \lambda_i (\Delta \mathbf{q}_{tot})_i, \quad (4.114)$$

the vector  $\mathbf{t}_i$  becomes

$$\mathbf{t}_i = \begin{bmatrix} \Delta \lambda_i (\Delta \mathbf{q}_{tot})_i \\ \Delta \lambda_i \end{bmatrix} \quad (4.115)$$

The vector  $\mathbf{t}_i$  is termed hypothetical because the correct sign of  $\Delta \lambda_i$  is not yet known.

The projection of  $\mathbf{t}_i$  on  $\mathbf{t}_{i-1}$  is

$$\mathbf{t}_i \cdot \mathbf{t}_{i-1} = \Delta \lambda_i (\Delta \mathbf{q}_{tot})_i^T \Delta \mathbf{q}_{i-1} + \Delta \lambda_i \Delta \lambda_{i-1} \quad (4.116)$$

which reduces to

$$\mathbf{t}_i \cdot \mathbf{t}_{i-1} = \Delta \lambda_i [(\Delta \mathbf{q}_{tot})_i^T \Delta \mathbf{q}_{i-1} + \Delta \lambda_{i-1}] \quad (4.117)$$

If the projection of  $\mathbf{t}_i$  on  $\mathbf{t}_{i-1}$  is negative then the slope of the equilibrium path at  $i$  is negative and the load parameter  $\Delta \lambda_i$  should be negative so that the external load on the

structure is reduced, thereby producing an unloading effect. If the projection of  $\mathbf{t}_i$  on  $\mathbf{t}_{i-1}$  is positive then the slope of the equilibrium path at  $i$  is positive and  $\Delta\lambda_i$  should be positive indicating that the external load is increasing.

#### 4.5.3 Riks-Wempner Method on a Sphere

As with Riks-Wempner on a normal plane, iteration begins by defining a partitioned tangent vector  $\mathbf{t}_i$  and continues as shown in Fig. 4.10. The tangent vector is equal to

$$\mathbf{t}_i = \begin{bmatrix} \Delta\mathbf{q}_i \\ \Delta\lambda_i \end{bmatrix} \quad (4.118)$$

where the incremental change in load  $\Delta\lambda_i$  is given by Eq. 4.112 and the incremental displacements  $\Delta\mathbf{q}_i$  are given by Eq. 4.114. The basic difference between the Riks-Wempner method on a normal plane and the Riks-Wempner method on a sphere is the way in which iterations are constrained for a given load increment. The Riks-Wempner method on a sphere constrains the iterative process to a sphere centered at point  $i$  with a radius that is equal to the magnitude,  $\Delta S_i$ , of the tangent vector  $\mathbf{t}_i$ . The constraint equation may be written as

$$\mathbf{r}_k \cdot \mathbf{r}_k = \Delta S_i^2 \quad (4.119)$$

The vector  $\mathbf{r}_k$  locates the position of the point, from point  $i$ , where a tangent from point  $k$  intersects with the sphere. The vector  $\mathbf{r}_k$  is given by

$$\mathbf{r}_k = \begin{bmatrix} \Delta\mathbf{q}_i + \Delta\mathbf{q}_k \\ \Delta\lambda_i - \Delta\lambda_k \end{bmatrix} \quad (4.120)$$

The constraint equation becomes

$$(\Delta\lambda_i - \Delta\lambda_k)^2 + \Delta\mathbf{q}_i^T \Delta\mathbf{q}_i + 2 \Delta\mathbf{q}_i^T \Delta\mathbf{q}_k + \Delta\mathbf{q}_k^T \Delta\mathbf{q}_k = \Delta S_i^2 \quad (4.121)$$

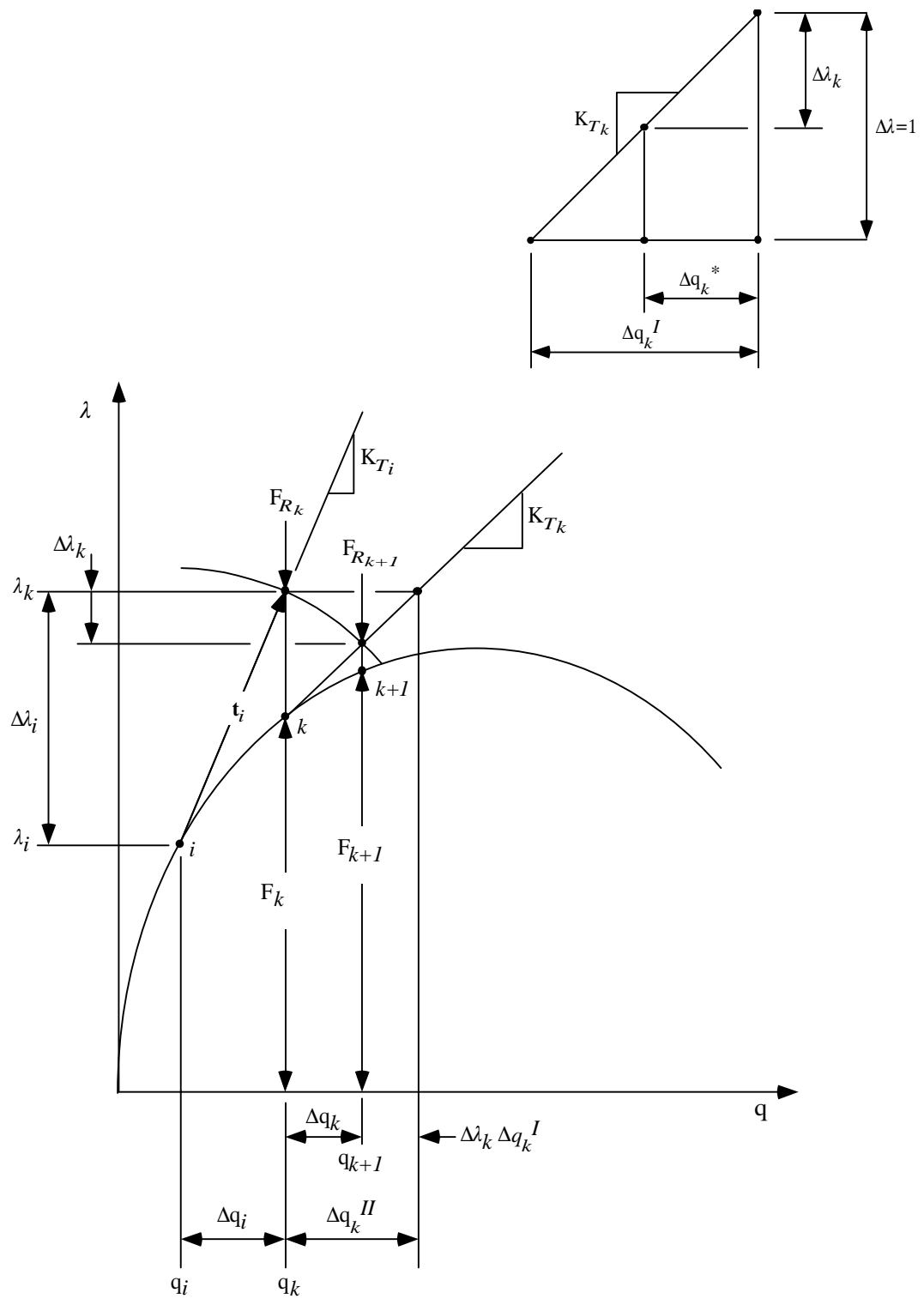


Figure 4.10 Riks-Wempner method on a sphere for a single degree-of-freedom system.

The term  $\Delta S_i^2$  is equal to

$$\Delta S_i^2 = \mathbf{t}_i \cdot \mathbf{t}_i = \Delta \lambda_i^2 + \Delta \mathbf{q}_i^T \Delta \mathbf{q}_i \quad (4.122)$$

Substituting the expression for  $\Delta S_i^2$  into the constraint equation and simplifying results in a constraint equation of the form

$$\Delta \lambda_k^2 - 2 \Delta \lambda_i \Delta \lambda_k + 2 \Delta \mathbf{q}_i^T \Delta \mathbf{q}_k + \Delta \mathbf{q}_k^T \Delta \mathbf{q}_k = 0 \quad (4.123)$$

where  $\Delta \lambda_k$  is the unknown incremental change in load and  $\Delta \mathbf{q}_k$  is the vector of unknown incremental displacements. Just as in the method of Riks-Wempner on a normal plane, the unknown displacements  $\Delta \mathbf{q}_k$  will be broken into two parts. The resulting expression for  $\Delta \mathbf{q}_k$  is (Eq. 4.94)

$$\Delta \mathbf{q}_k = \Delta \mathbf{q}_k^{II} - \Delta \lambda_k \Delta \mathbf{q}_k^I \quad (4.124)$$

The displacements  $\Delta \mathbf{q}_k^I$  are found using Eq. 4.97 and the displacements  $\Delta \mathbf{q}_k^{II}$  are found using Eq. 4.99. Substituting the expression for  $\Delta \mathbf{q}_k$  into Eq. 4.123 results in a constraint equation which is a function of only  $\Delta \lambda_k$ ,

$$\begin{aligned} & \left(1 + \Delta \mathbf{q}_k^{IT} \Delta \mathbf{q}_k^I\right) \Delta \lambda_k^2 - 2 \left(\Delta \lambda_i + \Delta \mathbf{q}_i^T \Delta \mathbf{q}_k^I + \Delta \mathbf{q}_k^{IT} \Delta \mathbf{q}_k^{II}\right) \Delta \lambda_k \\ & + \left(2 \Delta \mathbf{q}_i^T \Delta \mathbf{q}_k^{II} + \Delta \mathbf{q}_k^{IT} \Delta \mathbf{q}_k^{II}\right) = 0 \end{aligned} \quad (4.125)$$

The unknown value of  $\Delta \lambda_k$  may be found by solving the above quadratic equation which has two roots:  $(\Delta \lambda_k)_1$  and  $(\Delta \lambda_k)_2$ .

For subsequent iterations a more general form of the constraint equation is given by

$$\mathbf{r}_{k+1} \cdot \mathbf{r}_{k+1} = \Delta S_k^2 = \mathbf{r}_k \cdot \mathbf{r}_k \quad (4.126)$$

where the vector  $\mathbf{r}_k$  was given by Eq. 4.120 and the vector  $\mathbf{r}_{k+1}$  is equal to



$$\mathbf{r}_{k+1} = \begin{bmatrix} \Delta \mathbf{q}_i + \Delta \mathbf{q}_k + \Delta \mathbf{q}_{k+1} \\ \Delta \lambda_i - \Delta \lambda_k - \Delta \lambda_{k+1} \end{bmatrix} \quad (4.127)$$

The unknown incremental displacements  $\Delta \mathbf{q}_{k+1}$  are once again broken into two parts as in Eq. 4.124, which results in

$$\Delta \mathbf{q}_{k+1} = \Delta \mathbf{q}_{k+1}^{II} - \Delta \lambda_{k+1} \Delta \mathbf{q}_{k+1}^I \quad (4.128)$$

The resulting expression for the unknown load increment  $\Delta \lambda_{k+1}$  is

$$\begin{aligned} & \left( 1 + \Delta \mathbf{q}_{k+1}^{I^T} \Delta \mathbf{q}_{k+1}^I \right) \Delta \lambda_{k+1}^2 \\ & - 2 \left[ (\Delta \lambda_i - \Delta \lambda_k) + (\Delta \mathbf{q}_i^T + \Delta \mathbf{q}_k^T) \Delta \mathbf{q}_{k+1}^I \right. \\ & \quad \left. + \Delta \mathbf{q}_{k+1}^{I^T} \Delta \mathbf{q}_{k+1}^{II} \right] \Delta \lambda_{k+1} \\ & + \left[ 2(\Delta \mathbf{q}_i^T + \Delta \mathbf{q}_k^T) \Delta \mathbf{q}_{k+1}^{II} + \Delta \mathbf{q}_{k+1}^{II^T} \Delta \mathbf{q}_{k+1}^{II} \right] = 0 \end{aligned} \quad (4.129)$$

Solution of this equation results in the two roots  $(\Delta \lambda_{k+1})_1$  and  $(\Delta \lambda_{k+1})_2$ .

The correct value of  $\Delta \lambda_{k+1}$  is found by looking at the value of the cosine of the angle between the vector  $\mathbf{r}_k$  and tentative vectors  $\mathbf{r}_{k+1}$  which are formed using the two roots  $(\Delta \lambda_{k+1})_1$  and  $(\Delta \lambda_{k+1})_2$  (Crisfield 1991). The cosine of the angle between  $\mathbf{r}_k$  and  $\mathbf{r}_{k+1}$  is

$$\cos \theta = \frac{\mathbf{r}_k \cdot \mathbf{r}_{k+1}}{\Delta S_k^2} \quad (4.130)$$

The vectors  $\mathbf{r}_k$  and  $\mathbf{r}_{k+1}$  are given by Eqs. 4.120 and 4.127. The tentative incremental displacement vectors  $\Delta \mathbf{q}_{k+1}$  are computed using Eq. 4.128 and  $\Delta \lambda_{k+1}$  which is equal to one of the two roots  $(\Delta \lambda_{k+1})_1$  or  $(\Delta \lambda_{k+1})_2$ . The resulting expression for the cosine of  $\theta$  is

$$\cos \theta = 1 + \frac{(\Delta \mathbf{q}_i + \Delta \mathbf{q}_k) \Delta \mathbf{q}_{k+1} - (\Delta \lambda_i - \Delta \lambda_k) \Delta \lambda_{k+1}}{\Delta S_k^2} \quad (4.131)$$

The value of  $(\Delta \lambda_{k+1})_1$  or  $(\Delta \lambda_{k+1})_2$  that yields the maximum value of  $\cos \theta$  is the correct value of  $\Delta \lambda_{k+1}$ .

One major problem with the Riks-Wempner method on a sphere occurs when the roots of Eq. 4.129 are not real (Crisfield 1981; Meek and Tan 1984). When this situation is encountered, the load increment  $\Delta \lambda_i$  is reduced by half and the iterative process begins again from the previous equilibrium point  $i$ . A major advantage of Riks-Wempner on a sphere is that the iterative process converges to the correct solution for a larger variety of problems than any other of the methods mentioned so far.

#### 4.5.4 Convergence Criteria

In all three of the methods covered above, iteration must continue until some convergence criterion is met. Two types of convergence criteria are usually used when solving nonlinear systems of equations during a finite element analysis.

The first criterion ensures that the incremental displacements  $\Delta \mathbf{q}_k$  are small. The criterion used in this work ensures that the norm of the incremental displacements  $\Delta \mathbf{q}_k$  is small compared to the total displacement  $\mathbf{q}_{k+1}$ . This criterion is stated as

$$\frac{\|\Delta \mathbf{q}_k\|}{\|\mathbf{q}_{k+1}\|} \leq \delta_d \quad (4.132)$$

where  $\delta_d$  is a small user specified tolerance on the order of  $10^{-3}$ .

The second, and most important, convergence criterion involves the residual or out of balance forces  $\mathbf{F}_{R_{k+1}}$ . The idea behind this criterion is to ensure that the residual forces themselves, or that the norm of the vector  $\mathbf{F}_{R_{k+1}}$ , is small. For the three-dimensional finite element, and all problems with rotational variables, additional problems arise because the

residual vector contains both forces and moments. Therefore, when computing the norm of  $\mathbf{F}_{R_{k+1}}$ , quantities with different units must be added together. Because of the units involved in the analysis, the moments can be much larger than the forces and therefore contribute much more to the calculation of the norm of  $\mathbf{F}_{R_{k+1}}$ . This problem can cause convergence of the solution to be obtained based solely on the moments rather than on the combination of both forces and moments. To solve this problem, scaling of the residual force vector is recommended (Crisfield 1981, 1991; Fellipa 1988). The convergence criterion for the out of balance forces, used in this work, is

$$\frac{\sqrt{\mathbf{F}_{R_{k+1}}^T \mathbf{S}_i \mathbf{F}_{R_{k+1}}}}{\lambda_{k+1} \sqrt{\mathbf{Q}^T \mathbf{S}_i \mathbf{Q}}} \leq \delta_f \quad (4.133)$$

The matrix  $\mathbf{S}_i$  is a diagonal scaling matrix that contains the inverse of the diagonal elements of the tangent stiffness matrix,  $\mathbf{K}_{T_i}$ . As previously defined, the vector  $\mathbf{Q}$  contains the external loads and  $\lambda_{k+1}$  is the current total load increment. The quantity  $\delta_f$  is a small user specified tolerance on the order of  $10^{-4}$ . Using this type of criterion ensures that the residual forces are small compared to the total applied load on the structure. One major drawback associated with this criterion is that larger residual forces are allowed as the external load is increased. In practice, this is usually not a problem since the value of  $\delta_f$  is small.

Many other convergence criteria have been proposed (Bathe 1982; Fellipa 1988; Cook et al. 1989; Crisfield 1991) and each has its own benefits and drawbacks for certain types of problems. The above criteria have been successfully implemented by Crisfield (1981) and have proven to be reliable for a variety of problems.

## 4.6 EXAMPLE PROBLEMS

The proposed finite element formulation is verified using seven examples that have exact solutions or have been solved by other researchers using different finite element formulations. All seven example problems were solved using Riks-Wempner on a sphere and a displacement tolerance,  $\delta_d$ , equal to 0.001, and a residual force tolerance,  $\delta_f$ , of 0.0001.

### 4.6.1 Single Element Eigenvalue Test

A single element eigenvalue test (Bathe 1982; Cook et al. 1989) was run to identify any spurious energy modes that may exist in the proposed element. The single unsupported element has a length of 10 and a circular cross-section as shown in Fig. 4.11. The various geometric and material properties are also shown in Fig. 4.11. The eigenvalue test results in six non-zero eigenvalues and six zero eigenvalues which correspond to the six rigid body modes for the element. This indicates that the element has no zero-energy deformation modes and that the element can accurately represent the required number of rigid body modes.

### 4.6.2 Cantilever Beam with a Concentrated End Moment

A cantilever beam with a concentrated end moment is shown in Fig. 4.12 along with the necessary geometric and material properties. The cantilever beam was modeled using 5, 10, and 20 elements. The results for the non-dimensional tip displacements  $u/L$ ,  $v/L$ , and  $\phi/2\pi$  are plotted against the non-dimensional moment parameter  $ML/2\pi EI$ , in Fig. 4.12. The exact solution for the tip deflection is the equation of a circle (Crivelli 1991), with a radius equal to

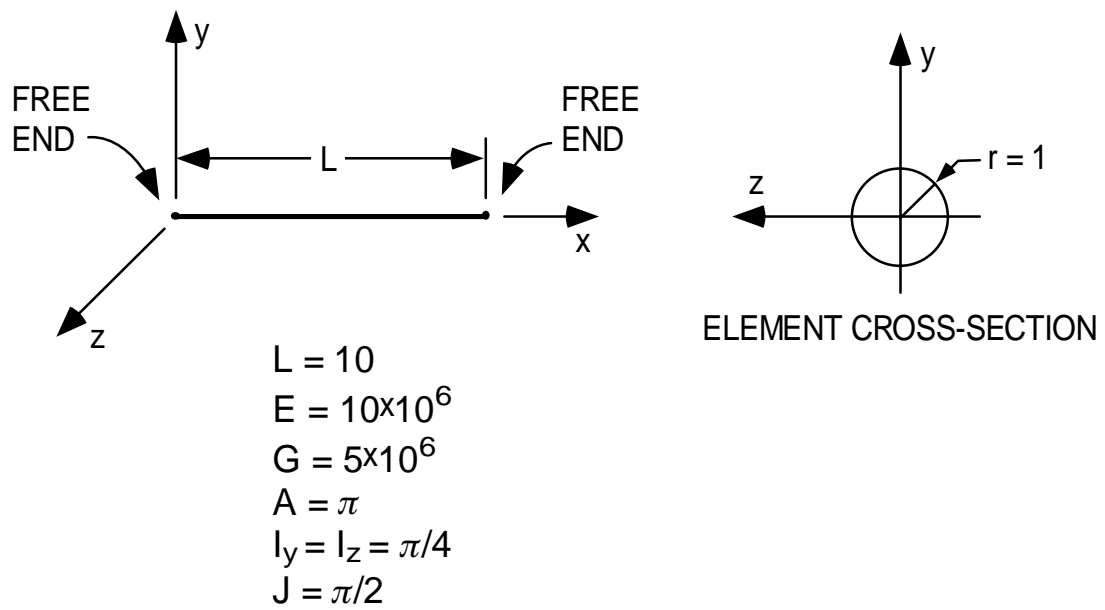


Figure 4.11 Geometry for the single element eigenvalue test.

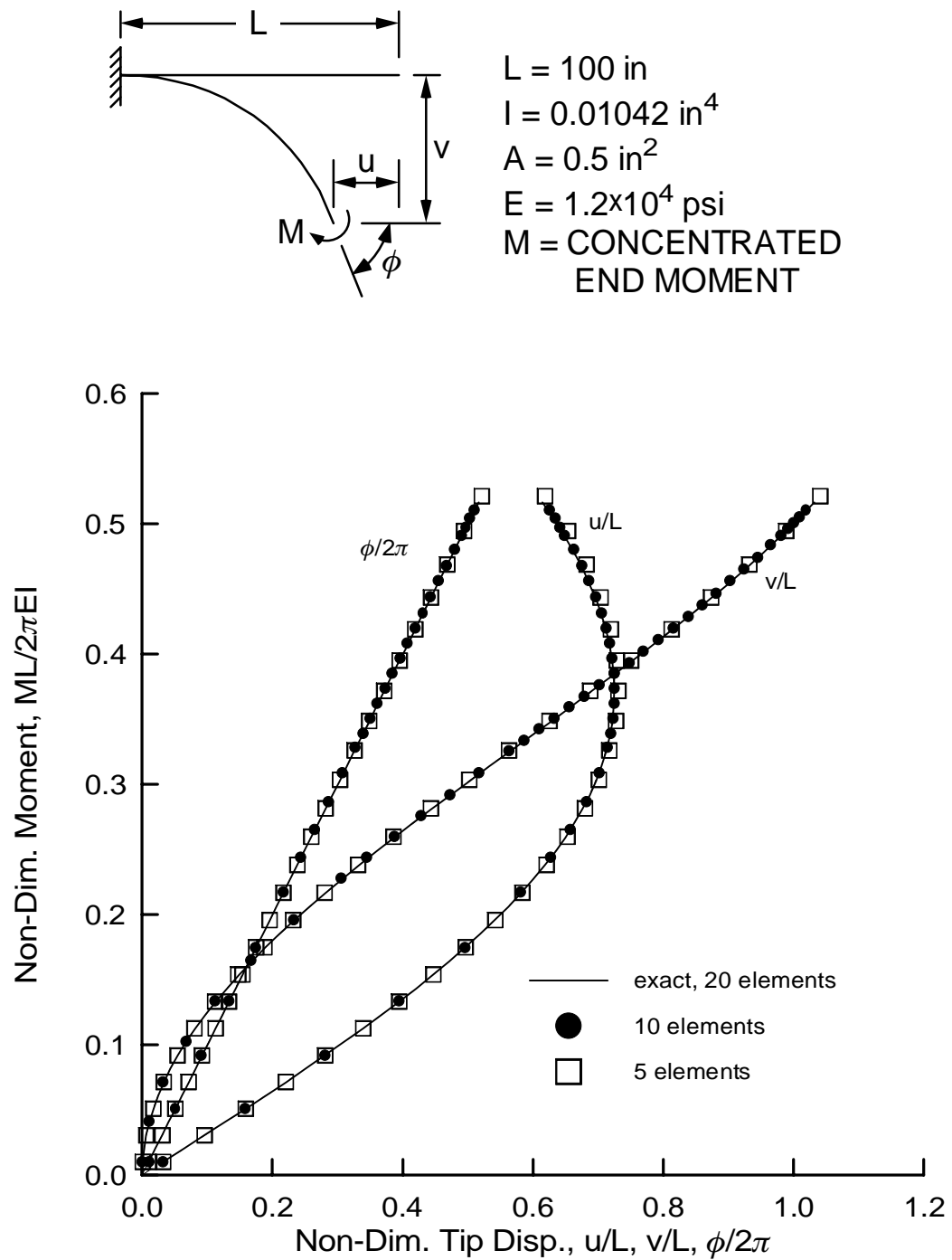


Figure 4.12 Load-deflection curves for the cantilever with a concentrated end moment.

$$r = \frac{EI}{M} \quad (4.134)$$

The exact solution is also shown in Fig. 4.12. The coarse five element solution compares well with the exact solution for the displacements  $v$  and  $\phi$ , but is slightly different for large values of  $u$ . The 10 and 20 element solutions compare almost exactly with the analytic solution for all three tip displacements.

#### 4.6.3 Cantilever Beam with a Concentrated End Load

A second cantilever beam is shown in Fig. 4.13. The beam is loaded with a concentrated end load and has the geometric and material properties shown in Fig. 4.13. An exact solution for this problem was presented by Fertis (1993) and is plotted in Fig. 4.13. For the finite element solution, the cantilever beam was discretized using eight elements. The resulting non-dimensional tip displacement is plotted against the normalized load  $PL^2/EI$  in Fig. 4.13. The results from the finite element model compare well with the results presented by Fertis (1993).

#### 4.6.4 45-Degree Circular Bend

The 45-degree circular bend, as presented by Bathe and Bolourchi (1979), is shown in Fig. 4.14. The circular bend has a fixed support at the left end and is loaded by a concentrated end load at the right end. The required geometric and material properties are also given in Fig. 4.14. The circular bend was modeled using eight finite elements. The results for the non-dimensional tip displacements  $-u/R$ ,  $v/R$ , and  $-w/R$  are plotted against the non-dimensional load  $PR^2/EI$  in Fig. 4.14. Also shown in Fig. 4.14 are the solutions from Bathe and Bolourchi (1979) who also used eight elements. The results from both analyses are nearly the same.

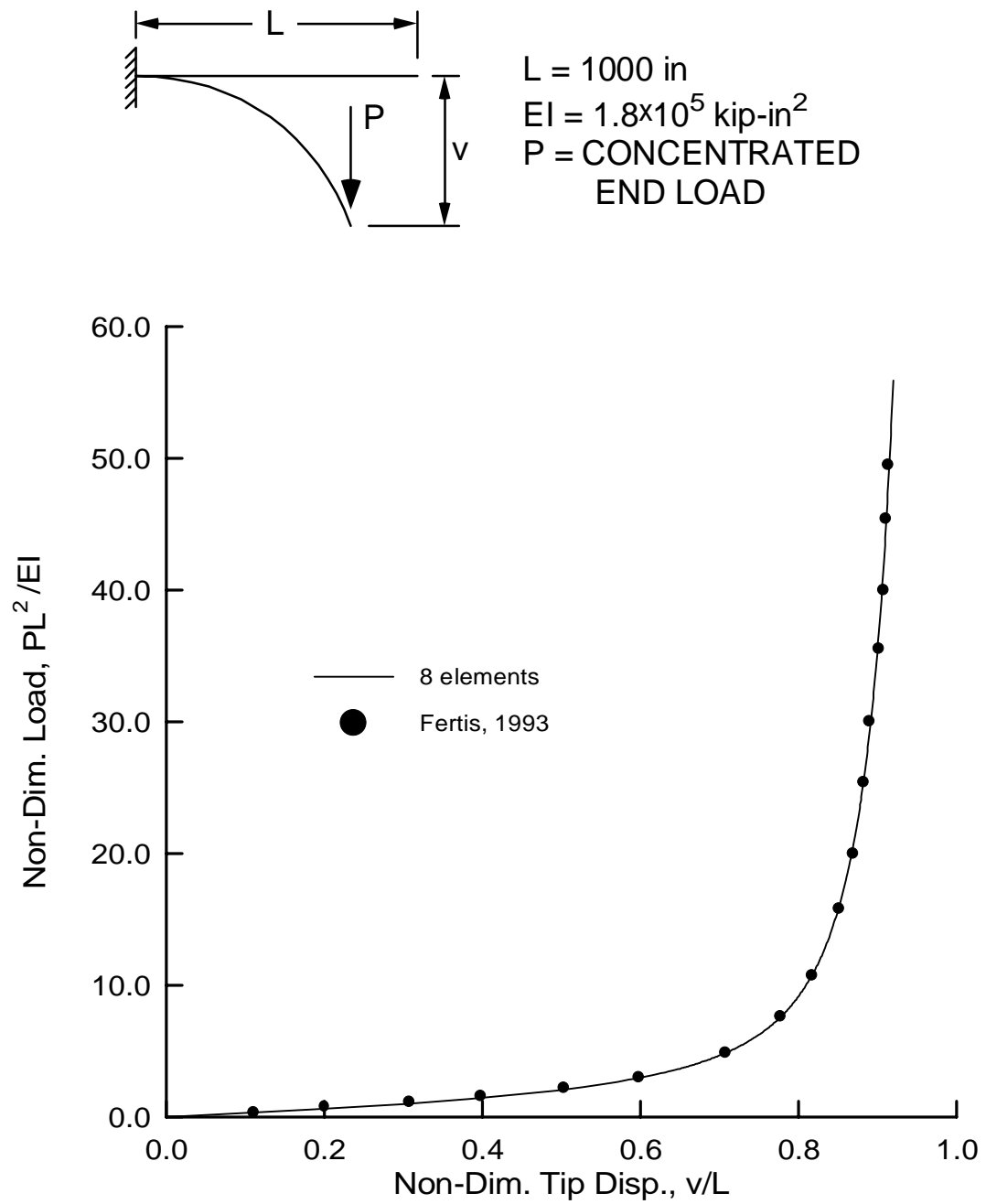


Figure 4.13 Load-deflection curve for the cantilever beam with a concentrated end load.



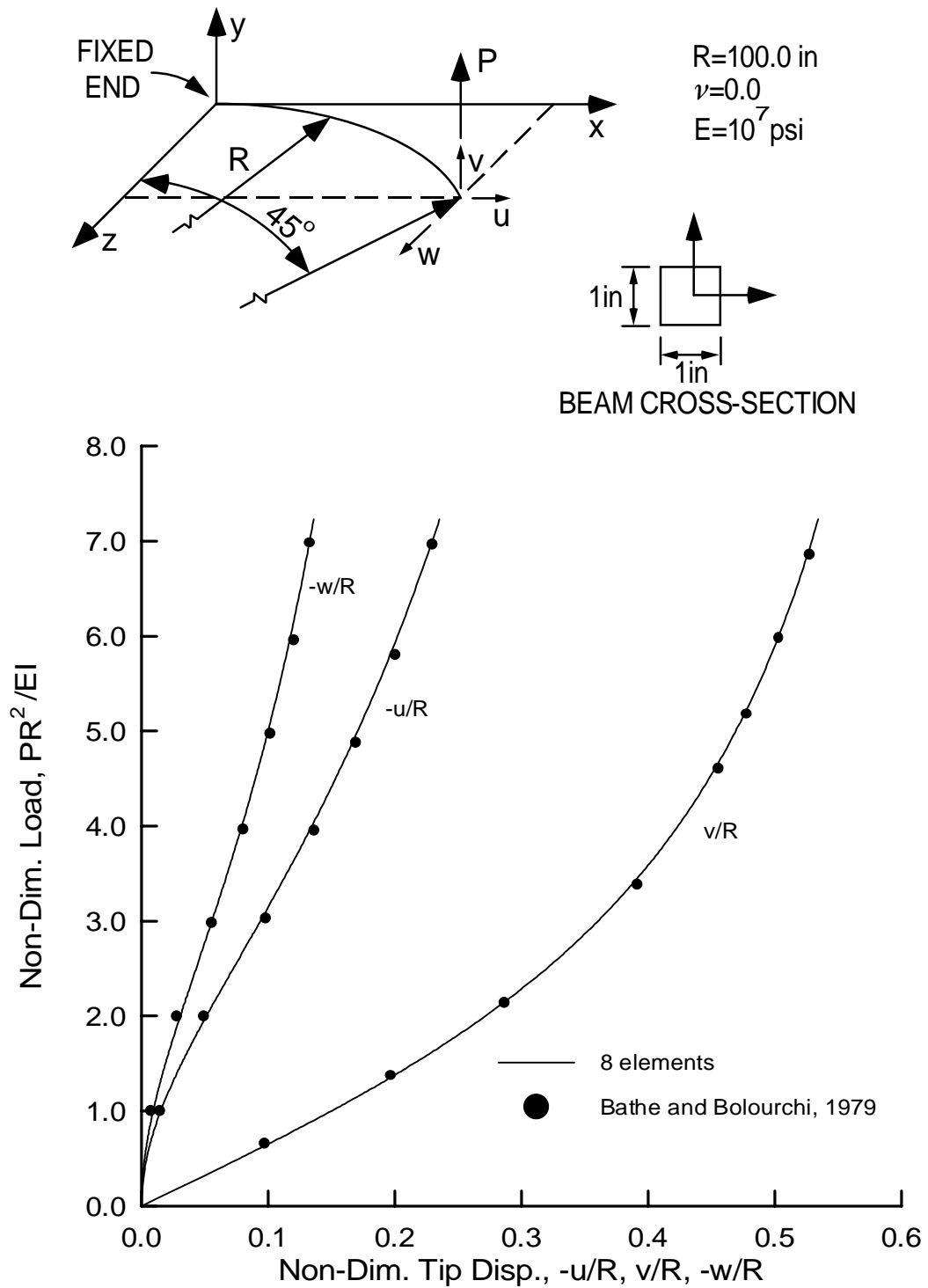


Figure 4.14 Load-deflection curves for the 45-degree circular bend.

#### 4.6.5 Williams' Toggle Frame

The frame shown in Fig. 4.15 was first investigated by Williams (1964). The frame is fixed against translation and rotation at both the left and right ends, and has a concentrated load applied at the apex. The values of  $EA$  and  $EI$  are given in Fig. 4.15 along with the rise and the span of the frame. The entire frame was modeled using 8, 10, 20, and 40 elements. The results for load versus apex deflection are plotted in Fig. 4.15. Also shown, are the finite element results from Davalos (1989) and Crivelli (1991). Davalos (1989) used four three-noded elements to model the entire frame, and Crivelli (1991) used 10 total elements with a correction to better approximate the behavior of the thin members. The 8 and 10 element models for the proposed formulation are too stiff and produce deflections that are smaller, for a given load, than those predicted by Davalos (1989) and Crivelli (1991). However, the 20 and 40 element models produce results that are very similar to the results from Davalos (1989) and Crivelli (1991).

#### 4.6.6 12-Member Hexagonal Frame

A 12 member hexagonal frame is shown in Fig. 4.16. The material and cross-sectional properties for the members are also given in Fig. 4.16. Finite element models were created for one, two, four, and eight elements in each diagonal member, and one element in the remaining six elements around the base of the frame. The resulting load versus apex displacement curves for the four different models are shown in Fig. 4.17. Also, the results from Meek and Tan (1984) are given in Fig. 4.17. For the proposed formulation, the single element case is very stiff, but the two element case falls beneath the results presented by Meek and Tan (1984). When the mesh was refined to four elements per member, the load-displacement curve fell even more, and finally converged for the eight element case. In order to verify the results of the analysis, both the two and the

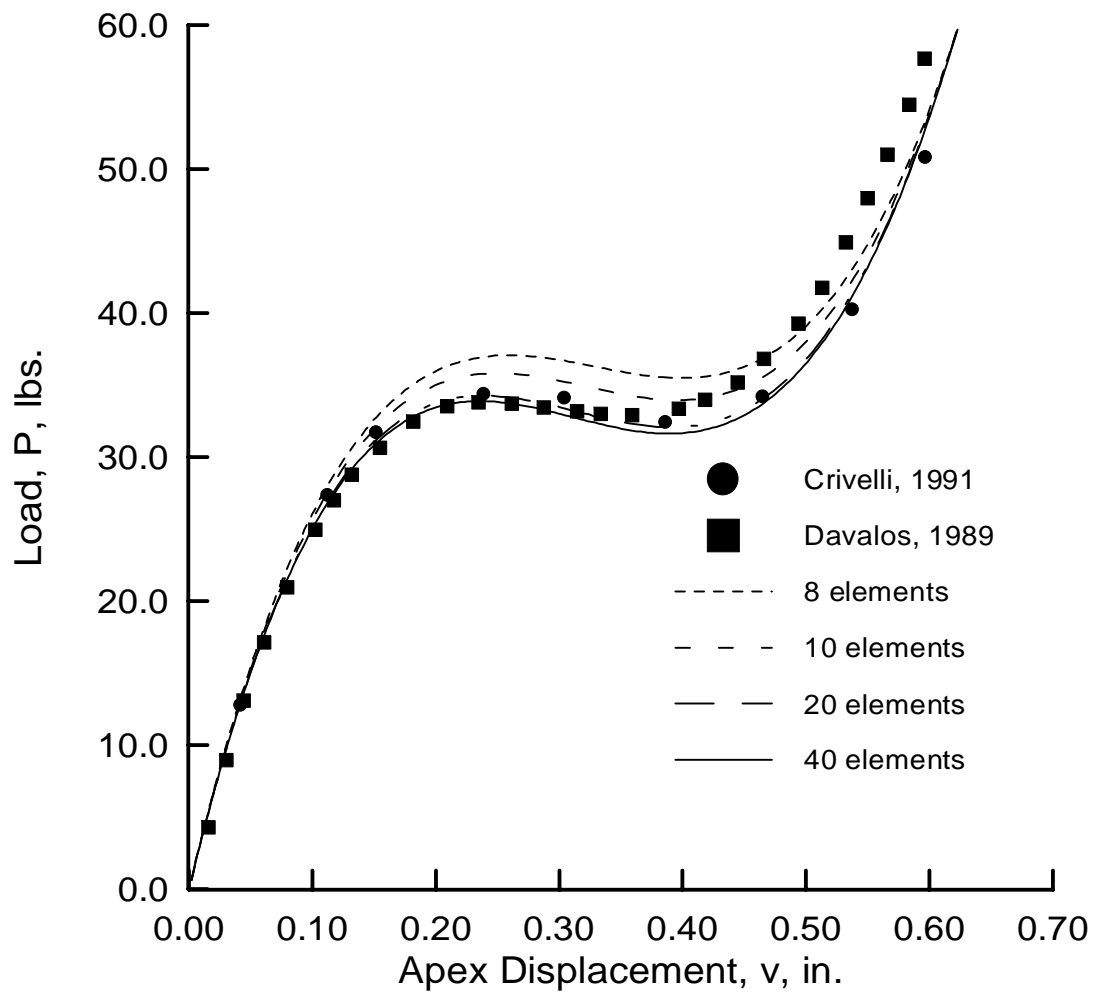
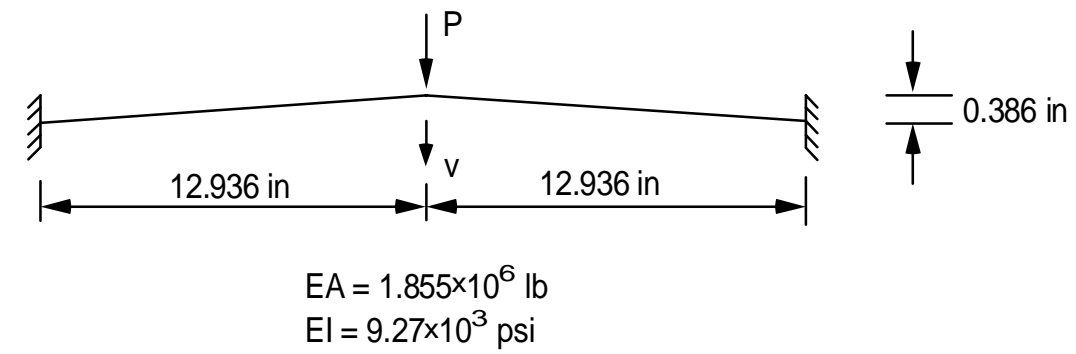


Figure 4.15 Load-deflection curves for Williams' toggle frame.

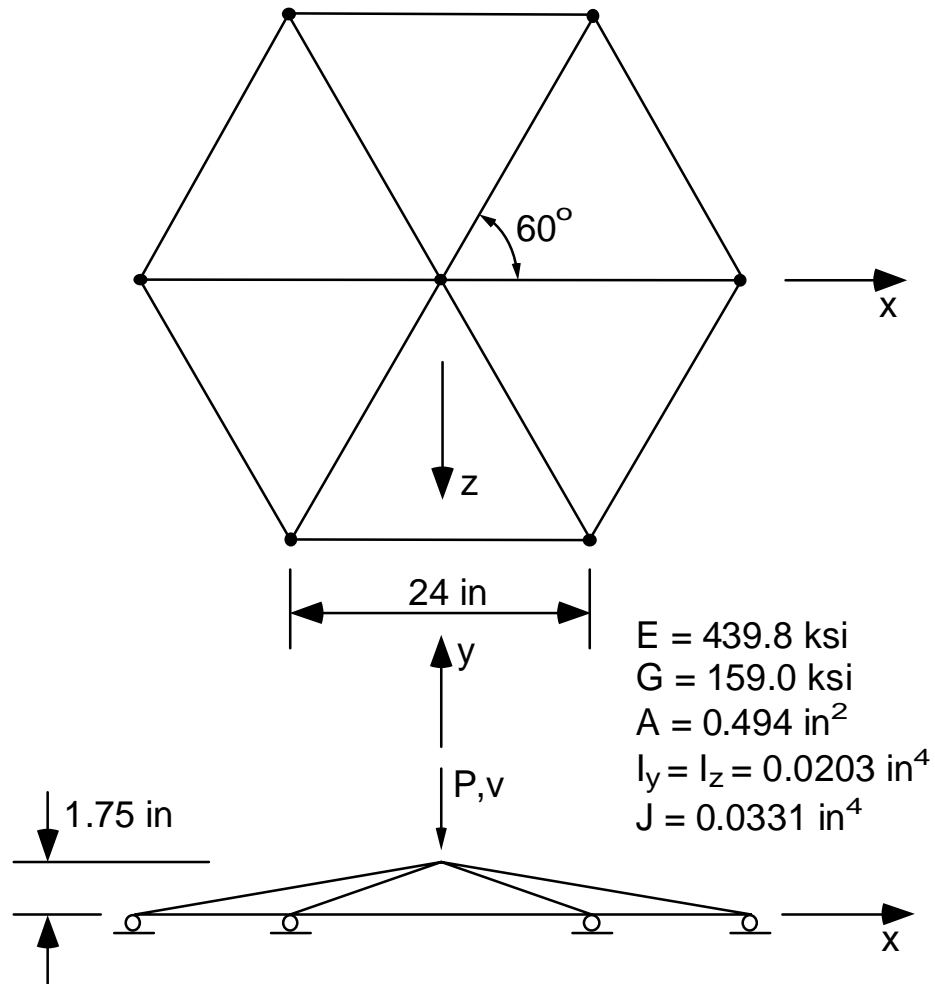


Figure 4.16 Geometry for the 12-member hexagonal frame.

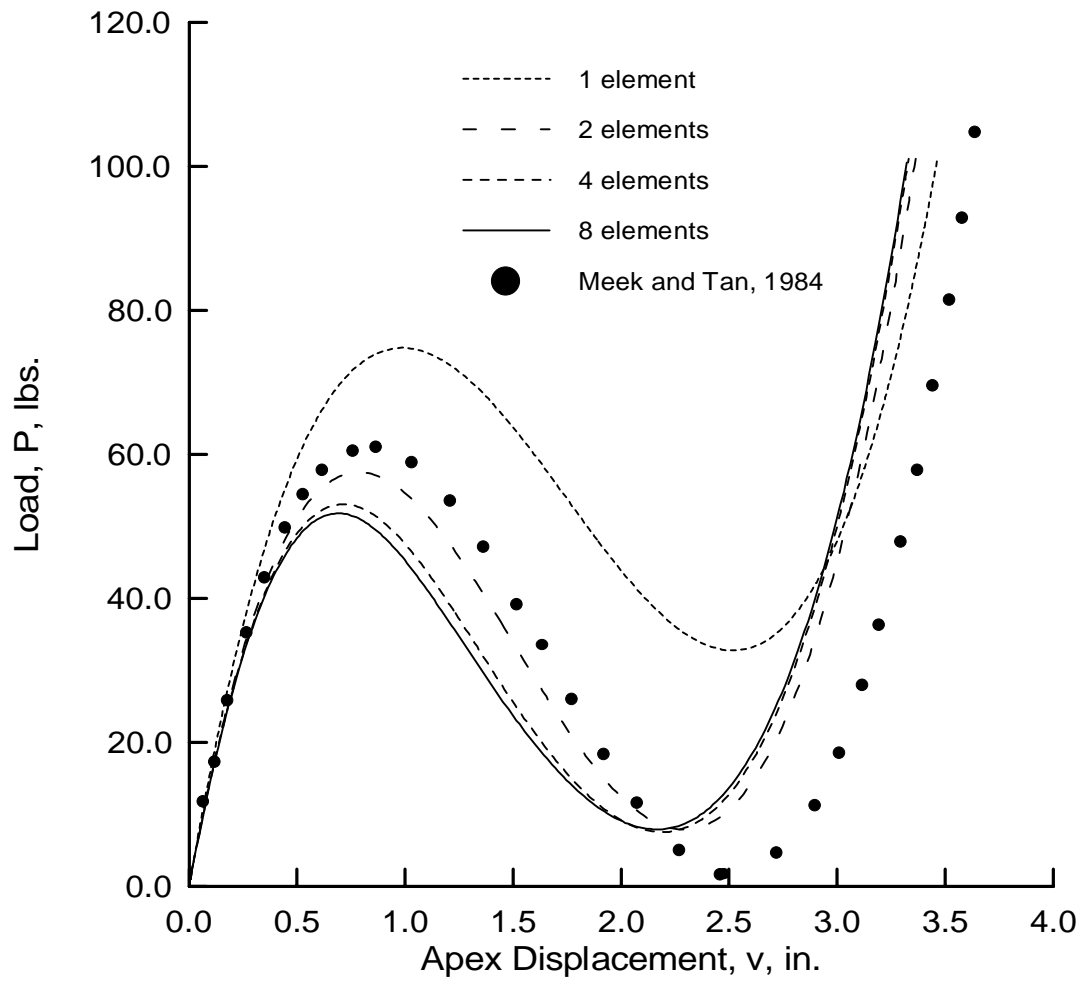


Figure 4.17 Load-deflection curves for the 12-member hexagonal frame; demonstrating convergence of the proposed formulation.

eight element results were compared to similar results from ABAQUS (1988) using a two-noded shear-deformable (B31) element. The results are shown in Fig. 4.18. Both solutions are very close to one another for the eight element case, which indicates that the proposed element does converge to the correct solution.

#### **4.6.7 24-Member Hexagonal Star-Shaped Shallow Cap**

The response of the 24-member star-shaped cap has been examined by many researchers (i.e. Holzer et al. 1980) by using truss elements to model the individual members. For the example presented here, the star-shaped cap is treated as a rigid frame with joints capable of transferring bending moments. This problem was first studied by Meek and Tan (1984). The geometry of the cap and the required cross-sectional and material properties are shown in Fig. 4.19. The shallow cap is acted upon by a concentrated load at the apex. The star-shaped cap was modeled using two, four, and eight elements for all of the members except the six that form the base of the hexagon. These six members were modeled using only two elements. The results from Meek and Tan (1984) and those from the proposed formulation are shown in Fig. 4.20. The two element case was very stiff and gave results that were well above those from the four element case. The eight element case produced results that were only slightly different from those of the four element case, which indicates convergence of the solution. The results from the eight element case agree very well with those from Meek and Tan (1984).

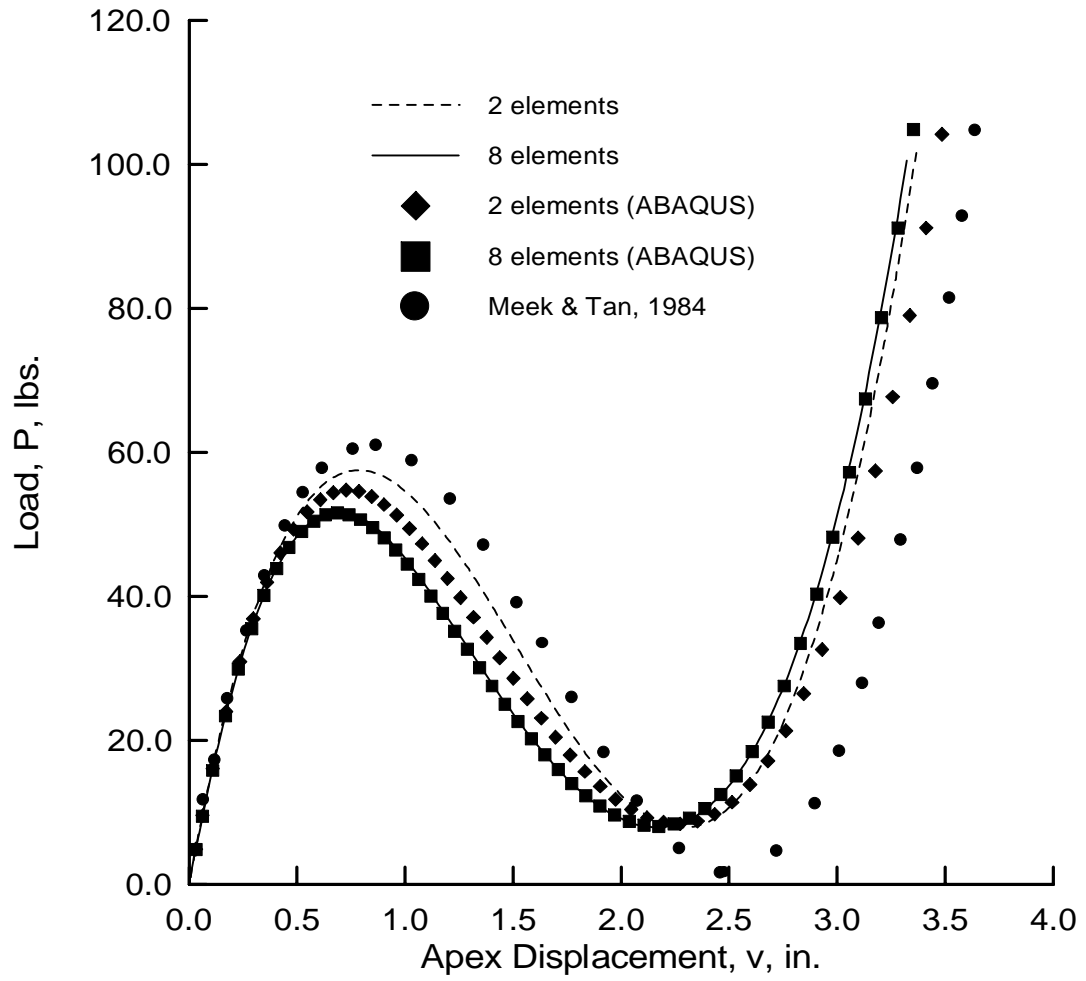


Figure 4.18 Load-deflection curves for the 12-member hexagonal frame using the proposed formulation and ABAQUS.

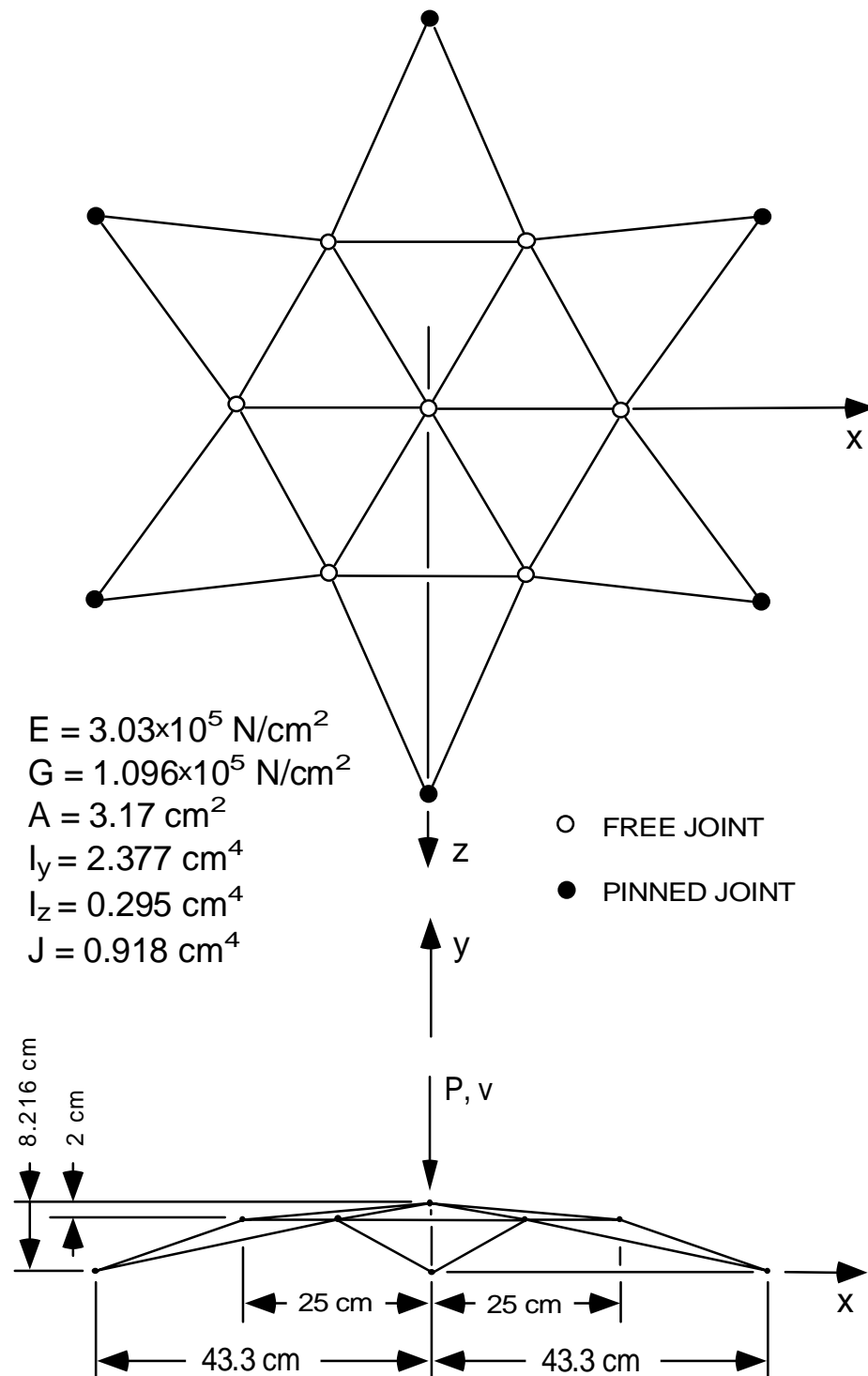


Figure 4.19 Geometry for the 24-member shallow reticulated cap.



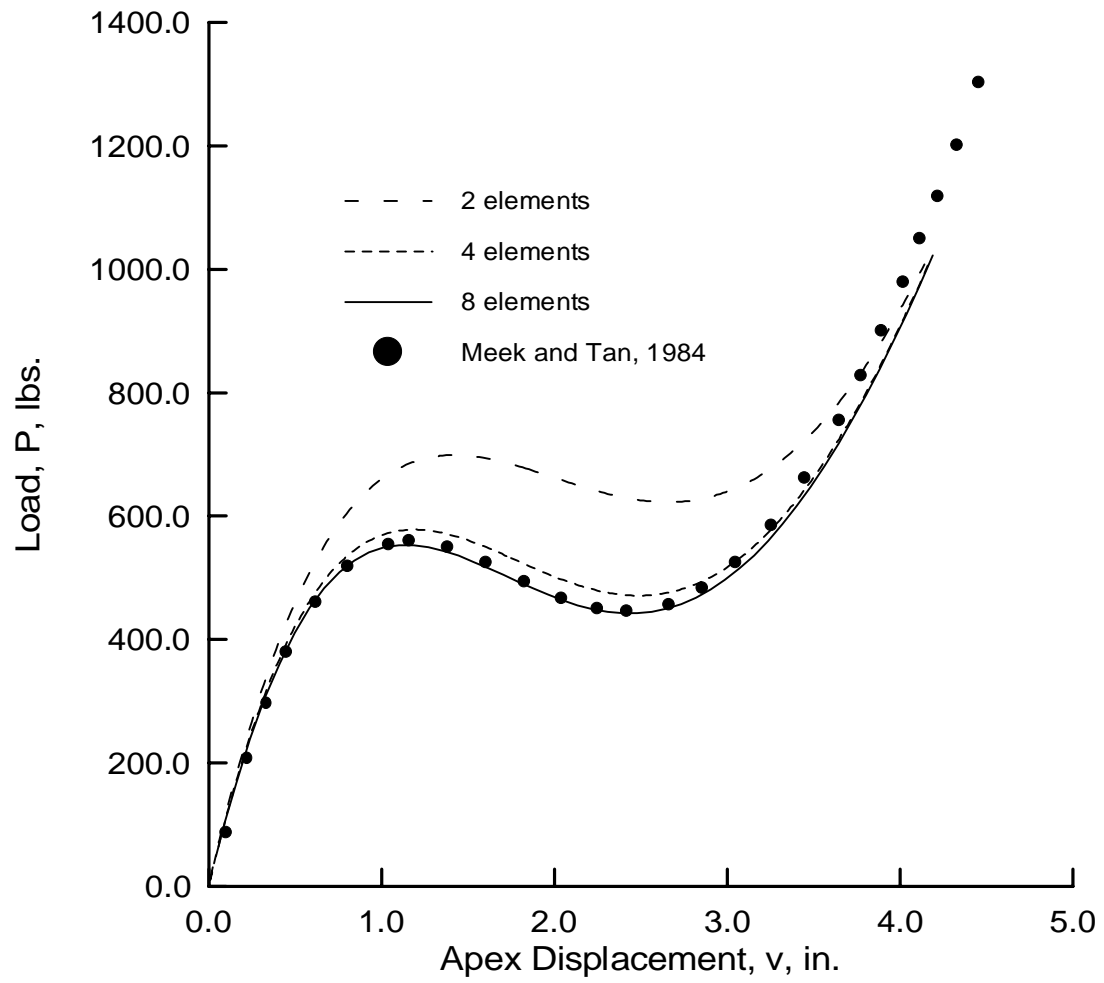


Figure 4.20 Load-deflection curves for the 24-member shallow cap.

## **CHAPTER 5**

### **RELIABILITY ANALYSIS**

### **AND**

### **RESPONSE SURFACE METHODS**

Probabilistic methods attempt to model the variabilities of given system parameters with random variables, resulting in a realistic assessment of the reliability of a system. Reliability is defined as the probabilistic measure of assurance of performance of a design in its intended environment (Ang and Tang 1984). Various methods have been proposed for calculating the reliability of a system. Some of the more interesting are the computational methods and in particular the second-moment methods. In these methods, all random variables are modeled using only the first and second moments of each variable. The first and second moments of a random variable are more commonly referred to as the mean and variance. The most common of the second-moment methods is the first-order second-moment method which models the response of a system at a point using a first-order surface, or plane. The second-moment methods give excellent results using very little information about the random variables but problems arise when an exact expression for the response of the system is not known.

Current methods for reliability analysis require that the response of the system be given as an explicit function of the random variables involved. To circumvent this problem, response surface methods have been used to model the response of a system in a specified region of interest. Response surface methods, in their most basic form, combine

least squares methods with designed experiments to fit a surface to experimental output from the system under consideration. More elaborate response surface methods are used to search for areas of minimum or maximum yield of the system being studied. When combined with the first-order second-moment method, the response surface method allows the reliability of a system to be calculated without an explicit relationship between the response of the system and the random variables involved.

## 5.1 CONCEPTS OF RELIABILITY

Methods of reliability analysis depend on the ability to calculate probability of failure. The concept of probability of failure is best described by considering the specific example of supply ( $X_1$ ) versus demand ( $X_2$ ). Failure for this problem is defined when demand is greater than or equal to supply, or when  $X_1 - X_2 \leq 0$ . In a reliability analysis, the variables  $X_1$  and  $X_2$  are treated as random variables with probability density functions as shown in Fig. 5.1. If the supply and demand are statistically independent, then the expression for the probability of failure is (Ang and Tang 1984)

$$p_f = \int_{-\infty}^{+\infty} [1 - F_{X_2}(x_1)] f_{X_1}(x_1) dx \quad (5.1)$$

where  $F_{X_2}(x_1)$  is the cumulative distribution of  $X_2$  at  $x_1$  and  $f_{X_1}(x_1)$  is the probability density of  $X_1$  at  $x_1$ .

The supply and demand problem may be reformulated in terms of the safety margin (Ang and Tang 1984),

$$G(\mathbf{X}) = X_1 - X_2 \quad (5.2)$$

where  $X_1$  and  $X_2$  are independent normally distributed random variables. Failure is defined when

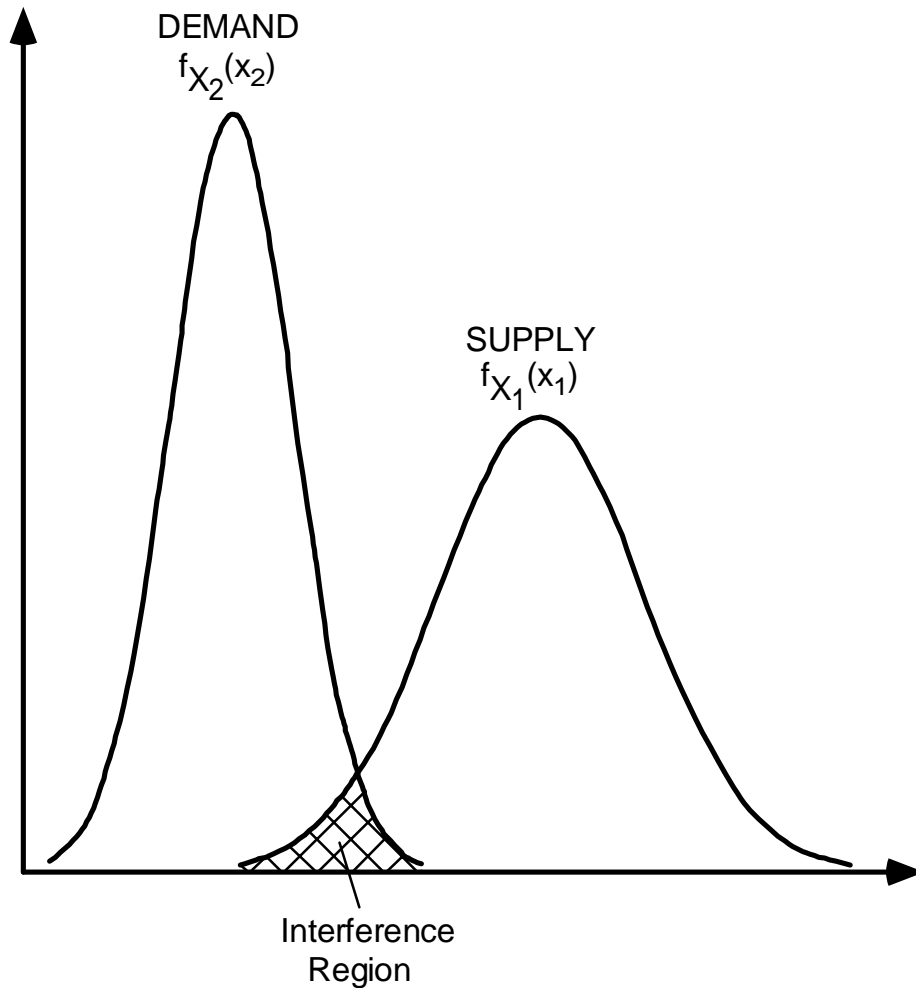


Figure 5.1 Probability distributions of supply and demand (Ang and Tang 1984).

$$G(\mathbf{X}) = X_1 - X_2 \leq 0 \quad (5.3)$$

Since the safety margin  $G(\mathbf{X})$  is a function of two independent normally distributed random variables,  $G(\mathbf{X})$  itself is a normally distributed random variable with probability density function,  $f_G(g)$ . The mean value of  $G(\mathbf{X})$  is given by

$$\mu_G = \mu_{X_1} - \mu_{X_2}, \quad (5.4)$$

and the standard deviation of  $G(\mathbf{X})$  is

$$\sigma_G = \sqrt{\sigma_{X_1}^2 + \sigma_{X_2}^2} \quad (5.5)$$

The probability of failure is equal to

$$p_f = \int_{-\infty}^0 f_G(g) dg = F_G(0) \quad (5.6)$$

which is represented by the cross-hatched area shown in Fig. 5.2. If  $\beta$  is the number of standard deviations  $\sigma_G$  from the mean value  $\mu_G$  to the failure region, then failure occurs when

$$\mu_G - \beta\sigma_G = 0, \quad (5.7)$$

or when

$$\beta = \frac{\mu_G}{\sigma_G} = \frac{\mu_{X_1} - \mu_{X_2}}{\sqrt{\sigma_{X_1}^2 + \sigma_{X_2}^2}} \quad (5.8)$$

Substituting Eq. 5.8 into Eq. 5.6, the probability of failure becomes

$$p_f = F_G\left(\frac{\mu_G}{\sigma_G}\right) = 1 - \Phi(\beta) \quad (5.9)$$

where  $\Phi(\beta)$  is the standard normal cumulative density function evaluated at  $\beta$ . The quantity  $\beta$  is often referred to as the reliability or safety index.

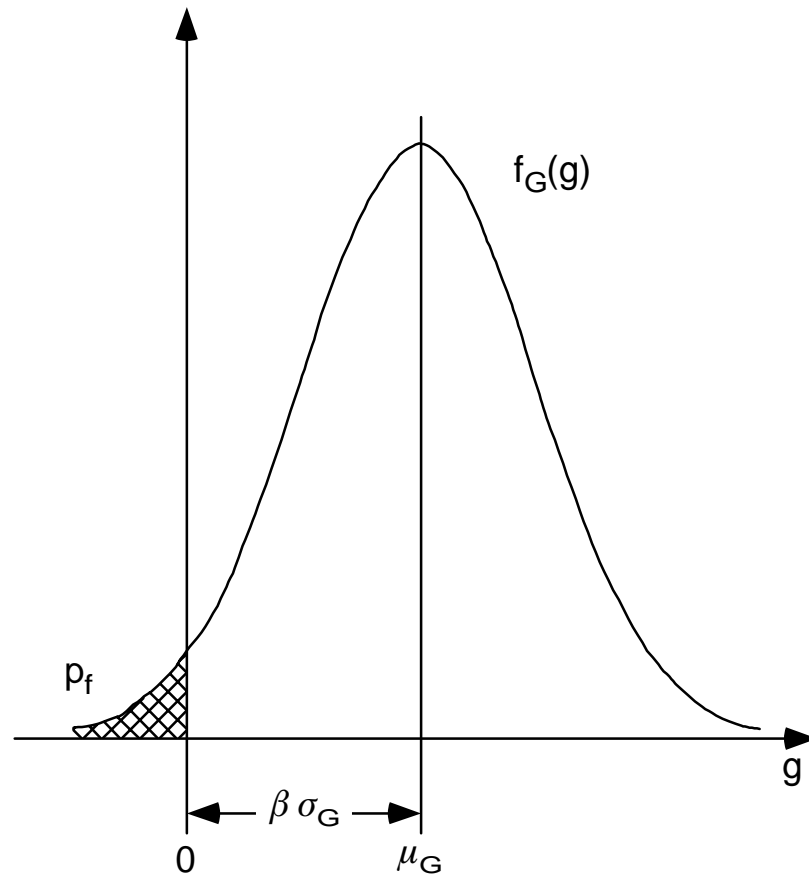


Figure 5.2 Probability density function for the safety margin  $G$  (Ang and Tang 1984).

## 5.2 FIRST-ORDER SECOND-MOMENT METHOD

In general, the response of a system may be function of many random variables. The response of a system is usually given in the form of a performance function (Ang and Tang 1984),

$$g(\mathbf{X}) = g(X_1, X_2, \dots, X_n) \quad (5.10)$$

where  $\mathbf{X}$  is a vector of random variables that defines the state of the system. The performance function describes all possible responses of the system that are of interest. The failure surface or limit state of the system is the transition of the system from a safe to an unsafe state, and is defined by setting the performance function equal to zero,  $g(\mathbf{X}) = 0$ .

The probability of failure for a general system may be calculated by

$$p_f = \int \int \dots \int_{g(\mathbf{X}) \leq 0} f_{X_1 X_2 \dots X_k}(x_1, x_2, \dots, x_k) dx_1 dx_2 \dots dx_k \quad (5.11)$$

where  $f_{X_1 X_2 \dots X_k}(x_1, x_2, \dots, x_k)$  is the joint probability density function of the variables  $X_1, X_2, \dots, X_k$ . For independent variables, Eq. 5.11 reduces to

$$p_f = \int \int \dots \int_{g(\mathbf{X}) \leq 0} f_{X_1}(x_1) f_{X_2}(x_2) \dots f_{X_k}(x_k) dx_1 dx_2 \dots dx_k \quad (5.12)$$

where  $f_{X_i}(x_i)$  is the probability density function for the variable  $X_i$ . However, for most problems the exact distributions of the random variables involved are not known. Therefore, a second-moment formulation (Ang and Tang 1984) is often used to approximate the exact solution given by Eqs. 5.11 and 5.12. A second-moment formulation provides an estimate of the probability of failure by using only the first and second moments of each random variable. The first and second moments are more

commonly referred to as the mean and the variance. Use of the second-moment approach, is in general limited to systems having linear performance functions and uncorrelated normally distributed random variables. But, the method may be adapted to systems having nonlinear performance functions and correlated nonnormal random variables.

The objective of the second-moment method is to find the point on the failure surface that has a minimum distance  $B$  to the origin of a normalized coordinate system. This point is often referred to as the most probable failure point, and has coordinates  $X_i^*$ . The shortest distance is found by minimizing  $B$  under the constraint that  $g(\mathbf{X}) = 0$ . Ang and Tang (1984) have shown that the method of Lagrange multipliers may be used to solve this problem. For a general nonlinear limit state, the distance  $B$  to a point on the failure surface is

$$B = \sqrt{S_1^2 + \dots + S_n^2} = \sqrt{\mathbf{S}^T \mathbf{S}} \quad (5.13)$$

where the  $S_i$  are standardized normal variables which are equal to

$$S_i = \frac{X_i - \mu_{X_i}}{\sigma_{X_i}} \quad (5.14)$$

By using standardized normal variables, measurements along all the normalized axes are the same, and are expressed in units of number of standard deviations. Using a Lagrange multiplier gives (Ang and Tang 1984)

$$L = B + \lambda g(\mathbf{S}), \quad (5.15)$$

or

$$L = \sqrt{\mathbf{S}^T \mathbf{S}} + \lambda g(\mathbf{S}) \quad (5.16)$$

Minimizing  $L$  with respect to  $\mathbf{S}$  and  $\lambda$  requires that

$$\frac{\partial L}{\partial \mathbf{S}} = \frac{\mathbf{S}}{\sqrt{\mathbf{S}^T \mathbf{S}}} + \lambda \frac{\partial g}{\partial \mathbf{S}} = 0 \quad (5.17)$$



and

$$\frac{\partial L}{\partial \lambda} = g(\mathbf{S}) = 0 \quad (5.18)$$

The vector  $\partial g / \partial \mathbf{S}$  is the gradient of the function  $g$  and is often written as

$$\nabla_s g(\mathbf{S}) = \begin{bmatrix} \frac{\partial g}{\partial S_1} \\ \frac{\partial g}{\partial S_2} \\ \vdots \\ \frac{\partial g}{\partial S_n} \end{bmatrix} \quad (5.19)$$

Using the chain rule,  $\partial g / \partial S_i$  may be written as

$$\frac{\partial g}{\partial S_i} = \frac{\partial g}{\partial X_i} \frac{\partial X_i}{\partial S_i} = \sigma_{X_i} \frac{\partial g}{\partial X_i} \quad (5.20)$$

Therefore, the gradient of  $g$  is given by

$$\nabla_s g(\mathbf{S}) = \boldsymbol{\sigma}_X \nabla_x g(\mathbf{X}) \quad (5.21)$$

where  $\boldsymbol{\sigma}_X$  is a diagonal matrix whose elements are the standard deviations of each random variable.

Simultaneous solution of Eqs. 5.17 and 5.18 yields the minimum distance to the limit state and the most probable failure point,  $(S_1^*, S_2^*, \dots, S_n^*)$ . Equation 5.17 may be rewritten as

$$\frac{\mathbf{S}}{\sqrt{\mathbf{S}^T \mathbf{S}}} + \lambda \nabla_s g(\mathbf{S}) = 0 \quad (5.22)$$

or

$$\mathbf{S} = -\lambda B \nabla_s g(\mathbf{S}) \quad (5.23)$$

Substituting Eq. 5.23 into the expression for  $B$  gives

$$B = \lambda B [\nabla_s^T g(\mathbf{S}) \nabla_s g(\mathbf{S})]^{\frac{1}{2}} \quad (5.24)$$

The expression for the Lagrange multiplier is

$$\lambda = \left( \nabla_s^T g(\mathbf{S}) \nabla_s g(\mathbf{S}) \right)^{-\frac{1}{2}} \quad (5.25)$$

The resulting vector  $\mathbf{S}$  is found by substituting Eq. 5.25 into Eq. 5.23 which gives

$$\mathbf{S} = -B \frac{\nabla_s g(\mathbf{S})}{\left( \nabla_s^T g(\mathbf{S}) \nabla_s g(\mathbf{S}) \right)^{\frac{1}{2}}} = -B \boldsymbol{\alpha} \quad (5.26)$$

The vector  $\boldsymbol{\alpha}$  contains the direction cosines along the axes. Premultiplying the above equation by  $\boldsymbol{\alpha}^T$  and rearranging gives a distance  $B$  equal to

$$B = -\boldsymbol{\alpha}^T \mathbf{S} \quad (5.27)$$

Substituting  $B$  into the limit state equation gives the minimum distance

$$B_{min} = \beta = -\boldsymbol{\alpha}^{*T} \mathbf{S}^* \quad (5.28)$$

Once  $\beta$  is known, the most probable failure point can be found by

$$\mathbf{S}^* = -\beta \boldsymbol{\alpha}^* \quad (5.29)$$

The reliability index,  $\beta$ , may also be found by expanding the performance function  $g(\mathbf{X})$  in a Taylor series about a point  $\mathbf{X}^*$  on the failure surface (Ang and Tang 1984). The resulting expression is

$$\begin{aligned} g(\mathbf{X}) &= g(\mathbf{X}^*) + (\mathbf{X} - \mathbf{X}^*)^T \nabla_x g(\mathbf{X}^*) \\ &\quad + \frac{1}{2} (\mathbf{X} - \mathbf{X}^*)^T \mathbf{H}(\mathbf{X}^*) (\mathbf{X} - \mathbf{X}^*) + \dots \end{aligned} \quad (5.30)$$

where the matrix  $\mathbf{H}(\mathbf{X})$  is the Hessian which contains the terms

$$H_{ij} = \frac{\partial^2 g}{\partial X_i \partial X_j} \quad (5.31)$$

Neglecting the higher order terms and recognizing that  $g(\mathbf{X}^*) = 0$  gives

$$g(\mathbf{X}) = (\mathbf{X} - \mathbf{X}^*)^T \nabla_{\mathbf{x}} g(\mathbf{X}^*) \quad (5.32)$$

Changing to standardized normal variables the vector  $\mathbf{X} - \mathbf{X}^*$  becomes

$$\mathbf{X} - \mathbf{X}^* = \sigma_{\mathbf{x}}(\mathbf{S} - \mathbf{S}^*) \quad (5.33)$$

and the gradient becomes

$$\nabla_{\mathbf{x}} g(\mathbf{X}) = \sigma_{\mathbf{x}}^{-1} \nabla_{\mathbf{s}} g(\mathbf{S}) \quad (5.34)$$

The first-order expansion may be rewritten as

$$g(\mathbf{S}) = (\mathbf{S} - \mathbf{S}^*)^T \nabla_{\mathbf{s}} g(\mathbf{S}^*) \quad (5.35)$$

The first-order approximation of the mean value is

$$\mu_g = -\mathbf{S}^{*T} \nabla_{\mathbf{s}} g(\mathbf{S}^*) \quad (5.36)$$

and the corresponding first-order approximation of the variance is

$$\sigma_g^2 = \nabla_{\mathbf{s}}^T g(\mathbf{S}^*) \nabla_{\mathbf{s}} g(\mathbf{S}^*) \quad (5.37)$$

The reliability index is given by

$$\beta = \frac{\mu_g}{\sigma_g} = \frac{-\mathbf{S}^{*T} \nabla_{\mathbf{s}} g(\mathbf{S}^*)}{\left( \nabla_{\mathbf{s}}^T g(\mathbf{S}^*) \nabla_{\mathbf{s}} g(\mathbf{S}^*) \right)^{\frac{1}{2}}} \quad (5.38)$$

or

$$\beta = -\boldsymbol{\alpha}^{*T} \mathbf{S}^* \quad (5.39)$$

This value of  $\beta$ , obtained from a first-order expansion of  $g(\mathbf{X})$ , is the same as the value from Eq. 5.28. For this reason, the second-moment method is often referred to as the first-order second-moment method. More accurate estimates of  $\beta$  may be found by using higher order terms in the expansion of  $g(\mathbf{X})$  about the failure surface, but in most cases the cost increases drastically because the higher derivatives must also be computed.

For a nonlinear performance function, the reliability index  $\beta$  is found using an iterative procedure that incorporates the results of the Lagrange multiplier method presented above. The following iterative algorithm was proposed by Rackwitz (1976):

1. ) Assume initial values of  $X_i^*$  and obtain the standardized normal variables

$$S_i^* = \frac{X_i^* - \mu_{X_i}}{\sigma_{X_i}}$$

- 2.) Evaluate  $\nabla_s g(\mathbf{S}^*)$  and  $\alpha^*$ .
- 3.) Form  $X_i^* = \mu_{X_i} - \alpha_i^* \sigma_{X_i} \beta$ .
- 4.) Substitute  $X_i^*$  into  $g(\mathbf{X}^*) = 0$  and solve for  $\beta$ .
- 5.) Using  $\beta$  from step 4, reevaluate  $S_i^* = -\alpha_i^* \beta$ .
- 6.) Repeat steps 2 through 5 until the change in  $\beta$  or the changes in  $S_i^*$  are sufficiently small.

The resulting probability of failure is found from the expression

$$p_f = 1 - \Phi(\beta) \quad (5.40)$$

## 5.3 LEAST SQUARES ANALYSIS

### 5.3.1 Linear Approximation

To fit a linear surface to a given set of data requires an equation of the form

$$Y = \hat{\psi}_0 + \sum_{i=1}^k \hat{\psi}_i X_i \quad (5.41)$$

where there are a total of  $p = k + 1$  unknown coefficients in the model and  $k$  is the total

number of independent variables included in the analysis. To solve for the unknown coefficients,  $\hat{\psi}_i$ , in Eq. 5.41, a series of experiments must be run at various levels of each independent variable  $X_i$ . The number of experiments run must be greater than the number of independent variables included in the analysis. The experimental data for  $n$  experiments is typically written in the form (Myers 1971)

$$\begin{array}{ccccc} Y_1 & X_{11} & X_{21} & \cdots & X_{k1} \\ Y_2 & X_{12} & X_{22} & \cdots & X_{k2} \\ \vdots & \vdots & \vdots & \ddots & \vdots \\ Y_n & X_{1n} & X_{2n} & \cdots & X_{kn} \end{array}$$

where  $n > k$ . Using the experimental results, the assumed linear model may be written as

$$\mathbf{Y}_{n \times 1} = \mathbf{\Xi}_{n \times p} \mathbf{\Psi}_{p \times 1} + \mathbf{e}_{n \times 1} \quad (5.42)$$

where  $\mathbf{e}$  is a vector of random variables that represents the difference between the experimental results and the results predicted by the linear model. The  $e_i$  for each experiment are assumed to be independent with zero mean and variance  $\sigma^2$  (Myers 1971).

The vector  $\mathbf{Y}$  contains the results of the  $n$  experimental runs and is given by

$$\mathbf{Y}_{n \times 1} = \begin{bmatrix} Y_1 \\ Y_2 \\ \vdots \\ Y_n \end{bmatrix} \quad (5.43)$$

The vector  $\mathbf{\Psi}$  contains the unknown coefficients and may be expressed as

$$\mathbf{\Psi}_{p \times 1} = \begin{bmatrix} \psi_0 \\ \psi_1 \\ \psi_2 \\ \vdots \\ \psi_n \end{bmatrix} \quad (5.44)$$

and the matrix  $\mathbf{\Xi}$  contains the various levels of the independent variables  $X_i$  and has the form

$$\mathbf{\Xi}_{n \times p} = \begin{bmatrix} 1 & X_{11} & X_{21} & \cdots & X_{k1} \\ 1 & X_{12} & X_{22} & \cdots & X_{k2} \\ \vdots & \vdots & \vdots & \ddots & \vdots \\ 1 & X_{1n} & X_{2n} & \cdots & X_{kn} \end{bmatrix} \quad (5.45)$$

The method of least squares finds the coefficients,  $\mathbf{\Psi}$ , that minimizes the sum of the squares of the random values  $e_i$  for each experiment. Therefore, the coefficients  $\mathbf{\Psi}$  may be found by minimizing

$$L = \sum_{i=1}^n e_i^2 = \mathbf{e}^T \mathbf{e} \quad (5.46)$$

Equation 5.46 may also be written as

$$L = \left( \mathbf{Y}_{n \times 1} - \mathbf{\Xi}_{n \times p} \hat{\mathbf{\Psi}}_{p \times 1} \right)^T \left( \mathbf{Y}_{n \times 1} - \mathbf{\Xi}_{n \times p} \hat{\mathbf{\Psi}}_{p \times 1} \right) \quad (5.47)$$

where  $\hat{\mathbf{\Psi}}$  are the estimated values of the coefficients  $\mathbf{\Psi}$ , resulting from the least squares approximation. The expanded form of Eq. 5.47 is

$$L = \mathbf{Y}_{1 \times n}^T \mathbf{Y}_{n \times 1} - 2 \hat{\mathbf{\Psi}}_{1 \times p}^T \mathbf{\Xi}_{p \times n}^T \mathbf{Y}_{n \times 1} + \hat{\mathbf{\Psi}}_{1 \times p}^T \mathbf{\Xi}_{p \times n}^T \mathbf{\Xi}_{n \times p} \hat{\mathbf{\Psi}}_{p \times 1} \quad (5.48)$$

To solve for the coefficients  $\hat{\mathbf{\Psi}}$ ,  $L$  must be minimized and set equal to zero giving

$$\frac{\partial L}{\partial \hat{\mathbf{\Psi}}} = -2 \mathbf{\Xi}_{p \times n}^T \mathbf{Y}_{n \times 1} + 2 \mathbf{\Xi}_{p \times n}^T \mathbf{\Xi}_{n \times p} \hat{\mathbf{\Psi}}_{p \times 1} = 0 \quad (5.49)$$

The resulting vector  $\hat{\mathbf{\Psi}}$  is found by solving the linear system,

$$\left( \mathbf{\Xi}_{p \times n}^T \mathbf{\Xi}_{n \times p} \right)_{p \times p} \hat{\mathbf{\Psi}}_{p \times 1} = \mathbf{\Xi}_{p \times n}^T \mathbf{Y}_{n \times 1} \quad (5.50)$$

The system of equations given in Eq. 5.50 are called the normal equations for estimating  $\hat{\mathbf{\Psi}}$  (Myers 1971).

### 5.3.2 Quadratic Approximation

The procedure used to fit a linear function may be extended to fit a function of the form

$$Y = \hat{\psi}_0 + \sum_{i=1}^k \hat{\psi}_i X_i + \sum_{i=1}^k \hat{\psi}_{ii} X_i^2 + \sum_{i=1}^k \sum_{j>i}^k \hat{\psi}_{ij} X_i X_j \quad (5.51)$$

where there are now  $p = 1 + 2k + k(k-1)/2$  parameters in the model rather than the  $p = k + 1$  parameters in the linear approximation. The assumed quadratic model may be written in the same form as the linear model

$$\mathbf{Y} = \mathbf{\Xi} \mathbf{\Psi} + \mathbf{e}, \quad (5.52)$$

$\begin{matrix} n \times 1 & n \times p & p \times 1 & n \times 1 \end{matrix}$

but the matrix  $\mathbf{\Xi}$  now has extra columns to account for the quadratic terms in the model. The vector  $\mathbf{\Psi}$  also has extra rows to account for the additional coefficients. For the case that includes only two independent variables, the matrix  $\mathbf{\Xi}$  is

$$\mathbf{\Xi}_{n \times 6} = \begin{bmatrix} 1 & X_{11} & X_{21} & X_{11}^2 & X_{11}X_{21} & X_{21}^2 \\ 1 & X_{12} & X_{22} & X_{12}^2 & X_{12}X_{22} & X_{22}^2 \\ \vdots & \vdots & \vdots & \vdots & \vdots & \vdots \\ 1 & X_{1n} & X_{2n} & X_{1n}^2 & X_{1n}X_{2n} & X_{2n}^2 \end{bmatrix} \quad (5.53)$$

and the vector  $\mathbf{\Psi}$  is given by

$$\mathbf{\Psi}_{6 \times 1} = \begin{bmatrix} \psi_0 \\ \psi_1 \\ \psi_2 \\ \psi_{11} \\ \psi_{12} \\ \psi_{22} \end{bmatrix} \quad (5.54)$$

Just as in the linear case, the vector of coefficients  $\hat{\mathbf{\Psi}}$  is found by solving the linear system of equations

$$(\mathbf{\Xi}^T \mathbf{\Xi})_{p \times n} \hat{\mathbf{\Psi}}_{n \times 1} = \mathbf{\Xi}^T \mathbf{Y}_{n \times 1} \quad (5.55)$$

## 5.4 EXPERIMENTAL DESIGNS

### 5.4.1 Two-Level Factorial Designs

The success of the response surface method depends to a large extent on the  $n$  experimental runs used in the least squares analysis. Designed experiments are often used to maximize the efficiency and the accuracy of the least squares analysis. One important class of experimental designs is factorial experimentation, and in particular factorial experiments with each independent variable at two levels. This type of design is called the  $2^k$  factorial design, and has two major advantages over the more common one-factor-at-a-time procedure (Myers 1971). For a study that includes three independent variables, a total of  $2^3 = 8$  experiments are required for the  $2^k$  factorial design:

	$X_1$	$X_2$	$X_3$
1	$L$	$L$	$L$
2	$H$	$L$	$L$
3	$L$	$H$	$L$
4	$H$	$H$	$L$
5	$L$	$L$	$H$
6	$H$	$L$	$H$
7	$L$	$H$	$H$
8	$H$	$H$	$H$

(5.56)

where  $H$  indicates the high level and  $L$  indicates the low level of the independent variable  $X_i$ . One example of a one factor at a time design includes four experiments (Myers 1971):

	$X_1$	$X_2$	$X_3$
1	$L$	$L$	$L$
2	$H$	$L$	$L$
3	$L$	$H$	$L$
4	$L$	$L$	$H$

(5.57)

The first advantage of the factorial design is that interaction between the independent



variables can automatically be measured because there are enough experiments in the design to include the coefficients  $\hat{\psi}_{ij}$  in the least squares analysis. However, there is not enough information in the  $2^k$  factorial design to gain any information about the pure quadratic terms by finding the coefficients  $\hat{\psi}_{ii}$ . The second advantage is that the variance of a typical coefficient from the  $2^k$  factorial design is much less than the variance of a typical coefficient from the one-factor-at-a-time analysis (Myers 1971). Therefore, the coefficients from the factorial design are considered to be more precise than those from the one-factor-at-a-time design.

When using the  $2^k$  factorial design the independent variables are often transformed so that the high and low levels of each are  $H = +1$  and  $L = -1$ . The resulting transformation is

$$\zeta_i = 2 \left( \frac{X_i - \bar{X}_i}{d_i} \right) \quad (5.58)$$

where the variables  $\zeta_i$  are referred to as coded variables. The quantity  $d_i$  is the difference between the high and low value of  $X_i$ , and  $\bar{X}_i$  is the average of the high and low value for  $X_i$ . The various combinations of the coded variables for a  $2^k$  design are placed in a design matrix **D**. The design matrix for the case where there are three independent variables is

$$\mathbf{D} = \begin{bmatrix} -1 & -1 & -1 \\ 1 & -1 & -1 \\ -1 & 1 & -1 \\ 1 & 1 & -1 \\ -1 & -1 & 1 \\ 1 & -1 & 1 \\ -1 & 1 & 1 \\ 1 & 1 & 1 \end{bmatrix} \quad (5.59)$$

Note that there is a pattern to the design matrix and that in every column there are  $2^{(i-1)}$  ( $i$  = column number) clusters of the high and low level of each coded variable. This

pattern holds for any number of independent variables and makes computer generation of the design matrix fairly straightforward. When used with the linear least squares analysis, the design matrix is incorporated into the  $\Xi$  matrix as the last  $k$  columns. For the three variable case, the matrix  $\Xi$  is

$$\Xi = \begin{bmatrix} 1 & -1 & -1 & -1 \\ 1 & 1 & -1 & -1 \\ 1 & -1 & 1 & -1 \\ 1 & 1 & 1 & -1 \\ 1 & -1 & -1 & 1 \\ 1 & 1 & -1 & 1 \\ 1 & -1 & 1 & 1 \\ 1 & 1 & 1 & 1 \end{bmatrix} \quad (5.60)$$

Use of the coded variables also simplifies the matrix  $\Xi^T \Xi$  which is required for the solution of the unknown coefficients. For  $k$  independent variables the matrix  $\Xi^T \Xi$  is the diagonal matrix

$$\Xi^T \Xi = \begin{bmatrix} 2^k & & & 0 \\ & 2^k & & \\ & & \ddots & \\ 0 & & & 2^k \end{bmatrix} = 2^k \mathbf{I}_{p \times p} \quad (5.61)$$

Besides making the solution for the coefficients much easier, the fact that  $\Xi^T \Xi$  is diagonal also implies that the covariance between any two coefficients is equal to zero which makes the  $2^k$  factorial design part of a larger class of designs known as orthogonal designs (Myers 1971).

#### 5.4.2 Central Composite Design

As mentioned above, the standard  $2^k$  factorial design does not provide enough data to determine the coefficients of the pure quadratic terms in the least squares analysis. However, the  $2^k$  factorial design may be supplemented with axial data points at some

distance  $\alpha$  along the axis of each independent variable. Also, at least one center point must be added to the design. The resulting experimental design is called the Central Composite Design (CCD), and is shown in Fig. 5.3 for three independent variables. As a result of adding more experimental points, the design matrix has additional rows. For  $k$  independent variables, the additional portion of the design matrix is

$$\begin{array}{ccccc}
 \zeta_1 & \zeta_2 & \zeta_3 & \cdots & \zeta_k \\
 \left[ \begin{array}{ccccc}
 0 & 0 & 0 & \cdots & 0 \\
 -\alpha & 0 & 0 & \cdots & 0 \\
 \alpha & 0 & 0 & \cdots & 0 \\
 0 & -\alpha & 0 & \cdots & 0 \\
 0 & \alpha & 0 & \cdots & 0 \\
 0 & 0 & -\alpha & \cdots & 0 \\
 0 & 0 & \alpha & \cdots & 0 \\
 \cdots & \cdots & \cdots & \cdots & \cdots \\
 0 & 0 & 0 & \cdots & -\alpha \\
 0 & 0 & 0 & \cdots & \alpha
 \end{array} \right] & (5.62)
 \end{array}$$

The distance  $\alpha$  is chosen by the user, but in most cases only varies between 1.0 and  $\sqrt{k}$  (Myers and Montgomery 1995). For three independent variables the first value of 1.0 places all of the axial points on the faces of a hypercube, and the second value,  $\sqrt{k}$ , places all the axial points on a sphere. There are various choices for the value of  $\alpha$  (Myers and Montgomery 1995), all of which have some desirable effect on the response surface analysis. The value of  $\alpha$  that will be used in this work is the value that causes the design to be orthogonal. The value of  $\alpha$  needed to make the central composite design orthogonal is computed using (Myers 1971)

$$\alpha = \left( \frac{QF}{4} \right)^{\frac{1}{4}} \quad (5.63)$$

where

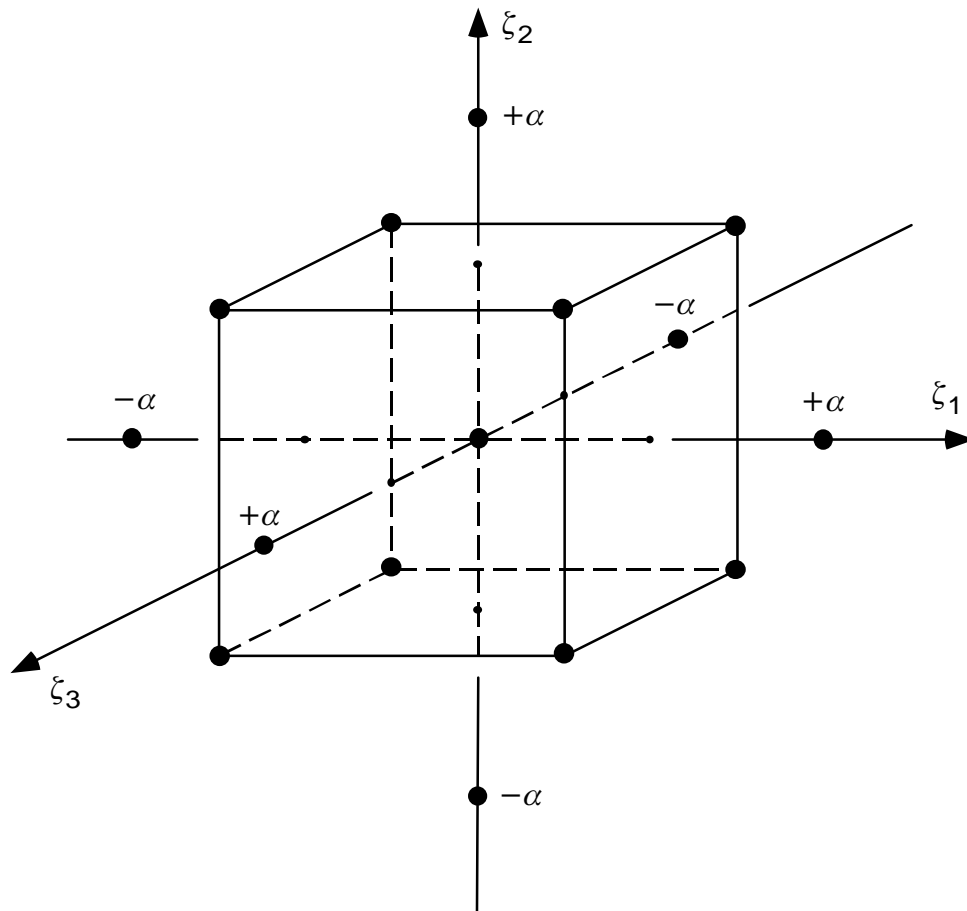


Figure 5.3 The Central Composite Design for Three Variables (Myers 1995).

$$Q = \left( \sqrt{F + T} - \sqrt{F} \right)^2, \quad (5.64)$$

$F$  is the number of factorial points in the design, and  $T$  is the number of additional points needed for the Central Composite Design. For three independent variables  $F = 2^3 = 8$ ,  $T = 2 \times 3 + 1 = 7$ , and  $\alpha = 1.216$ .

### 5.4.3 Two-Level Fractional Factorial Designs

The example shown earlier pointed out that the coefficients obtained using a  $2^k$  factorial design were more accurate than those using the one-factor-at-a-time approach, but the  $2^k$  factorial design required twice the number of experiments. If the cost of running experiments is very high and the difference in accuracy of the coefficients is not a problem, then the one-factor-at-a-time approach may appear to be a better alternative. However, it turns out that fractions of the  $2^k$  factorial design may be used without sacrificing the accuracy or the orthogonality of the design. The  $m$ th fraction of a  $2^k$  factorial design is abbreviated as a  $2^{k-m}$  factorial design. If  $m = 1$  then the design is a  $1/2$  fraction of the  $2^k$  factorial design and only  $1/2$  of the full number of experiments are required for the analysis.

The fraction chosen for the  $2^{k-m}$  design depends on which coefficients the user is most interested in knowing. When using a fractional factorial design, there is no longer enough experimental data to uniquely estimate each coefficient. Therefore, some of the coefficients lose their independence or they become confused with one another. When the values of two coefficients are not unique there is said to be aliasing in the design. The objective in using a  $2^{k-m}$  design is to not have aliasing between any two coefficients of interest. As an example, if a user wants to fit a linear surface to a set of experimental data then it is imperative that no two coefficients of linear terms be aliased with one another. If

the user wishes to fit a quadratic model to a set of data then there must be no aliasing between first-order terms, between first and second-order terms, or between any two second-order terms. A design of the latter type is said to be of Resolution V or better (Montgomery 1991). Resolution III designs guarantee that no two linear terms are aliased with one another and Resolution IV designs guarantee that no two linear terms are aliased with one another and that no linear terms are aliased with quadratic terms.

Once a design resolution has been specified, the fraction  $m$  of the full  $2^k$  design is also known. The question that remains is how to choose which rows in the design matrix **D** will be used to actually conduct the experiments. The first step is to identify a defining contrast, which basically determines which terms will be aliased in the analysis. As an example, consider the  $2^{3-1}$  design which is a resolution III design. The defining contrast for this design is

$$I = \zeta_1 \zeta_2 \zeta_3 \quad (5.65)$$

To determine which experiments must be run, the defining contrast may be rewritten as

$$I = \zeta_1^{\gamma_1=1} \zeta_2^{\gamma_2=1} \zeta_3^{\gamma_3=1} \quad (5.66)$$

where  $\gamma_i$  is equal to 0 or 1 and determines whether or not the corresponding variable  $\zeta_i$  is included in the defining contrast. New variables  $z_i$  which correspond to  $X_i$  are defined such that  $z_i = 1$  if  $X_i$  is at the high level and  $z_i = 0$  if  $X_i$  is at the low level. A value  $L$  is computed for every row in the design matrix using the expression

$$L = \gamma_1 z_1 + \gamma_2 z_2 + \gamma_3 z_3 = z_1 + z_2 + z_3 \quad (5.67)$$

Then for every value  $L$ , a value  $t$  is computed by the expression

$$t = L \text{ modulo}(2), \quad (5.68)$$

or

$$t = L - INT\left(\frac{L}{2}\right)*2 \quad (5.69)$$

This method causes the value of  $t$  to be either 0 or 1. When applied to the three variable case, the resulting values of  $t$  are

$\zeta_1$	$\zeta_2$	$\zeta_3$	$t$
-1	-1	-1	0
1	-1	-1	1
-1	1	-1	1
1	1	-1	0
-1	-1	1	1
1	-1	1	0
-1	1	1	0
1	1	1	1

The result is two sets of experiments, one having  $t = 0$  and the other having  $t = 1$ . Either set may be used to run the actual experiments. The general procedure for finding the appropriate rows to use for an  $m$ th fraction design having  $k$  variables is explained by Myers (1971). In general there will be  $m$  defining contrasts in a  $2^{k-m}$  design. Therefore, there will be  $m$  values of  $L$ ,  $L_i$ , and  $m$  values of  $t$ ,  $t_i$ . The correct rows of **D** are chosen from one of the  $2^m$  sets of  $t_i$  generated using the above process. Tables of defining contrasts for various resolutions and various numbers of independent variables are given by Montgomery (1991).

## 5.5 SIGNIFICANCE OF INDIVIDUAL REGRESSION COEFFICIENTS

When using a technique like the response method it is often difficult to decide which independent variables must be included in the model. Since experimentation is costly it is best to only include those variables which influence the response of the system the most. One method for determining which variables are most significant involves the use of a screening experiment. In a screening experiment, all independent variables of

interest are included in the analysis and a first-order surface is fit to the experimental results. The effect of each independent variable  $X_i$  is assessed by testing the coefficients  $\hat{\psi}_i$ .

One simple method for comparing the effects of the variables  $X_i$  is to simply compare the magnitudes of the individual coefficients  $\hat{\psi}_i$ . The major problem with this method is that differences in units among the independent variables may cause some of the coefficients to appear artificially small when compared to the rest. In the response surface method, hypothesis testing is normally used to determine the significance of each independent variable. The hypotheses used for testing the significance of individual coefficients are (Montgomery 1991),

$$\begin{aligned} H_0 : \hat{\psi}_i &= 0 \\ H_1 : \hat{\psi}_i &\neq 0 \end{aligned} \quad (5.70)$$

The test statistic for the above hypotheses is (Myers and Montgomery 1995)

$$t_0 = \frac{\hat{\psi}_i}{\sqrt{\hat{\sigma}^2 C_i}} \quad (5.71)$$

where  $C_i$  is the  $i$ th diagonal element of the matrix  $(\mathbf{\Xi}^T \mathbf{\Xi})^{-1}$ . The term  $\hat{\sigma}^2$  is estimated from the mean square error as (Myers 1971)

$$MSE = \frac{\mathbf{Y}^T \mathbf{Y} - \mathbf{\Psi}^T \mathbf{\Xi}^T \mathbf{Y}}{n - p} = \frac{SSE}{n - p} \quad (5.72)$$

where  $SSE$  is referred to as the error sum of squares which is computed using the differences between each experimental result and the corresponding least squares prediction. The variable  $n$  is the total number of experiments used in the analysis and  $p$  is the total number of coefficients in the model. The hypothesis  $H_0 : \hat{\psi}_i = 0$  is rejected if

$$|t_0| > t_{\alpha/2, n-p} \quad (5.73)$$



where  $\alpha$  is equal to one minus the confidence level and  $t_{\alpha/2, n-p}$  is the percentile value of the students t-distribution with  $(n - p)$  degrees of freedom. The hypothesis test basically reflects a certain user specified confidence that a specific coefficient  $\hat{\psi}_i$  should be included in the model.

The hypothesis test presented above does have one major disadvantage in that the coefficients  $\hat{\psi}_i$  are assumed to be statistically independent (Montgomery 1991). In general, the off-diagonal terms in the matrix  $(\Xi^T \Xi)^{-1}$  are not zero indicating that there is some correlation between the coefficients  $\hat{\psi}_i$ . But, if a two-level full or fractional factorial design is used to conduct the experiments the design is orthogonal, the matrix  $(\Xi^T \Xi)^{-1}$  is diagonal, and the coefficients  $\hat{\psi}_i$  are independent. In this case the hypothesis test gives good results.

Once the hypothesis test has been performed on all of the coefficients then all of the independent variables which are not significant can be dropped from the analysis. In many cases this can significantly reduce the amount of experimentation and therefore make the response surface method a cost effective alternative for estimating the response of a system.

## 5.6 MODELING OF THE PERFORMANCE FUNCTION

### 5.6.1 Linear Model

The performance function needed for the first-order second-moment method may be generated by using the least squares method combined with designed experiments. If the experiments in the analysis are performed in accordance with a two-level factorial design, using coded variables, a linear performance function of the following form may be generated:

$$g(\boldsymbol{\zeta}) = \hat{\omega}_0 + \sum_{i=1}^k \hat{\omega}_i \zeta_i \quad (5.74)$$

where the coded variables  $\zeta_i$  are now random variables. To fit into the first-order second-moment method, the resulting performance function must be written in terms of standardized normal variables,  $S_i$ . The expression for the variables  $X_i$  in terms of  $S_i$  is

$$X_i = \mu_{X_i} + \sigma_{X_i} S_i \quad (5.75)$$

Substituting Eq. 5.75 into the equation for the coded variables, Eq. 5.58, gives

$$\zeta_i = a_i + b_i S_i \quad (5.76)$$

where

$$a_i = \frac{2(\mu_{X_i} - \bar{X}_i)}{d_i}, \quad (5.77)$$

and

$$b_i = \frac{2\sigma_{X_i}}{d_i} \quad (5.78)$$

The performance function may be written in terms of  $S_i$  by substituting Eq. 5.76 into Eq. 5.74:

$$g(\boldsymbol{\zeta}) = \hat{\omega}_0 + \sum_{i=1}^k \hat{\omega}_i (a_i + b_i S_i), \quad (5.79)$$

or

$$g(\mathbf{S}) = \hat{\omega}_0 + \sum_{i=1}^k \hat{\omega}_i a_i + \sum_{i=1}^k \hat{\omega}_i b_i S_i \quad (5.80)$$

The most probable failure point is given by

$$S_i^* = -\beta \alpha_i^* \quad (5.81)$$

where

$$\alpha_i^* = \frac{\frac{\partial g(\mathbf{S}^*)}{\partial S_i}}{\left( \nabla_s^T g(\mathbf{S}^*) \nabla_s g(\mathbf{S}^*) \right)^{\frac{1}{2}}} \quad (5.82)$$

Using the chain rule, one may write  $\partial g(\mathbf{S})/\partial S_i$  as

$$\frac{\partial g(\mathbf{S}^*)}{\partial S_i} = \frac{\partial g(\boldsymbol{\zeta})}{\partial \zeta_i} \frac{\partial \zeta_i}{\partial S_i} = \frac{2\sigma_{X_i}}{d_i} \hat{\omega}_i \quad (5.83)$$

Setting Eq. 5.80 equal to zero yields the equation of the limit state which is given by

$$g(\mathbf{S}) = \hat{\omega}_0 + \sum_{i=1}^k \hat{\omega}_i a_i + \sum_{i=1}^k \hat{\omega}_i b_i S_i = 0 \quad (5.84)$$

At the most probable failure point the limit state becomes

$$\hat{\omega}_0 + \sum_{i=1}^k \hat{\omega}_i a_i - \beta \sum_{i=1}^k \hat{\omega}_i b_i \alpha_i^* = 0 \quad (5.85)$$

Solution for the reliability index  $\beta$  yields

$$\beta = \frac{\hat{\omega}_0 + \sum_{i=1}^k \hat{\omega}_i a_i}{\sum_{i=1}^k \hat{\omega}_i b_i \alpha_i^*} \quad (5.86)$$

### 5.6.2 Quadratic Model

The procedure presented above may be modified slightly to include a quadratic model of the performance function. The vector form of the second-order performance function may be written as

$$g(\boldsymbol{\zeta}) = \hat{\omega}_0 + \hat{\boldsymbol{\omega}}^T \boldsymbol{\zeta} + \boldsymbol{\zeta}^T \hat{\boldsymbol{\Omega}} \boldsymbol{\zeta} \quad (5.87)$$

where

$$\hat{\boldsymbol{\omega}} = \begin{bmatrix} \hat{\omega}_1 \\ \hat{\omega}_2 \\ \vdots \\ \hat{\omega}_k \end{bmatrix} \quad (5.88)$$

and

$$\hat{\boldsymbol{\Omega}} = \begin{bmatrix} \hat{\omega}_{11} & \hat{\omega}_{12}/2 & \cdots & \hat{\omega}_{1k}/2 \\ & \hat{\omega}_{22} & \cdots & \hat{\omega}_{2k}/2 \\ & & \ddots & \vdots \\ sym. & & & \hat{\omega}_{kk} \end{bmatrix} \quad (5.89)$$

The vector form of the relationship between  $\boldsymbol{\zeta}$  and  $\mathbf{S}$  is

$$\boldsymbol{\zeta} = \mathbf{a} + \mathbf{B}\mathbf{S} \quad (5.90)$$

where

$$\mathbf{a} = 2 \begin{bmatrix} \frac{(\mu_{X_1} - \bar{X}_1)}{d_1} \\ \frac{(\mu_{X_2} - \bar{X}_2)}{d_2} \\ \vdots \\ \frac{(\mu_{X_k} - \bar{X}_k)}{d_k} \end{bmatrix} \quad (5.91)$$

and

$$\mathbf{B} = \begin{bmatrix} \frac{2\sigma_{X_1}}{d_1} & & & 0 \\ & \frac{2\sigma_{X_2}}{d_2} & & \\ & & \ddots & \\ 0 & & & \frac{2\sigma_{X_k}}{d_k} \end{bmatrix} \quad (5.92)$$

Substituting Eq. 5.90 into the performance function gives

$$g(\mathbf{S}) = g + \mathbf{S}^T \mathbf{g} + \mathbf{S}^T \mathbf{G} \mathbf{S} \quad (5.93)$$

where

$$g = \hat{\omega}_0 + \hat{\boldsymbol{\omega}}^T \mathbf{a} + \mathbf{a}^T \hat{\boldsymbol{\Omega}} \mathbf{a}, \quad (5.94)$$

$$\mathbf{g} = \mathbf{B}^T \hat{\boldsymbol{\omega}} + 2\mathbf{a}^T \hat{\boldsymbol{\Omega}} \mathbf{B}, \quad (5.95)$$

and

$$\mathbf{G} = \mathbf{B}^T \hat{\boldsymbol{\Omega}} \mathbf{B} \quad (5.96)$$

The vector  $\boldsymbol{\alpha}$  is given by

$$\boldsymbol{\alpha} = \frac{\nabla_s g(\mathbf{S})}{\left( \nabla_s^T g(\mathbf{S}) \nabla_s g(\mathbf{S}) \right)^{\frac{1}{2}}} \quad (5.97)$$

where  $\nabla_s g(\mathbf{S})$  is equal to

$$\nabla_s g(\mathbf{S}) = \mathbf{g} + 2 \mathbf{G} \mathbf{S} \quad (5.98)$$

The most probable failure point is

$$\mathbf{S}^* = -\beta \boldsymbol{\alpha}^* \quad (5.99)$$

The equation of the limit state at the most probable failure point is

$$g(\mathbf{S}^*) = g - \left( \boldsymbol{\alpha}^{*T} \mathbf{g} \right) \beta + \left( \boldsymbol{\alpha}^{*T} \mathbf{G} \boldsymbol{\alpha}^* \right) \beta^2 = 0 \quad (5.100)$$

The resulting quadratic equation is then solved for the unknown reliability index  $\beta$ .

When the response surface method is used to model the performance function, the general iterative procedure for the first-order second-moment method may be rewritten as:

- 1.) Assume initial values  $X_i^*$  and make these values the center of the designed experiment.
- 2.) Set the upper and lower values (usually  $\pm \sigma_{X_i}$ ) for the experimental region and conduct a response surface analysis to predict a model for the performance function over the experimental region.
- 3.) Evaluate  $\nabla_s g(\mathbf{S}^*)$  and  $\boldsymbol{\alpha}^*$ .

- 4.) Solve  $g(\mathbf{S}^*) = 0$  for the reliability index  $\beta$ .
- 5.) Using  $\beta$  from step 4, reevaluate  $S_i^* = -\alpha_i^* \beta$  and correspondingly  $X_i^*$ .
- 6.) Make the new values of  $X_i^*$  the center of a new designed experiment and perform the necessary experiments.
- 7.) Repeat steps 2 through 6 until the change in  $\beta$  or the changes in  $S_i^*$  are sufficiently small.

## **CHAPTER 6**

### **STABILITY ANALYSIS WITH RANDOM IMPERFECTIONS**

Most of the work pertaining to stability analysis with random imperfections deals with the modeling of imperfections which are known at discrete points on the structure, or with finding a critical imperfection shape that causes the largest reduction in the critical load for the structure. Questions about the modeling of imperfections arise when a structure is designed for the first time and no information is available about the initial imperfections. Usually, a maximum allowable limit on the imperfection at any point on the structure is specified by a design code or dictated by the manufacturing process used to build the structure itself, or the various members in the structure. The objective is to model the imperfections in a realistic manner, by treating the imperfections as random fields, so that a resulting distribution of the imperfect critical load may be calculated using the techniques presented in Chapter 5.

#### **6.1 IMPERFECTION MODELING**

The objective in modeling the initial geometric imperfections is to obtain the variance of the modal imperfection amplitudes. Modeling of the initial geometric imperfections is accomplished using four basic assumptions. The first assumption only allows translational imperfections at the imperfect nodes. This means that crooked members are modeled by translational movements of the nodes of the finite elements used

to discretize each structural member. The second assumption forces the shape of the initial imperfection to be characterized by a summation of  $n$  linear buckling modes. The third assumption specifies that the variance of the amplitude of the initial imperfection is found from a specified maximum allowable imperfection magnitude. The fourth assumption limits the nodal imperfections to be independent normally distributed random values. For the work presented here, the mean value of the initial imperfection is assumed to be zero.

The first step in applying imperfections to a structural model is to define which joints or nodes will be allowed to have imperfections. The next step is to create a matrix of eigenvectors,  $\Phi$ , that only contains the components corresponding to the imperfect degrees of freedom. The imperfection vector for the entire structure may be written as

$$\underset{N_I \times 1}{\Delta} = \underset{N_I \times n}{\Phi} \underset{n \times 1}{\mathbf{a}} \quad (6.1)$$

where  $\Phi$  is the matrix of eigenvectors mentioned above,  $\mathbf{a}$  is a vector containing the modal imperfection magnitudes, and  $N_I$  is the number of imperfect degrees of freedom. The imperfection,  $\Delta$ , given by Eq. 6.1 is basically like the imperfections described in Chapter 2. The eigenvectors contained in  $\Phi$  determine the shape of the imperfection and the amplitudes contained in the vector  $\mathbf{a}$  determine the magnitude of the imperfection. If the nodal imperfections are known, the modal imperfection magnitudes may be found using

$$\underset{n \times 1}{\mathbf{a}} = \underset{n \times N_I}{\Phi^*} \underset{N_I \times 1}{\Delta} \quad (6.2)$$

where the matrix  $\Phi^*$  is the pseudo-inverse of the matrix  $\Phi$ . The pseudo-inverse is calculated using least squares as described in Chapter 5, which in this case yields

$$\Phi^* = (\Phi^T \Phi)^{-1} \Phi^T \quad (6.3)$$

Unlike the imperfections described in Chapter 2, the imperfection vector,  $\Delta$ , for the structure is not known and the modal imperfection vector,  $\mathbf{a}$ , is not easily found.



The goal of modeling the imperfections is to find the mean and variance of the modal imperfection vector,  $\mathbf{a}$ . To avoid specification of the exact nodal imperfections, the variance of the nodal imperfections may be specified. From Eq. 6.2, a typical modal amplitude is given by

$$a_i = \sum_{j=1}^{N_I} \Phi_{ij}^* \Delta_j \quad (6.4)$$

Therefore, each modal amplitude is a linear function of the nodal imperfections. If the nodal imperfections,  $\Delta_j$ , are independent normally distributed random variables then the mean value and variance of each modal amplitude is given by (Ang and Tang 1975):

$$\mu_{a_i} = \sum_{j=1}^{N_I} \Phi_{ij}^* \mu_{\Delta_j} \quad (6.5)$$

$$\sigma_{a_i}^2 = \sum_{j=1}^{N_I} (\Phi_{ij}^*)^2 \sigma_{\Delta_j}^2 \quad (6.6)$$

For the work presented here, the mean values of the nodal imperfections are assumed to be zero which means that the mean values of the modal amplitudes will also be zero.

If the nodal variances are known, Eq. 6.6 may be used to calculate the variance of the modal amplitudes. Most specifications require that the maximum allowable imperfection be no greater than a prescribed value,  $\Delta_{max}$ . This means that the imperfection,  $\Delta_k$ , at any imperfect node  $k$  on the structure should be less than or equal to  $\Delta_{max}$ . The prescribed maximum imperfection,  $\Delta_{max}$ , may be used to calculate a maximum allowable standard deviation for any imperfect node  $k$  using

$$s_{max} = \frac{\Delta_k - \mu_{\Delta_k}}{\sigma_{\Delta_k}} = \frac{\Delta_{max} - \mu_{\Delta_k}}{\sigma_{\Delta_k}}, \quad (6.7)$$

or

$$\sigma_{\Delta_k} = \frac{\Delta_{max} - \mu_{\Delta_k}}{s_{max}} \quad (6.8)$$

where the mean value,  $\mu_{\Delta_k}$ , of the imperfection at any imperfect node  $k$  is assumed to be zero. Using Eq. 6.8 ensures that the maximum imperfection will be located at  $\pm s_{max}$ , where  $s_{max}$  is the specified number of standard deviations from  $\mu_{\Delta_k} = 0$ . Therefore, the maximum allowable standard deviation, at any imperfect node  $k$  on the structure, is given by

$$\sigma_{\Delta_k} = \frac{\Delta_{max}}{s_{max}} \quad (6.9)$$

Tentative values of the nodal variances may be found using a unit variance for the modal amplitudes and

$$\sigma_{\Delta_j}^2 = \sum_{i=1}^n (\Phi_{ji})^2 \sigma_{a_i}^2 \quad (6.10)$$

The resulting values of  $\sigma_{\Delta_j}^2$  are then normalized with respect to the largest value of  $\sigma_{\Delta_j}^2$  and are then multiplied by  $\sigma_{\Delta_k}^2$  from Eq. 6.9. This procedure locates the imperfect node in the structure with the largest variance and then makes this variance equal to the maximum allowable variance calculated by using Eq. 6.9. The result is a normalized group of nodal variances whose maximum value is  $\sigma_{\Delta_k}^2$ . The modal variances are found using Eq. 6.6 and the normalized nodal variances,  $\sigma_{\Delta_j}^2$ . With the variances of the modal imperfection magnitudes known, a study of the distribution of the buckling load for a structure can be performed.

## 6.2 RELIABILITY ANALYSIS

### 6.2.1 Definition of the Limit State

For this study, the reliability or probability of survival,  $p_s$ , of a structure is defined as the probability that an imperfect structure will become unstable at a load greater than a specified percentage of the critical load for the perfect structure. The probability of failure,  $p_f$ , is equal to

$$p_f = 1 - p_s, \quad (6.11)$$

or the probability that an imperfect structure will become unstable at a load less than a given fraction of the perfect critical load for the structure. The limit state or failure surface for this problem is defined by

$$(Q_{cr})_{imp} - \lambda_{frac}(Q_{cr})_{perf} = 0 \quad (6.12)$$

where  $(Q_{cr})_{perf}$  is the critical load for the perfect structure,  $(Q_{cr})_{imp}$  is the critical load for the imperfect structure, and  $\lambda_{frac}$  is a specified fraction of the perfect critical load. For the general multiple degree of freedom problem, the load  $Q_{cr}$  becomes a vector  $\mathbf{Q}$  which is multiplied by a scalar  $\lambda_{cr}$ . The resulting failure surface is

$$[(\lambda_{cr})_{imp} - \lambda_{frac}(\lambda_{cr})_{perf}]\mathbf{Q} = 0, \quad (6.13)$$

or

$$(\lambda_{cr})_{imp} - \lambda_{frac}(\lambda_{cr})_{perf} = 0 \quad (6.14)$$

The above equation may be normalized by dividing both sides by  $(\lambda_{cr})_{perf}$  which gives

$$\frac{(\lambda_{cr})_{imp}}{(\lambda_{cr})_{perf}} - \lambda_{frac} = 0 \quad (6.15)$$

If  $\lambda_{frac}$  is equal to one, Eq. 6.15 becomes

$$\frac{(\lambda_{cr})_{imp}}{(\lambda_{cr})_{perf}} - 1 = 0 \quad (6.16)$$

and the resulting probability of failure,  $p_f$ , is the probability that an imperfect structure will have a critical load less than that of the perfect structure.

### 6.2.2 Response Surface/First-Order Second-Moment Method

With the imperfections modeled by the method presented in Section 6.1, the probability of failure may be calculated using Eq. 6.15 and the combined response surface/first-order second-moment (RS/FOSM) method presented in Chapter 5. The value of  $(\lambda_{cr})_{imp}$  is in general a nonlinear function of the modal imperfection amplitudes,  $a_i$ . A  $2^k$  factorial design is used to fit a first-order surface over an experimental region bounded by  $\pm \sigma_{a_i}$  for each random variable and centered at the mean values which are zero. Using a first-order surface, the reliability index,  $\beta$ , may be found using Eq. 5.87. With the reliability index known, a new estimate of the most probable imperfection amplitudes,  $a_i^*$ , may be calculated. For the next iteration, the experimental design is centered at  $a_i^*$  and, if the values of  $a_i^*$  are inside of the previous experimental region then the size of the new experimental region is reduced by half. Otherwise, the bounds of the experimental region remain at  $\pm \sigma_{a_i}$  until the predicted values of  $a_i^*$  fall inside the current experimental region. Iteration using the first-order approximation continues until the values of  $a_i^*$  are inside the experimental region and the difference between the values of  $\beta$  for two successive iterations is less than or equal to a specified tolerance,  $\delta_\beta$ . After meeting the two previously mentioned criteria, a second-order surface is fit over the current experimental region. The second-order surface is fit by supplementing the experimental data for the  $2^k$  factorial design with the data necessary to form a Central Composite Design (Sect. 5.4.2). The final value of the reliability index is found by solving

Eq. 5.101.

### 6.3 EXAMPLE PROBLEMS

Two example problems are presented that demonstrate the use of the RS/FOSM method for determining the probability that the critical load for the structure will be less than a specified fraction,  $\lambda_{frac}$ , of the perfect critical load. The first example is Williams' toggle frame and the second is the star-shaped reticulated cap. The analysis of the perfect structure for each problem was presented in Chapter 4. The RS/FOSM method is used for both examples and the results are compared with the results from numerical simulations.

#### 6.3.1 Example 1: Williams' Toggle Frame

The analysis for the perfect version of Williams' toggle frame was presented in Chapter 4. The frame was modeled using 10 elements per member. The analysis in Chapter 4 revealed that the structure becomes unstable at a limit point where the load multiplier,  $(\lambda_{cr})_{perf}$ , is equal to 0.57110. This value of  $(\lambda_{cr})_{perf}$  corresponds to a critical load of 34.266 pounds. Two different cases of Williams' toggle frame are considered. The first uses an imperfection shape derived from the first 10 linear buckling modes, and the second with an imperfection shape composed of the first six linear buckling modes. Both cases assume the maximum allowable imperfection anywhere on the structure to be less than five percent of the height of the apex or,

$$\Delta_{max} = 0.05 \times 0.386 \text{ in.} = 0.0193 \text{ in.} \quad (6.17)$$

With  $\Delta_{max}$  known, the maximum allowable variance at any imperfect node in the structure may be calculated using Eq. 6.9 and  $s_{max}$  equal to three:

$$\sigma_{\Delta_k}^2 = \left( \frac{\Delta_{max}}{s_{max}} \right)^2 = \left( \frac{0.0193 \text{ in.}}{3} \right)^2 = 4.138 \times 10^{-6} \quad (6.18)$$

In both cases, all of the translational degrees of freedom are allowed to be imperfect, which results in  $N_I = 38$  imperfect degrees of freedom.

### 6.3.1.1 Case 1: 10 mode imperfection

For the first case, the shape of the imperfection was modeled by the first ten linear buckling mode shapes which are shown in Figs. 6.1 and 6.2. The modal variances were found using the procedure outlined in Section 6.1 and the maximum allowable variance from Eq. 6.18. The resulting modal variances are shown in Table 6.1. The RS/FOSM method was then used to find the probability that the imperfect critical load will be less than the fractions,  $\lambda_{frac}$ , of the perfect critical load, which are located in the first column of Table 6.2. The number of numerical experiments was reduced by using a fractional factorial design with only  $2^{10-3} = 128$  experiments instead of the standard factorial design which requires  $2^{10} = 1024$  experiments. The value of  $\delta_\beta$  used in the analysis is 0.01. Table 6.3 contains the predicted most probable imperfection amplitudes,  $a_i^*$ , and the reliability index,  $\beta$ , for each iteration of a RS/FOSM analysis with  $\lambda_{frac}$  equal to 0.968. The resulting failure probabilities, for all of the values of  $\lambda_{frac}$ , are given in the fourth column of Table 6.2.

A 10,000 data point simulation was run to verify the results from the RS/FOSM method. During the simulation, the modal imperfection amplitudes were treated as normally distributed random numbers with variances as shown in Table 6.1. A frequency density diagram which shows the resulting distribution of the imperfect critical load is given in Fig. 6.3. The number of cells in the frequency density diagram is given by (Sturges, 1926)

$$N_C \approx 1 + 3.3 \log_{10}(\text{number of data points}) \quad (6.19)$$

For 10,000 data points  $N_C$  is approximately 14. The frequency density diagram was used

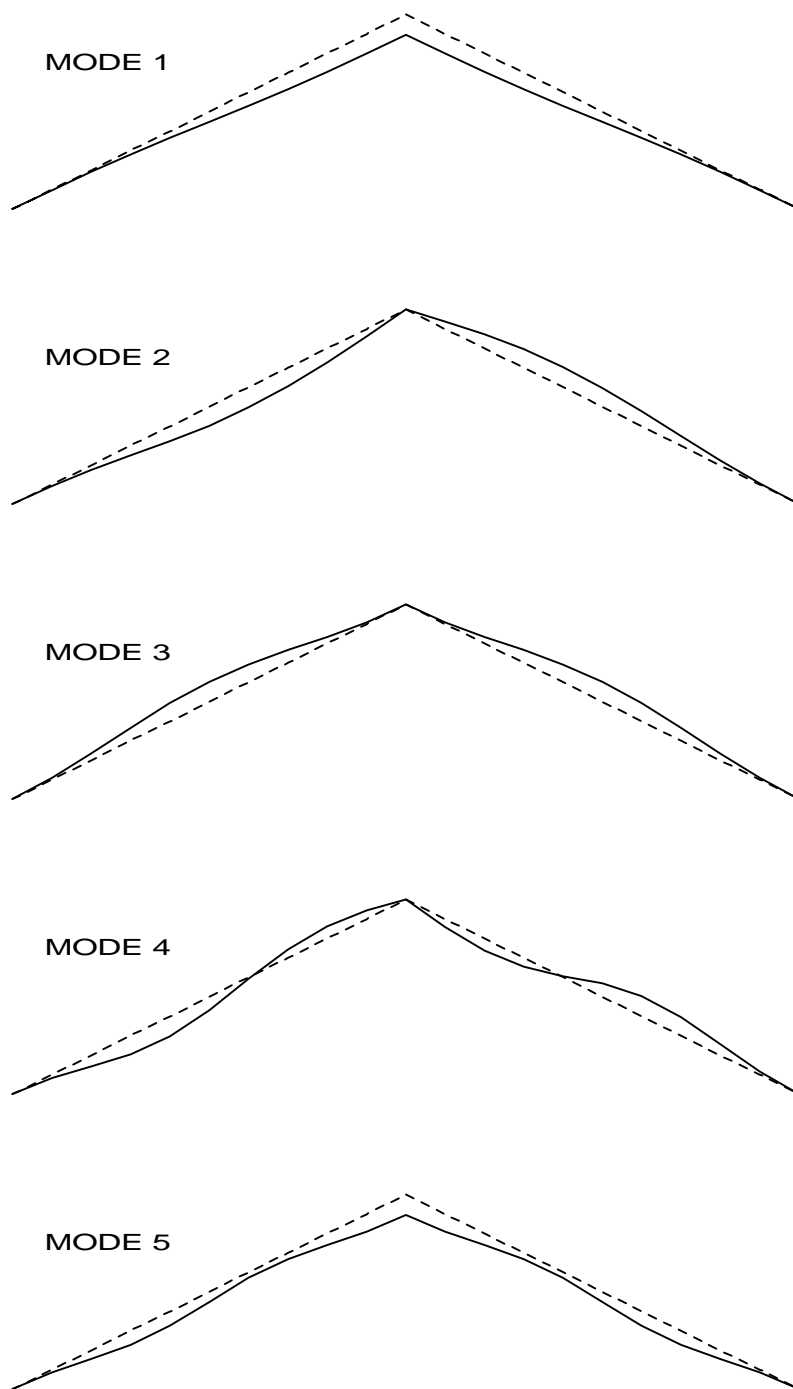


Figure 6.1 Linear buckling modes 1-5 for Williams' toggle frame.

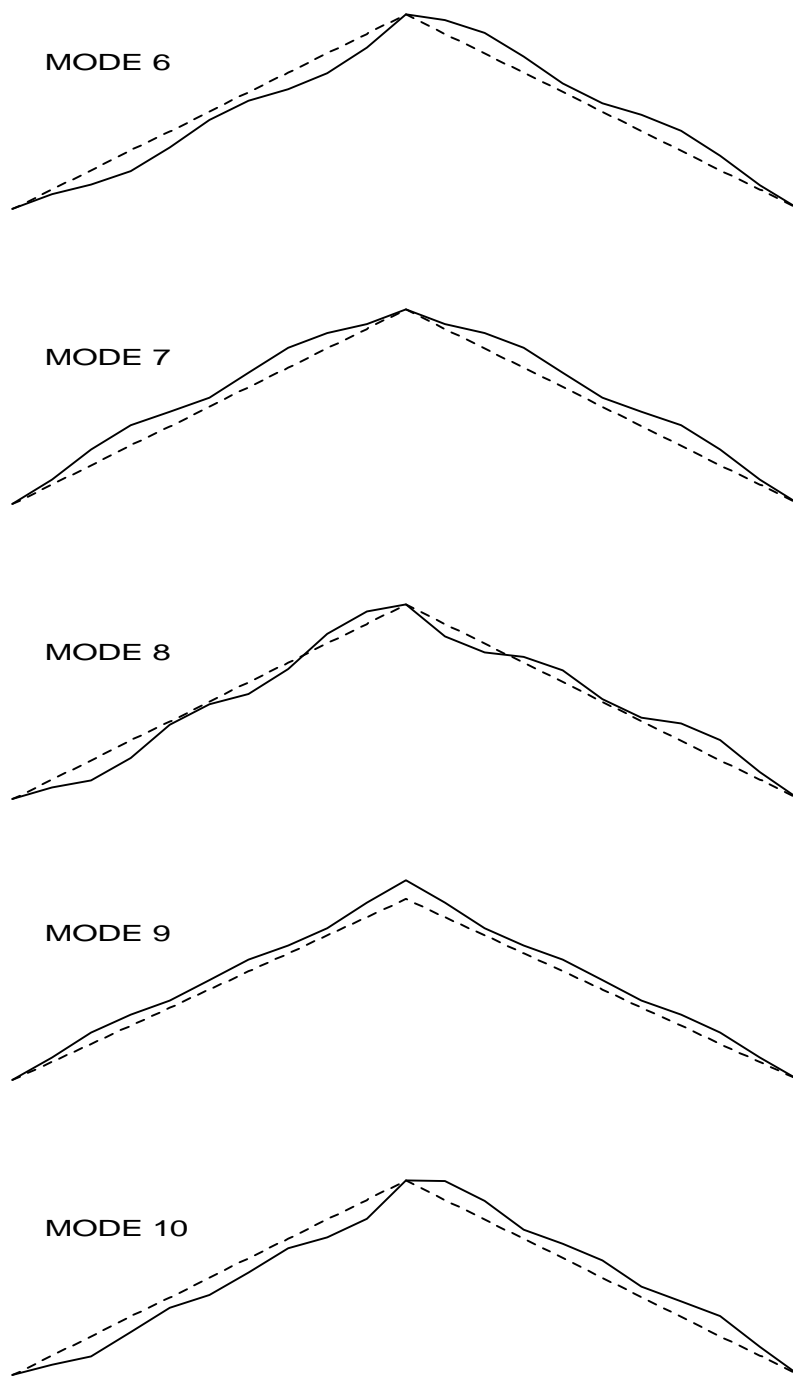


Figure 6.2 Linear buckling modes 6-10 for Williams' toggle frame.



Table 6.1 Modal variances for the 10 mode case for Williams' toggle frame.

Mode No.	Modal Variance, $\sigma_{a_i}^2$
1	5.499E-06
2	4.906E-06
3	6.003E-06
4	2.792E-06
5	1.422E-05
6	8.880E-06
7	6.185E-06
8	3.397E-06
9	1.857E-05
10	7.667E-06

Table 6.2 Calculated failure probabilities, for the 10 mode case for Williams' toggle frame, using simulation data and the RS/FOSM method.

	Simulation Histogram (10)	Simulation Histogram (10/3)*	Response Surface (10)	Response Surface (10/3)*
$\lambda_{frac}$	$p_f$	$p_f$	$p_f$	$p_f$
0.952	0.000400	0.000300	0.000396	0.000396
0.968	0.015400	0.014700	0.013584	0.013585
0.984	0.148900	0.133000	0.138119	0.137459
0.992	0.308900	0.283300	0.293650	0.293620
1.000	0.526600	0.494100	0.500065	0.500003
1.008	0.728000	0.699700	0.704518	0.704483
1.016	0.869200	0.854000	0.858316	0.857534
1.024	0.953000	0.943500	0.944813	0.944788
1.032	0.985900	0.981600	0.982945	0.982933
1.040	0.995800	0.995300	0.995809	0.995807
1.048	0.998900	0.998600	0.999182	0.999182
1.056	0.999900	0.999900	0.999873	0.999873
1.064	1.000000	1.000000	0.999984	0.999984

\* Results using the three most dominant imperfection modes, and the same variances as if all 10 imperfection modes were included in the analysis.

Table 6.3 RS/FOSM results for the 10 mode case for Williams' toggle frame, with  $\lambda_{frac}$  equal to 0.968.

$a_i^*$	iter. #1	iter. #2	iter. #3	iter. #4	quadratic
1	0.392E-02	0.398E-02	0.403E-02	0.404E-02	0.404E-02
2	0.206E-07	-0.161E-07	0.263E-07	0.839E-08	0.919E-07
3	0.298E-07	-0.588E-07	-0.217E-06	-0.383E-06	-0.345E-06
4	0.697E-07	-0.135E-07	-0.143E-06	-0.656E-07	-0.412E-07
5	0.361E-02	0.375E-02	0.379E-02	0.381E-02	0.381E-02
6	0.258E-07	0.200E-07	-0.846E-07	-0.123E-07	-0.291E-07
7	-0.181E-07	0.483E-07	-0.144E-06	-0.251E-06	-0.228E-06
8	-0.172E-07	0.186E-07	-0.236E-07	-0.738E-08	0.195E-07
9	-0.385E-02	-0.398E-02	-0.403E-02	-0.404E-02	-0.404E-02
10	0.152E-07	-0.376E-07	0.416E-07	0.778E-08	-0.308E-07
$\beta$	2.124	2.174	2.200	2.207	2.209

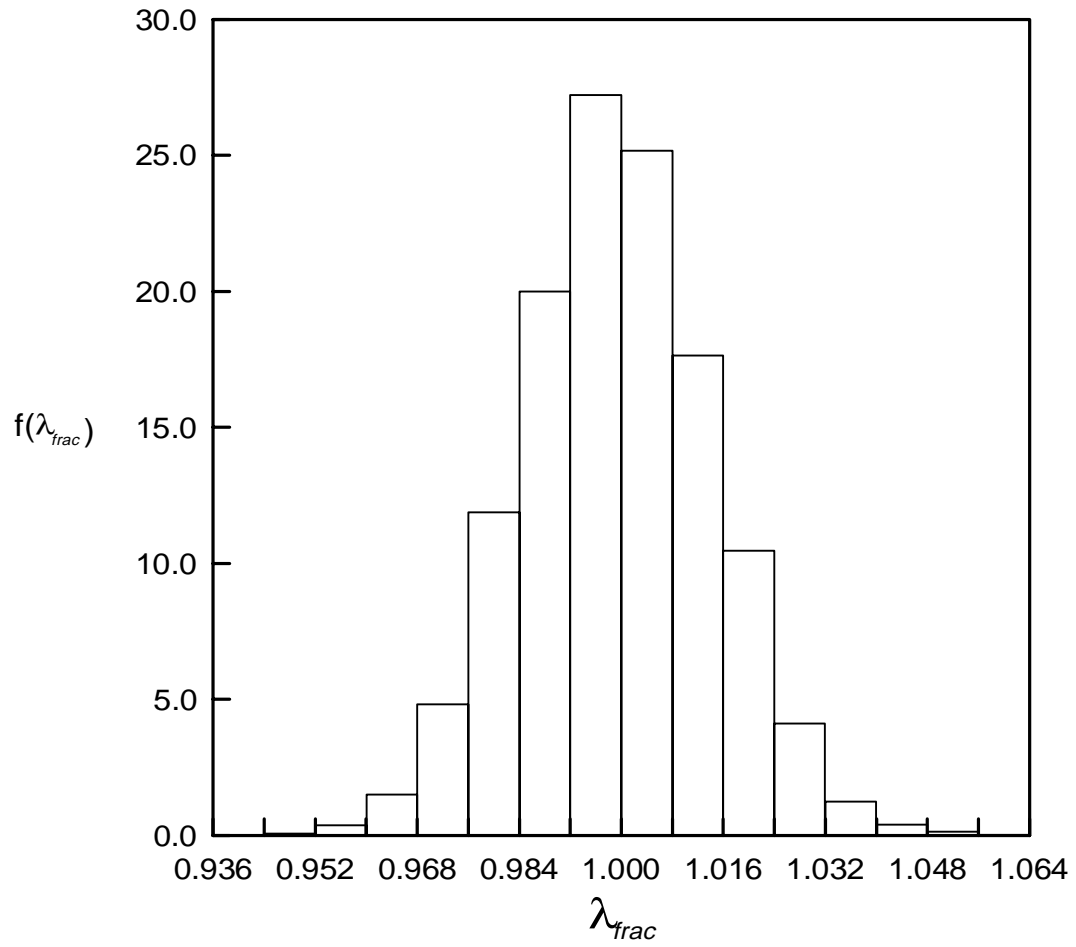


Figure 6.3 Frequency density diagram for the full 10 mode simulation for Williams' toggle frame.

to calculate the failure probabilities corresponding to the values of  $\lambda_{frac}$  found in the first column of Table 6.2. The resulting failure probabilities are given in the second column of Table 6.2. The results from the RS/FOSM method are comparable to those from the simulation. The maximum percent difference is approximately 12 percent and occurs at a value of  $\lambda_{frac}$  equal to 0.968. The cumulative distribution function using the simulation data, and the response surface data are both plotted in Fig. 6.4.

The fractional factorial design used above reduced the number of numerical experiments significantly, but the CPU time required to complete the analysis was still large. To further reduce the number of numerical experiments, a screening experiment was run to determine which imperfection modes had the most significant effect on the critical load. The significance of each imperfection mode was determined by using the hypothesis test presented in Section 5.5. The value of  $t_0$  for each imperfection mode is given in Table 6.4. The values of  $t_0$  are compared to the tabulated value of the students t-distribution at a 95 percent level of confidence. The tabulated value for this example is

$$t_{5\%/2, (128-11)} = 1.658 \quad (6.20)$$

Comparing the values of  $t_0$  with the tabulated value of 1.658 reveals that only the first, fifth, and ninth modes have a significant effect on the critical load. This information can also be obtained from Table 6.3 by noticing that for all but the first, fifth, and ninth modes, the most probable modal imperfections are nearly zero for each iteration. The RS/FOSM method was then used with only the three dominant imperfection modes, but the modal variances remained the same as if all 10 modes were included in the analysis. The new results from the RS/FOSM analysis are given in the fifth column of Table 6.2. The results using the three most influential mode shapes are very close to the RS/FOSM results using all 10 modes, and are comparable to the simulation results.

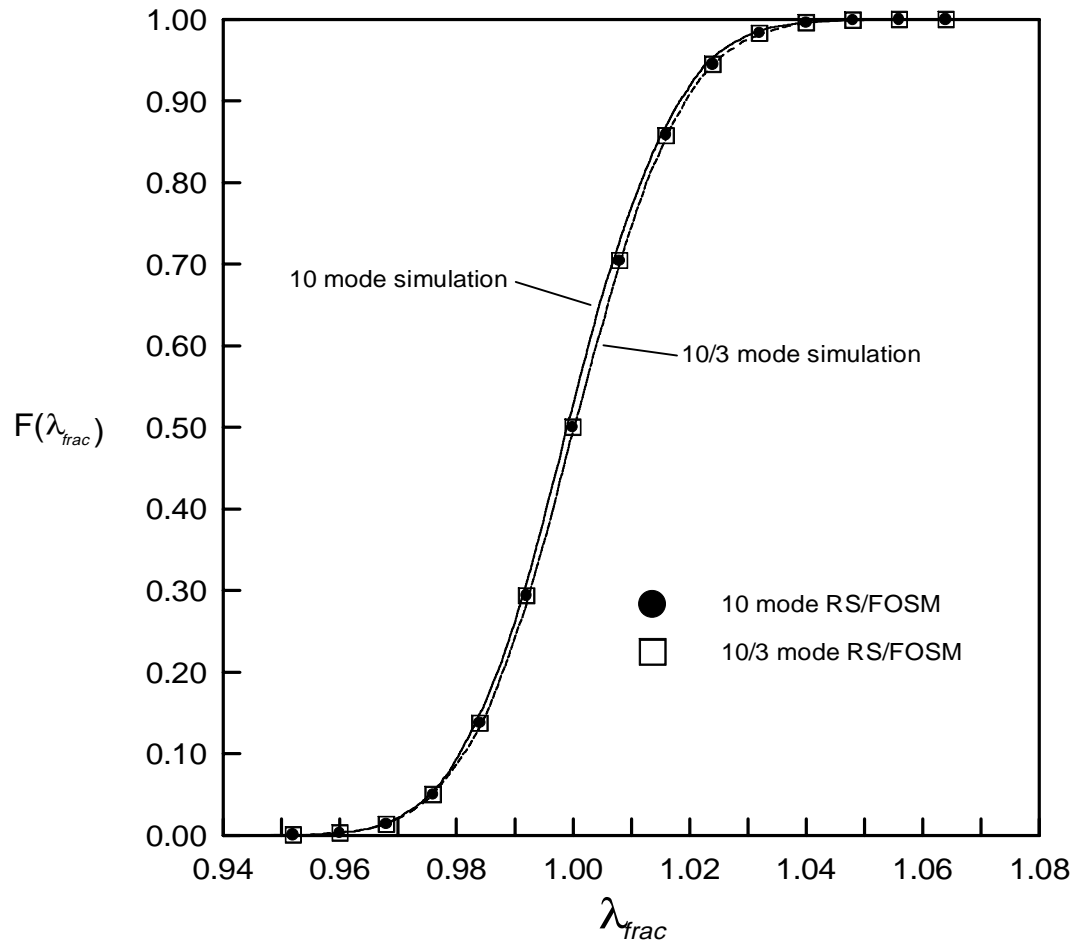


Figure 6.4 Cumulative distribution functions, for the 10 mode case, for Williams' toggle frame.

Table 6.4 Values of  $t_0$  for the 10 modal imperfection amplitudes for Williams' toggle frame.

Mode No.	$t_0$
1	-182.030
2	-1.015E-03
3	-1.324E-03
4	-4.542E-03
5	-104.038
6	-9.444E-04
7	7.936E-04
8	1.020E-03
9	97.345
10	-6.000E-04

NOTE: All values of  $t_0$  are compared to the tabulated value of  $t_{5\%/2,(128-11)} = 1.658$

A second simulation was run to examine the effects of using only three of the 10 imperfection modes. This simulation was run with only the three dominant modal imperfections as random variables. As in the second RS/FOSM analysis, the modal variances remained the same as if all 10 modes were included in the analysis. The resulting distribution of the imperfect critical load is also shown in the form of a frequency density diagram (Fig. 6.5). Using the frequency density diagram, the failure probabilities are calculated and tabulated in the third column of Table 6.2. Comparison of the 10 mode simulation data and the 3 mode simulation data shows that the seven non-dominant modes do have a small impact on the calculated failure probabilities. The results from the three mode simulation and both RS/FOSM analyses are all very close to each other indicating that the RS/FOSM method basically ignores the seven non-dominant imperfection modes when calculating the probability of failure. The cumulative distribution function for the simulation data is plotted in Fig. 6.4 along with the full 10 mode simulation data and the results from the RS/FOSM method.

### **6.3.1.2 Case 2: 6 mode imperfection**

The second case for Williams' toggle frame uses the first six of the linear buckling modes, shown in Figs. 6.1 and 6.2, to model the imperfection. As with the first case, the modal variances are found using the procedure presented in Section 6.1 and the maximum allowable variance from Eq. 6.18. The resulting modal variances are shown in Table 6.5, and are in general larger than the variances from the 10 mode analysis (Table 6.1). The reason for this is that the same maximum allowable variance is now spread over fewer modes which results in higher modal variances. The RS/FOSM method was again used to find the failure probabilities for the values of  $\lambda_{frac}$  from the first column of Table 6.6. The required number of numerical experiments was reduced from the required  $2^6 = 64$  to



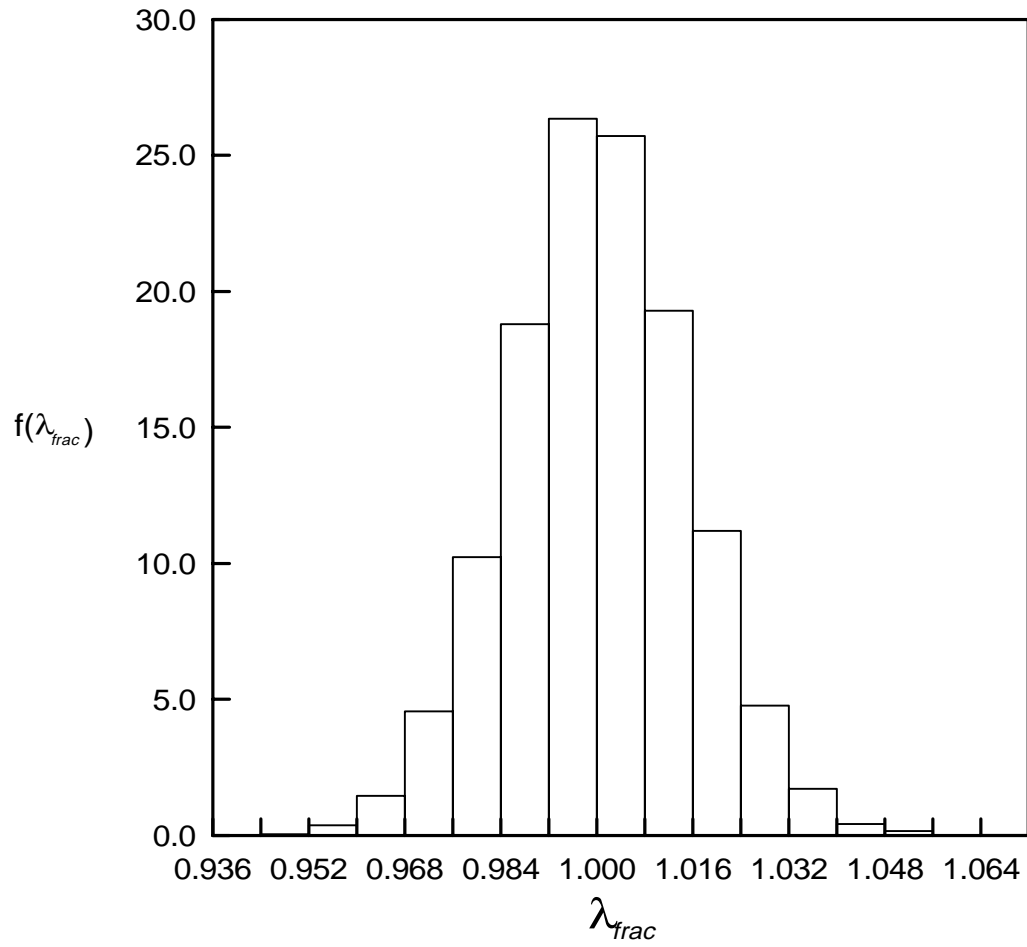


Figure 6.5 Frequency density diagram for the 10/3 mode simulation data for Williams' toggle frame.

Table 6.5 Modal variances for the 6 mode case for Williams' toggle frame.

Mode No.	Modal Variance, $\sigma_{a_i}^2$
1	1.486E-05
2	1.366E-05
3	8.798E-06
4	5.060E-06
5	2.039E-05
6	1.256E-05

Table 6.6 Calculated failure probabilities, for the 6 mode case for Williams' toggle frame, using simulation data and the RS/FOSM method.

	Simulation Histogram (6) $p_f$	Simulation Histogram (6/2)* $p_f$	Response Surface (6) $p_f$	Response Surface (6/2)* $p_f$
$\lambda_{frac}$				
0.930	0.000200	0.000300	0.000166	0.000166
0.940	0.001400	0.001200	0.001167	0.001169
0.950	0.007900	0.007100	0.006011	0.006014
0.970	0.081800	0.067200	0.069451	0.069472
0.980	0.185200	0.160300	0.163189	0.164005
0.990	0.338900	0.314700	0.313737	0.313789
1.000	0.525400	0.495400	0.499944	0.500019
1.010	0.709600	0.679100	0.683549	0.683590
1.020	0.844800	0.829000	0.828507	0.828569
1.030	0.932200	0.924400	0.921079	0.921122
1.040	0.972500	0.972500	0.969284	0.969297
1.050	0.992000	0.990700	0.989894	0.989897
1.060	0.997600	0.997400	0.997186	0.997187
1.070	0.999900	0.999300	0.999335	0.999336
1.080	1.000000	0.999900	0.999867	0.999867

\* Results using the two most dominant imperfection modes, and the same variances as if all six imperfection modes were included in the analysis.

$2^{6-1} = 32$  experiments by using a fractional factorial design. The predicted values of the most probable modal imperfections are given in Table 6.7 for each iteration and a value of  $\lambda_{frac}$  equal to 0.95. The predicted values of the reliability index for each iteration are also shown in Table 6.7. The resulting failure probabilities, for all of the values of  $\lambda_{frac}$ , are shown in the fourth column of Table 6.6.

A 10,000 data point simulation was run to verify the results from the RS/FOSM method. As for the previous simulations, the modal imperfection amplitudes were treated as normally distributed random numbers with variances as given in Table 6.5. A frequency density diagram showing the distribution of the imperfect critical load is given in Fig. 6.6. The frequency density diagram was used to calculate the failure probabilities found in the second column of Table 6.6. As with the first case, the values from the RS/FOSM analysis and the simulation are comparable but for small failure probabilities the percent difference is very high with a maximum of approximately 24 percent at a value of  $\lambda_{frac}$  equal to 0.95. The results from the RS/FOSM and the simulation are plotted in the form of a cumulative distribution function in Fig. 6.7.

The number of numerical experiments was further reduced by noting, from Table 6.4, that the first and fifth modes are the most dominant of the first six modal imperfections. The RS/FOSM method was again used to calculate the failure probabilities corresponding to the values of  $\lambda_{frac}$  given in Table 6.6. The modal variances are the same variances used for the RS/FOSM analysis using all six modes. The resulting failure probabilities are shown in the last column of Table 6.6. The results using only the two dominant mode shapes are very similar to the results for the RS/FOSM method using all six modes. Once again, the results do not compare well with the results from the full six mode numerical simulation.

Table 6.7 RS/FOSM results for the 6 mode case for Williams' toggle frame, with  $\lambda_{frac}$  equal to 0.95.

$a_i^*$	iter. #1	iter. #2	iter. #3	iter. #4	quadratic
1	0.849E-02	0.884E-02	0.889E-02	0.890E-02	0.891E-02
2	0.911E-07	0.578E-07	0.350E-07	0.115E-07	0.668E-06
3	-0.872E-07	0.122E-06	-0.139E-06	0.218E-06	0.278E-06
4	-0.234E-07	0.360E-06	-0.501E-06	0.679E-06	0.730E-06
5	0.412E-02	0.439E-02	0.441E-02	0.442E-02	0.442E-02
6	0.895E-07	0.560E-07	0.329E-07	0.941E-08	-0.266E-06
$\beta$	2.386	2.491	2.506	2.510	2.512

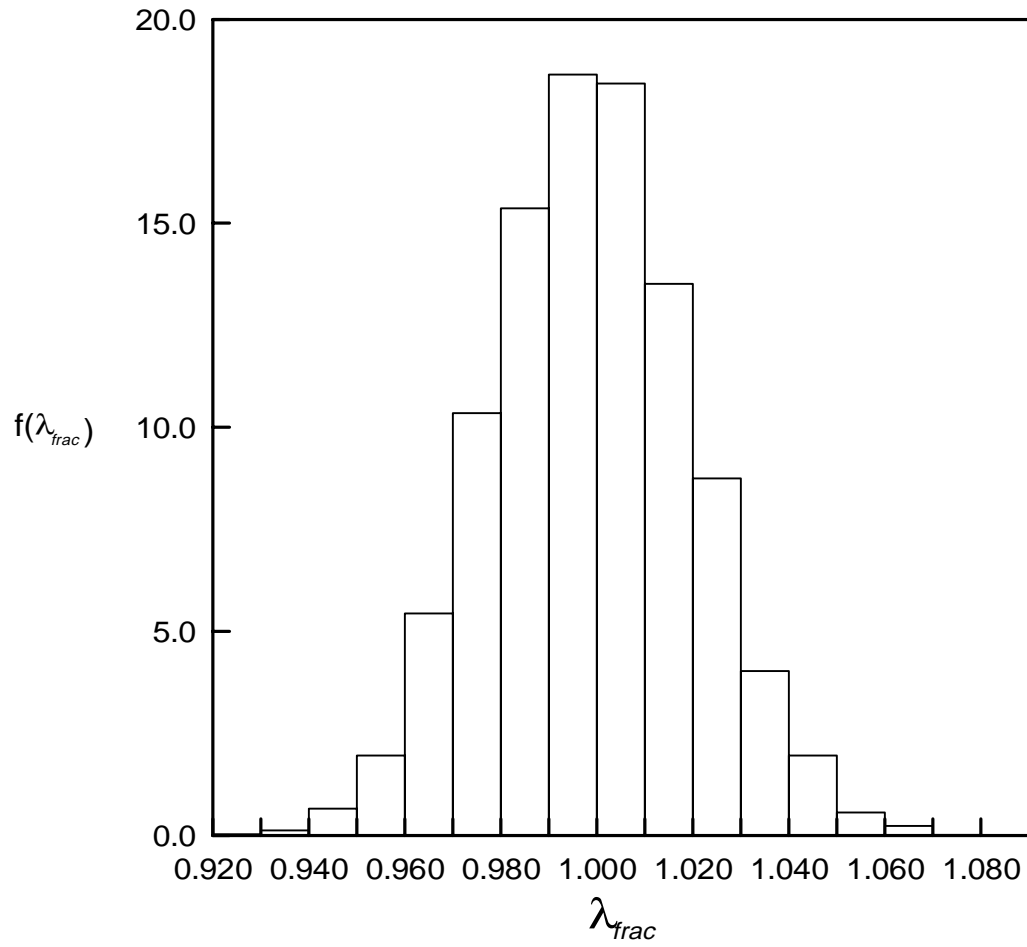


Figure 6.6 Frequency density diagram for the 6 mode simulation for Williams' toggle frame.

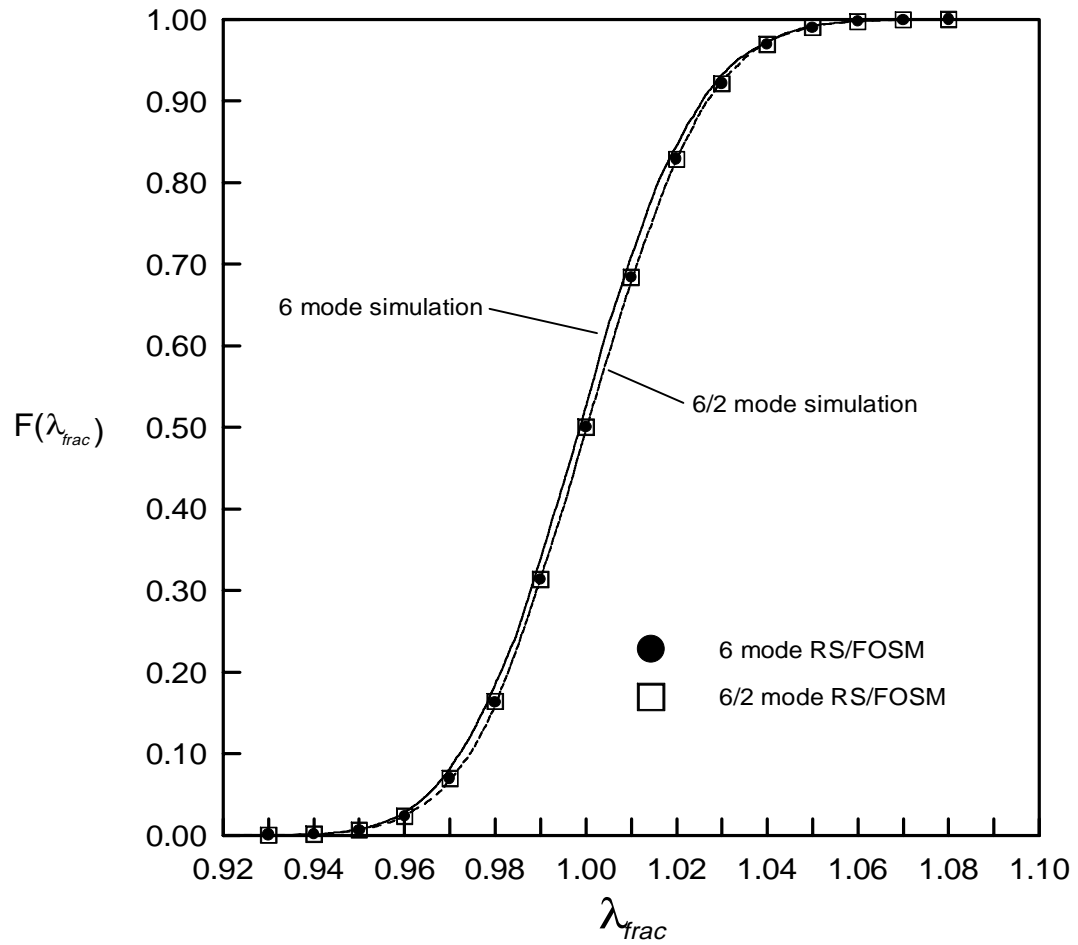


Figure 6.7 Cumulative distribution functions for the 6 mode case for Williams' toggle frame.

A second simulation was run using only the two dominant imperfection modes as random variables. The variances for the two dominant imperfection modes remain the same as in the full six mode simulation. The distribution of the imperfect critical load is given by the frequency density diagram (Fig. 6.8). The failure probabilities were calculated using the frequency density diagram, and are tabulated in the third column of Table 6.6. The results from both the RS/FOSM method with six modes and the two most dominant modes are closer to the results from the two mode simulation than for the full six mode simulation. As in the 10 mode case, the RS/FOSM analysis essentially ignores the non-dominant imperfection modes. The cumulative distribution for the two mode simulation data is plotted in Fig. 6.7 along with the six mode simulation data and the RS/FOSM results.

### 6.3.2 Example 2: Star-Shaped Cap

Analysis of the perfect 24-member hexagonal star-shaped cap was presented in Chapter 4. The structure was modeled using eight elements per member for all members except those that form the base of the hexagon, and those six members were discretized using only two elements per member. The total number of members used in the analysis was 156 and the total number of nodes was 145. For the imperfect analysis, all translational degrees of freedom were allowed to be imperfect, which resulted in a total of  $N_I = 417$  imperfect degrees of freedom. The perfect star-shaped cap was found to become unstable at a limit point where the load multiplier,  $(\lambda_{cr})_{perf}$ , was equal to 0.55348. The corresponding critical load was equal to 553.48 pounds. The imperfection shape for the structure was taken to be a combination of the first 20 linear buckling mode shapes. The maximum allowable imperfection,  $\Delta_{max}$ , anywhere on the structure, was limited to four millimeters or 0.4 centimeters. The maximum allowable variance at any



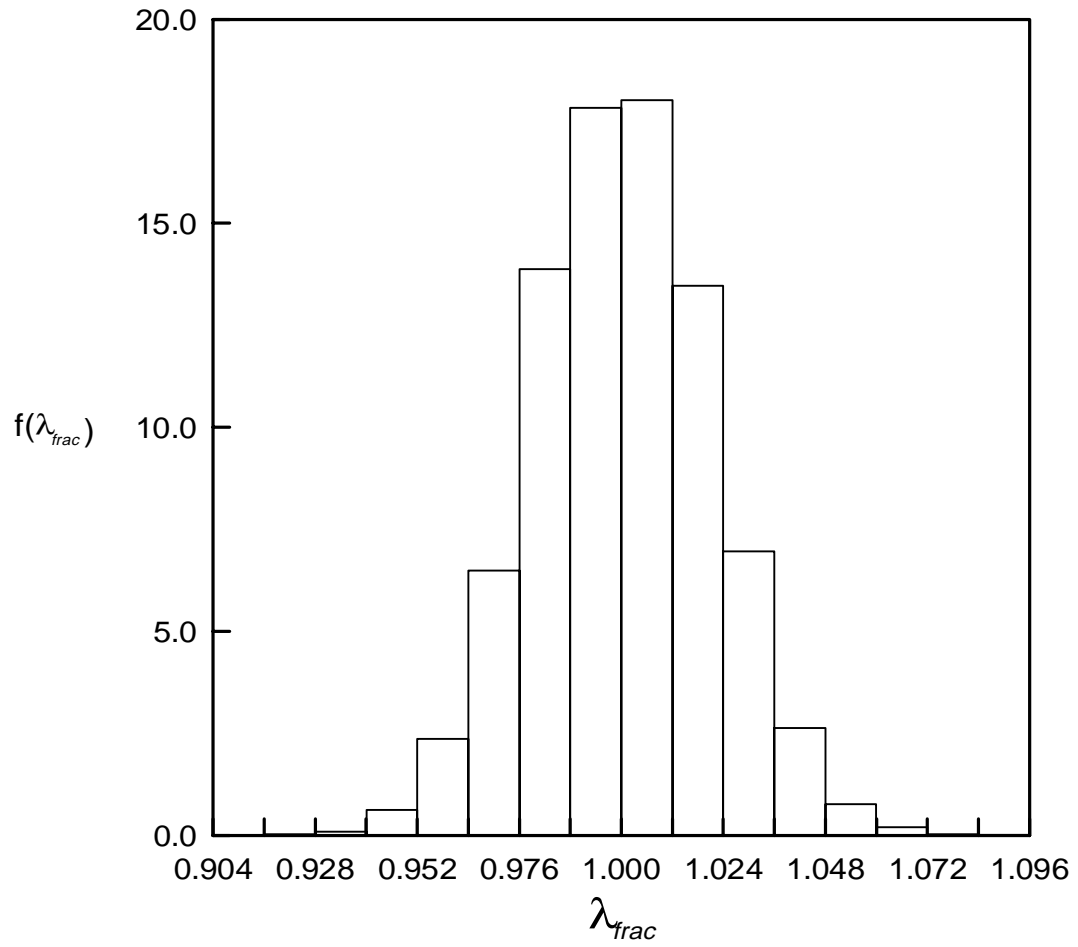


Figure 6.8 Frequency density diagram for the 6/2 mode simulation for Williams' toggle frame.

point on the structure was calculated using Eq. 6.9 and  $s_{max}$  equal to three. The resulting allowable variance is

$$\sigma_{\Delta_k}^2 = \left( \frac{\Delta_{max}}{s_{max}} \right)^2 = \left( \frac{0.4 \text{ cm}}{3} \right)^2 = 1.778 \times 10^{-2} \quad (6.21)$$

As mentioned above, the imperfection is modeled by using the first 20 linear buckling modes for the structure. The modal variances were found using the least-squares technique presented in Section 6.1 and the maximum allowable variance from Eq. 6.21. The variances for each imperfection mode are shown in Table 6.8. The next step was to run a RS/FOSM analysis, but the analysis could not be completed because, for such a large problem, the number of required numerical experiments was too high. A screening experiment was run to reduce the total number of imperfection modes included in the analysis. Because of the large number of experiments involved, the screening procedure using the hypothesis test presented in Section 5.5 could not be used. Instead, the direction cosines

$$\alpha_i = \frac{\frac{\partial g}{\partial a_i}}{\sqrt{\sum_{i=1}^n \left( \frac{\partial g}{\partial a_i} \right)^2}} \sigma_{a_i} \quad (6.22)$$

were used to examine the effects of each imperfection mode on the perfect structure. The partial derivatives were calculated using central differences:

$$\frac{\partial g}{\partial a_i} = \frac{g(a_i + \frac{h}{2}) - g(a_i - \frac{h}{2})}{h} \quad (6.23)$$

where  $h$  is equal to  $1.1\sigma_{a_i}$  and  $g$  is the performance function

$$g = \frac{(\lambda_{cr})_{imp}}{(\lambda_{cr})_{perf}} - 1 \quad (6.24)$$

The resulting direction cosines were then normalized with respect to the largest direction

Table 6.8 Modal variances for the 20 mode analysis for the shallow reticulated cap.

Mode No.	Modal Variance, $\sigma_{a_i}^2$
1	2.576E-03
2	3.658E-03
3	3.799E-03
4	2.744E-03
5	2.159E-03
6	2.832E-03
7	1.452E-03
8	3.894E-03
9	4.342E-03
10	1.070E-03
11	1.385E-03
12	6.642E-04
13	1.080E-03
14	4.072E-03
15	4.579E-03
16	6.418E-04
17	1.336E-03
18	1.419E-03
19	6.091E-03
20	6.848E-03

cosine and used to rank the modal imperfections. The modal rankings and corresponding direction cosines,  $\alpha_i$ , are given in Table 6.9.

Using the 10 most influential imperfection modes from Table 6.9, a RS/FOSM analysis was run to predict the failure probabilities for the values of  $\lambda_{frac}$  given in the first column of Table 6.10. A fractional factorial design was used to reduce the number of required experiments to  $2^{10-3} = 128$ . The value of  $\delta_\beta$  used in the analysis was 0.1, due to the large amount of CPU time required for the analysis. Predicted values for the most probable modal amplitudes,  $a_i^*$ , and the reliability index,  $\beta$ , are shown in Table 6.11 for  $\lambda_{frac}$  equal to 0.94. The failure probabilities for all of the values of  $\lambda_{frac}$  are shown in the fourth column of Table 6.10.

A 5,000 data point simulation was run to verify the results from the RS/FOSM analysis. The simulation treated all 20 modal imperfection amplitudes as random variables with variances as shown in Table 6.8. The distribution of the imperfect critical load is shown using a frequency density diagram (Fig. 6.9). The calculated failure probabilities are given in the second column of Table 6.10. The results from the simulation and the RS/FOSM analysis are comparable, but for small failure probabilities the percent difference is high with a maximum of approximately 36 percent at  $\lambda_{frac}$  equal to 0.88. The results from the simulation and the RS/FOSM analysis are used to plot cumulative distribution functions which are shown in Fig. 6.10.

A second 5,000 data point simulation was run to examine the effects of using only 10 of the 20 imperfection modes. In this simulation, only the 10 most dominant imperfection modes were used in the simulation, and the modal imperfection amplitudes were treated as random variables with the same variance (Table 6.8) as if all 20 modes were used in the analysis. The results of the simulation are presented in the form of a frequency density diagram which is shown in Fig. 6.11. The simulation data was then used

Table 6.9 Modal ranking and direction cosines for the 20 modal imperfection amplitudes for the shallow reticulated cap.

Mode No.	$\alpha_i$
1	1.000000
13	0.179522
4	0.063373
3	0.037874
2	0.037078
8	0.014320
9	0.014121
5	0.010386
7	0.010312
6	0.010250
12	0.006755
11	0.006691
10	0.006483
15	0.005256
14	0.005100
19	0.005049
20	0.004735
16	0.003211
17	0.003112
18	0.003092

Table 6.10 Calculated failure probabilities, for the 20 mode analysis for the shallow reticulated cap with a 4 mm imperfection, using simulation data and the RS/FOSM method.

	Simulation Histogram (20)	Simulation Histogram (20/10)*	Response Surface (20/10)*	Response Surface (20/2)**
$\lambda_{frac}$	$P_f$	$P_f$	$P_f$	$P_f$
0.88	0.018800	0.019200	0.011993	0.011938
0.94	0.185000	0.185800	0.141951	0.139019
1.00	0.587000	0.586200	0.500881	0.500910
1.06	0.891200	0.890200	0.849521	0.845737
1.12	0.984400	0.984800	0.975760	0.975864

\* Results using the 10 most dominant imperfection modes, and the same variances as if all 20 imperfection modes were included in the analysis.

\*\* Results using the two most dominant imperfection modes, and the same variances as if all 20 imperfection modes were included in the analysis.

Table 6.11 RS/FOSM results for the 10 mode analysis for the shallow reticulated cap,  
with  $\lambda_{frac}$  equal to 0.94.

$a_i^*$	iter. #1	iter. #2	quadratic
1	-0.450D-01	-0.463D-01	-0.533D-01
13	0.220D-05	0.244D-05	-0.226D-04
4	0.472D-04	0.504D-04	0.606D-04
3	0.201D-02	0.210D-02	0.239D-02
2	-0.339D-05	-0.369D-05	-0.564D-05
8	-0.248D-04	-0.245D-04	-0.249D-04
9	0.624D-05	0.637D-05	0.392D-07
5	0.584D-07	0.215D-06	-0.335D-04
7	-0.112D-04	-0.115D-04	-0.198D-04
6	-0.562D-02	-0.590D-02	-0.679D-02
$\beta$	0.905	0.931	1.072

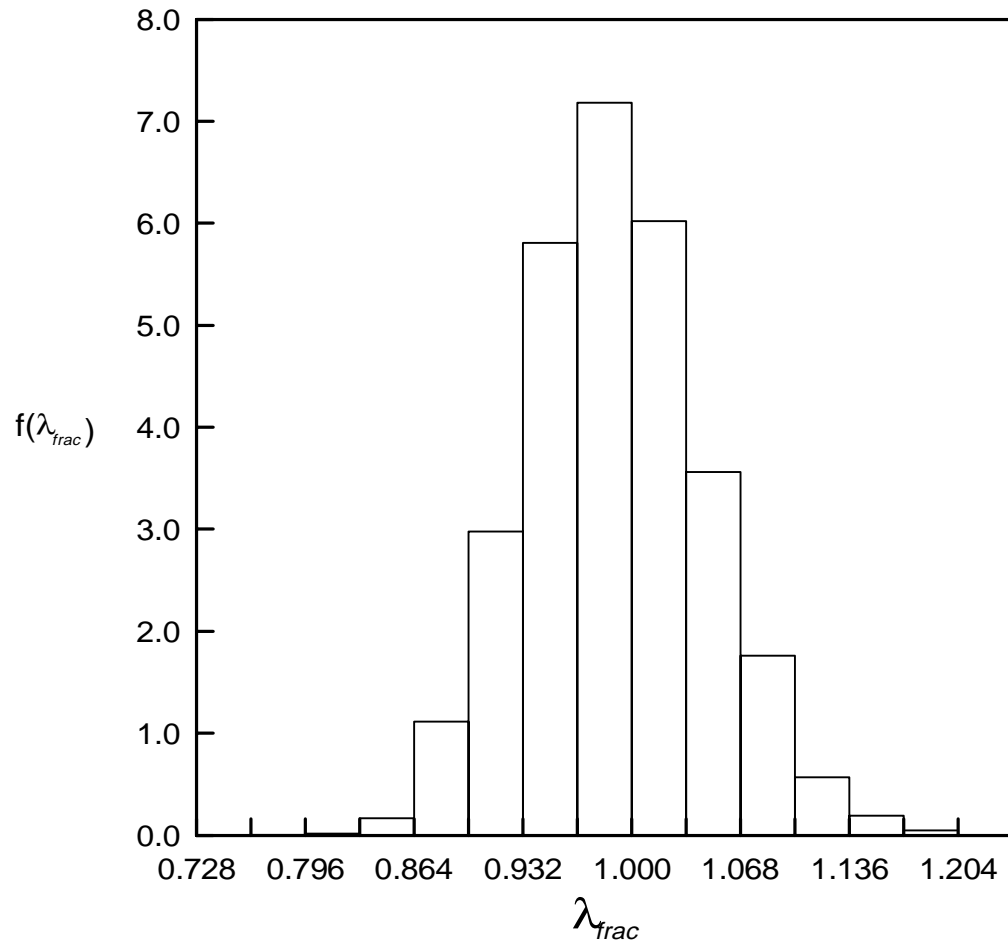


Figure 6.9 Frequency density diagram for the 20 mode simulation for the shallow reticulated cap.



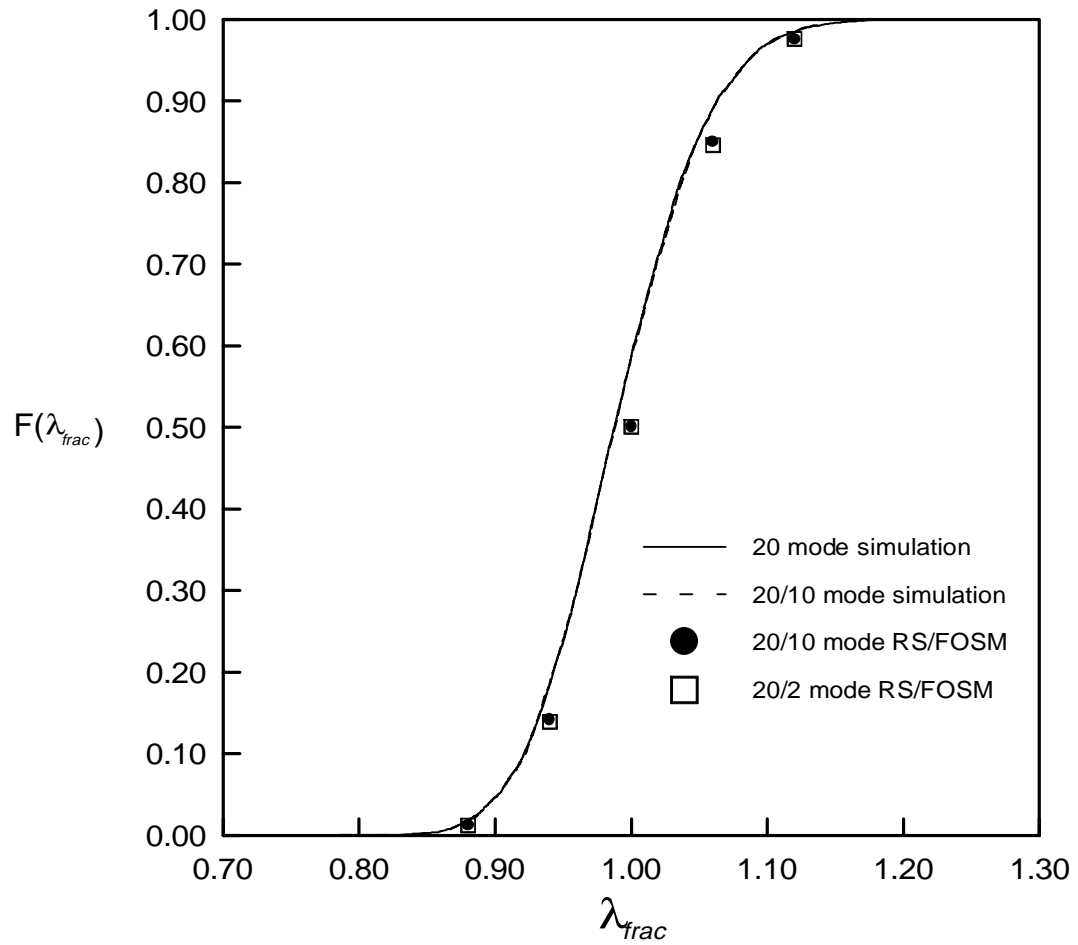


Figure 6.10 Cumulative distribution functions for the shallow reticulated cap.

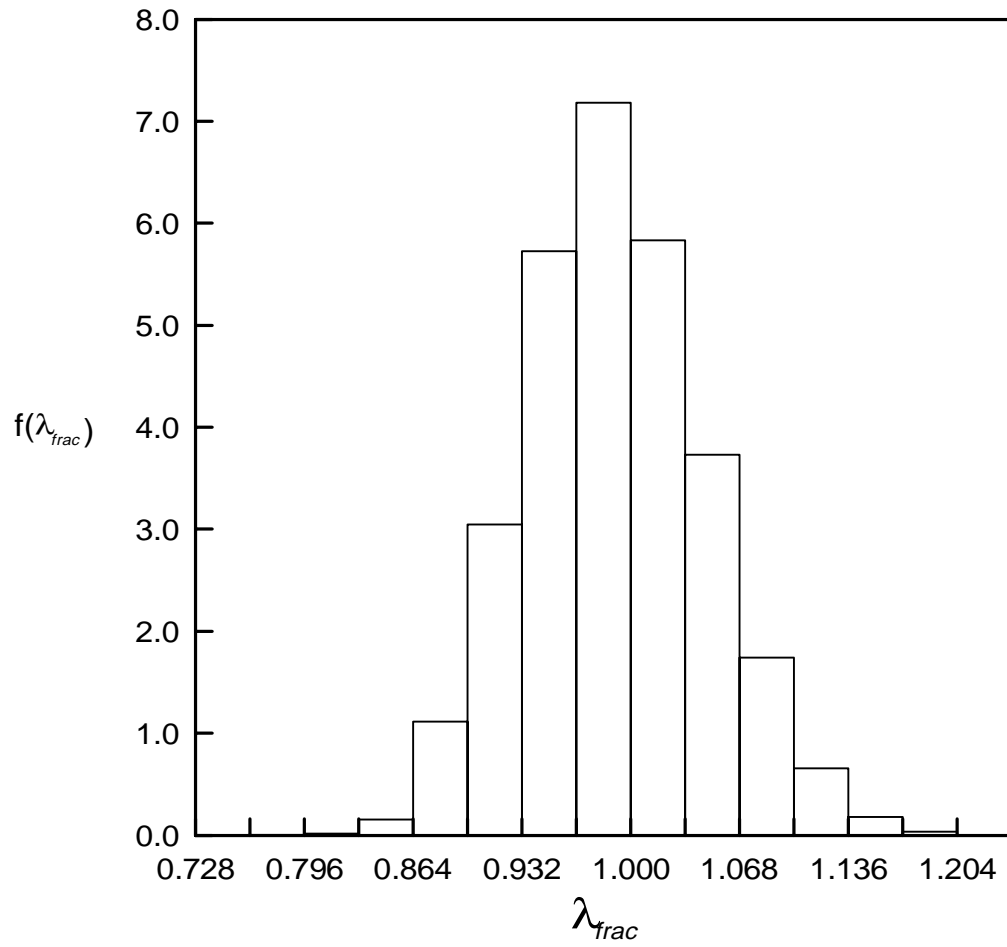


Figure 6.11 Frequency density diagram for the 10 mode simulation for the shallow reticulated cap.

to calculate the failure probabilities for the given values of  $\lambda_{frac}$ . The calculated failure probabilities are given in the third column of Table 6.10. The results from the 10 mode simulation compare well with the results from the full 20 mode simulation, indicating that the 10 non-dominant imperfection modes do not contribute much to the calculation of the failure probabilities. Once again, results from the 10 mode simulation and the 10 mode RS/FOSM analysis are comparable, but a large percent difference is found for the smaller failure probabilities. Results from the 10 mode simulation are plotted in the form of a cumulative distribution function in Fig. 6.10.

Further examination of the modal sensitivities (Table 6.9) reveals that the first and thirteenth modes are by far the most dominant imperfection modes. A RS/FOSM analysis was run using only the two most dominant imperfection modes with the same variances (Table 6.8) as if all 20 modes were included in the analysis. The failure probabilities for the given values of  $\lambda_{frac}$  are included in the fifth column of Table 6.10. The results from the two mode RS/FOSM analysis compare well with the results from the 10 mode RS/FOSM analysis, but very poorly with the simulation results. This indicates that the RS/FOSM is basically ignoring all but the two most dominant imperfection modes when calculating the probability of failure.

## **CHAPTER 7**

### **CONCLUSIONS AND FURTHER RESEARCH**

Probabilistic stability analysis of structures with random initial geometric imperfections is an interesting topic that has drawn the attention of many investigators over the years. The problem of approximating or simulating initial geometric imperfections is a relatively new field of research. In the past, imperfection patterns for a structure were developed from available imperfection data from similar structures. With the increasing use of lightweight reticulated structures, a method for approximating the initial imperfections must be available for structures where there is no previous imperfection data. Once an appropriate initial imperfection pattern is determined, an efficient technique must be used to determine the probability of failure for the structure. A method for approximating the initial geometric imperfections and calculating the probability of failure for a structure was presented in Chapter 6. This method produces acceptable imperfection patterns and is relatively efficient in calculating the probability of failure, but the method has several undesirable features which are discussed below.

#### **7.1 CONCLUSIONS**

A method for modeling initial geometric imperfections was presented in Chapter 6. The major problem with the proposed method is determining which or how many of the linear buckling modes should be used to model the imperfection. This problem leads to two other significant problems. The first problem is that the total variance, or total

variability, changes depending upon the number of linear buckling modes used to model the imperfection. Examining the modal variances for the 10 and six mode toggle frame analyses (Tabs. 6.1 and 6.5), reveals that the total variance is not the same. The second problem deals with the use of modal imperfections that do not have a significant influence on the critical load. As shown for the example problems in Chapter 6 (Tables 6.4 and 6.8), many of the imperfection modes have almost no influence on the critical load. When selecting the number of linear buckling modes to model the imperfection, enough modes should be chosen so that there will be more than one dominant imperfection mode. Using the method proposed in Chapter 6, it is difficult to determine how many modes should be used to guarantee that a certain number of dominant modes will be present in the analysis. Also, difficulties arise when trying to decide the number of dominant modes that should be included in the analysis.

Two different methods were used in Chapter 6 to determine the probability of failure, or the probability that the critical load will fall below a specified fraction of the perfect critical load. The first method was a numerical simulation that treated the modal imperfection amplitudes as random variables with zero mean and variances determined from the proposed imperfection modeling scheme. The results from the simulation are considered to be the most accurate, but the number of required simulations makes the method impractical for general use. The only real problems to be expected from the simulation deal with choosing enough simulations to obtain accurate results. Also, certain random number generators are more effective than others at generating values in the tails of the normal distribution. This can have a significant effect when calculating small failure probabilities.

The second method presented was the response surface/first-order second-moment (RS/FOSM) method. Results from the first-order second-moment (FOSM) method

depend on the accuracy of the direction cosines,  $\alpha_i$ , which are computed from the derivatives of the performance function with respect to the various random variables included in the analysis. The values of  $\alpha_i$ , along with the performance function, are used to predict the reliability index,  $\beta$ . If an explicit expression for the performance function is known, then the values of  $\alpha_i$  may be calculated accurately and the results from the FOSM method are very good. For the examples presented in Chapter 6, the response surface method was used to determine an approximation of the performance function over a specified region. The direction cosines,  $\alpha_i$ , and the reliability index,  $\beta$ , were then calculated using the approximate function. Therefore, the results from the RS/FOSM method depend entirely on the approximate performance function whose coefficients were estimated from a least squares analysis. Once again, the significance of the individual imperfection modes becomes a problem. The iterative results from the 6 and 10 mode analysis of Williams' toggle frame (Tables 6.3 and 6.7) and the 10 mode analysis for the shallow reticulated cap (Table 6.11) show that the predicted most probable imperfection amplitudes, for the non-dominant modes, change throughout the RS/FOSM analysis. In most cases the predicted values, even though small, do not even follow a trend throughout the iterative process. This indicates that the RS/FOSM method is not accurately predicting the most probable imperfection amplitudes for the non-dominant imperfection modes and that the derivatives of the performance function with respect to the non-dominant values of  $a_i$  are not accurate. Even though the values of  $\alpha_i$  for the non-dominant modes are small compared to the others, the predicted value of the reliability index can be affected enough to cause a significant difference in the predicted probability of failure. As noted in Chapter 6, small errors in the probability of failure will cause a significant percent difference for small failure probabilities.

The results from the example problems presented in Chapter 6 (Tables 6.2, 6.6, and 6.10) show that the RS/FOSM method produces reasonably good estimates of the failure probability when compared with the results from the numerical simulations. Even though the results of the RS/FOSM are good, they still may not be good enough to use for calculating a high accuracy estimate of the reliability of the structure. However, the results from the RS/FOSM method may be useful to a designer who only wants a quick estimate of the distribution of the critical load for a preliminary design.

Problems with the invariance of the total variability and lack of guidelines for choosing the number of imperfection modes implies that the calculated failure probabilities are only good for the imperfection being considered. In other words, changing the number of modes used to model the imperfection will change the probability of failure. This can be a serious drawback if a designer plans to compare the distribution of the critical load for two perspective designs that are similar in construction but may require a different number of imperfection modes to get the same number of dominant modes. In general, the method presented in Chapter 6 is not good for accurately comparing the probability of failure for two different structures.

Another drawback to the RS/FOSM method is that large numbers of random variables cannot be included in the analysis. The  $2^k$  factorial analysis used in the response surface method causes the required number of experiments to become large for moderate values of  $k$ . Even if a fractional factorial analysis,  $2^{k-m}$ , is used and  $k - m$  is larger than 10, the response surface method will still require at least 1,024 experiments for one iteration. For even larger values of  $k - m$  the number experiments approaches the number of runs required for a full numerical simulation. Since the results from a simulation are more accurate, use of the RS/FOSM method is no longer an option.

## 7.2 FURTHER RESEARCH

Future research in stability of structures with random geometric imperfections should examine new methods for modeling imperfections that will resolve the problem of invariance of the total variability. Also, some guidelines should be established for determining the number of imperfection modes used in the analysis and how many of these modes should be dominant modes.

A second topic for future work is the solution of problems where the limit state is a discontinuous function of the imperfection amplitudes. Such problems may occur for structures that become unstable at an unstable symmetric bifurcation point. For problems like these, the FOSM method will not work because of the discontinuity at the point on the failure surface where the imperfections are zero. Previous research dealt with this problem by assuming a non-zero mean imperfection which moves the analysis to a smooth continuous portion of the limit state. Further work should include different methods for determining a mean imperfection shape with an amplitude based on recommended fabrication tolerances. Also, methods other than the response surface method should be used to solve these problems since it is possible for the experimental region to straddle the discontinuity and produce erratic approximations of the performance function.

A third topic for future work would be the use of methods other than probabilistic methods. Since the failure probabilities from the RS/FOSM are not very accurate, and only problems with smooth performance functions can be solved, it is natural to wonder if probabilistic methods are even appropriate for this type of problem. As an alternative, fuzzy methods could be used to analyze the behavior of the critical load. In a fuzzy analysis, the modal imperfection amplitudes would be modeled using membership functions with shapes determined by an expert. The result of the fuzzy analysis would be a value for the failure possibility rather than the probability of failure. Use of fuzzy



methods would eliminate many of the difficulties that occur when trying to model, or approximate, the performance function in a FOSM analysis.

## REFERENCES

- ABAQUS (1987). *Theory Manual, ver. 4.6*. Hibbitt, Karlsson, and Sorensen, Providence, RI.
- ABAQUS (1988). *User's Manual, ver. 4.7*. Hibbitt, Karlsson, and Sorensen, Providence, RI.
- Amazigo, J.C. (1976). "Buckling of Stochastically Imperfect Structures." Buckling of Structures, IUTAM Symposium, June 17-24, 1974, Budiansky, B. (Ed.). Springer-Verlag, N.Y., 173-182.
- Ang, A. H-S., and Tang, W.H. (1975). *Probability Concepts in Engineering Planning and Design, Vol. I*. John Wiley and Sons, N.Y.
- Ang, A. H-S., and Tang, W.H. (1984). *Probability Concepts in Engineering Planning and Design, Vol. II*. John Wiley and Sons, N.Y.
- Arbocz, J., and Hol, J.M.A.M. (1991). "Collapse of Axially Compressed Cylindrical Shells with Random Imperfections." *AIAA J.*, Vol. 29, No. 12, 2247-2256.
- Bathe, K.J., and Bolourchi, S. (1979). "Large Displacement Analysis of Three-Dimensional Beam Structures." *Int. J. Num. Meth. Eng.*, Vol. 14, 961-986.
- Bathe, K.J., and Cimento, A.P. (1980). "Some Practical Procedures for the Solution of Nonlinear Finite Element Equations." *Comp. Meth. Appl. Mech. & Eng.*, Vol. 22, 59-85.
- Bathe, K.J. (1982). *Finite Element Procedures in Engineering Analysis*. Prentice-Hall, New Jersey.
- Ben-Haim, Y., and Elishakoff, I. (1990). *Convex Models of Uncertainty in Applied Mechanics*, Elsevier, Amsterdam.
- Bolotin, V.V. (1958). *Statistical Methods in the Nonlinear Theory of Elastic Shells*. NASA TTF-85, 1962.

- Blachut, J., and Galletly, G.D. (1990). "Buckling Strength of Imperfect Spherical Caps-Some Remarks." *AIAA J.*, Vol. 28, No. 7, 1317-1319.
- Bucher, C.G., and Borgund, U. (1990). "A Fast Efficient Response Surface Approach for Structural Reliability Problems." *Structural Safety*, Vol. 7, 57-66.
- Brendel, B., and Ramm, E. (1980). "Linear and Nonlinear Stability Analysis of Cylindrical Shells." *Comp. & Struct.*, Vol. 12, 549-558.
- Brenner, C.E., and Bucher, C. (1995). "A Contribution to the SFE-Based Reliability Assessment of Nonlinear Structures under Dynamic Loading." *Prob. Eng. Mech.*, Vol. 10, 265-273.
- Casciati, F., and Faravelli, L. (1991). *Fragility Analysis of Complex Structural Systems*. Research Studies Press, England
- Chryssanthopoulos, M.K., Baker, M.J., and Dowling, P.J. (1991a). "Statistical Analysis of Imperfections in Stiffened Cylinders." *J. Struct. Eng. Div.*, Vol. 117, No. 7, 1979-1997.
- Chryssanthopoulos, M.K., Baker, M.J., and Dowling, P.J. (1991b). "Imperfection Modeling for Buckling Analysis of Stiffened Cylinders." *J. Struct. Eng. Div.*, Vol. 117, No. 7, 1998-2017.
- Clarke, M.J., and Hancock, G.J. (1990). "A Study of Incremental-Iterative Strategies for Nonlinear Analysis." *Int. J. Num. Meth. Eng.*, Vol. 29, 1365-1391.
- Cook, R.D., Malkus, D.S., and Plesha, M.E. (1989). *Concepts and Applications of Finite Element Analysis*. John Wiley and Sons, New York.
- Crisfield, M.A. (1981). "A Fast Incremental/Iterative Solution Procedure that Handles Snap-Through." *Comp. & Struct.*, Vol. 13, 55-62.
- Crisfield, M.A. (1991a). *Nonlinear Finite Element Analysis of Solids and Structures, Vol. I*. John Wiley and Sons, England.
- Crisfield, M.A., and Shi, J. (1991b). "A Review of Solution Procedures and Path-Following Techniques in Relation to the Nonlinear Finite Element Analysis of Structures." *Nonlinear Computational Mechanics (State of the Art)*, Wriggers, P., and Wagner, W. (Eds.). Springer-Verlag, N.Y., 283-302.
- Crivelli, L.A. (1991). "A Total-Lagrangian Beam Element for Analysis of Nonlinear Space Structures." Ph.D. Dissertation, University of Colorado at Boulder.

- Davalos, J.F. (1989). "Geometrically Nonlinear Finite Element Analysis of a Glulam Timber Dome." Ph.D. Dissertation, Virginia Polytechnic Institute and State University.
- Dym, C.L., and Shames, I.H. (1973). *Solid Mechanics, A Variational Approach*. McGraw-Hill, New York.
- Elishakoff, I. (1979). "Buckling of a Stochastically Imperfect Finite Column on a Nonlinear Elastic Foundation, A Reliability Study." *J. Appl. Mech.*, Vol. 46, 411-416.
- Elishakoff, I., and Arbocz, J. (1982). "Reliability of Axially Compressed Cylindrical Shells with Random Imperfections." *Int. J. Solids Structures*, Vol. 18, No. 7, 563-585.
- Elishakoff, I., van Manen, S., Vermeulen, P.G., and Arbocz, J. (1987). "First-Order Second-Moment Analysis of the Buckling of Shells with Random Imperfections." *AIAA J.*, Vol. 25, No. 8, 1113-1117.
- El Naschie, M.S. (1990). *Stress, Stability, and Chaos in Structural Engineering: An Energy Approach*. McGraw-Hill, London.
- Faravelli, L. (1989). "Response-Surface Approach for Reliability Analysis." *J. Eng. Mech. Div.*, Vol. 115, No. 12, 2763-2781.
- Faravelli, L. (1992). "Structural Reliability via Response Surface." *Nonlinear Stochastic Mechanics: IUTAM Symposium, Turin, 1991*, Bellomo, N., and Casciati, F. (Eds.). Springer-Verlag, Berlin, 213-223.
- Fellipa, C.A. (1988). "Solution of Nonlinear Equations." *Finite Element Analysis for Engineering Design*, Reddy, J.N., Krishnamoorthy, C.S., and Seetharamu, K.N. (Eds.). Springer-Verlag, N.Y., Vol. 37, 274-309.
- Fellippa, C.A., and Crivelli, L.A. (1991). "A Congruential Formulation of Nonlinear Finite Elements." *Nonlinear Computational Mechanics (State of the Art)*, Wriggers, P., and Wagner, W. (Eds.). Springer-Verlag, N.Y., 283-302.
- Fertis, D.G. (1993). *Nonlinear Mechanics*. CRC Press, Florida.
- Fung, Y.C. (1965). *Foundations of Solid Mechanics*. Prentice-Hall, New Jersey.
- Galletly, G.D., and Blachut, J. (1991). "Buckling Design of Imperfect Welded Hemispherical Shells Subjected to External Pressure." *J. Mech. Eng. Sci.*, Vol. 205, No. C3, 175-188.

- Hartono, W., and Nishino, F. (1991). "Imperfection Behavior of Elastic Nonlinear Systems Illustrated by a Three-Degree-of-Freedom Model." *AIAA J.*, Vol. 29, No. 9, 1507-1514.
- Holzer, S.M., Plaut, R.H., Somers, A.E., and White, W.S. (1980). "Stability of Lattice Structures Under Combined Loads." *J. Eng. Mech. Div.*, Vol. 106, No. EM2, 289-305.
- Holzer, S.M. (1985). *Computer Analysis of Structures, Matrix Structural Analysis Structured Programming*. Elsevier, New York.
- Hughes, P.C. (1986). *Spacecraft Attitude Dynamics*. John Wiley and Sons, New York.
- Ibrahimbegovic, A., Frey, F., and Kozar, I. (1995). "Computational Aspects of Vector-Like Parametrization of Three-Dimensional Finite Rotations." *Int. J. Num. Meth. Eng.*, Vol. 38, 3653-3673.
- Ikeda, K., and Murota, K. (1990a). "Computation of Critical Initial Imperfection of Truss Structures." *J. Eng. Mech. Div.*, Vol. 116, No. 10, 2101-2117.
- Ikeda, K., and Murota, K. (1990b). "Critical Imperfection of Structures." *Int. J. Solids Structures*, Vol. 26, No. 8, 865-886.
- Ikeda, K., and Murota, K. (1991). "Random Initial Imperfections of Structures." *Int. J. Solids Structures*, Vol. 28, No. 8, 1003-1021.
- Ikeda, K., and Murota, K. (1993). "Statistics of Normally Distributed Initial Imperfections." *Int. J. Solids Structures*, Vol. 30, No. 18, 2445-2467.
- Ikeda, K., Murota, K., and Elishakoff, I. (1996). "Reliability of Structures Subject to Normally Distributed Initial Imperfections." *Comp. & Struct.*, Vol. 59, No. 3, 463-469.
- Janajreh, I.M. (1992). "An Efficient Technique for Structural Reliability with Applications." Ph.D. Dissertation, Virginia Polytechnic Institute and State University.
- Janajreh, I., Heller, R.A., and Thangjitham, S. (1994). "Safety Index Approach to Predicting the Storage Life of Rocket Motors." *J. Spacecraft and Rockets*, Vol. 31, No. 6, 1072-1078.
- Junkins, J.L., and Turner, J.D. (1986). *Optimal Spacecraft Rotational Maneuvers*. Elsevier, New York.

- Khuri, A.I., and Cornell, J.A. (1987). *Response Surfaces, Designs and Analyses*. Marcel Dekker, New York.
- Koiter, W.T. (1945). "On the Stability of Elastic Equilibrium." Thesis, Polytechnic Institute Delft, NASA TTF-10833, 1967.
- Liaw, D.G., and Yang, H.T.Y. (1991a). "Reliability of Initially Compressed Uncertain Laminated Plates in Supersonic Flow." *AIAA J.*, Vol. 29, No. 6, 952-960.
- Liaw, D.G., and Yang, H.T.Y. (1991b). "Reliability of Uncertain Laminated Shells Due to Buckling and Supersonic Flutter." *AIAA J.*, Vol. 29, No. 10, 1698-1708.
- Lindberg, H.E. (1988). "Random Imperfections for Dynamic Pulse Buckling." *J. Eng. Mech. Div.*, Vol. 114, No. 7, 1144-1165.
- Madsen, H.O., Krenk, S., and Lind, N.C. (1986). *Methods of Structural Safety*. Prentice-Hall, New Jersey.
- Meek, J.L., and Tan, H.S. (1984). "Geometrically Nonlinear Analysis of Space Frames by an Incremental Iterative Technique." *Comp. Meth. Appl. Mech. Eng.*, Vol. 47, 261-282.
- Meek, J.L., and Loganathan, S. (1989a). "Large Displacement Analysis of Space-Frame Structures." *Comp. Meth. Appl. Mech. & Eng.*, Vol. 72, 57-75.
- Meek, J.L., and Loganathan, S. (1989b). "Geometrically Nonlinear Behavior of Space-Frame Structures." *Comp. & Struct.*, Vol. 31(1), 35-45.
- Myers, R.H. (1971). *Response Surface Methodology*. Allyn and Bacon, Boston.
- Myers, R.H., and Montgomery, D.C. (1995). *Response Surface Methodology, Process and Product Optimization Using Designed Experiments*. John Wiley and Sons, N.Y.
- Montgomery, D.C. (1991). *Design and Analysis of Experiments*. John Wiley and Sons, N.Y.
- Morris, N.F. (1991). "Effect of Imperfections on Lattice Shells." *J. Struct. Eng. Div.*, Vol. 117, No. 6, 1796-1814.
- Murota, K., and Ikeda, K. (1991). "Critical Imperfection of Symmetric Structures." *SIAM J. Appl. Math.*, Vol. 51, No. 5, 1222-1254.

- Nishino, F., and Hartono, W. (1989). "Influential Mode of Imperfection on Carrying Capacity of Structures." *J. Eng. Mech. Div.*, Vol. 115, No. 10, 2150-2165.
- Novozhilov, V.V. (1953). *Foundations of the Nonlinear Theory of Elasticity*, [translated from the 1st (1948) Russian edition by F. Bagemihl, H. Komm, and W. Seidel]. Graylock Press, New York.
- Oran, C. (1973). "Tangent Stiffness in Space Frames." *J. Struct. Eng. Div.*, Vol. 99, No. ST6, 997-1001.
- Oran, C., and Kassimali, A. (1976). "Large Deformations of Framed Structures Under Static and Dynamic Loads." *Comp. & Struct.*, Vol. 6, 539-547.
- Rackwitz, R. (1976). "Practical Probabilistic Approach to Design." Bulletin 112, Comite European du Beton, Paris, France.
- Ramm, E. (1981). "Strategies for Tracing the Nonlinear Response Near Limit Points." *Nonlinear Finite Element Analysis in Structural Mechanics: Proceedings of the Europe-U.S. Workshop, Ruhr-Universitat Bochum, Germany, July 28-31, 1980*, Wunderlich, W., Stein, E., and Bathe, K.J. (Eds.). Springer-Verlag, N.Y., 63-89.
- Reddy, J.N. (1988). "Variational Formulations and Methods." *Finite Element Analysis for Engineering Design*, Reddy, J.N., Krishnamoorthy, C.S., and Seetharamu, K.N. (Eds.). Springer-Verlag, N.Y., Vol. 37, 16-40.
- Riks, E. (1972). "The Application of Newton's Methods to the Problem of Elastic Stability." *J. Appl. Mech.*, Vol. 39, 1060-1065.
- Riks, E. (1979). "An Incremental Approach to the Solution of Snapping and Buckling Problems." *Int. J. Solids Structures*, Vol. 15, 529-551.
- Roorda, J. (1972). "Concepts in Elastic Structural Stability." *Mechanics Today*, Nemat-Nasser, S. (Ed.), Vol. 1, 322-372.
- Simitses, G.J. (1986). "Buckling and Postbuckling of Imperfect Shells: A Review." *Appl. Mech. Rev.*, Vol. 39, No. 10, 1517-1524.
- Sturges, H.A. (1926). "The Choice of a Class Interval." *J. Am. Stat. Assoc.*, Vol. 21, 65-66.
- Thoft-Christensen, P. and Baker, M.J. (1982). *Structural Reliability Theory and Its Applications*. Springer-Verlag, New York.

- Watson, L.T., and Holzer, S.M. (1983). "Quadratic Convergence of Crisfield's Method." *Comp. & Struct.*, Vol. 17, 69-72.
- Wempner, G.A. (1971). "Discrete Approximations Related to Nonlinear Theories of Solids." *Int. J. Solids Structures*, Vol. 7, 1581-1599.
- Williams, F.W. (1964). "An Approach to the Non-linear Behavior of the Members of a Rigid Jointed Plane Framework with Finite Deflections." *Quart. J. Mech. Appl. Math.*, Vol. 17, 451-469.



## APPENDIX A

### FIRST VARIATION OF ROTATION AND DERIVATIVE OF ROTATION MATRICES

#### A.1 FIRST VARIATION OF THE ROTATION MATRIX

The rotation matrix for the three variable form of the Euler axis/angle parametrization is given in Chapter 3. In symbolic form, the rotation matrix is

$${}^2\mathbf{R} = \mathbf{I} + {}^2b_2 {}^2\mathbf{R}_{II} + {}^2b_3 {}^2\mathbf{R}_{III} \quad (\text{A.1})$$

where

$${}^2\mathbf{R}_{II} = \begin{bmatrix} 0 & -{}^2\phi_3 & {}^2\phi_2 \\ {}^2\phi_3 & 0 & -{}^2\phi_1 \\ -{}^2\phi_2 & {}^2\phi_1 & 0 \end{bmatrix} \quad (\text{A.2})$$

$${}^2\mathbf{R}_{III} = \begin{bmatrix} -({}^2\phi_2^2 + {}^2\phi_3^2) & {}^2\phi_1 {}^2\phi_2 & {}^2\phi_1 {}^2\phi_3 \\ {}^2\phi_1 {}^2\phi_2 & -({}^2\phi_1^2 + {}^2\phi_3^2) & {}^2\phi_2 {}^2\phi_3 \\ {}^2\phi_1 {}^2\phi_3 & {}^2\phi_2 {}^2\phi_3 & -({}^2\phi_1^2 + {}^2\phi_2^2) \end{bmatrix} \quad (\text{A.3})$$

and

$${}^2b_2 = -|{}^2\phi|^{-1} \sin|{}^2\phi| \quad (\text{A.4})$$

$${}^2b_3 = 2|{}^2\phi|^{-2} \sin^2 \frac{|{}^2\phi|}{2} \quad (\text{A.5})$$

A typical component,  ${}^2R_{ij}$ , of the rotation matrix is given by

$${}^2\mathbf{R}_{ij} = \mathbf{I} + {}^2b_2 {}^2\mathbf{R}_{II_{ij}} + {}^2b_3 {}^2\mathbf{R}_{III_{ij}} \quad (\text{A.6})$$

and is in general a function of all three rotation angles  ${}^2\phi_i$ .

The first variation of  ${}^2\mathbf{R}_{ij}$  is equal to

$$\begin{aligned} \delta({}^2\mathbf{R}_{ij}) &= \delta({}^2b_2) {}^2\mathbf{R}_{II_{ij}} + {}^2b_2 \delta({}^2\mathbf{R}_{II_{ij}}) \\ &\quad + \delta({}^2b_3) {}^2\mathbf{R}_{III_{ij}} + {}^2b_3 \delta({}^2\mathbf{R}_{III_{ij}}) \end{aligned} \quad (\text{A.7})$$

The terms  $\delta({}^2\mathbf{R}_{II_{ij}})$  and  $\delta({}^2\mathbf{R}_{III_{ij}})$  are equal to

$$\delta({}^2\mathbf{R}_{II_{ij}}) = \sum_{k=1}^3 \frac{\partial({}^2\mathbf{R}_{II_{ij}})}{\partial({}^2\phi_k)} \delta({}^2\phi_k) \quad (\text{A.8})$$

and

$$\delta({}^2\mathbf{R}_{III_{ij}}) = \sum_{k=1}^3 \frac{\partial({}^2\mathbf{R}_{III_{ij}})}{\partial({}^2\phi_k)} \delta({}^2\phi_k) \quad (\text{A.9})$$

Therefore, the first variation of each rotation component will in general have three terms.

To simplify future computations the first variations of  ${}^2\mathbf{R}_{II}$  and  ${}^2\mathbf{R}_{III}$  will be stored in the  $9 \times 1$  column vectors  $\delta({}^2\mathbf{R}_{II})$  and  $\delta({}^2\mathbf{R}_{III})$ . The expression for  $\delta({}^2\mathbf{R}_{II})$  is

$$\delta \left( \underset{9 \times 1}{{}^2\mathbf{R}_{II}} \right) = \underset{9 \times 3}{\mathbf{DR}_{II}} \delta \left( \underset{3 \times 1}{{}^2\phi} \right) \quad (\text{A.10})$$

where the matrix  $\mathbf{DR}_{II}$  is

$$\mathbf{DR}_{II} = \begin{bmatrix} 0 & 0 & 0 \\ 0 & 0 & -1 \\ 0 & 1 & 0 \\ 0 & 0 & 1 \\ 0 & 0 & 0 \\ -1 & 0 & 0 \\ 0 & -1 & 0 \\ 1 & 0 & 0 \\ 0 & 0 & 0 \end{bmatrix} \quad (\text{A.11})$$

The expression for  $\delta(^2\mathbf{\tilde{R}}_{III})$  is

$$\delta\left(^2\mathbf{\tilde{R}}_{III}\right) = \mathbf{DRIII} \delta\left(^2\boldsymbol{\phi}\right) \quad (\text{A.12})$$

and the matrix  $\mathbf{DRIII}$  is

$$\mathbf{DRIII} = \begin{bmatrix} 0 & -2^2\phi_1 & -2^2\phi_1 \\ ^2\phi_2 & ^2\phi_1 & 0 \\ ^2\phi_3 & 0 & ^2\phi_1 \\ ^2\phi_2 & ^2\phi_1 & 0 \\ -2^2\phi_1 & 0 & -2^2\phi_3 \\ 0 & ^2\phi_3 & ^2\phi_2 \\ ^2\phi_3 & 0 & ^2\phi_1 \\ 0 & ^2\phi_3 & ^2\phi_2 \\ -2^2\phi_1 & -2^2\phi_2 & 0 \end{bmatrix} \quad (\text{A.13})$$

The scalars  $^2b_2$  and  $^2b_3$  are also functions of all three rotation angles. Therefore, the first variation of each will result in three terms. The first variation of  $^2b_2$  is

$$\delta(^2b_2) = \sum_{k=1}^3 \frac{\partial(^2b_2)}{\partial(^2\phi_k)} \delta(^2\phi_k) \quad (\text{A.14})$$

where

$$\frac{\partial(^2b_2)}{\partial(^2\phi_k)} = \left(|^2\boldsymbol{\phi}|^{-2} \sin|^2\boldsymbol{\phi}| - |^2\boldsymbol{\phi}|^{-1} \cos|^2\boldsymbol{\phi}|\right) \frac{\partial(|^2\boldsymbol{\phi}|)}{\partial(^2\phi_k)}, \quad (\text{A.15})$$

and

$$\frac{\partial(|^2\boldsymbol{\phi}|)}{\partial(^2\phi_k)} = |^2\boldsymbol{\phi}|^{-1} ^2\phi_k \quad (\text{A.16})$$

Similarly, the first variation of  $^2b_3$  is

$$\delta(^2b_3) = \sum_{k=1}^3 \frac{\partial(^2b_3)}{\partial(^2\phi_k)} \delta(^2\phi_k) \quad (\text{A.17})$$

where

$$\begin{aligned} \frac{\partial(^2b_3)}{\partial(^2\phi_k)} = & \left( 2|^2\phi|^{-2} \sin \frac{|^2\phi|}{2} \cos \frac{|^2\phi|}{2} \right. \\ & \left. - 4|^2\phi|^{-3} \sin^2 \frac{|^2\phi|}{2} \right) \frac{\partial(|^2\phi|)}{\partial(^2\phi_k)} \end{aligned} \quad (\text{A.18})$$

With the first variations of the various portions of the rotation matrix known, the vector form of the first variation of the rotation matrix may be expressed as

$$\delta \begin{pmatrix} ^2\mathbf{R} \\ 9 \times 1 \end{pmatrix} = \mathbf{DR02}_{9 \times 3} \delta \begin{pmatrix} ^2\phi \\ 3 \times 1 \end{pmatrix} \quad (\text{A.19})$$

where each row of **DR02** is computed using Eqs. A.11 and A.13 along with Eqs. A.14-A.18.

## A.2 FIRST VARIATION OF THE DERIVATIVE OF THE ROTATION MATRIX

The expression for the first derivative of the rotation matrix was given in Chapter 3. The expanded form of the first derivative of the rotation matrix is shown in Fig. A.1. The first variation of the derivative of the rotation components, just like the rotation components themselves, will be stored in vector form. The resulting expression is

$$\delta \begin{pmatrix} ^2\mathbf{R}' \\ 0 \\ 9 \times 1 \end{pmatrix} = \begin{bmatrix} \mathbf{OMGM1}_{9 \times 9} & \mathbf{RM1}_{9 \times 3} \end{bmatrix} \begin{bmatrix} \delta \begin{pmatrix} ^2\mathbf{R} \\ 9 \times 1 \end{pmatrix} \\ \delta \begin{pmatrix} ^2\omega \\ 3 \times 1 \end{pmatrix} \end{bmatrix} \quad (\text{A.20})$$

The matrices **OMGM1** and **RM1** are given in Fig. A.2.

The vector  $^2\omega$  is related to the first derivative of the rotation vector by Eq. 3.43. When written in a form that is compatible with that of the rotation matrix, the expression for  $^2\omega$  becomes

$${}^0_3\mathbf{R}' = \begin{bmatrix} {}^2\omega_3 {}^2R_{21} - {}^2\omega_2 {}^2R_{31} & {}^2\omega_3 {}^2R_{22} - {}^2\omega_2 {}^2R_{32} & {}^2\omega_3 {}^2R_{23} - {}^2\omega_2 {}^2R_{33} \\ {}^2\omega_1 {}^2R_{31} - {}^2\omega_3 {}^2R_{11} & {}^2\omega_1 {}^2R_{32} - {}^2\omega_3 {}^2R_{12} & {}^2\omega_1 {}^2R_{33} - {}^2\omega_3 {}^2R_{13} \\ {}^2\omega_2 {}^2R_{11} - {}^2\omega_1 {}^2R_{21} & {}^2\omega_2 {}^2R_{12} - {}^2\omega_1 {}^2R_{22} & {}^2\omega_2 {}^2R_{13} - {}^2\omega_1 {}^2R_{23} \end{bmatrix}$$

Figure A.1 Expanded form of the first derivative of the rotation matrix.

$$\mathbf{OMGM1} = \begin{bmatrix} 0 & 0 & 0 & {}^2\omega_3 & 0 & 0 & -{}^2\omega_2 & 0 & 0 \\ 0 & 0 & 0 & 0 & {}^2\omega_3 & 0 & 0 & -{}^2\omega_2 & 0 \\ 0 & 0 & 0 & 0 & 0 & {}^2\omega_3 & 0 & 0 & -{}^2\omega_2 \\ -{}^2\omega_3 & 0 & 0 & 0 & 0 & 0 & {}^2\omega_1 & 0 & 0 \\ 0 & -{}^2\omega_3 & 0 & 0 & 0 & 0 & 0 & {}^2\omega_1 & 0 \\ 0 & 0 & -{}^2\omega_3 & 0 & 0 & 0 & 0 & 0 & {}^2\omega_1 \\ {}^2\omega_2 & 0 & 0 & -{}^2\omega_1 & 0 & 0 & 0 & 0 & 0 \\ 0 & {}^2\omega_2 & 0 & 0 & -{}^2\omega_1 & 0 & 0 & 0 & 0 \\ 0 & 0 & {}^2\omega_2 & 0 & 0 & -{}^2\omega_1 & 0 & 0 & 0 \end{bmatrix}$$

$$\mathbf{RM1} = \begin{bmatrix} 0 & -{}^2R_{31} & {}^2R_{21} \\ 0 & -{}^2R_{32} & {}^2R_{22} \\ 0 & -{}^2R_{33} & {}^2R_{23} \\ {}^2R_{31} & 0 & -{}^2R_{11} \\ {}^2R_{32} & 0 & -{}^2R_{12} \\ {}^2R_{33} & 0 & -{}^2R_{13} \\ -{}^2R_{21} & {}^2R_{11} & 0 \\ -{}^2R_{22} & {}^2R_{12} & 0 \\ -{}^2R_{23} & {}^2R_{13} & 0 \end{bmatrix}$$

Figure A.2 Matrices **OMGM1** and **RM1** from the matrix expression for the first variation of the derivative of the rotation components.

$${}^2\boldsymbol{\omega} = (\mathbf{I} + {}^2c_2 {}^2\mathbf{R}_{II} + {}^2c_3 {}^2\mathbf{R}_{III}) {}^2_0\boldsymbol{\phi}' = {}^2\mathbf{D} {}^2_0\boldsymbol{\phi}' \quad (\text{A.21})$$

The scalars  ${}^2c_2$  and  ${}^2c_3$  are given in Chapter 3 but are repeated here for convenience;

$$c_2 = -2|{}^2\boldsymbol{\phi}|^{-2} \sin^2 \frac{|{}^2\boldsymbol{\phi}|}{2}, \quad (\text{A.22})$$

and

$$c_3 = |{}^2\boldsymbol{\phi}|^{-3} (|{}^2\boldsymbol{\phi}| - \sin |{}^2\boldsymbol{\phi}|) \quad (\text{A.23})$$

The first variation of  ${}^2\boldsymbol{\omega}$  may be written as

$$\delta({}^2\boldsymbol{\omega}) = \delta({}^2\mathbf{D}) {}^2_0\boldsymbol{\phi}' + {}^2\mathbf{D} \delta({}^2_0\boldsymbol{\phi}') \quad (\text{A.24})$$

or in terms of partitioned matrices as

$$\delta \begin{pmatrix} {}^2\boldsymbol{\omega} \\ {}_{3 \times 1} \end{pmatrix} = \begin{bmatrix} \mathbf{PHPM1} & {}^2\mathbf{D} \\ {}_{3 \times 9} & {}_{3 \times 3} \end{bmatrix} \begin{bmatrix} \delta \begin{pmatrix} {}^2\mathbf{R} \\ {}_{9 \times 1} \end{pmatrix} \\ \delta \begin{pmatrix} {}^2_0\boldsymbol{\phi}' \\ {}_{3 \times 1} \end{pmatrix} \end{bmatrix} \quad (\text{A.25})$$

where the matrix **PHPM1** is shown in Fig. A.3. Using Eq. A.25, the partitioned vector

$$\begin{bmatrix} \delta \begin{pmatrix} {}^2\mathbf{R} \\ {}_{9 \times 1} \end{pmatrix} \\ \delta \begin{pmatrix} {}^2\boldsymbol{\omega} \\ {}_{3 \times 1} \end{pmatrix} \end{bmatrix} = \begin{bmatrix} \mathbf{I} & 0 & 0 \\ 0 & \mathbf{PHPM1} & {}^2\mathbf{D} \\ {}_{9 \times 9} & {}_{3 \times 9} & {}_{3 \times 3} \end{bmatrix} \begin{bmatrix} \delta \begin{pmatrix} {}^2\mathbf{R} \\ {}_{9 \times 1} \end{pmatrix} \\ \delta \begin{pmatrix} {}^2\mathbf{D} \\ {}_{9 \times 1} \end{pmatrix} \\ \delta \begin{pmatrix} {}^2_0\boldsymbol{\phi}' \\ {}_{3 \times 1} \end{pmatrix} \end{bmatrix} \quad (\text{A.26})$$

The first variation of the components of  ${}^2\mathbf{D}$  is computed in the same way as the first variation of the components of  ${}^2\mathbf{R}$ . The resulting expression for the first variation of a typical component of  ${}^2\mathbf{D}$  is

$$\begin{aligned} \delta({}^2D_{ij}) &= \delta({}^2c_2) {}^2R_{II_{ij}} + {}^2c_2 \delta({}^2R_{II_{ij}}) \\ &\quad + \delta({}^2c_3) {}^2R_{III_{ij}} + {}^2c_3 \delta({}^2R_{III_{ij}}) \end{aligned} \quad (\text{A.27})$$

where  $\delta({}^2R_{II_{ij}})$  and  $\delta({}^2R_{III_{ij}})$  are given by Eqs. A.8 and A.9. Computation of the first

$$\mathbf{PHPM1} = \begin{bmatrix} {}^2\phi_1 & {}^2\phi_2 & {}^2\phi_3 & 0 & 0 & 0 & 0 & 0 & 0 \\ 0 & 0 & 0 & {}^2\phi_1 & {}^2\phi_2 & {}^2\phi_3 & 0 & 0 & 0 \\ 0 & 0 & 0 & 0 & 0 & 0 & {}^2\phi_1 & {}^2\phi_2 & {}^2\phi_3 \end{bmatrix}$$

Figure A.3 Matrix **PHPM1** required for the calculation of  ${}^2\omega$ .



variation of the scalars  ${}^2c_2$  and  ${}^2c_3$  is similar to that for  ${}^2b_2$  and  ${}^2b_3$ :

$$\delta({}^2c_2) = \sum_{k=1}^3 \frac{\partial({}^2c_2)}{\partial({}^2\phi_k)} \delta({}^2\phi_k), \quad (\text{A.28})$$

and

$$\delta({}^2c_3) = \sum_{k=1}^3 \frac{\partial({}^2c_3)}{\partial({}^2\phi_k)} \delta({}^2\phi_k) \quad (\text{A.29})$$

The partial derivatives are given by

$$\begin{aligned} \frac{\partial({}^2c_2)}{\partial({}^2\phi_k)} = & \left( 2|{}^2\phi|^{-2} \sin \frac{|{}^2\phi|}{2} \cos \frac{|{}^2\phi|}{2} \right. \\ & \left. - 4|{}^2\phi|^{-3} \sin^2 \frac{|{}^2\phi|}{2} \right) \frac{\partial(|{}^2\phi|)}{\partial({}^2\phi_k)} \end{aligned} \quad (\text{A.30})$$

and

$$\frac{\partial({}^2c_3)}{\partial({}^2\phi_k)} = \left( \frac{-2}{|{}^2\phi|^3} - \frac{\cos |{}^2\phi|}{|{}^2\phi|^3} + \frac{3\sin |{}^2\phi|}{|{}^2\phi|^4} \right) \frac{\partial(|{}^2\phi|)}{\partial({}^2\phi_k)} \quad (\text{A.31})$$

Just as with the vector form of  $\delta({}^2\mathbf{\tilde{R}})$ , the vector form of  $\delta({}^2\mathbf{\tilde{D}})$  may be written in terms of the rotation vector,  ${}^2\phi$ , as

$$\delta \begin{pmatrix} {}^2\mathbf{\tilde{D}} \\ 9 \times 1 \end{pmatrix} = \mathbf{DD02}_{9 \times 3} \delta \begin{pmatrix} {}^2\phi \\ 3 \times 1 \end{pmatrix} \quad (\text{A.32})$$

where each row of **DD02** contains the three terms that result from the first variation of the various portions of the matrix  ${}^2\mathbf{\tilde{D}}$ . The partitioned vector from the right-hand side of Eq. A.26 can now be written as

$$\begin{bmatrix} \delta \begin{pmatrix} 2\mathbf{\tilde{R}} \\ 9 \times 1 \end{pmatrix} \\ \delta \begin{pmatrix} 2\mathbf{\tilde{D}} \\ 9 \times 1 \end{pmatrix} \\ \delta \begin{pmatrix} 2\phi' \\ 0 \\ 3 \times 1 \end{pmatrix} \end{bmatrix} = \begin{bmatrix} \mathbf{DR02} & 0 \\ \mathbf{DD02} & 0 \\ 0 & \mathbf{I} \end{bmatrix} \begin{bmatrix} \delta \begin{pmatrix} 2\phi \\ 3 \times 1 \end{pmatrix} \\ \delta \begin{pmatrix} 2\phi' \\ 0 \\ 3 \times 1 \end{pmatrix} \end{bmatrix} \quad (\text{A.33})$$

Using Eqs. A.20, A.26, A.33, and carrying out the required matrix multiplication yields the final expression for the variation of the first derivative of the rotation matrix which is given in Fig. A.4. A more compact expression for  $\delta \begin{pmatrix} 2\mathbf{R}' \\ 0 \\ 9 \times 1 \end{pmatrix}$  is

$$\delta \begin{pmatrix} 2\mathbf{R}' \\ 0 \\ 9 \times 1 \end{pmatrix} = \begin{bmatrix} \mathbf{DRP1} & \mathbf{DRP2} \\ 9 \times 3 & 9 \times 3 \end{bmatrix} \begin{bmatrix} \delta \begin{pmatrix} 2\phi \\ 3 \times 1 \end{pmatrix} \\ \delta \begin{pmatrix} 2\phi' \\ 0 \\ 3 \times 1 \end{pmatrix} \end{bmatrix} \quad (\text{A.34})$$

$$\delta \begin{pmatrix} 2 \\ 0 \\ 9 \times 1 \end{pmatrix} \mathbf{R}' = \begin{bmatrix} (\mathbf{OMGM1} \mathbf{DR02} + \mathbf{RM1} \mathbf{PHPM1} \mathbf{DD02}) & \mathbf{RM1} \mathbf{^2D} \\ \underset{9 \times 9}{\phantom{(\mathbf{OMGM1} \mathbf{DR02} + \mathbf{RM1} \mathbf{PHPM1} \mathbf{DD02})}} & \underset{9 \times 3}{\phantom{\mathbf{RM1} \mathbf{^2D}}} \end{bmatrix} \begin{bmatrix} \delta \begin{pmatrix} 2 \\ 3 \times 1 \end{pmatrix} \boldsymbol{\phi} \\ \delta \begin{pmatrix} 2 \\ 0 \\ 3 \times 1 \end{pmatrix} \boldsymbol{\phi}' \end{bmatrix}$$

Figure A.4 Final expression for the variation of the first derivative of the rotation matrix.

## APPENDIX B

### EXPANSION AND LINEARIZATION OF THE LARGE ROTATION MATRIX

The incremental form of the large rotation matrix is

$${}^2\mathbf{R} = {}^1\mathbf{R} + \mathbf{R} \quad (\text{B.1})$$

where the rotation matrix  $\mathbf{R}$  is linear in the rotation angles  $\phi_i$ . From Appendix A, the expanded form of  ${}^2\mathbf{R}$  is

$${}^2\mathbf{R} = \mathbf{I} + {}^2b_2 {}^2\mathbf{R}_{II} + {}^2b_3 {}^2\mathbf{R}_{III} \quad (\text{B.2})$$

The incremental form of Eq. B.2 is

$${}^2\mathbf{R} = \mathbf{I} + ({}^1b_2 + b_2)({}^1\mathbf{R}_{II} + \mathbf{R}_{II}) + ({}^1b_3 + b_3)({}^1\mathbf{R}_{III} + \mathbf{R}_{III}) \quad (\text{B.3})$$

When expanded,  ${}^2\mathbf{R}$  becomes

$$\begin{aligned} {}^2\mathbf{R} = & \underbrace{\mathbf{I} + {}^1b_2 {}^1\mathbf{R}_{II} + {}^1b_3 {}^1\mathbf{R}_{III}}_{{}^1\mathbf{R}} \\ & + \underbrace{{}^1b_2 \mathbf{R}_{II} + b_2 {}^1\mathbf{R}_{II} + {}^1b_3 \mathbf{R}_{III} + b_3 {}^1\mathbf{R}_{III}}_{\mathbf{R}} \end{aligned} \quad (\text{B.4})$$

The matrix  ${}^1\mathbf{R}$  is the arbitrarily large rotation matrix which has the same form as  ${}^2\mathbf{R}$  from Chapter 3 and the matrix  $\mathbf{R}$  represents a small incremental rotation from configuration 1 to the final configuration 2.

The small rotation matrix  $\mathbf{R}$  is found by expanding the large rotation matrix  ${}^2\mathbf{R}$  in terms of the small rotation angles  $\phi_i$ . The expansion of the matrix  ${}^2\mathbf{R}_{II}$  is

$${}^2\mathbf{R}_{II} = {}^1\mathbf{R}_{II} + \mathbf{R}_{II} \quad (\text{B.5})$$

where

$${}^1\mathbf{R}_{II} = \begin{bmatrix} 0 & -{}^1\phi_3 & {}^1\phi_2 \\ {}^1\phi_3 & 0 & -{}^1\phi_1 \\ -{}^1\phi_2 & {}^1\phi_1 & 0 \end{bmatrix} \quad (\text{B.6})$$

and

$$\mathbf{R}_{II} = \begin{bmatrix} 0 & -\phi_3 & \phi_2 \\ \phi_3 & 0 & -\phi_1 \\ -\phi_2 & \phi_1 & 0 \end{bmatrix} \quad (\text{B.7})$$

Expansion and linearization of the matrix  ${}^2\mathbf{R}_{III}$  leads to

$${}^2\mathbf{R}_{III} = {}^1\mathbf{R}_{III} + \mathbf{R}_{III} \quad (\text{B.8})$$

where the matrices  ${}^1\mathbf{R}_{III}$  and  $\mathbf{R}_{III}$  are given in Fig. B.1.

The incremental forms of the scalars  ${}^2b_2$  and  ${}^2b_3$  are found by using the incremental rotation angles

$${}^2\phi_i = {}^1\phi_i + \phi_i \quad (\text{B.9})$$

From Chapter 3, the expression for  ${}^2b_2$  is

$${}^2b_2 = -|{}^2\phi|^{-1} \sin|{}^2\phi| \quad (\text{B.10})$$

The magnitude of the rotation angle is given by

$$|{}^2\phi| = \left( {}^2\phi_1^2 + {}^2\phi_2^2 + {}^2\phi_3^2 \right)^{\frac{1}{2}} = \left( {}^2\phi^T {}^2\phi \right)^{\frac{1}{2}} \quad (\text{B.11})$$

The incremental form of  $|{}^2\phi|$  is

$$|{}^2\phi| = \left( {}^1\phi^T {}^1\phi + 2 {}^1\phi^T \phi + \phi^T \phi \right)^{\frac{1}{2}} \quad (\text{B.12})$$

Taking a binomial series expansion of  $|{}^2\phi|$  and neglecting all higher order terms in  $\phi_i$  leads to

$${}^1\mathbf{R}_{III} = \begin{bmatrix} -({}^1\phi_2^2 + {}^1\phi_3^2) & {}^1\phi_1 {}^1\phi_2 & {}^1\phi_1 {}^1\phi_3 \\ {}^1\phi_1 {}^1\phi_2 & -({}^1\phi_1^2 + {}^1\phi_3^2) & {}^1\phi_2 {}^1\phi_3 \\ {}^1\phi_1 {}^1\phi_3 & {}^1\phi_2 {}^1\phi_3 & -({}^1\phi_1^2 + {}^1\phi_2^2) \end{bmatrix}$$

$$\mathbf{R}_{III} = \begin{bmatrix} -2({}^1\phi_2\phi_2 + {}^1\phi_3\phi_3) & ({}^1\phi_1\phi_2 + {}^1\phi_2\phi_1) & ({}^1\phi_1\phi_3 + {}^1\phi_3\phi_1) \\ ({}^1\phi_1\phi_2 + {}^1\phi_2\phi_1) & -2({}^1\phi_1\phi_1 + {}^1\phi_3\phi_3) & ({}^1\phi_2\phi_3 + {}^1\phi_3\phi_2) \\ ({}^1\phi_1\phi_3 + {}^1\phi_3\phi_1) & ({}^1\phi_2\phi_3 + {}^1\phi_3\phi_2) & -2({}^1\phi_1\phi_1 + {}^1\phi_2\phi_2) \end{bmatrix}$$

Figure B.1 Matrices  ${}^1\mathbf{R}_{III}$  and  $\mathbf{R}_{III}$  from the expansion of the matrix  ${}^2\mathbf{R}_{III}$ .

$$|^2\phi| = |^1\phi| + |^1\phi|^{-1} (^1\phi^T \phi) \quad (\text{B.13})$$

The expression for  $\sin(|^2\phi|)$  may be expanded using Eq. B.13 and the trigonometric identity

$$\sin(\alpha + \beta) = \sin\alpha \cos\beta + \cos\alpha \sin\beta \quad (\text{B.14})$$

where

$$\alpha = |^1\phi| \quad (\text{B.15})$$

and

$$\beta = |^1\phi|^{-1} (^1\phi^T \phi) \quad (\text{B.16})$$

Making the substitution gives

$$\begin{aligned} \sin(|^2\phi|) &= \sin(|^1\phi|) \cos(|^1\phi|^{-1} (^1\phi^T \phi)) \\ &\quad + \cos(|^1\phi|) \sin(|^1\phi|^{-1} (^1\phi^T \phi)) \end{aligned} \quad (\text{B.17})$$

Since the  $\phi_i$  are small

$$\sin(|^2\phi|) = \sin(|^1\phi|) + \cos(|^1\phi|) \left( |^1\phi|^{-1} (^1\phi^T \phi) \right) \quad (\text{B.18})$$

Expanding  $|^2\phi|^{-1}$  using a binomial expansion and neglecting higher order terms  $\phi_i$  gives

$$|^2\phi|^{-1} = |^1\phi|^{-1} - |^1\phi|^{-3} (^1\phi^T \phi) \quad (\text{B.19})$$

The expression for  $^2b_2$  reduces to

$$\begin{aligned} ^2b_2 &= \underbrace{-|^1\phi|^{-1} \sin|^1\phi|}_{^1b_2} \\ &\quad + \underbrace{\left( |^1\phi|^{-3} \sin(|^1\phi|) - |^1\phi|^{-2} \cos(|^1\phi|) \right)}_{b_2} (^1\phi^T \phi) \end{aligned} \quad (\text{B.20})$$

The expression for  ${}^2b_3$ , from Chapter 3, is

$${}^2b_3 = 2 |{}^2\phi|^{-2} \sin^2 \frac{|{}^2\phi|}{2} \quad (\text{B.21})$$

Using Eq. B.18, the term

$$\sin^2 \frac{|{}^2\phi|}{2} = \sin^2 \frac{|{}^1\phi|}{2} + |{}^1\phi|^{-1} \sin \frac{|{}^1\phi|}{2} \cos \frac{|{}^1\phi|}{2} ({}^1\phi^T \phi) \quad (\text{B.22})$$

Using a binomial expansion and neglecting higher order terms, the expression for

$$|{}^2\phi|^{-2} = |{}^1\phi|^{-2} - 2|{}^1\phi|^{-4} ({}^1\phi^T \phi) \quad (\text{B.23})$$

Combining Eqs. B.22 and B.23, the expansion of  ${}^2b_3$  is

$$\begin{aligned} {}^2b_3 = & \underbrace{2 |{}^1\phi|^{-2} \sin^2 \frac{|{}^1\phi|}{2}}_{{}^1b_3} \\ & + \underbrace{\left( 2 |{}^1\phi|^{-3} \sin \frac{|{}^1\phi|}{2} \cos \frac{|{}^1\phi|}{2} - 4 |{}^1\phi|^{-4} \sin^2 \frac{|{}^1\phi|}{2} \right)}_{b_3} ({}^1\phi^T \phi) \end{aligned} \quad (\text{B.24})$$

The product  ${}^1b_2 \mathbf{R}_{II}$  is stored in a  $9 \times 1$  vector  $\mathbf{R}_A$  which is equal to

$$\mathbf{R}_A = \mathbf{RAM01} \phi \quad (\text{B.25})$$

$\mathbf{R}_A$  is a  $9 \times 1$  vector,  $\mathbf{RAM01}$  is a  $9 \times 3$  matrix, and  $\phi$  is a  $9 \times 3$  vector.

where

$$\mathbf{RAM01} = {}^1b_2 \begin{bmatrix} 0 & 0 & 0 \\ 0 & 0 & -1 \\ 0 & 1 & 0 \\ 0 & 0 & 1 \\ 0 & 0 & 0 \\ -1 & 0 & 0 \\ 0 & -1 & 0 \\ 1 & 0 & 0 \\ 0 & 0 & 0 \end{bmatrix} \quad (\text{B.26})$$

The product of  $b_2$  and  $\mathbf{R}_{II}$  can be calculated by writing the scalar  $b_2$  as



$$b_2 = B_2({}^1\phi_1 \phi_1 + {}^1\phi_2 \phi_2 + {}^1\phi_3 \phi_3) \quad (\text{B.27})$$

where

$$B_2 = \left( |{}^1\phi|^{-3} \sin(|{}^1\phi|) - |{}^1\phi|^{-2} \cos(|{}^1\phi|) \right) \quad (\text{B.28})$$

The product  $b_2 {}^1\mathbf{R}_{II}$  is stored in the  $9 \times 1$  vector  $\tilde{\mathbf{R}}_B$  which is given by

$$\tilde{\mathbf{R}}_B = \mathbf{RBM01} \phi \quad (\text{B.29})$$

$\underset{9 \times 1}{\tilde{\mathbf{R}}_B}$ 
 $=$ 
 $\underset{9 \times 3}{\mathbf{RBM01}}$ 
 $\underset{9 \times 3}{\phi}$

where

$$\mathbf{RBM01} = B_2 \begin{bmatrix} 0 & 0 & 0 \\ -{}^1\phi_1 {}^1\phi_3 & -{}^1\phi_2 {}^1\phi_3 & -{}^1\phi_3 {}^1\phi_3 \\ {}^1\phi_1 {}^1\phi_2 & {}^1\phi_2 {}^1\phi_2 & {}^1\phi_2 {}^1\phi_3 \\ {}^1\phi_1 {}^1\phi_3 & {}^1\phi_2 {}^1\phi_3 & {}^1\phi_3 {}^1\phi_3 \\ 0 & 0 & 0 \\ -{}^1\phi_1 {}^1\phi_1 & -{}^1\phi_1 {}^1\phi_2 & -{}^1\phi_1 {}^1\phi_3 \\ -{}^1\phi_1 {}^1\phi_2 & -{}^1\phi_2 {}^1\phi_2 & -{}^1\phi_2 {}^1\phi_3 \\ {}^1\phi_1 {}^1\phi_1 & {}^1\phi_1 {}^1\phi_2 & {}^1\phi_1 {}^1\phi_3 \\ 0 & 0 & 0 \end{bmatrix} \quad (\text{B.30})$$

The product  ${}^1b_3 \mathbf{R}_{III}$  is stored in the  $9 \times 1$  vector  $\tilde{\mathbf{R}}_C$  which is given by

$$\tilde{\mathbf{R}}_C = \mathbf{RCM01} \phi \quad (\text{B.31})$$

$\underset{9 \times 1}{\tilde{\mathbf{R}}_C}$ 
 $=$ 
 $\underset{9 \times 3}{\mathbf{RCM01}}$ 
 $\underset{9 \times 3}{\phi}$

where

$$\mathbf{RCM01} = {}^1b_3 \begin{bmatrix} 0 & -2{}^1\phi_2 & -2{}^1\phi_3 \\ {}^1\phi_2 & {}^1\phi_1 & 0 \\ {}^1\phi_3 & 0 & {}^1\phi_1 \\ {}^1\phi_2 & {}^1\phi_1 & 0 \\ -2{}^1\phi_1 & 0 & -2{}^1\phi_3 \\ 0 & {}^1\phi_3 & {}^1\phi_2 \\ {}^1\phi_3 & 0 & {}^1\phi_1 \\ 0 & {}^1\phi_3 & {}^1\phi_2 \\ -2{}^1\phi_1 & -2{}^1\phi_2 & 0 \end{bmatrix} \quad (\text{B.32})$$

The scalar  $b_3$  can be rewritten as

$$b_3 = B_3({}^1\phi_1 \phi_1 + {}^1\phi_2 \phi_2 + {}^1\phi_3 \phi_3) \quad (\text{B.33})$$

where

$$B_3 = \left( 2|{}^1\phi|^{-3} \sin \frac{|{}^1\phi|}{2} \cos \frac{|{}^1\phi|}{2} - 4|{}^1\phi|^{-4} \sin^2 \frac{|{}^1\phi|}{2} \right) \quad (\text{B.34})$$

The product of  $b_3$  and  ${}^1\mathbf{R}_{III}$  is then expressed as

$$\underset{9 \times 1}{\mathbf{R}_D} = \underset{9 \times 3}{\mathbf{RDM01}} \underset{9 \times 3}{\phi} \quad (\text{B.35})$$

where the matrix **RDM01** is shown in Fig. B.2. The resulting vector form of the small rotation matrix **R** is

$$\underset{9 \times 1}{\mathbf{R}} = \underset{9 \times 3}{\mathbf{RTM01}} \underset{9 \times 3}{\phi} \quad (\text{B.36})$$

where the matrix **RTM01** is

$$\underset{9 \times 3}{\mathbf{RTM01}} = \underset{9 \times 3}{\mathbf{RAM01}} + \underset{9 \times 3}{\mathbf{RBM01}} + \underset{9 \times 3}{\mathbf{RCM01}} + \underset{9 \times 3}{\mathbf{RDM01}} \quad (\text{B.37})$$

$$\mathbf{RDM01}_{9 \times 3} = B_3 \begin{bmatrix} -({}^1\phi_2^2 + {}^1\phi_3^2){}^1\phi_1 & -({}^1\phi_2^2 + {}^1\phi_3^2){}^1\phi_2 & -({}^1\phi_2^2 + {}^1\phi_3^2){}^1\phi_3 \\ {}^1C_{12}{}^1\phi_1 & {}^1C_{12}{}^1\phi_2 & {}^1C_{12}{}^1\phi_3 \\ {}^1C_{13}{}^1\phi_1 & {}^1C_{13}{}^1\phi_2 & {}^1C_{13}{}^1\phi_3 \\ {}^1C_{12}{}^1\phi_1 & {}^1C_{12}{}^1\phi_2 & {}^1C_{12}{}^1\phi_3 \\ -({}^1\phi_1^2 + {}^1\phi_3^2){}^1\phi_1 & -({}^1\phi_1^2 + {}^1\phi_3^2){}^1\phi_2 & -({}^1\phi_1^2 + {}^1\phi_3^2){}^1\phi_3 \\ {}^1C_{23}{}^1\phi_1 & {}^1C_{23}{}^1\phi_2 & {}^1C_{23}{}^1\phi_3 \\ {}^1C_{13}{}^1\phi_1 & {}^1C_{13}{}^1\phi_2 & {}^1C_{13}{}^1\phi_3 \\ {}^1C_{23}{}^1\phi_1 & {}^1C_{23}{}^1\phi_2 & {}^1C_{23}{}^1\phi_3 \\ -({}^1\phi_1^2 + {}^1\phi_2^2){}^1\phi_1 & -({}^1\phi_1^2 + {}^1\phi_2^2){}^1\phi_2 & -({}^1\phi_1^2 + {}^1\phi_2^2){}^1\phi_3 \end{bmatrix}$$

$${}^1C_{12} = {}^1\phi_1 {}^1\phi_2$$

$${}^1C_{13} = {}^1\phi_1 {}^1\phi_3$$

$${}^1C_{23} = {}^1\phi_2 {}^1\phi_3$$

Figure B.2 Matrix **RDM01** from the expression for the vector  $\tilde{\mathbf{R}}_D$ .

## APPENDIX C

### EXPANSION AND LINEARIZATION OF THE DERIVATIVE OF THE LARGE ROTATION MATRIX

The derivative of the rotation matrix was given in Chapter 3 as

$${}^2_0\mathbf{R}' = - {}^2\tilde{\omega} {}^2\mathbf{R} \quad (\text{C.1})$$

The incremental form of this expression is

$${}^2_0\mathbf{R}' = - ({}^1\tilde{\omega} + \tilde{\omega})({}^1\mathbf{R} + \mathbf{R}) \quad (\text{C.2})$$

which when expanded gives

$${}^2_0\mathbf{R}' = \underbrace{- {}^1\tilde{\omega} {}^1\mathbf{R}}_{{}^1_0\mathbf{R}'} + \underbrace{(- {}^1\tilde{\omega} \mathbf{R} - \tilde{\omega} {}^1\mathbf{R})}_{{}_0\mathbf{R}'} \quad (\text{C.3})$$

The above expansion neglects the higher order terms resulting from the product of  $\tilde{\omega}$  and  $\mathbf{R}$ . The matrix  ${}^1_0\mathbf{R}'$  represents the derivative of the large rotation from the initial configuration 0 to the intermediate configuration 1. The matrix  ${}_0\mathbf{R}'$  contains the derivative of the small rotation from configuration 1 to the final configuration 2. A  $9 \times 1$  vector  ${}_0\tilde{\mathbf{R}}'$  will be used to store the components of the matrix  ${}_0\mathbf{R}'$ . The vector  ${}_0\tilde{\mathbf{R}}'$  will be computed in two parts and stored in the two vectors  ${}_0\tilde{\mathbf{R}}'_A$  and  ${}_0\tilde{\mathbf{R}}'_B$ .

The first portion of  ${}_0\tilde{\mathbf{R}}'$  contains the results of the matrix product

$${}_0\mathbf{R}'_A = - {}^1\tilde{\omega} \mathbf{R} \quad (\text{C.4})$$

where the vector form is given by

$${}^0_{\tilde{9} \times 1} \mathbf{R}'_A = \mathbf{OMGM01} {}^9_{9 \times 9} \mathbf{R} {}^9_{\tilde{9} \times 1} \quad (\text{C.5})$$

The vector  $\tilde{\mathbf{R}}$  is the vector form of the incremental rotation  $\mathbf{R}$  and the matrix **OMGM01** is given in Fig. C.1.

The second part of  ${}^0_{\tilde{9}} \mathbf{R}'$  is the vector form of the matrix product

$${}^0_{\tilde{9}} \mathbf{R}'_B = -\tilde{\omega} {}^1 \mathbf{R} \quad (\text{C.6})$$

The vector form of  ${}^0_{\tilde{9}} \mathbf{R}'_B$  is

$${}^0_{\tilde{9} \times 1} \mathbf{R}'_B = \mathbf{RM01} {}^9_{9 \times 3} \omega {}^3_{3 \times 1} \quad (\text{C.7})$$

where the matrix **RM01** is

$$\mathbf{RM01} = {}^9_{9 \times 3} = \begin{bmatrix} 0 & -{}^1R_{31} & {}^1R_{21} \\ 0 & -{}^1R_{32} & {}^1R_{22} \\ 0 & -{}^1R_{33} & {}^1R_{23} \\ {}^1R_{31} & 0 & -{}^1R_{11} \\ {}^1R_{32} & 0 & -{}^1R_{12} \\ {}^1R_{33} & 0 & -{}^1R_{13} \\ -{}^1R_{21} & {}^1R_{11} & 0 \\ -{}^1R_{22} & {}^1R_{12} & 0 \\ -{}^1R_{23} & {}^1R_{13} & 0 \end{bmatrix} \quad (\text{C.8})$$

and the vector  $\omega$  is the incremental form of the angular velocity vector which is yet to be determined.

The angular velocity vector is related to the first derivative of the rotation angles,  ${}^2_0 \phi'_i$ , by the expression

$${}^2 \omega = {}^2 \mathbf{D}_0 {}^2 \phi' \quad (\text{C.9})$$

The incremental form of this expression is

$${}^2 \omega = \underbrace{{}^1 \mathbf{D}_0 {}^1 \phi'}_{{}^1 \omega} + \underbrace{{}^1 \mathbf{D}_0 \phi' + \mathbf{D}_0 {}^1 \phi'}_{\omega} \quad (\text{C.10})$$

$$\mathbf{OMGM01}_{9 \times 9} = \begin{bmatrix} 0 & 0 & 0 & {}^1\omega_3 & 0 & 0 & -{}^1\omega_2 & 0 & 0 \\ 0 & 0 & 0 & 0 & {}^1\omega_3 & 0 & 0 & -{}^1\omega_2 & 0 \\ 0 & 0 & 0 & 0 & 0 & {}^1\omega_3 & 0 & 0 & -{}^1\omega_2 \\ -{}^1\omega_3 & 0 & 0 & 0 & 0 & 0 & {}^1\omega_1 & 0 & 0 \\ 0 & -{}^1\omega_3 & 0 & 0 & 0 & 0 & 0 & {}^1\omega_1 & 0 \\ 0 & 0 & -{}^1\omega_3 & 0 & 0 & 0 & 0 & 0 & {}^1\omega_1 \\ {}^1\omega_2 & 0 & 0 & -{}^1\omega_1 & 0 & 0 & 0 & 0 & 0 \\ 0 & {}^1\omega_2 & 0 & 0 & -{}^1\omega_1 & 0 & 0 & 0 & 0 \\ 0 & 0 & {}^1\omega_2 & 0 & 0 & -{}^1\omega_1 & 0 & 0 & 0 \end{bmatrix}$$

Figure C.1 Matrix **OMGM01** from the expression for  ${}_0\mathbf{R}'_A$ .

where the higher order terms,  $\mathbf{D}_0 \phi'$ , have been neglected. The incremental form of the angular velocity,  $\omega$ , will be computed in two parts.

The first part of  $\omega$  is stored in  $\omega_A$  and is equal to

$$\omega_A = \begin{matrix} 1\mathbf{D} \\ 3 \times 1 \end{matrix} \begin{matrix} 0\phi' \\ 3 \times 3 \end{matrix} \begin{matrix} 3 \times 1 \end{matrix} \quad (\text{C.11})$$

where the matrix  ${}^1\mathbf{D}$  takes on the same form as the matrix  ${}^2\mathbf{D}$  given in Chapter 3. The second part of  $\omega$  is given by

$$\omega_B = \begin{matrix} \mathbf{PHPM01} \mathbf{D} \\ 3 \times 1 \end{matrix} \begin{matrix} 3 \times 9 \\ 9 \times 1 \end{matrix} \quad (\text{C.12})$$

The  $9 \times 1$  vector  $\mathbf{D}$  is the vector form of the matrix  $\mathbf{D}$  which contains the linearized portion of  ${}^2\mathbf{D}$ , and will be computed in the next section. The transpose of the matrix  $\mathbf{PHPM01}$  is

$$\mathbf{PHPM01}^T = \begin{bmatrix} \begin{matrix} 1\phi'_1 \\ 0\phi'_1 \end{matrix} & 0 & 0 \\ \begin{matrix} 1\phi'_2 \\ 0\phi'_2 \end{matrix} & 0 & 0 \\ \begin{matrix} 1\phi'_3 \\ 0\phi'_3 \end{matrix} & 0 & 0 \\ 0 & \begin{matrix} 1\phi'_1 \\ 0\phi'_1 \end{matrix} & 0 \\ 0 & \begin{matrix} 1\phi'_2 \\ 0\phi'_2 \end{matrix} & 0 \\ 0 & \begin{matrix} 1\phi'_3 \\ 0\phi'_3 \end{matrix} & 0 \\ 0 & 0 & \begin{matrix} 1\phi'_1 \\ 0\phi'_1 \end{matrix} \\ 0 & 0 & \begin{matrix} 1\phi'_2 \\ 0\phi'_2 \end{matrix} \\ 0 & 0 & \begin{matrix} 1\phi'_3 \\ 0\phi'_3 \end{matrix} \end{bmatrix} \quad (\text{C.13})$$

The matrices  ${}^2\mathbf{D}$  and  ${}^2\mathbf{R}$  are similar in structure, therefore the expansion and linearization of  ${}^2\mathbf{D}$  proceeds in the same way as the expansion and linearization of the matrix  ${}^2\mathbf{R}$ . The incremental form of the matrix  ${}^2\mathbf{D}$  is

$$\begin{aligned} {}^2\mathbf{D} = & \underbrace{\mathbf{I} + {}^1c_2 {}^1\mathbf{R}_{II} + {}^1c_3 {}^1\mathbf{R}_{III}}_{{}^1\mathbf{D}} \\ & + \underbrace{{}^1c_2 \mathbf{R}_{II} + c_2 {}^1\mathbf{R}_{II} + {}^1c_3 \mathbf{R}_{III} + c_3 {}^1\mathbf{R}_{III}}_{\mathbf{D}} \end{aligned} \quad (\text{C.14})$$

The vector form of  $\mathbf{D}$  will be stored in a  $9 \times 1$  vector  $\mathbf{\tilde{D}}$  that will be computed in four parts corresponding to the four matrices given in the above expression. The expressions for the matrices  ${}^1\mathbf{R}_{II}$ ,  $\mathbf{R}_{II}$ ,  ${}^1\mathbf{R}_{III}$ , and  $\mathbf{R}_{III}$  were given in Appendix B. The incremental forms of the scalars  ${}^2c_2$  and  ${}^2c_3$  are computed in the same way as the incremental forms of the scalars  ${}^2b_2$  and  ${}^2b_3$ .

The expression for  ${}^1c_2$  is the same as the expression for  ${}^1b_3$  (Appendix B). Therefore, the incremental form of  ${}^2c_2$  is

$$\begin{aligned} {}^2c_2 = & \underbrace{2|{}^1\phi|^{-2} \sin^2 \frac{|{}^1\phi|}{2}}_{{}^1c_2} \\ & + \underbrace{\left( 2|{}^1\phi|^{-3} \sin \frac{|{}^1\phi|}{2} \cos \frac{|{}^1\phi|}{2} - 4|{}^1\phi|^{-4} \sin^2 \frac{|{}^1\phi|}{2} \right)}_{c_2} ({}^1\phi^T \phi) \end{aligned} \quad (\text{C.15})$$

The expression for  ${}^2c_3$  is

$${}^2c_3 = |{}^2\phi|^{-3} (|{}^2\phi| - \sin |{}^2\phi|) \quad (\text{C.16})$$

From Appendix B, the incremental form of  $|{}^2\phi|$  is

$$|{}^2\phi| = ({}^1\phi^T {}^1\phi + 2 {}^1\phi^T \phi + \phi^T \phi)^{\frac{1}{2}} \quad (\text{C.17})$$

The expression for  $|{}^2\phi|^{-3}$  can be written as

$$|{}^2\phi|^{-3} = ({}^1\phi^T {}^1\phi + 2 {}^1\phi^T \phi + \phi^T \phi)^{-\frac{3}{2}} \quad (\text{C.18})$$

Taking a binomial expansion of the above relationship and ignoring higher order terms gives

$$|{}^2\phi|^{-3} = |{}^1\phi|^{-3} - 3|{}^1\phi|^{-5} ({}^1\phi^T \phi) \quad (\text{C.19})$$

The incremental expression for  $\sin |{}^2\phi|$  was given in Appendix B, and when combined with Eq. C.19 yields the incremental expression for  ${}^2c_3$  which is equal to



$$\begin{aligned}
{}^2c_3 = & \underbrace{|{}^1\phi|^{-3}(|{}^1\phi| - \sin|{}^1\phi|)}_{{}^1c_3} \\
& + \underbrace{|{}^1\phi|^{-4}\left(3|{}^1\phi|^{-1}\sin|{}^1\phi| - 2 - \cos|{}^1\phi|\right)}_{c_3} ({}^1\phi^T \phi)
\end{aligned} \tag{C.20}$$

The first part of  $\mathbf{\tilde{D}}$  is found from the product  ${}^1c_2 \mathbf{R}_{II}$  and is stored in the vector  $\mathbf{\tilde{D}}_A$ .

The resulting expression for  $\mathbf{\tilde{D}}_A$  is

$$\mathbf{\tilde{D}}_A = \mathbf{DAM01} \phi \tag{C.21}$$

$9 \times 1$ 
 $9 \times 3$ 
 $3 \times 1$

and the matrix **DAM01** is

$$\mathbf{DAM01} = {}^1c_2 \begin{bmatrix} 0 & 0 & 0 \\ 0 & 0 & -1 \\ 0 & 1 & 0 \\ 0 & 0 & 1 \\ 0 & 0 & 0 \\ -1 & 0 & 0 \\ 0 & -1 & 0 \\ 1 & 0 & 0 \\ 0 & 0 & 0 \end{bmatrix} \tag{C.22}$$

The second part of  $\mathbf{\tilde{D}}$  is found from the product of  $c_2 {}^1\mathbf{R}_{II}$ . The result is stored in the vector  $\mathbf{\tilde{D}}_B$  which is calculated from

$$\mathbf{\tilde{D}}_B = \mathbf{DBM01} \phi \tag{C.23}$$

$3 \times 1$ 
 $9 \times 3$ 
 $3 \times 1$

where the matrix **DBM01** is given by

$$\mathbf{DBM01}_{9 \times 3} = C_2 \begin{bmatrix} 0 & 0 & 0 \\ -{}^1\phi_1 {}^1\phi_3 & -{}^1\phi_2 {}^1\phi_3 & -{}^1\phi_3 {}^1\phi_3 \\ {}^1\phi_1 {}^1\phi_2 & {}^1\phi_2 {}^1\phi_2 & {}^1\phi_2 {}^1\phi_3 \\ {}^1\phi_1 {}^1\phi_3 & {}^1\phi_2 {}^1\phi_3 & {}^1\phi_3 {}^1\phi_3 \\ 0 & 0 & 0 \\ -{}^1\phi_1 {}^1\phi_1 & -{}^1\phi_1 {}^1\phi_2 & -{}^1\phi_1 {}^1\phi_3 \\ -{}^1\phi_1 {}^1\phi_2 & -{}^1\phi_2 {}^1\phi_2 & -{}^1\phi_2 {}^1\phi_3 \\ {}^1\phi_1 {}^1\phi_1 & {}^1\phi_1 {}^1\phi_2 & {}^1\phi_1 {}^1\phi_3 \\ 0 & 0 & 0 \end{bmatrix}, \quad (\text{C.24})$$

and the term  $C_2$  is equal to

$$C_2 = \left( 2|{}^1\phi|^{-3} \sin \frac{|{}^1\phi|}{2} \cos \frac{|{}^1\phi|}{2} - 4|{}^1\phi|^{-4} \sin^2 \frac{|{}^1\phi|}{2} \right) \quad (\text{C.25})$$

The third part of  $\mathbf{\tilde{D}}$  is placed in the vector  $\mathbf{\tilde{D}}_C$  whose elements are computed from  ${}^1c_3 \mathbf{R}_{III}$  which in vector form is

$$\mathbf{\tilde{D}}_C = \mathbf{DCM01}_{9 \times 3} \boldsymbol{\phi}_{3 \times 1} \quad (\text{C.26})$$

The matrix  $\mathbf{DCM01}$  is

$$\mathbf{DCM01}_{9 \times 3} = {}^1c_3 \begin{bmatrix} 0 & -2{}^1\phi_2 & -2{}^1\phi_3 \\ {}^1\phi_2 & {}^1\phi_1 & 0 \\ {}^1\phi_3 & 0 & {}^1\phi_1 \\ {}^1\phi_2 & {}^1\phi_1 & 0 \\ -2{}^1\phi_1 & 0 & -2{}^1\phi_3 \\ 0 & {}^1\phi_3 & {}^1\phi_2 \\ {}^1\phi_3 & 0 & {}^1\phi_1 \\ 0 & {}^1\phi_3 & {}^1\phi_2 \\ -2{}^1\phi_1 & -2{}^1\phi_2 & 0 \end{bmatrix} \quad (\text{C.27})$$

The final portion of  $\mathbf{\tilde{D}}$  is given by the vector form of the product  $c_3 {}^1\mathbf{R}_{III}$ . The result is stored in a vector  $\mathbf{\tilde{D}}_D$  which is computed by,

$$\mathbf{\tilde{D}}_D = \mathbf{DDM01}_{9 \times 3} \boldsymbol{\phi}_{3 \times 1} \quad (\text{C.28})$$

where the matrix **DDM01** is shown in Fig. C.2. With the various pieces of  $\mathbf{\tilde{D}}$  defined, the final expression for  $\mathbf{\tilde{D}}$  can be written as

$$\mathbf{\tilde{D}}_{3 \times 1} = \mathbf{DTM01}_{9 \times 3} \phi_{3 \times 1} \quad (\text{C.29})$$

where the matrix **DTM01** is equal to

$$\mathbf{DTM01}_{9 \times 3} = \mathbf{DAM01}_{9 \times 3} + \mathbf{DBM01}_{9 \times 3} + \mathbf{DCM01}_{9 \times 3} + \mathbf{DDM01}_{9 \times 3} \quad (\text{C.30})$$

Using Eqs. C.5 and C.7 the vector  ${}_0\mathbf{\tilde{R}}'$  may be written as

$${}_0\mathbf{\tilde{R}}' = \mathbf{OMGM01}_{9 \times 9} \mathbf{R}_{9 \times 1} + \mathbf{RM01}_{9 \times 3} \omega_{3 \times 1} \quad (\text{C.31})$$

From Appendix B

$$\mathbf{\tilde{R}} = \mathbf{RTM01}_{9 \times 3} \phi_{3 \times 1} \quad (\text{C.32})$$

which makes the vector  ${}_0\mathbf{\tilde{R}}'$  equal to

$${}_0\mathbf{\tilde{R}}' = \mathbf{OMGM01}_{9 \times 9} \mathbf{RTM01}_{9 \times 3} \phi_{3 \times 1} + \mathbf{RM01}_{9 \times 3} \omega_{3 \times 1} \quad (\text{C.33})$$

Using Eqs. C.9, C.10, and C.12 the vector  $\omega$  is equal to

$$\omega_{3 \times 1} = \mathbf{PHPM01}_{3 \times 9} \mathbf{\tilde{D}}_{9 \times 1} + {}^1\mathbf{D}_{3 \times 3} {}_0\phi'_{3 \times 1} \quad (\text{C.34})$$

Substituting Eq. C.29 into the previous expression gives

$$\omega_{3 \times 1} = \mathbf{PHPM01}_{3 \times 9} \mathbf{DTM01}_{9 \times 3} \phi_{3 \times 1} + {}^1\mathbf{D}_{3 \times 3} {}_0\phi'_{3 \times 1} \quad (\text{C.35})$$

The above expression for  $\omega$  is then substituted into the expression for  ${}_0\mathbf{\tilde{R}}'$  (Eq. C.33) which yields

$$\begin{aligned} {}_0\mathbf{\tilde{R}}'_{9 \times 1} &= \mathbf{OMGM01}_{9 \times 9} \mathbf{RTM01}_{9 \times 3} \phi_{3 \times 1} + \mathbf{RM01}_{9 \times 3} \mathbf{PHPM01}_{3 \times 9} \mathbf{DTM01}_{9 \times 3} \phi_{3 \times 1} \\ &\quad + \mathbf{RM01}_{9 \times 3} {}^1\mathbf{D}_{3 \times 3} {}_0\phi'_{3 \times 1} \end{aligned} \quad (\text{C.36})$$

After grouping the coefficients of  $\phi$  and  ${}_0\phi'$ , the vector  ${}_0\mathbf{\tilde{R}}'$  becomes

$$\mathbf{DDM01}_{9 \times 3} = C_3 \begin{bmatrix} -({}^1\phi_2^2 + {}^1\phi_3^2){}^1\phi_1 & -({}^1\phi_2^2 + {}^1\phi_3^2){}^1\phi_2 & -({}^1\phi_2^2 + {}^1\phi_3^2){}^1\phi_3 \\ {}^1C_{12}{}^1\phi_1 & {}^1C_{12}{}^1\phi_2 & {}^1C_{12}{}^1\phi_3 \\ {}^1C_{13}{}^1\phi_1 & {}^1C_{13}{}^1\phi_2 & {}^1C_{13}{}^1\phi_3 \\ {}^1C_{12}{}^1\phi_1 & {}^1C_{12}{}^1\phi_2 & {}^1C_{12}{}^1\phi_3 \\ -({}^1\phi_1^2 + {}^1\phi_3^2){}^1\phi_1 & -({}^1\phi_1^2 + {}^1\phi_3^2){}^1\phi_2 & -({}^1\phi_1^2 + {}^1\phi_3^2){}^1\phi_3 \\ {}^1C_{23}{}^1\phi_1 & {}^1C_{23}{}^1\phi_2 & {}^1C_{23}{}^1\phi_3 \\ {}^1C_{13}{}^1\phi_1 & {}^1C_{13}{}^1\phi_2 & {}^1C_{13}{}^1\phi_3 \\ {}^1C_{23}{}^1\phi_1 & {}^1C_{23}{}^1\phi_2 & {}^1C_{23}{}^1\phi_3 \\ -({}^1\phi_1^2 + {}^1\phi_2^2){}^1\phi_1 & -({}^1\phi_1^2 + {}^1\phi_2^2){}^1\phi_2 & -({}^1\phi_1^2 + {}^1\phi_2^2){}^1\phi_3 \end{bmatrix}$$

$${}^1C_{12} = {}^1\phi_1 {}^1\phi_2$$

$${}^1C_{13} = {}^1\phi_1 {}^1\phi_3$$

$${}^1C_{23} = {}^1\phi_2 {}^1\phi_3$$

$$C_3 = |{}^1\phi|^{-4} \left( 3|{}^1\phi|^{-1} \sin|{}^1\phi| - 2 - \cos|{}^1\phi| \right)$$

Figure C.2 Matrix **DDM01** from the expression for  $\mathbf{D}_D$ .

$$\underset{9 \times 1}{\overset{0}{\mathbf{R}'}} = \begin{bmatrix} \underset{9 \times 3}{\mathbf{RPR1}} & \underset{9 \times 3}{\mathbf{RPR2}} \end{bmatrix} \begin{bmatrix} \underset{3 \times 1}{\phi} \\ \underset{3 \times 1}{\overset{0}{\phi'}} \end{bmatrix} \quad (\text{C.37})$$

where the matrix **RPR1** is equal to

$$\underset{9 \times 3}{\mathbf{RPR1}} = \underset{9 \times 9}{\mathbf{OMGM01}} \underset{9 \times 3}{\mathbf{RTM01}} + \underset{9 \times 3}{\mathbf{RM01}} \underset{3 \times 9}{\mathbf{PHPM01}} \underset{9 \times 3}{\mathbf{DTM01}}, \quad (\text{C.38})$$

and the matrix **RPR2** is equal to

$$\underset{9 \times 3}{\mathbf{RPR2}} = \underset{9 \times 3}{\mathbf{RM01}} \underset{3 \times 3}{\mathbf{D}} \quad (\text{C.39})$$

## **Vita**

J.E. Warren was born in Newport News, Virginia on June 9, 1965. In 1983 he graduated from Tabb High School in York County, Virginia. Later that same year he began his undergraduate studies at Virginia Polytechnic Institute and State University and received a B.S. in Civil Engineering from VPI&SU in June of 1987. In September of 1987 he began his graduate study and successfully completed the requirements for a M.S. in Civil Engineering (Structures) from VPI&SU during February of 1989. After working for Newport News Shipbuilding for a short time, the author continued his graduate work and successfully fulfilled the requirements for a Ph.D. in Engineering Mechanics during January of 1997.

J.E. Warren